Acoustical Physics, Vol. 49, No. 6, 2003, pp. 615–619. Translated from Akusticheskiĭ Zhurnal, Vol. 49, No. 6, 2003, pp. 725–730.

Correlation Reception of Thermal Acoustic Radiation

A. A. Anosov[1,3], Yu. N. Barabanenkov[1,2], and A. G. Sel'skiĭ[1,2]

[1] *ELDIS Research Center, Russian Academy of Sciences, Russia*

[2] *Institute of Radio Engineering and Electronics, Russian Academy of Sciences, Moscow, Russia*

[3] *Sechenov Medical Academy, Moscow, Russia*

e-mail: anosov@hotmail.ru

Received November 18, 2002

Abstract—Correlated signals of thermal acoustic radiation from heated sources extending in the transverse direction (a pair of narrow plasticine plates and a wide plasticine strip) are measured. The measurements are performed by multiplying together the signals that are shifted in time with respect to each other and detected by two piezoelectric transducers. The values of the correlated signals of thermal acoustic radiation are determined by the spatial variation of temperature in the medium under study. © *2003 MAIK "Nauka/Interperiodica".*

To measure the in-depth temperature of biological objects, it is possible to use a passive acoustic thermal tomograph based on the detection of thermal acoustic radiation [1]. The first experiments on measuring the in-depth temperature distribution [2] and localizing the thermal sources in model objects [3] with the help of noncoherent reception of thermal acoustic radiation were conducted earlier. The same technique was used to measure the internal temperature profile in the human hand [4]. The thermal acoustic emission from heated soft tissues of a biological object was measured in [5]. The opportunities offered by the correlation reception of thermal acoustic radiation as the basis of passive acoustic thermal tomography were discussed theoretically in a series of papers [6–8]. Experimental studies of the correlation reception of acoustic (nonthermal) noise radiation [9] and the focused reception of thermal acoustic radiation [10, 11] were conducted for the same purpose. Space and space–time correlation functions for the pressure of thermal acoustic radiation were measured and studied experimentally [1, 12–14]. Theoretical studies of the correlation reception of thermal acoustic radiation are currently in progress [8, 15, 16].

In our previous paper [14], we experimentally demonstrated the possibility of obtaining a nonzero correlated signal (a space–time correlation function of pressure) of thermal acoustic radiation using a pair of piezoelectric transducers by shifting in time the measured signals with respect to each other. The radiation source was a motionless narrow heated plate. The small characteristic size of the source, which was smaller than the half-period of the spatial correlation function, was needed to obtain a nonzero correlated signal [12]. However this requirement is inadmissible in the case of thermal tomography of biological objects. The purpose of this work is to investigate experimentally the feasibility of the correlation reception of thermal acoustic radiation from extended sources whose transverse size has no strict limitations.

The experimental setup was analogous to that presented in [14] and included a water-filled basin *1* (Fig. 1). Two circular flat piezoelectric transducers (PT_1 and PT_2) with a radius of $a = 5$ mm and a distance between the centers of $D = 18$ mm served as the receivers of thermal acoustic radiation. The acoustic axes of the piezoelectric transducers lay in the horizontal plane and intersected at a distance of $z = 200$ mm from the transducers on the x axis. The piezoelectric transducers, whose average reception frequency was $f = 2.2$ MHz and whose transmission band was $\Delta f = 0.6$ MHz, were equipped with quarter-wavelength layers and had approximately equal sensitivities. Two sources of thermal acoustic radiation were used: a pair of parallel narrow plasticine plates (not shown in Fig. 1) with a width (along the x axis) of $d = 4$ mm (the distance between the plates was 4 mm) and a wide plasticine strip *2*. The strip width and also the lengths (the vertical dimensions) of the plates and the strip were greater than the transverse dimension of the spread functions of the receivers of thermal acoustic radiation. The thickness of the sources was 5 mm, which implied an almost complete absorption of ultrasound in plasticine. The sources of thermal acoustic radiation were positioned in a cell *3* with foam-plastic walls and acoustically transparent windows. The cell was also filled with water, which was heated with respect to the basin.

The method of signal detection coincided with that described in [14]. The sound pressures at PT_1 and PT_2 were transformed into electric signals, which were transmitted through preamplifiers *4*, *5* (designed by M.A. Antonov [12]) and then through amplifiers *6*, *7* (U3-29 and U3-33). Using an 8-bit card (LA-n10MPCI, manufactured by ZAO Rudnev–Shilyaev, Russia), the amplified signals were stored in a

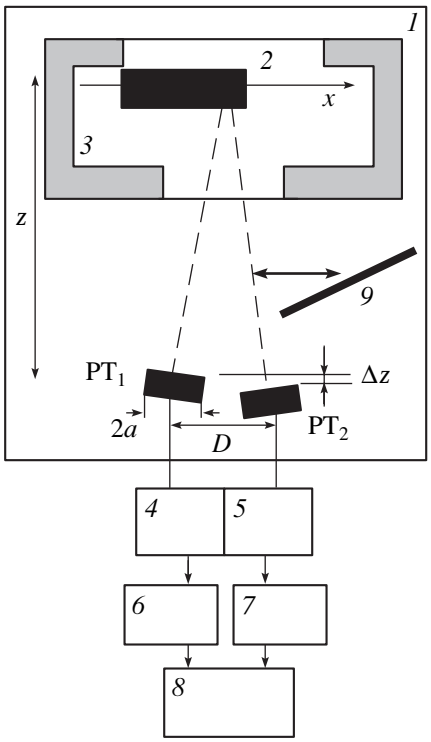

Fig. 1. Experimental setup: (*1*) basin, (*2*) plasticine strip, (*3*) cell, (*4*, *5*) preamplifiers, (*6*) U3-39 amplifier, (*7*) U3-33 amplifier, (*8*) personal computer, and (*9*) reflecting plate; PT_1 and PT_2 are piezoelectric transducers with a radius a; D is the distance between their centers; z is the distance from the x axis to the piezoelectric transducers; and Δz is the shift of one transducer with respect to the other.

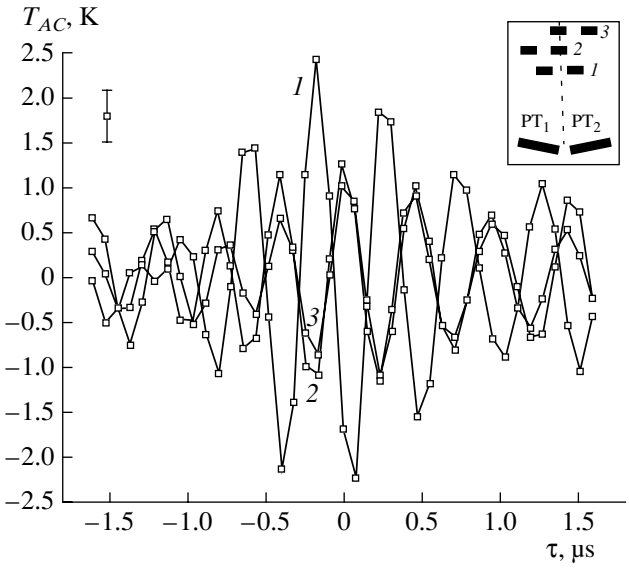

Fig. 2. Measured correlated acoustic brightness temperatures T_{AC} of a pair of plates vs. the delay time τ of one signal with respect to the other. The inset shows the geometry of the experiment (the experimental curves correspond to the plate positions).

personal computer *8*. The pickup frequency was 12.5 MHz; 256 KB of the card memory were available for two channels. The signals were time-shifted with respect to each other in the computer, and the average value of the products of signal readings was determined. The measurements were repeated to obtain statistically significant results (the integration time was about 40 s).

The measurements were conducted in two modes: in the first case (the "open" state), the signal arriving at a piezoelectric transducer originated from the source, and in the second case (the "closed" state), a reflecting duralumin plate *9* was positioned between the piezoelectric transducer and the cell; i.e., the signal arriving at the transducer originated from the basin, the temperatures of the transducer and the basin coinciding. To eliminate signal drift and possible nonacoustic sources of correlation, the difference between the averaged functions in the first and second modes was calculated. To normalize the correlated signals in degrees, the intensity of thermal acoustic radiation (the acoustic brightness temperature) was measured by each transducer in the open and closed states from the wide strip completely spanning the spread function of the piezoelectric transducers. In this case, the strip is an acoustic blackbody and the difference between the intensities of thermal acoustic radiation in the open and closed states is proportional to the difference in the temperatures of the strip and the basin. We call the correlated signal in degrees the correlated acoustic brightness temperature T_{AC} (as proposed in [12]).

The correlated signal for a pair of plates was measured with three positions of the source (see the inset in Fig. 2): (*1*) the plates positioned vertically and symmetrically with respect to the acoustic axis of the system, (*2*) the plates shifted to the left, and (*3*) the plates shifted to the right by 4 mm. Figure 2 presents the measured correlated acoustic brightness temperatures T_{AC} of thermal acoustic radiation as functions of the time shift (delay) τ of one signal relative to the other. The experimental data for three positions of the source are connected for illustration by broken lines (*1*, *2*, and *3*, respectively). The standard measurement error averaged over all shifts is shown in the plot in the upper left corner. The correlated signal for a wide strip was also measured for three positions of the source (see the inset in Fig. 3): (*1*) the strip "fills" half of the spread function of the piezoelectric transducers and also a 3-mm-wide section to the left of the acoustic axis of the system, (*2*) the strip is shifted to the right by 4 mm, and (*3*) the strip completely covers the spread function. Figure 3 presents the measured correlated acoustic brightness temperatures $T_{AC}(\tau)$ for all three positions of the source, which are connected for illustration by broken lines (*1*, *2*, and *3*, respectively).

All measured correlated signals (except for curve *3* in Fig. 3) are oscillating functions with envelopes that are maximal at $\tau \approx 0$ and decrease with increasing delay

τ. Such a shape of the correlated signal is related to the finite transmission band of the piezoelectric transducers Δf.

The time period of the correlation function (correlated acoustic brightness temperature) is determined by the average reception frequency and is equal to $T = 1/f = 0.45$ μs. As confirmed by our experiments [1, 12, 13], the spatial period of the correlated signal is equal to $\Lambda = \lambda z/D \approx 8$ mm, where λ is the acoustic wavelength in water for the average reception frequency f. If we shift the source along the horizontal x axis by half the spatial period, the new correlated signal must be antiphase with respect to the old one. One can see from Figs. 2 (curves *1*, *2* and *1*, *3*) and 3 (curves *1*, *2*) that the results of measurements satisfy this condition. Note that a pair of plates (see the inset in Fig. 2) is shifted from position *2* to position *3* by 8 mm (a full period) and that curves *2* and *3* (Fig. 2) vary in phase.

Figure 3 presents the correlated signal (curve *3*) measured when the wide strip with a constant temperature completely covered the spread function of the receiving system. Note that theoretical estimates for such a case, which were presented in [8, 12, 13], show that the signal must be zero, and we obtained experimentally a zero correlated signal for a wide strip at $\tau = 0$ in [12, 13]. Experimental data confirm the theoretical estimates: curve *3* (Fig. 3) oscillates near zero within the limits of the measurement error.

The signal of thermal acoustic radiation depends on the ultrasonic absorption in the medium and on the temperature of the medium. The acoustic brightness temperature T_A is determined for a medium whose temperature T and energy absorption coefficient γ depend on only the depth z, according to the formula proposed in [17] and tested experimentally in [18]:

$$T_A = \int_0^\infty \gamma(z) T(z) \exp\left[-\int_0^z \gamma(z)\,dz\right] dz. \qquad (1)$$

In the experimental setup, the basin models an infinite weakly absorbing medium with a constant temperature T_0 coinciding with the temperature of the receivers of thermal acoustic radiation. In this case, the acoustic brightness temperature T_A is equal to the thermodynamic temperature, $T_A = T_0$, and the correlated signal is zero. The cell heated to the temperature ΔT with respect to the basin creates a temperature inhomogeneity. If we do not put plasticine into the cell, the signal of thermal acoustic radiation will be almost undetectable, $T_A \approx T_0$, because of the small ultrasonic absorption in a water medium with limited thickness. If we put plasticine strips (acoustic blackbodies) into the cell, the integration of Eq. (1) over the depth in the plasticine gives the following result:

$$T_A = T_0 + K\Delta T, \qquad (2)$$

where the coefficient is $K = 1$ when the wide strip covers the whole aperture of the receiving system. If the strip does not cover the whole aperture, the energy absorption coefficient γ depends not only on depth z but also on transverse coordinate x. In this case, Eq. (2) is also valid [10] and coefficient K is equal to the ratio of angular dimension θ of the strip to angular dimension Ω of the spread function of the piezoelectric transducers: $K = \theta/\Omega$. Thus, the utilization of acoustic blackbodies in the experiment simplifies the taking of the absorption of thermal acoustic radiation into consideration.

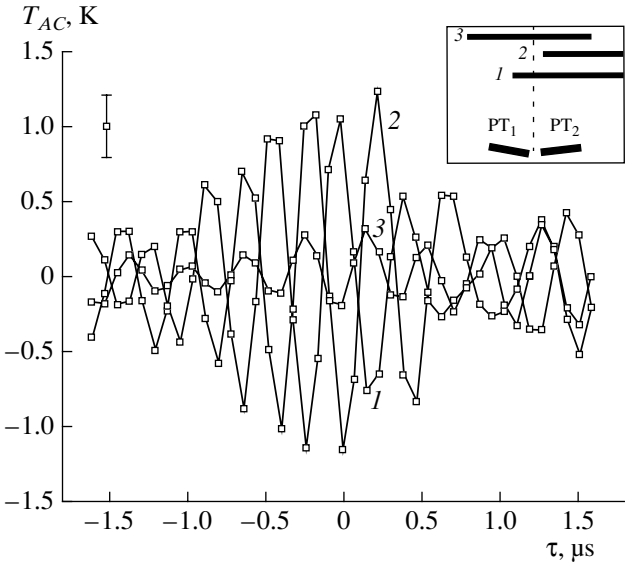

Fig. 3. Measured correlated acoustic brightness temperatures T_{AC} of the wide strip vs. delay time τ of one signal with respect to the other. The inset shows the geometry of the experiment (the experimental curves correspond to the plate positions).

The calculation of the acoustic brightness temperature of a plate limited along the x axis by coordinates x_1 and x_2 ($d = x_2 - x_1$) and infinite along the y axis can be conducted using the results of [12, 14, 19]. If we model the piezoelectric transducers by vertical infinite strips with a thickness of $2a$, use the Fraunhofer approximation, and assume that the transmission band of the piezoelectric transducers Δf is rectangular and sufficiently narrow ($\Delta f/f \ll 1$), the correlated acoustic brightness temperature of the plate will be determined by the formula

$$T_{AC}(\tau) = \Delta T \frac{2a}{\lambda} \int_{x_1}^{x_2} \frac{\sin^2 \frac{2\pi a x}{\lambda z} \sin^2 \frac{\pi \Delta f}{f}\left(\frac{Dx}{\lambda z} - f\tau\right)}{\left(\frac{2\pi a x}{\lambda z}\right)^2 \left[\frac{\pi \Delta f}{f}\left(\frac{Dx}{\lambda z} - f\tau\right)\right]} \times \cos 2\pi\left(\frac{Dx}{\lambda z} - f\tau\right)\frac{dx}{z}, \qquad (3)$$

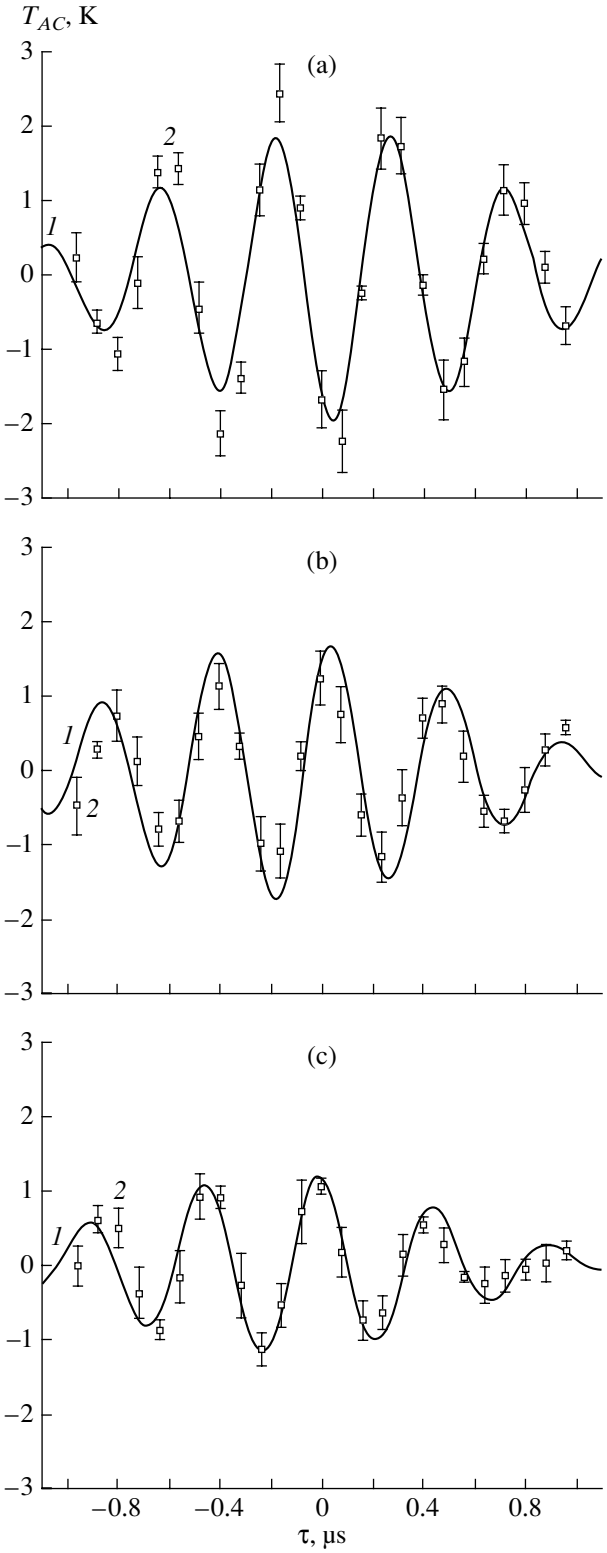

Fig. 4. Calculated functions $T_{AC}(\tau)$ (curves *1*) and experimental data (dots *2*) (a) for a pair of plates symmetric with respect to the acoustic axis (in the calculations, the temperature difference between the plates and the basin was assumed to be $\Delta T = 8$ K), (b) for a pair of plates shifted with respect to the acoustic axis ($\Delta T = 8$ K), and (c) for a wide strip covering more than half of the aperture of the receiving system ($\Delta T = 15$ K).

where the factor $\sin^2\frac{2\pi ax}{\lambda z}/\left(\frac{2\pi ax}{\lambda z}\right)^2$ is determined by equal spread functions of the piezoelectric transducers, the factor $\sin^2\frac{\pi\Delta f}{f}\left(\frac{Dx}{\lambda z} - f\tau\right)/\left[\frac{\pi\Delta f}{f}\left(\frac{Dx}{\lambda z} - f\tau\right)\right]^2$ is determined by equal finite transmission bands of the piezoelectric transducers, and the factor $\cos 2\pi\left(\frac{Dx}{\lambda z} - f\tau\right)$ determines the oscillating character of the correlated signal. The presence of the temperature difference ΔT between the source and the ambient medium in Eq. (3) is connected with the fact that a nonzero correlated signal arises only in the presence of temperature variation in space.

Let us demonstrate that Eq. (3) is valid for noncoherent reception at $D = 0$ and $\tau = 0$. If the source width d is greater than the transverse dimension of the spread function of the piezoelectric transducers ($\theta = d/z > \Omega = \lambda/2a$), the acoustic brightness temperature (and, more precisely, the increment of the acoustic brightness temperature, i.e., the difference between the acoustic brightness temperatures of the source and the basin) is equal to the thermodynamic temperature: $\Delta T_A = \Delta T$. For the source positioned at the acoustic axis of the system, from Eq. (3) it follows that its acoustic brightness temperature is determined by the way it fills the aperture: $\Delta T_A = 2ad/\lambda z\Delta T = \theta/\Omega\Delta T$. Both results are consistent with the above argumentation.

Figure 4 presents the correlated acoustic brightness temperatures T_{AC} (curves *1*), calculated by the numerical integration of Eq. (3), as functions of delay time τ for three cases: the cases shown in the inset in Fig. 2, positions *1* and *2* (Figs. 4a and 4b, respectively) and the case shown in the inset in Fig. 3, position *1* (Fig. 4c). The corresponding experimental data are also shown in Fig. 4 (dots *2*). Note that in the process of calculation we used the value of the temperature difference ΔT between the cell and the basin as an adjustable parameter. This is connected with the fact that the scheme of measurements did not allow us to maintain a constant value of ΔT over a long time (a slow heat transfer between the cell and the basin occurred through the cell windows covered by a thin lavsan film).

One can see from Fig. 4a (4b) that the minimum (maximum) of the correlation function is shifted to the right by $\Delta\tau \approx 0.05$ μs with respect to $\tau = 0$, where it must occur according to the geometry of experiment (see the inset in Fig. 2, position *1* (position *2*)). This is apparently connected with the shift Δz of the piezoelectric transducers along the z axis (see Fig. 1). The shift value $\Delta z = 0.1$ mm taken into account in the calculations is connected with the inaccuracy of positioning the piezoelectric transducers in the basin.

Analyzing the form of the acoustic brightness temperature $T_{AC}(\tau)$ (Fig. 4c) for a wide strip filling approximately half of the spread function of the piezoelectric

transducers (see the inset in Fig. 3), it is necessary to note that, according to Eq. (3), the shift in the x coordinate is analogous to time shift τ. If at $\tau = 0$ the strip fills the whole spread function of the piezoelectric transducers or exactly half of the spread function, the correlated signal is zero (this follows from the parity of the integrand in Eq. (3)). Shifting the strip along the x axis, for example, by 3 mm, leads to the appearance of a nonzero correlation component, which is determined by a thin strip 3 mm in width. Further shifting leads to damped oscillations of the correlated signal. An analogous situation occurs in the case of a shift in time. The function $T_{AC}(\tau)$ calculated from Eq. (3) has a positive value at $\tau = 0$. This can be explained by the fact that the strip fills half of the spread function of the piezoelectric transducers plus 3 mm.

It is necessary to note that a similar result can be obtained using the idea of a receiving system as a filter of spatial frequencies with its own spatial frequency $D/\lambda z$ [19]. The spatial spectrum of a wide strip (a step) is white noise, from which the filter selects the corresponding frequency band.

As one can see from Figs. 4a–4c, the calculated curves adequately approximate the experimental points at a preset ΔT.

Thus, we experimentally obtained nonzero correlated signals from sources of thermal acoustic radiation whose transverse dimensions considerably vary. This is a necessary first step towards a comprehensive investigation of the direct problem of passive acoustic thermal tomography based on the correlation reception of thermal acoustic radiation. It should be noted that we experimentally demonstrated the possibility of distinguishing the sources of thermal acoustic radiation only in the plane perpendicular to the acoustic axis of the system. Further investigation must take into account the extension of the sources in depth and the absorption of acoustic waves in the medium.

ACKNOWLEDGMENTS

This work was supported by the Russian Foundation for Basic Research, project no. 02-02-17371.

REFERENCES

1. V. I. Pasechnik, A. A. Anosov, and K. M. Bograchev, Biomed. Radioélektron., No. 2, 3 (1999).
2. V. I. Passechnik, A. A. Anosov, M. G. Isrefilov, and A. V. Erofeev, Ultrasonics **37**, 63 (1999).
3. E. V. Krotov, S. Yu. Ksenofontov, A. D. Mansfel'd, *et al.*, Izv. Vyssh. Uchebn. Zaved., Radiofiz. **42** (5), 479 (1999).
4. A. A. Anosov, V. I. Pasechnik, and K. M. Bograchev, Akust. Zh. **44**, 725 (1998) [Acoust. Phys. **44**, 629 (1998)].
5. R. A. Kruger, D. R. Reinecke, and G. A. Kruger, Med. Phys. **26**, 1832 (1999).
6. R. Hessemer, T. Perper, and T. Bowen, U.S. Patent No. 4,416,552 (22 November 1983).
7. V. I. Pasechnik, Akust. Zh. **43**, 563 (1997) [Acoust. Phys. **43**, 485 (1997)].
8. V. A. Burov, P. I. Darialashvili, and O. D. Rumyantseva, Akust. Zh. **48**, 474 (2002) [Acoust. Phys. **48**, 412 (2002)].
9. V. V. Gerasimov, Yu. V. Gulyaev, A. V. Mirgorodskiĭ, *et al.*, Akust. Zh. **45**, 487 (1999) [Acoust. Phys. **45**, 433 (1999)].
10. A. A. Anosov, V. I. Pasechnik, and V. V. Shablinskiĭ, Akust. Zh. **37**, 610 (1991) [Sov. Phys. Acoust. **37**, 315 (1991)].
11. E. V. Krotov, A. D. Mansfel'd, A. M. Reĭman, and V. A. Vilkov, in *Proceedings of XI Session of the Russian Acoustical Society*, Vol. 3: *Acoustics of Speech. Medical and Biological Acoustics* (GEOS, Moscow, 2001), pp. 165–169.
12. A. A. Anosov, M. A. Antonov, and V. I. Pasechnik, Akust. Zh. **46**, 28 (2000) [Acoust. Phys. **46**, 21 (2000)].
13. A. A. Anosov and V. I. Passechnik, Akust. Zh. **49**, 161 (2003) [Acoust. Phys. **49**, 129 (2003)].
14. V. I. Passechnik, A. A. Anosov, Yu. N. Barabanenkov, and A. G. Sel'skiĭ, Akust. Zh. **49** (5) (2003) [Acoust. Phys. **49**, 580 (2003)].
15. V. I. Passechnick and Yu. N. Barabanenkov, J. Acoust. Soc. Am. **99**, 65 (1996).
16. V. I. Passechnik, Akust. Zh. **48**, 675 (2002) [Acoust. Phys. **48**, 589 (2002)].
17. V. I. Babiĭ, Morsk. Gidrofiz. Issled., No. 2 (65), 189 (1974).
18. V. I. Passechnik, Ultrasonics **32**, 293 (1994).
19. N. A. Esepkina, D. V. Korol'kov, and Yu. N. Pariĭskiĭ, *Radio Telescopes and Radiometers* (Nauka, Moscow, 1973).

Translated by M. Lyamshev

Acoustical Physics, Vol. 49, No. 6, 2003, pp. 620–626. Translated from Akusticheskiĭ Zhurnal, Vol. 49, No. 6, 2003, pp. 731–737.

Active Control of Sound in a Room: Method of Global Impedance Matching

Yu. I. Bobrovnitskiĭ

Blagonravov Institute of Mechanical Engineering, Russian Academy of Sciences, Malyĭ Khariton'evskiĭ per. 4, Moscow, 101990 Russia

e-mail: bobrovni@orc.ru

Received May 21, 2003

Abstract—The problem of acoustic identity of two different rooms is formulated and solved theoretically by using an active closed surface. The corresponding law governing the operation of active elements is based on the matching of impedance matrices. The solution obtained is validated by a simple example. © *2003 MAIK "Nauka/Interperiodica".*

The development of active methods of sound and vibration control has proceeded vigorously in the last few years. Despite their complexity (they require additional sound sources, i.e., actuators with the corresponding control devices), their practical application is often feasible and justified thanks to the progress in microelectronics and digital data processing. The use of active noise control methods in solving various practical problems of noise control in industry, especially in the low-frequency range where conventional (passive) methods are ineffective, is described, for example, in [1, 2].

The main purpose of using active methods in rooms is to reduce the noise levels, e.g., in shops, offices, aircraft cabins, automobiles, and other vehicles. As a rule, this problem is solved with one of three approaches. The first of them, the conventional approach, was proposed by the founder of active methods [3] and then developed by other specialists [1]. It consists in the superposition of the initial sound field and the secondary sound field, which is produced by acoustic actuators and differs in sign from the initial field. The interference of the initial and secondary fields leads to their mutual suppression in the whole room or part of it. The second approach is based on the effect of vibration actuators on the elastic walls. This effect changes the conditions of sound transmission into the room from outside, for example, the penetration of noise produced by turboprop engines into an aircraft cabin [2, 4]. The third approach, which is closest to that considered in this paper, consists in changing the impedance of the walls of the room by sound or vibration actuators with the aim of reducing the reflections and/or increasing the absorption of sound. This approach is called the method of active impedance matching. Owing to its high efficiency in suppressing resonance vibrations, it is often used for solving noise control problems in rooms of different types and, specifically, in air duct systems [1, 5–9].

Another problem often solved by active methods is improvement in the quality of musical sounds in concert halls and sound-recording studios. Changes in the character of sounds produced by an orchestra or a human voice are achieved via the amplification (or suppression) of certain signal components by acoustic actuators [10].

This paper presents the formulation and the solution of a new, more complicated problem: to make two different rooms acoustically identical. In other words, it is required that, in a given room (e.g., in an ordinary living room), an arbitrary sound source should produce a sound field identical to that produced by the same source in another room or in some other acoustical conditions, e.g., in the open.

In this paper, it is shown that the problem formulated above has a solution in the form of an active ("intellectual") closed surface S, which may geometrically coincide with the boundaries (walls) of a given room or may lie inside this room. When the operation of actuators occurs according to a certain law, the sound field produced in the volume V inside surface S by an arbitrary source will be identical to the field produced by the same source in a similar volume V in another room. In practice, such an active surface may consist of a set of identical active thin panels positioned on surface S with a sufficient density (no less than one panel per square area of a half-wavelength on a side). Each panel is assumed to have one vibration actuator, one accelerometer and a microphone, as well as electronic devices for preliminary signal processing, interfaces, and control circuits. All panels are connected to form a single computer-controlled network. In the literature [7, 9, 11–13], one can find descriptions of active panels

1063-7710/03/4906-0620$24.00

designed for different purposes. Many elements of these panels can be used in the realization of the active surface proposed in this paper.

As will be shown below, the field inside the closed surface S and, hence, the acoustic characteristics of the room are mainly determined by the impedances of the exterior of S, and the effect of actuators on S is equivalent to a change in these external impedances. In the proposed method, the actuators are controlled so as to transform the external impedance matrix of one room to the external impedance matrix of another (given) room. Hence, we are actually dealing with the method of active impedance matching. However, the versions of this method described in the literature are based on the local impedance matching [6–9], whereas the method proposed in this paper is based on matching the complete impedance matrices. This difference is of a fundamental nature: below, it will be shown that no locally responding surface S, neither active nor passive, can solve the problem under study.

Initially, the development of the method proposed in this paper was aimed at the design of a low-frequency anechoic chamber in an arbitrary room. However, the area of practical application of this method proves to be much wider. The ability of a closed active surface to be acoustically transparent (nonscattering) or blocking (totally reflecting) in a selective manner for outer and inner sound sources offers the possibility for a radical solution of the classical problem of noise control in a room, as well as for solving this problem with respect to selected sound sources. In addition, the ability of the active surface to reproduce any acoustical environment in a given spatial region (inside S) makes using the proposed active system promising for sound-recording studios and for research purposes. The theory of the method of global impedance matching is described below together with an analytical example validating this method.

Consider a spatial region V (which can also be called a room) filled with a medium and bounded by a closed surface S. Assume that a source of sound is placed inside this region. Let us divide surface S into N elements and assume that the dimensions of the elements ΔS_j are small compared to the sound wavelength, so that the complex amplitudes of both pressure p_j and normal velocity v_j within these elements are constant ($j = 1, 2, \ldots, N$). The positive direction of the velocity and other vector quantities is taken to be the direction of the outer normal to S. Let us introduce two $N \times N$ impedance matrices, Z_i and Z, determined with respect to boundary S. Now, we show that these matrices, together with the parameters of the source, completely characterize the acoustic properties of spatial region V. By definition, the internal impedance matrix Z_i determines the relation between the N-vector of external forces $f = [f_1, \ldots, f_N]^T$ applied to region V at surface elements ΔS_j and the N-vector of the responses to these forces, i.e., normal velocities $v = [v_1, \ldots, v_N]^T$ of elements ΔS_j:

$$f = Z_i v. \tag{1}$$

The time dependence is assumed to be harmonic, and the factor $\exp(-i\omega t)$ is omitted in the following calculations. Similarly, the $N \times N$ matrix of external impedances Z characterizes the properties of the exterior of surface S:

$$q = Zu, \tag{2}$$

where $q = [q_1, \ldots, q_N]^T$ is the vector of forces applied to the exterior of S at surface elements ΔS_j, and $u = [u_1, \ldots, u_N]^T$ are the amplitudes of the normal velocities of elements ΔS_j moving under the effect of these forces.

Using the impedance matrices introduced by Eqs. (1) and (2), we calculate the field produced in region V by a source positioned inside it. According to the theorem proved in [14], the pressure field in V can be represented as a sum of two components:

$$p(x) = p_0(x) + p_1(x), \quad x \in V. \tag{3}$$

The first component $p_0(x)$ is the field of the source operating in region V with the boundary S at rest:

$$v_0(s) = 0, \quad s \in S. \tag{4}$$

The second component is the field of forced combined vibrations of region V with the exterior of S under the action of the external force $b(s)$ distributed over S when the source is turned off. In [14], it was shown that the distributed force $b(s)$ is equal to the pressure $p_0(s)$, i.e., to the force with which the first component of the field acts on the stationary boundary S. With allowance for the discretization of surface S, this force is in our case described by the N-vector

$$b = [p_0(s_1)\Delta S_1, \ldots, p_0(s_N)\Delta S_N]^T, \tag{5}$$

where s_j is the coordinate of some point on the jth element of the surface. To calculate the second component of solution (3), it is necessary to use the boundary conditions at surface S: the normal velocities v_1 of the particles of the medium inside S and the velocities u_1 of the exterior of S should be equal, and the sum of forces f_1 and q_1 acting on region V and the exterior of S, respectively, should be equal to force (5):

$$v_1 = u_1, \quad f_1 + q_1 = b.$$

Substituting Eqs. (1) and (2) into these relations, we obtain the solution for the second field component in the form

$$v_1 = (Z_i + Z)^{-1} b, \quad f_1 = Z_i (Z_i + Z)^{-1} b. \tag{6}$$

This solution is determined only at surface S. Although, from this solution, it is possible to calculate unambiguously the values of the second pressure component at surface S, $p_1(s_j) = -f_{j1}/\Delta S_j$, as well as at any inner point

$x \in V$, the following consideration is limited to using this solution, because, for the proposed method of matched impedances, it is sufficient to know only the boundary values of the field given by Eq. (6). It should be noted that, according to Eq. (6), the field in region V (or, more precisely, its second component $p_1(x)$) is determined by the parameters of the sound source (or by vector b), the internal impedances of the room Z_i, and the impedances Z of its exterior (its boundary).

Now, at all elements of surface S, we introduce additional (active) external forces with the amplitudes $f_a = [f_{a1}, \ldots, f_{aN}]^T$ and formulate the problem as follows: it is necessary to find such forces f_a that make the field given by Eqs. (3), (6) identical to the field of the same source in region V of a room with other external impedances Z'. Let us show that the desired active forces should be proportional to the difference between the external impedance matrices:

$$f_a = (Z - Z')v, \tag{7}$$

where v are total normal velocities at all N elements of surface S. Indeed, under the action of forces (5) and (7), the normal velocities of the second field component at S satisfy the vector equation

$$\begin{aligned} v_1 &= (Z_i + Z)^{-1}(b + f_a) = (Z_i + Z)^{-1}b \\ &\quad + (Z_i + Z)^{-1}(Z - Z')v_1, \end{aligned} \tag{8}$$

from which we obtain

$$v_1 = (Z_i + Z')^{-1}b. \tag{9}$$

Since the velocities of the first field component are equal to zero (see Eq. (4)), velocities v of the total field at surface S are expressed by formula (9), i.e., $v = v_1$. Comparing solutions (6) and (9) and taking into account that the boundary values of velocity (9) unambiguously determine the field in the whole region V, one can readily see that active forces (7) change the field in V in such a way that it becomes identical to the field arising when this region V is loaded with the external impedances Z' instead of Z. In other words, the effect of active forces (7) is equivalent to the replacement of impedances Z by Z' and, hence, to the corresponding changes in the acoustic properties of the region (room) under consideration. Thus, an active force obeying the control law given by Eq. (7) completely solves the above-stated problem.

For the practical realization of active action (7), current velocity amplitude v_j should be measured and force f_{aj} should be formed at every surface element ΔS_j of surface S. The external impedance matrices are assumed to be known for both the given room Z and the desired room Z'. (The method of their measurement is described in detail in [15]. In addition to the velocity measurements, this method requires pressure measurements at every surface element ΔS_j.) Therefore, the proposed active system must consist of a set of sensors (accelerometers and microphones) and vibration actuators positioned on boundary surface S: one device of each kind at every element ΔS_j. In addition, the system must contain a controller that forms the control signals for the actuators according to Eq. (7). The stability of the operation of this system is determined by the properties of the matrix operator

$$L = (Z_i + Z')^{-1}(Z_i + Z). \tag{10}$$

This operator appears as a result of adding the term ξ caused by extraneous sources (noise) to Eq. (8). In this case, the term $L\xi$ is added to the right-hand side of solution (9). A detailed study of the stability of the proposed system, its precision, and other aspects of its realization will be the subject of subsequent publications. In this paper, we consider only a simple example, which illustrates the performance of the method and provides the estimates of the fields, control forces, and operator (10) in the framework of one specific problem.

As an example, we consider the acoustic field in a spherical room bounded by a closed spherical wall S of radius R with a local impedance Z_w. The problem is formulated as follows: using a distributed active force of type (7) acting on the wall, it is necessary to change the acoustic field of an arbitrary source positioned inside the room so as to make it identical to the field produced by the same source in a free space. This problem can be solved analytically. Therefore, instead of dividing the boundary into elements and introducing the corresponding impedance matrices, it is possible to use continuous dependences and impedances with respect to forces and velocities continuously distributed in the spherical harmonics. In this case, matrices (1) and (2) are infinite-dimensional but diagonal due to the orthogonality of the spherical functions. This fact allows us to reduce all matrix operations to calculations for individual spherical harmonics.

Let us first assume that the field is excited in the room by a monopole source with a volume velocity g, and this source is positioned at a distance $l < R$ from the center of the sphere. The exact solution to this radiation problem can be obtained by the conventional method [16] in the form of a series expansion in spherical functions. Omitting the intermediate calculations, the pressure amplitude at the point with the spherical coordinates (r, φ, θ) inside the room can be represented as

$$\begin{aligned} &p_{ex}(r, \theta) \\ &= Q\sum_{n=0}^{\infty} P_n(\theta) j_n(kl)\left[h_n(kr) - \frac{\delta_n}{\Delta_n} j_n(kr)\right]. \end{aligned} \tag{11}$$

Here, $Q = \rho c k^2 g/4\pi$, ρc is the characteristic impedance of the medium; $k = \omega/c$ is the wave number; $P_n(\cdot)$ is an nth-order Legendre polynomial of the first kind; j_n and h_n are nth-order Bessel and Hankel spherical functions; angle θ is measured with respect to the straight line

connecting the monopole with the sphere center, which serves as the origin of coordinates; and

$$\delta_n = h_n(kR) + (iZ_w/\rho c)h_n'(kR), \quad (12)$$

$$\Delta_n = j_n(kR) + (iZ_w/\rho c)j_n'(kR), \quad (13)$$

where the prime denotes a derivative with respect to the argument. Solution (11) consists of traveling waves (h_n) and standing waves (j_n). The roots of the equations $\Delta_n = 0$ ($n = 0, 1, \ldots$) determine the eigenfrequencies of the room. At these frequencies, the field of the standing waves is maximal. Expression (12) can be represented in the form

$$\delta_n = \frac{h_n'}{i\rho c}(Z_n^\infty - Z_w), \quad (14)$$

where

$$Z_n^\infty = i\rho c\frac{h_n(kR)}{h_n'(kR)} \quad (15)$$

is the local impedance (the pressure-to-velocity ratio) of an unbounded medium with parameters ρ and c of the exterior of the sphere of radius R when the pressure and the velocity are distributed over S according to the nth spherical harmonic [16]. From Eqs. (11) and (14) it follows that, when all δ_n are equal to zero, the field in the room corresponds to the conditions of a free space:

$$p_{ex}(r, \theta) = Q\sum_{n=0}^{\infty} P_n(\theta)j_n(kl)h_n(kr) = Qh_0(kr_1) = p^\infty(r, \theta), \quad (16)$$

where $r_1 = |r - l|$ is the distance from the monopole to the point of observation. The summation of series (16) was performed using the spherical function summation theorem [16]. From Eqs. (11) and (14) it also follows that no passive coating with a local impedance Z_w (homogeneous or inhomogeneous in the s coordinate) can provide the free space conditions. An exception is the high-frequency range

$$kR \gg 1, \quad (17)$$

where, for all n, the approximate equalities $h_n' \approx ih_n$ and $Z_n^\infty \approx \rho c$ are valid. Choosing a passive coating with the local impedance $Z_w = \rho c$, one can approximately solve the above-stated problem for the frequencies determined by inequality (17), i.e., in the frequency range where the sound wavelengths are much smaller than the room dimensions.

Let us show that, by using an active force of type (7) continuously distributed over the wall, it is possible to obtain the solution to the problem for all frequencies, including the lowest ones.

First, we apply representation (3) to solution (11). Then, the first field component satisfying boundary condition (4) will have the form

$$p_0(r, \theta) = Q\sum_{n=0}^{\infty} P_n(\theta)j_n(kl)\left[h_n(kr) - \frac{h_n'(kR)}{j_n'(kR)}j_n(kr)\right]. \quad (18)$$

This component can be obtained in a conventional way as the field expansion in spherical functions [16]. Setting $r = R$ in Eq. (18), we obtain an expression for the pressure at the wall at rest:

$$b(\theta) = p_0(R, \theta) = \sum_{n=0}^{\infty} b_n P_n(\theta), \quad b_n = -\frac{iQ}{(kR)^2 j_n'(kR)}. \quad (19)$$

The second field component, according to Eq. (6), has the form

$$v_1(R, \theta) = \sum_{n=0}^{\infty} v_{1n}P_n(\theta), \quad v_{1n} = \frac{b_n}{Z_w + Z_{in}} = \frac{Qj_n(kl)}{\rho c(kR)^2\Delta_n}, \quad (20)$$

$$p_1(r, \theta) = \sum_{n=0}^{\infty} p_{1n}P_n(\theta)j_n(kr), \quad p_{1n} = \frac{iQj_n(kl)}{(kl)^2\Delta_n j_n'(kR)}. \quad (21)$$

Here, we used an equality that can be easily proved with Eq. (13):

$$\Delta_n = -\frac{j_n'(kR)}{i\rho c}(Z_w + Z_{in}),$$

where

$$Z_{in} = -i\rho c\frac{j_n(kR)}{j_n'(kR)} \quad (22)$$

is the impedance of the medium inside the sphere under the force acting on the boundary and distributed over it according to the nth spherical harmonic. Combining Eqs. (18) and (21), one can easily see that their sum coincides with solution (11).

Now, according to Eq. (7), we introduce an active force distributed over the boundary $r = R$:

$$f_a(\theta) = \sum_{n=0}^{\infty} f_{an}P_n(\theta), \quad f_{an} = (Z_w - Z_n^\infty)v_{an}, \quad (23)$$

where v_{an} are the expansion coefficients from the expansion of the total velocity at S in the spherical harmonics and Z_n^∞ is the impedance of the exterior of S in a free space (see Eq. (15)).

Since the total velocity is the response to forces (19) and (23), the following equality is satisfied (see also Eq. (20)):

$$\sum_{n=0}^{\infty} v_{an} P_n(\theta) = \sum_{n=0}^{\infty} P_n(\theta) \frac{b_n}{Z_w + Z_{in}} + \sum_{n=0}^{\infty} P_n(\theta) \frac{Z_w - Z_n^\infty}{Z_w + Z_{in}} v_{an}. \quad (24)$$

From Eq. (24), by virtue of the orthogonality of the Legendre polynomials, we obtain

$$v_{an} = \frac{b_n}{Z_n^\infty + Z_{in}} = \frac{Q}{i\rho c} j_n(kl) h_n'(kR). \quad (25)$$

From this velocity of the boundary, it is easy to calculate the second component of the field inside the spherical cavity under consideration:

$$p_{a1}(r, \theta) = Q \sum_{n=0}^{\infty} P_n(\theta) j_n(kl) \frac{h_n'(kR)}{j_n'(kR)} j_n(kr).$$

The sum of this component and the first component given by Eq. (18) yields the total pressure field with allowance for the effect of active forces:

$$p(r, \theta) = p_0(r, \theta) + p_{a1}(r, \theta) = Q \sum_{n=0}^{\infty} P_n(\theta) j_n(kl) h_n(kr). \quad (26)$$

One can readily see that pressure field (26) coincides with the field produced by the monopole in a free space, which is given by Eq. (16). This means that active force (23) transforms field (11) inside the region $r \le R$ to field (26): the "active" component of the field suppresses the standing wave component of field (11) and leaves unaffected the other component consisting of spherical waves of all orders that travel away from the source.

Since the result obtained above is valid for a monopole source positioned at any point of the acoustic cavity under consideration, it should also be valid for a set of several monopoles by virtue of the superposition principle. Since any source of sound can be modeled by a set of monopoles [17, 18], the result is valid for any arbitrary source. The difference is only in the values of the "blocked" pressure (19) and the coefficients b_n in Eqs. (24) and (25). Thus, the active forces given by Eqs. (7) and (23) transform the field of an arbitrary sound source in a spherical region with an impedance boundary to the field of the same source in a free space. Since we did not impose any limitations on the frequency, the solution is valid in the whole frequency range. Hence, the problem stated at the beginning of this paper is completely solved.

In closing, let us estimate the magnitude of the necessary active force given by Eq. (23) and also consider the behavior of the inevitable noise component under the effect of this force, i.e., consider the stability of our solution.

Let an additional field (noise) caused by extraneous sources (lying outside the region of interest) be present in the region under consideration, and let the pressure of this field at boundary S be described as

$$p_\xi(\theta) = \sum_{n=0}^{\infty} p_{\xi n} P_n(\theta). \quad (27)$$

Then, the velocity normal to S is expressed as

$$v_\xi(\theta) = \sum_{n=0}^{\infty} P_n(\theta) \frac{j_n'(kR)}{i\rho c} p_{\xi n}.$$

Adding this velocity to the right-hand side of Eq. (24) and repeating the calculations described above, we obtain the following expression for the pressure field inside the region $r \le R$:

$$p(r, \theta) = p^\infty(r, \theta) + \sum_{n=0}^{\infty} P_n(\theta) a_n p_{\xi n} \frac{j_n(kr)}{j_n(kR)}. \quad (28)$$

Here, p^∞ is the field of the source in a free space, which is given by Eqs. (16) and (26); the term under the summation sign is noise (27) changed by the active force (see also Eq. (10)). The amplification coefficient a_n for the nth spherical harmonic in Eq. (28) can be reduced, using Eqs. (13), (15), and (22), to the form

$$a_n = \frac{Z_{in} + Z_w}{Z_{in} + Z_n^\infty} j_n(kR) = -i h_n'(kR) j_n(kR) (kR)^2 \Delta_n. \quad (29)$$

Analysis of this expression shows that, at low frequencies ($kR \ll 1$), the absolute value $|a_n|$ tends to zero as $[(kR)^{n-1}/(2n-1)!!]$; at high frequencies ($kR \gg 1$), it decreases as $(kR)^{-1}$; and at intermediate frequencies, it is limited. Therefore, the amplification of noise by the active force is also limited. Hence, we can conclude that no type of noise can increase as far as one likes under the action of the active force.

Figure 1 presents the frequency dependence of the resulting amplification coefficient of noise under the

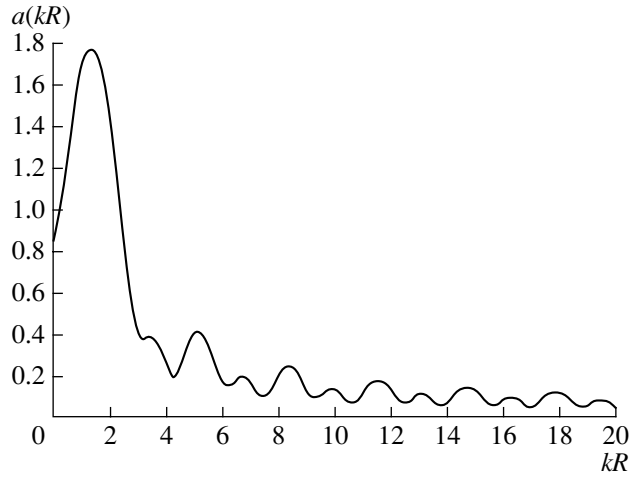

Fig. 1.

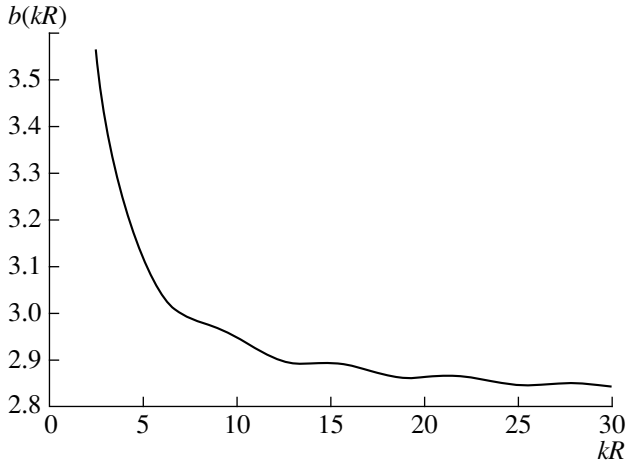

Fig. 2.

effect of the active force. The dependence is calculated by the formula

$$a = \left[\sum_{n=0}^{\infty} |a_n p_{\xi n}|^2 / \sum_{n=0}^{\infty} |p_{\xi n}|^2\right]^{1/2}. \quad (30)$$

The curve corresponds to a spherical room with an absorbing coating on its wall. The local impedance of the coating is assumed to be equal to $Z_w/\rho c = 0.3 + 3i$. The resonances of such a room are characterized by a quality factor of about 100. The noise is assumed to have a spatial spectrum of the type of $|p_{\xi n}| \sim n^{-1}$. The amplification coefficients of individual spherical harmonics are determined by Eq. (29). As one can see from Fig. 1, the maximal amplification is equal to 1.8 and occurs in the vicinity of the first antiresonance frequency of the room, $kR = 1.4$. At all other frequencies, the active system suppresses the noise.

Figure 2 shows the total active force (23) acting on the wall,

$$|f_a| = \left[\iint_S |f_a(\rho, \theta)|^2 dS\right]^{1/2},$$

divided by the pressure force (16) with which the source under consideration acts on surface $r = R$ in free space conditions:

$$|p^{\infty}| = \left[\iint_S |p^{\infty}(R, \theta)|^2 dS\right]^{1/2}.$$

As seen from the plot, the active force distributed over S has an amplitude on the same order of magnitude as the sound pressure produced by the source. However, at low frequencies, the active force increases as $1/kR$, which is a consequence of the poor choice of the source model: a preset volume velocity of the source means that, at low frequencies, the displacement amplitude of the source surface tends to infinity. If the displacement amplitude of the source is limited, the amplitude of the active force will also be limited.

Thus, analysis of the solution to the problem shows that an arbitrary closed room (in the case under study, a spherical cavity with an impedance boundary) can be transformed to a low-frequency anechoic chamber by using accessible means without any unwanted secondary effects.

ACKNOWLEDGMENTS

This work was supported in part by a grant from the President of the Russian Federation, no. NSh-2247.2003.1.

REFERENCES

1. P. A. Nelson and S. J. Elliott, *Active Control of Sound* (Academic, London, 1992).
2. C. R. Fuller, S. J. Elliott, and P. A. Nelson, *Active Control of Vibration* (Academic, London, 1996).
3. P. Lueg, U.S. Patent No. 2043416 (1936).
4. G. H. Koopmann and J. B. Fahnline, *Designing Quiet Structures* (Academic, San Diego, 1997).
5. H. F. Olson and E. G. May, J. Acoust. Soc. Am. **25**, 1130 (1953).
6. D. Guicking and E. Lorentz, Trans. ASME J. Vibr. Acoust. Stress Rel. Design **106** (1), 393 (1984).
7. T. R. Howarth, V. K. Varadan, X. Bao, and V. V. Varadan, J. Acoust. Soc. Am. **91**, 823 (1992).
8. O. Lacour, M. A. Galand, and D. Thenail, J. Sound Vibr. **230** (1), 69 (2000).
9. H. Zhu, R. Rajamani, and K. A. Stelson, J. Acoust. Soc. Am. **113**, 852 (2003).
10. M. Kleiner and P. Svensson, in *Proceedings of the 1995 International Symposium on Active Control of Sound*

and Vibration, ACTIVE 95, Newport Beach, CA, USA (1995), p. 39.

11. R. Gentilman, D. Fiore, R. Torri, and J. Glynn, in *Proceedings of 5th SPIE International Symposium on Smart Structures and Materials, San Diego, CA, USA* (1998), p. 1.
12. C. Guigou and C. R. Fuller, J. Sound Vibr. **220** (3), 541 (1999).
13. S. M. Hirsch, N. E. Meyer, M. A. Westervelt, *et al.*, J. Sound Vibr. **231** (4), 1023 (2000).
14. Yu. I. Bobrovnitskiĭ, Akust. Zh. **47**, 586 (2001) [Acoust. Phys. **47**, 507 (2001)].
15. Yu. I. Bobrovnitskiĭ and G. Pavic, J. Sound Vibr. **261** (3), 527 (2003).
16. E. Skudrzyk, *The Foundations of Acoustics: Basic Mathematics and Basic Acoustics* (Springer, New York, 1971; Mir, Moscow, 1976), Vol. 2.
17. V. D. Kupradze, Usp. Mat. Nauk **22** (2), 59 (1967).
18. Yu. I. Bobrovnitskiĭ and T. M. Tomilina, Akust. Zh. **41**, 737 (1995) [Acoust. Phys. **41**, 649 (1995)].

Translated by E. Golyamina

Acoustical Physics, Vol. 49, No. 6, 2003, pp. 627–637. Translated from Akusticheskiĭ Zhurnal, Vol. 49, No. 6, 2003, pp. 738–750.

Reconstruction of the Fine Structure of an Acoustic Scatterer Against the Distorting Influence of Its Large-Scale Inhomogeneities

V. A. Burov*, I. M. Grishina, O. I. Lapshenkina**, S. A. Morozov*, O. D. Rumyantseva*, and E. G. Sukhov****

** Physics Department, Moscow State University, Vorob'evy gory, Moscow, 119992 Russia*
e-mail: burov@phys.msu.su
*** Trapeznikov Institute of Control Problems, Russian Academy of Sciences, ul. Profsoyuznaya 65, Moscow, 117997 Russia*
e-mail: sukhov@ipu.rssi.ru
Received November 29, 2002

Abstract—In the ultrasonic diagnostics of small-size neoplasms of biological tissues at the earliest stage of their development, an efficient way to eliminate the distorting influence of high-contrast or large inhomogeneities of the biological medium is to apply the iterative technique. A simple approach is proposed, which makes it possible with only two iteration steps to achieve an efficient focusing of the tomograph array. At the first step, the unknown distribution of the large-scale inhomogeneities of sound velocity and absorption over the scatterer is reconstructed, where the large-scale inhomogeneities are those whose size exceeds several wavelengths. At the second step, the fine structure of the scatterer is reconstructed against the large-scale background, which can be performed with a high accuracy owing to the evaluation of the background at the first step. The possibility of simultaneous reconstruction of the large-scale and fine structures by the noniterative Grinevich–Novikov algorithm is considered as an alternative. This algorithm reconstructs in an explicit form two-dimensional refractive–absorbing acoustic scatterers of almost arbitrary shape and strength. Taking into account the effects of multiple scattering, this algorithm provides resolution of the fine structure almost as good as that achieved in reconstructing the same structure against an undistorting homogeneous background. The results of numerical simulations of both algorithms are presented. © *2003 MAIK "Nauka/Interperiodica"*.

One of the most important problems in medicine is the diagnostics of neoplasms of biological tissues. In many cases, for example, in the case of breast cancer, it is very important to detect the nucleation of pathology at the earliest stage of development. The detection of small neoplasms requires rigorous mathematical methods of solving inverse problems. The most used introscopy systems include X-ray tomographs, nuclear magnetic resonance (NMR) tomographs, and ultrasonic systems of the ultrasonic-scanning type. However, these systems have certain disadvantages. For example, X-ray tomographs cannot be considered completely safe. At the same time, their sensitivity to pathological structures of certain types is not always high [1]. At the moment, NMR tomographs provide unsurpassed quality of diagnostics, but they are too expensive to be widely used for routine prophylactic examinations. As for acoustic introscopy systems, their development occurs in two basic directions. On the one hand, there is improvement in the technical characteristics of devices. On the other hand, purely technological upgrading sooner or later leads to a kind of saturation after which further improvement of the device is impossible. This situation calls for a more comprehensive analysis of the physical principles underlying the operation of various types of introscopy systems.

In fact, all active ultrasonic introscopy systems are based on observation of disturbances in the regular propagation of the probing acoustic radiation. In medical problems, the reconstruction of the spatial distribution of acoustic parameters is reduced to a complete or partial solution of a particular inverse problem [2]. An acceptable quality of the reconstruction of a scatterer strongly distorting the incident wave is possible only upon taking into account the wave distortions inside the scatterer. The mathematical and physical aspects of these processes are described in [2]. For a single large-scale (in comparison with λ_0) region with a phase velocity other than c_0, the phase shift is

$$\Delta\psi \cong L\omega\left|\frac{1}{c_0} - \frac{1}{c_0 + \Delta c}\right| \approx Lk_0\frac{|\Delta c|}{c_0}. \qquad (1)$$

Here, c_0, λ_0, and k_0 are the sound velocity, wavelength, and wave number in the homogeneous background medium without an object; L is the linear size of a large region (in the limit, it is the full size of the object under investigation); and $|\Delta c|/c_0$ is the maximum relative variation of the phase velocity. The requirement that the

single scattering approximation (the first Born approximation) be valid, $\Delta\psi \ll \pi/2$, leads to the limitation

$$\frac{|\Delta c|}{c_0}\frac{L}{\lambda_0} \ll 1. \quad (2)$$

For a region of the same size L but consisting of a multitude of inhomogeneities of alternate contrast with the characteristic linear size of fluctuations l, the quantity $\Delta\psi$ is smaller,

$$\Delta\psi \cong k_0 l\sqrt{\frac{L}{l}}\frac{|\Delta c|}{c_0}, \quad (3)$$

and, therefore, the limitation is less strict:

$$\frac{|\Delta c|}{c_0}\frac{l}{\lambda_0}\sqrt{\frac{L}{l}} = \frac{|\Delta c|}{c_0}\frac{\sqrt{lL}}{\lambda_0} \ll 1. \quad (4)$$

Relations (2) and (4) determine the admissible limits and the possibility of using the concepts based on the Born approximation in ultrasonic systems. They mean that the phase shift must not lead to a defocusing of the array.

Let us consider a linear array with a size D not exceeding the size of the inhomogeneity L, i.e., $L \geq D$. In this case, only the difference between additional phase shifts for signals from different sections of the array is important in the formation of the image. This is connected with the fact that the influence of equal additional shifts manifests itself, first of all, only in a shift of the focusing point and image. The defocusing of the array is caused by the difference in the phase shifts, the value of this difference being determined by the propagation difference δx of signals from the central and peripheral parts of the linear array, $\delta x \approx 2(\sqrt{L^2 + (D/2)^2} - L)$. For $L \geq D$, this difference is $\delta x \approx (D/2)^2/L$. In this case, the quantity L in expressions (1) and (2) is replaced by δx, and condition (2) takes on the form

$$\frac{|\Delta c|}{c_0}\left(\frac{D}{2}\right)^2\frac{1}{L\lambda_0} \ll 1 \quad (L \geq D). \quad (5)$$

In complete tomographic systems the radiating and receiving apertures are developed to the maximum dimensions. Therefore, the influence of large contrast inhomogeneities on the reconstruction quality is maximal. On account of a large inhomogeneity with the size $L \approx 2R_0$ and the velocity $c_0 \pm \Delta c$, the defocusing phase shift in the case of focusing at the center of a ring array with radius R_0 is determined by relation (1) in which $L \approx 2R_0$. In this case, condition (2) takes the form

$$\frac{|\Delta c|}{c_0}\frac{2R_0}{\lambda_0} \ll 1. \quad (6)$$

Limitation (6) is more stringent than condition (5).

The presence of transmission data on the forward scattering in tomographic systems provides an opportunity to evaluate the inhomogeneities of all sizes. It is also possible to considerably improve the quality of the image. Both strict iterative algorithms and their approximate realizations, which provide a positive result, can be used for these purposes. Some novel techniques can also be used, and this possibility will be discussed below.

The most advanced iteration procedures form a broad class of algorithms for solving inverse problems. Their convergence is determined by the scatterer characteristics: dimensions, contrast, and degree of complexity of the spatial structure [3]. A detailed examination of these problems goes beyond the scope of this study. Here, we describe a two-step approach, simplified but efficient for medical applications, which we use to develop a prototype of a medical ultrasonic tomograph [4]. We also describe the noniterative Grinevich–Novikov algorithm. Both algorithms are applicable to early quantitative diagnostics of biological tissue disorders. We consider a situation typical in medical practice, namely, when it is necessary to reconstruct a scatterer consisting of small (with a linear size from several tenths of a millimeter-range wavelength to several wavelengths) characteristic details of an object, which occur against the background of large-scale (with a size of several wavelengths and larger) unknown inhomogeneities of the phase velocity, biological tissue density, and absorption coefficient. It is assumed that, in the absence of large inhomogeneities, these small details cause the scattering described in the Born approximation. A complete evaluation of the whole scatterer containing both large fragments and small details with the Born contrast is performed using the aforementioned algorithms.

TWO-STEP ALGORITHM

The idea of using the Born algorithm with allowance for the inhomogeneities of the background evaluated on the basis of experimental data is not new [1, 5, 6]. Here, we describe one of the algorithms of this type. Its feasibility is confirmed by numerical simulation. The approach is as follows. At the first step the reconstruction of large-scale inhomogeneities, i.e., the regions with large deviations of sound velocity $c(\mathbf{r})$ or amplitude coefficient of absorption $\alpha(\mathbf{r}, \omega)$ from constant values c_0 and α_0 in the background medium, is performed. This stage is necessary because of the wide range of variation of sound velocity and absorption in biological tissues, which reduces the resolution of the ultrasonic tomographs operating in the Born or Rytov approximations.

The measured propagation times of the pulsed signals intersecting the tomography region and their amplitude attenuation factors are used at the first step. In the reconstruction, we assume that signals propagate along direct rays. The diameter of the ray tube is about $\sqrt{L\lambda_0} \cong 1$ cm (at $\lambda_0 \cong 1$ mm and a scatterer size $L \cong 10$–

20 cm), which determines the resolution of the first step. The assumption that rays are rectilinear means ignoring the refraction processes. The reconstruction error caused by this approximation is partially compensated at the second step, which presumes the reconstruction of the fine (small-scale) structure of a scatterer against the background of the large-scale distribution known from the first step. At the second step it is sufficient to use one of the algorithms based on the Born approximation taking into account the background inhomogeneity. The reconstruction is performed by phasing the received signals with the use of amplitude-phase corrections taking into account the large-scale distribution of the velocity and absorption. It is important that such corrections are also evaluated under the assumption of a rectilinear wave propagation. As model studies have demonstrated, the errors of the first and second steps do cancel each other, which provides an opportunity to reduce the resolution loss characteristic of the phasing techniques that do not take into account the background inhomogeneity. As a result, the complete pattern of the velocity, absorption, and tissue density distributions is reconstructed.

It is necessary to stress that, despite the two-step character of the algorithm, the multiple forward scattering by large-scale inhomogeneities is taken into account in it, which manifests itself in the difference between the signal propagation times in the presence of an object and in its absence. At the second step, this leads to a high precision in the reconstruction of the fine structure of a scatterer against a large-scale background that may have a high contrast. The two-step algorithm can be used in two- and three-dimensional tomographic schemes. Two-step processing brings the tomographic resolution closer to the maximum attainable one, which is close to the quarter-wavelength at a given operating frequency. In the two-dimensional scheme, this concerns the resolution in the tomography plane. The results of two-dimensional tomography can be represented either layerwise or in the form of a synthesized three-dimensional image.

Analytical Description of the Two-Step Algorithm

The following two-dimensional tomography scheme is used. Transmitting–receiving transducers are positioned on an array ring of radius R_0. These transducers can be arranged uniformly along the whole array ring [1, 6] or in a specially selected irregular way. In the latter case, when combined with a discrete rotation of the array, 26 transmitting–receiving transducers provide a volume of scattering data equal to that obtained from 256 stationary transmitting–receiving transducers [4].

The first-step procedure is close to the procedure of X-ray tomography in diverging beams [7, 8] with an overdetermination of the measured quantities and evaluated parameters, which is natural for the transition to acoustic problems. The experimental data p_{SR} are measured for different source (index S)– receiver (index R) pairs. The geometric positions of the source and receiver in a polar coordinate system with the origin at the center of the array ring are given by the radius vectors $\mathbf{r}_S = \{R_0, \varphi\}$ and $\mathbf{r}_R = \{R_0, \varphi'\}$, respectively. The reconstruction of large-scale distributions of the slowness $1/\bar{\bar{c}}(\mathbf{r})$ and the amplitude absorption coefficient $\bar{\bar{\alpha}}(\mathbf{r}, \omega)$ occurs according to the same algorithm of time-of-flight type on the basis of p_{SR}. For evaluation of the slowness, $p_{SR} = t_{SR} - t_{SR}^0$, where t_{SR} and t_{SR}^0 are the times of signal propagation from source S to receiver R in the presence and absence of an object. In this case, the function $f(\mathbf{r}) = \dfrac{1}{\bar{\bar{c}}(\mathbf{r})} - \dfrac{1}{c_0}$ is reconstructed at each fixed point $\mathbf{r}$. For evaluation of the absorption, $p_{SR} = -\ln(A_{SR}/A_{SR}^0)$, where A_{SR} and A_{SR}^0 are the amplitudes of the signals arriving at receiver R from source S in the presence and absence of an object. Here, p_{SR} characterizes the degree of additional wave attenuation relative to damping on account of the wave front divergence. In this case, $f(\mathbf{r}) = \bar{\bar{\alpha}}(\mathbf{r}, \omega) - \alpha_0$. If, in the processing, a signal cannot be expanded into monochromatic components, the values of the absorption coefficient are taken to be average within the operating frequency range. Thus, according to the physical meaning, the values of p_{SR} are additional propagation times or absorption introduced by an object lying on the path from S to R. The reconstruction of $f(\mathbf{r})$ from the known $p_{SR} \equiv p(\varphi, \varphi')$ is performed by the expression

$$f(\mathbf{r}) = \frac{1}{4\pi^2}\int_0^{2\pi} g(\mathbf{r}, \varphi)\frac{1}{K^2(\mathbf{r}, \varphi)}d\varphi, \tag{7}$$

where

$$g(\mathbf{r}, \varphi) = \lim_{\delta_1, \delta_2 \to +0}\left[-\frac{R_0}{2}\left(\int_0^{\varphi'_{ex} - 2\delta_1} + \int_{\varphi'_{ex} + 2\delta_2}^{2\pi}\right)\right.$$
$$\times \frac{\left|\sin\left(\dfrac{\varphi' - \varphi}{2}\right)\right|}{\cos^2\left(\dfrac{\varphi' - \varphi}{2} - \gamma\right)} p(\varphi, \varphi')d\varphi' \tag{8}$$
$$\left. + R_0\left(\frac{1}{\delta_1} + \frac{1}{\delta_2}\right)\cos\gamma p(\varphi, \varphi'_{ex})\right];$$

$$K^2(\mathbf{r}, \varphi) = R_0^2 + x^2 + y^2 - 2R_0(x\cos\varphi + y\sin\varphi),$$
$$\mathbf{r} = \{x, y\};$$

$$\gamma = \gamma(\mathbf{r}, \varphi) = \arctan\left[\frac{x\sin\varphi - y\cos\varphi}{R_0 - (x\cos\varphi + y\sin\varphi)}\right],$$

$$\gamma \in \left[-\frac{\pi}{2}, \frac{\pi}{2}\right];$$

$$\varphi'_{ex} = (\varphi + 2\gamma + \pi)_{\mathrm{mod}2\pi}, \quad \varphi'_{ex} \in [0, 2\pi).$$

The meaning of the quantities involved in Eqs. (7) and (8) is shown in Fig. 1. The current positions of source S and receiver R are considered for each fixed point of reconstruction $\mathbf{r} = \{x, y\}$. Then, K is the distance between source S and point $\mathbf{r}$ and γ is the angle between the directions from point S to the coordinate origin O and point $\mathbf{r}$. An exclusive angle φ'_{ex} corresponds to receiver position R_{ex} at which the chord connecting points S and R_{ex} passes through point $\mathbf{r}$. The quantities K, γ, and φ'_{ex} depend only on the positions of source S and point $\mathbf{r}$. In the calculation of $g(\mathbf{r}, \varphi)$ according to Eq. (8), a small vicinity (not necessarily symmetric) $[\varphi'_{ex} + 2\delta_1, \varphi'_{ex} + 2\delta_2]$ of the exclusive angle is separated, since the integrand at point $\varphi' = \varphi'_{ex}$ has a singularity: $\cos\left(\frac{\varphi'_{ex} - \varphi}{2} - \gamma\right) = 0$. In the numerical calculation, the result of the calculation of $g(\mathbf{r}, \varphi)$ does not depend on the selected small values of δ_1 and δ_2 due to the presence of the additional nonintegral term in Eq. (8). Note that in the calculation by Eqs. (7) and (8), the transition from continuous to discrete quantities requires a certain attention. This is connected with the rapid change of the functions $1/K^2(\mathbf{r}, \varphi)$ and $g(\mathbf{r}, \varphi)$ (depending on φ, when the source is near point $\mathbf{r}$) and of the integrand $1/\cos^2\left(\frac{\varphi' - \varphi}{2} - \gamma\right)$ (depending on φ' in the vicinity of special angle φ'_{ex}).

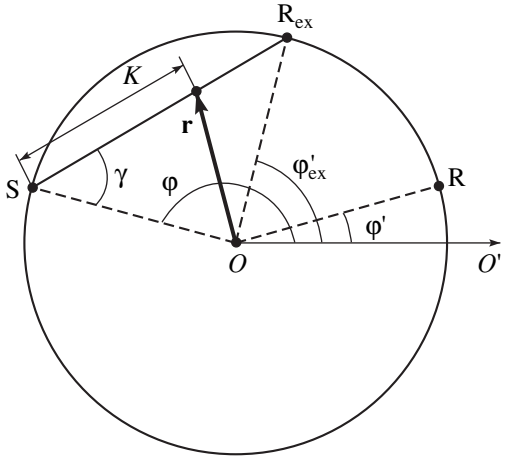

Fig. 1. Geometry of the X-ray algorithm in divergent beams: (OO') is the polar axis, S is the current position of the source, R is the current position of the receiver, R_{ex} is the exclusive position of the receiver, and $\mathbf{r}$ is the point of reconstruction.

The second-step procedure is based on the known algorithm of reconstructing weak scatterers, but now they are reconstructed against a known inhomogeneous background $\bar{\bar{c}}(\mathbf{r})$ and $\bar{\bar{\alpha}}(\mathbf{r})$, where $\bar{\bar{\alpha}}(\mathbf{r})$ is $\bar{\bar{\alpha}}(\mathbf{r}, \omega)$ averaged over ω. This procedure is described in sufficient detail in [9], and here we give only the basic details. The structure of a scatterer is described by the function $V(\mathbf{r})$. In the case of its reconstruction within the size of the resolution mesh (smaller than the wavelength), cylindrical fields can be replaced by effective plane waves, since the transducers are positioned at a considerable distance (over 20 wavelengths) from the object. Estimate $\hat{V}(\mathbf{r})$ of function $V(\mathbf{r})$ is constructed on the basis of the measured scattered fields $u_{sc}(\mathbf{r}_R, \mathbf{r}_S, t)$:

$$\hat{V}(\mathbf{r}) = -\frac{R_0^{3/2}}{2\pi^{3/2}\sqrt{\bar{c}}}\int_0^{2\pi} d\varphi \int_0^{2\pi} d\varphi' |\sin\Phi_{SR}|(\mathbf{r}) \times (|\mathbf{r}_R - \mathbf{r}| \times |\mathbf{r}_S - \mathbf{r}|)^{-1/2} \times B(\mathbf{r}_R, \mathbf{r}_S, \mathbf{r}) u_{sc}(\mathbf{r}_R, \mathbf{r}_S, t^*). \quad (9)$$

Here

$$t^* = t^*(\mathbf{r}_R, \mathbf{r}_S, \mathbf{r}) = t_0 + t(\mathbf{r}_S \longrightarrow \mathbf{r}) + t(\mathbf{r} \longrightarrow \mathbf{r}_R) - t(\mathbf{r}_S \longrightarrow 0); \quad (10)$$

$$B(\mathbf{r}_R, \mathbf{r}_S, \mathbf{r}) = \exp[A(\mathbf{r}_S \longrightarrow \mathbf{r}) + A(\mathbf{r} \longrightarrow \mathbf{r}_R)], \quad (11)$$

where

$$t(\mathbf{a} \longrightarrow \mathbf{b}) \equiv \int\limits_{\mathbf{a}\to\mathbf{b}} \frac{1}{\bar{\bar{c}}(\mathbf{r}')}|d\mathbf{r}'|$$

and

$$A(\mathbf{a} \longrightarrow \mathbf{b}) \equiv \int\limits_{\mathbf{a}\to\mathbf{b}} \bar{\bar{\alpha}}(\mathbf{r}')|d\mathbf{r}'|;$$

the integration is conducted along the axis $\mathbf{a} \longrightarrow \mathbf{b}$ of the ray tube. In Eq. (9), $\bar{c}$ is the value of $\bar{\bar{c}}(\mathbf{r})$ averaged over the region, and the value of $\Phi_{SR}(\mathbf{r})$ is equal to the angular distance between the directions to the source and to the receiver from the point with coordinate $\mathbf{r}$. Time point t^* involved in Eq. (9) depends (according to Eq. (10)) on the propagation time of a signal from source S to point $\mathbf{r}$ and from $\mathbf{r}$ to receiver R (t_0 is a constant that depends on the shape of the probing signals). Such a choice of t^* means phasing of the scattered signal to point $\mathbf{r}$ with allowance for the inhomogeneity of $\bar{\bar{c}}(\mathbf{r})$. The functional weighting factor $B(\mathbf{r}_R, \mathbf{r}_S, \mathbf{r})$ compensates for the attenuation of the signal amplitude due to absorption. In the calculation of the integrals in Eqs. (10) and (11), the trajectories along the axes of ray tubes were replaced by rectilinear trajectories.

Estimate $\hat{V}(\mathbf{r})$ gives the desired values of velocity $c(\mathbf{r})$, density $\rho(\mathbf{r})$, and $\alpha(\mathbf{r})$, which is the absorption coefficient $\alpha(\mathbf{r}, \omega)$ averaged over the operating frequency band:

$$V(\mathbf{r}) \approx \left(\frac{c_0^2}{\bar{\bar{c}}^2(\mathbf{r})} - \frac{c_0^2}{c^2(\mathbf{r})}\right)M_c + c_0^2\sqrt{\rho(\mathbf{r})}\nabla^2\left(\frac{1}{\sqrt{\rho(\mathbf{r})}}\right)M_\rho + c_0^2\frac{\alpha(\mathbf{r}) - \bar{\bar{\alpha}}(\mathbf{r})}{\bar{\bar{c}}(\mathbf{r})}M_\alpha, \quad (12)$$

where M_c, M_ρ, and M_α are the dimensional numerical complex coefficients depending only on the frequency spectrum of the probing signals [9]. Then, with the full scattering data being available (at omnidirectional irradiation and reception), it is sufficient to have the scattering data for a single frequency spectrum to extract $c(\mathbf{r})$ and $\alpha(\mathbf{r})$ from $\hat{V}(\mathbf{r})$ without considering the inhomogeneity of the density $\rho(\mathbf{r})$; when taking into account $\rho(\mathbf{r})$, the data for two frequency spectra are required [9]. If the scattering data are incomplete, the extraction of all three components of a scatterer, ($c(\mathbf{r})$, $\rho(\mathbf{r})$, and $\alpha(\mathbf{r})$) requires the data for three frequency spectra or for the polychromatic mode of operation at three different frequencies [10, 11].

Model Testing of the Two-Step Algorithm

The algorithm was tested using a numerical simulation of the scattering data from 256 receivers with sequential irradiation by 256 radiators. A large contrast inhomogeneity was preset as a stepwise change in the phase velocity by 3% (45 m/s) in half of the reconstructed region, which was a circle with radius R_0 = 0.135 m. Two halves of the circle were divided by a chord passing through the center of the circle and inclined with respect to the x axis at an angle of $\pi/256$. The value of the velocity in the upper part coincides with c_0 in the medium without scatterers and is equal to $c_1 = c_0 = 1500$ m/s; in the lower part, the velocity is $c_2 = 1545$ m/s. The central section of this inhomogeneity along the y axis is presented in Fig. 2b (dashed line). The reconstruction by Eq. (7) was conducted at the nodes of a coarse grid formed by splitting a square with a side of $2R_0$ into 16×16 meshes with the a side of $q_\mathrm{I} = 2R_0/16 \approx 18.6\lambda_0$. The wavelength $\lambda_0 \approx 0.91 \times 10^{-3}$ m is determined by a background velocity of c_0 and a frequency of $\nu_0 = 1.65$ MHz. The selected values of R_0, c_0, and ν_0 correspond to a specific tomographic setup [4]. Since the resolution of the first step is determined by the width of the ray tube $\cong\sqrt{2R_0\lambda_0} \approx 0.016$ m, the selected parameter q_I is acceptable for the reconstruction of the large-scale structure. The result of the reconstruction is a "smoothed" distribution of large-scale inhomogeneities (Figs. 2a, 2b).

The values reconstructed at the nodes of the coarse grid are interpolated further onto the nodes of a finer grid. The size q_II of the side of the fine grid mesh is matched to the expected resolution of the second step; i.e., it is equal to fractions of a millimeter. To do this in the process of numerical simulation, each mesh of the coarse grid was divided additionally into 16×16 meshes (therefore, $q_\mathrm{II} = q_\mathrm{I}/16 \approx 1.16\lambda_0$). At the first step, it is possible to reconstruct the values of large-scale inhomogeneities immediately at the nodes of the fine grid, which requires more computation, however, in this case interpolation is not needed. Finally, in a particular way, the large-scale distributions, $\bar{\bar{c}}(\mathbf{r})$ and $\bar{\bar{\alpha}}(\mathbf{r})$, are obtained on the fine grid, which serves as the estimate of the inhomogeneous background for the second step of reconstruction.

The most labor-consuming operation at the second step is the calculation of the propagation time (Eq. (10)) and total absorption (Eq. (11)) along all paths connecting all reconstructed points of object $\mathbf{r}$ with positions $\mathbf{r}^d$ of all transducers (a source or a receiver denoted by the index d). Since the paths are considered to be rectilinear and the grid is fine, the following estimates are admissible:

$$t(\mathbf{r} \longrightarrow \mathbf{r}^d) \approx \frac{|\mathbf{r} - \mathbf{r}^d|}{N_r^d}\sum_{n_r^d = 1}^{N_r^d}\frac{1}{\bar{\bar{c}}(n_r^d)};$$
$$A(\mathbf{r} \longrightarrow \mathbf{r}^d) \approx \frac{|\mathbf{r} - \mathbf{r}^d|}{N_r^d}\sum_{n_r^d = 1}^{N_r^d}\bar{\bar{\alpha}}(n_r^d). \quad (13)$$

Here, n_r^d are the numbers of the fine grid meshes, which are intersected by a segment with a length of $|\mathbf{r} - \mathbf{r}^d|$ connecting points $\mathbf{r}$ and $\mathbf{r}^d$, and N_r^d is the total number of such meshes. Tracing (13) is reduced to the multiplication of distance $|\mathbf{r} - \mathbf{r}^d|$ by the average value of slowness or the absorption coefficient along the path. The results of the numerical simulation confirmed the good accuracy of the approximate calculation by Eq. (13). In this case, the errors in the calculation of the values of $A(\mathbf{r} \longrightarrow \mathbf{r}^d)$ responsible for the correction of the signal amplitude are less important than the errors in the calculation of the values of $t(\mathbf{r} \longrightarrow \mathbf{r}^d)$ responsible for the correction of the signal phase. Moreover, to save calculation time, it is admissible to perform the tracing not for all points $\mathbf{r}$ lying at the nodes of the fine grid but for a smaller number of points. For example, tracing (13) is performed for points $\mathbf{r} = \mathbf{r}_\mathrm{coarse}$ lying at the nodes of the coarse grid and the corrections δt and δA are considered relative to the corresponding values in a homogeneous

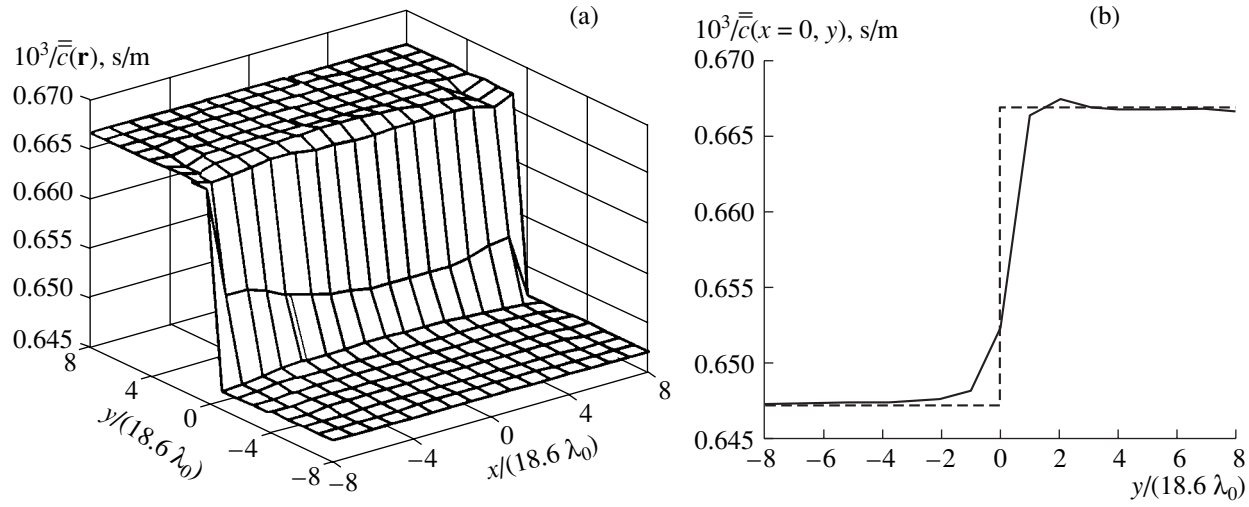

Fig. 2. Result of the reconstruction of a large-scale contrast inhomogeneity at the first step of the two-step algorithm: (a) the general form of the reconstructed inhomogeneity and (b) the central section along the *y* axis for the reconstructed (solid line) and true (dashed line) inhomogeneities.

medium:

$$\begin{aligned}\delta t(\mathbf{r} \longrightarrow \mathbf{r}^d) &= t(\mathbf{r} \longrightarrow \mathbf{r}^d) - |\mathbf{r} - \mathbf{r}^d|/c_0;\\ \delta A(\mathbf{r} \longrightarrow \mathbf{r}^d) &= A(\mathbf{r} \longrightarrow \mathbf{r}^d) - \alpha_0|\mathbf{r} - \mathbf{r}^d|.\end{aligned} \tag{14}$$

After this, four nodes lying at the corners of the mesh of the coarse grid, where point $\mathbf{r} = \mathbf{r}_{\text{fine}}$ of the fine grid belongs, are determined. At a fixed position of a transducer $\mathbf{r}^d$, the corrections $\delta t(\mathbf{r}_{\text{fine}} \longrightarrow \mathbf{r}^d)$ and $\delta A(\mathbf{r}_{\text{fine}} \longrightarrow \mathbf{r}^d)$ are obtained by linear interpolation of the corrections $\delta t(\mathbf{r}_{\text{coarse}} \longrightarrow \mathbf{r}^d)$ and $\delta A(\mathbf{r}_{\text{coarse}} \longrightarrow \mathbf{r}^d)$, which are known for these four nodes of the coarse grid. Then, $t(\mathbf{r}_{\text{fine}} \longrightarrow \mathbf{r}^d) \approx \delta t(\mathbf{r}_{\text{fine}} \longrightarrow \mathbf{r}^d) + |\mathbf{r}_{\text{fine}} - \mathbf{r}^d|/c_0$ and $A(\mathbf{r}_{\text{fine}} \longrightarrow \mathbf{r}^d) \approx \delta A(\mathbf{r}_{\text{fine}} \longrightarrow \mathbf{r}^d) + \alpha_0|\mathbf{r}_{\text{fine}} - \mathbf{r}^d|$. It is the interpolation of the corrections $\delta t(\mathbf{r}_{\text{coarse}} \longrightarrow \mathbf{r}^d)$ and $\delta A(\mathbf{r}_{\text{coarse}} \longrightarrow \mathbf{r}^d)$, and not of the full values $t(\mathbf{r}_{\text{coarse}} \longrightarrow \mathbf{r}^d)$ and $A(\mathbf{r}_{\text{coarse}} \longrightarrow \mathbf{r}^d)$, that provides an admissibly small error of evaluation.

The numerical simulation of the second step of reconstruction consisted in the determining the degree of distortion of the tomograph spread function $\hat{V}_\delta(\mathbf{r}|\mathbf{r}_0)$ because of the large inhomogeneity reconstructed approximately at the first step. The spread function is the response $\hat{V}(\mathbf{r}) \sim \hat{V}_\delta(\mathbf{r}|\mathbf{r}_0)$ of the processing algorithm (9) to the scattered signal from a "point" inhomogeneity $V(\mathbf{r}) \sim \delta(\mathbf{r} - \mathbf{r}_0)$ (see Eq. (12)) situated at point $\mathbf{r}_0 = \{x_0, y_0\}$. This test inhomogeneity (in velocity, density, or absorption) must be treated as the idealization used to construct spread function $\hat{V}_\delta(\mathbf{r}|\mathbf{r}_0)$. Function $\hat{V}_\delta(\mathbf{r}|\mathbf{r}_0 = \mathbf{r}')$ is the kernel of an integral equation of the local convolution type, which describes the process of the reproduction of arbitrary scatterer structure $V(\mathbf{r})$ by a tomograph: $\hat{V}(\mathbf{r}) = \int_{\Re} \hat{V}_\delta(\mathbf{r}|\mathbf{r}')\, V(\mathbf{r}')d\mathbf{r}'$, where $\Re$ is the scattering region. The negligibility of the spread function distortions caused by the presence of strong inhomogeneities provides a small error in reconstructing complex-structured objects, because in this case neither the resolution nor the capability of the algorithm for qualitative evaluation of a scatterer undergoes considerable changes. This means that the presence of a large contrast inhomogeneity leaves a weak inhomogeneity that is equally noticeable in the reconstruction as in the case of a homogeneous background.

In the numerical simulation, the test inhomogeneity was positioned at various points and image $\hat{V}_\delta(\mathbf{r}|\mathbf{r}_0)$ was constructed using Eq. (9). It was assumed that the spectrum of probing signals had a Gaussian shape $\sim \exp\left[-\left(\frac{\nu - \nu_0}{\Delta\nu/2}\right)^2\right]$; $\nu_0 = 1.65$ MHz, $\Delta\nu = 150$ kHz; and the value of the frequency ν was taken into account within the 300-kHz band ($|\nu - \nu_0| \le 150$ kHz).

Figure 3 presents the central sections $y = y_0$ of the spread functions for various positions of a point inhomogeneity on the *Oy* axis ($x_0 = 0$). To analyze the shape and width of the spread functions, their values are reconstructed on the grid corresponding to a discretization step of $q'_{\text{II}} = q_{\text{II}}/15 \approx 0.077\lambda_0$. A reference spread function is realized in the case of the absence of inhomogeneities in the large-scale background (Fig. 3a, dashed line). Such a spread function is almost real. The reconstruction error is characterized by the ratio $(\max|\text{Im}\,\hat{V}_\delta|)/(\max \text{Re}\,\hat{V}_\delta) \approx 0.09 \times 10^{-2}$. The width of the spread function at a level of 0.7 is $\approx\lambda_0/4 \approx 0.2$ mm. In the case of high-quality manufacture of a tomograph, its resolution may reach this value. The reference

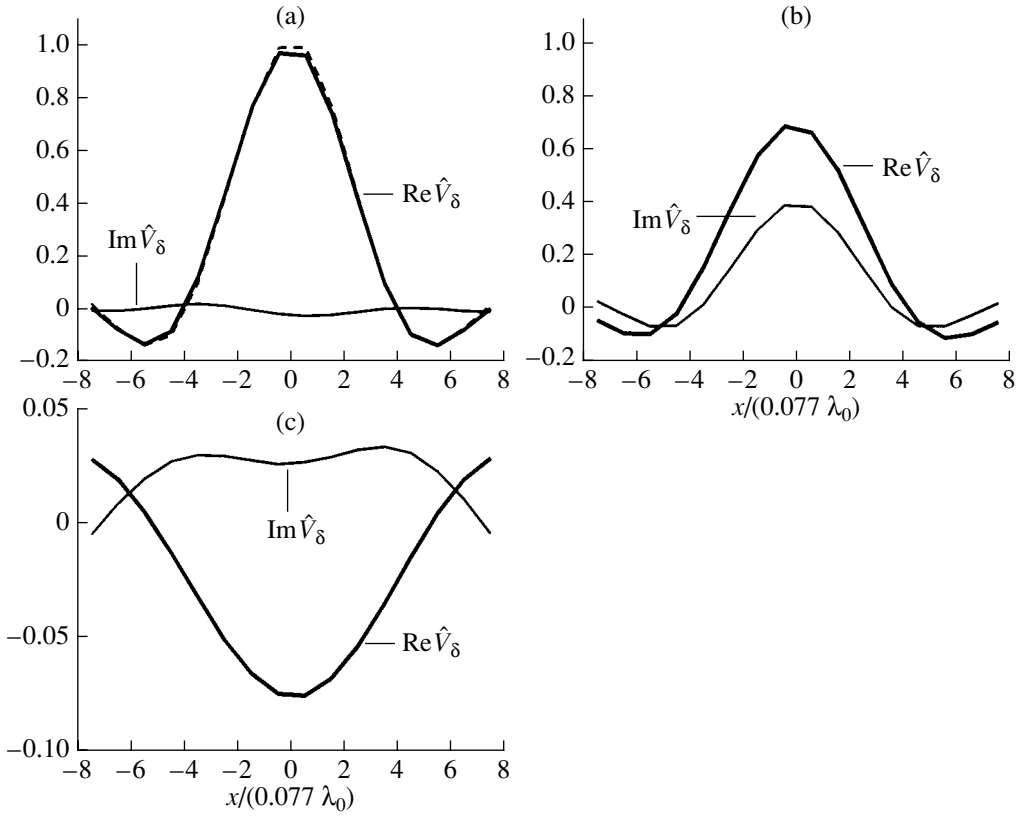

Fig. 3. Central sections of the spread functions $\hat{V}_\delta$ of the two-step algorithm, when normalized to the maximum value of the spread function for a homogeneous background medium (dashed line in Fig. 3a). (a, c) A point inhomogeneity is far from the sharp boundary of an inhomogeneous large-scale background medium; the spread function is obtained (a) with (solid line) and (c) without taking into account the background inhomogeneities. (b) A point inhomogeneity is near the boundary; the spread function is obtained by taking into account the background inhomogeneities.

spread function is almost the same for all positions $\mathbf{r}_0$ of a point inhomogeneity within the tomography region (including the immediate vicinity of the transmitting–receiving aperture), which is provided by the high angular density of scattering data.

The spread function in the case of an inhomogeneous background medium evaluated at the first step (Fig. 2a) almost does not differ from the spread function for a homogeneous background medium if a point inhomogeneity is located not very close to the boundary of the regions with velocities c_1 and c_2. The central section $y = y_0 = R_0/2$ of the spread function for the point of inhomogeneity localization $\mathbf{r}_0 = \{x_0 = 0, y_0 = R_0/2 = 0.0675\ \text{m}\}$ is presented in Fig 3a (solid line). In the process of reconstruction, tracing (13) was performed from the nodes of the fine grid and the reconstruction error was $(\max|\mathrm{Im}\,\hat{V}_\delta|)/(\max \mathrm{Re}\,\hat{V}_\delta) \approx 2.4 \times 10^{-2}$. In the case of tracing from the nodes of the coarse grid with further interpolation of corrections (14), the reconstruction error increases insignificantly (up to 4%). Small distortions of the spread function in the case of an inhomogeneous background medium confirm a good degree of cancellation of the reconstruction errors connected with the approximation of rectilinear propagation. This is an important practical result, since the stepwise change of the background velocity that was preset in the simulation is certainly stronger than possible changes in soft biological tissues. If the presence of large-scale inhomogeneities is not taken into account, the same stepwise velocity change leads to a strong distortion of the spread function up to a change of sign. For example, Fig. 3c gives the same section $y = y_0 = R_0/2$ of the spread function in the case when, in the process of tracing, an inhomogeneous large-scale background is replaced by a homogeneous one with the velocity $(c_1 + c_2)/2$. As a consequence, the spread function is completely destroyed. The inadmissible degree of distortion is also observed in the case when an inhomogeneous background is replaced by a homogeneous one with velocity c_1 or c_2.

It is important that, taking into account the inhomogeneities of the background medium, the spread function almost does not change (as in the case of an initially homogeneous background medium) when the point $\mathbf{r}_0$ moves within the tomography region. A noticeable reduction (1.4 times) of the maximum value of the real part of the spread function is observed only when a

point inhomogeneity is located near the boundary of a sharp velocity change (within ≅0.01 m ≈ $10\lambda_0$ from the boundary). In this case, its broadening almost does not occur. Moreover, the spread function acquires a complex part, which reaches a level of ≅0.6 of the real part (see Fig. 3b): $\mathbf{r}_0 = \{x_0 = 0, y_0 = 10R_0/128 = 0.0105$ m), $(\max \operatorname{Im} \hat{V}_\delta)/(\max \operatorname{Re} \hat{V}_\delta) \approx 0.57$. Thus, the negative influence of a sharp boundary turns out to be much stronger for the image points near it (because, in the process of wave transmission through the boundary, the refraction effects are greater for the angles of incidence close to grazing than for the angles of incidence close to normal).

GRINEVICH–NOVIKOV ALGORITHM

As an alternative to the two-step algorithm, we consider the possibility of simultaneously reconstructing both large-scale and fine structures of a scatterer in the framework of a single noniterative Grinevich–Novikov algorithm, which was initially developed in connection with the solution of inverse problems of quantum-mechanical scattering [12–14]. Possible application of this algorithm to inverse problems of acoustic scattering and also some results of its model studies were discussed in [15–18]. The algorithm shows considerable promise for application in medical and ocean tomography. It is important that it does not belong to the class of iterative algorithms and implies an analytical solution in an explicit form in reconstructing two-dimensional refractive–absorbing acoustic scatterers of almost arbitrary shape and sufficient strength. The scattering data are the values of scattered fields or the scattering amplitudes for all directions of incidence of plane (or synthesized in plane form) probing waves and for all directions of scattering. The algorithm takes into account the effects of multiple scattering, and, in this sense, it is rigorous. It has a high computation efficiency due to the small number of operations. The solution is determined in several stages. At each stage, a set of equations is solved, which is linear with respect to the unknown quantities (therefore, iteration techniques are unnecessary) and nonlinear with respect to the scattering data (in this way, it takes into account the effects of multiple scattering). The dimension of the sets of equations at each fixed stage is several orders of magnitude smaller than in the case of iterative methods. At the last stage, the scatterer function $V(\mathbf{r})$ is directly reconstructed. It is connected with the desired characteristics of the scatterer $c(\mathbf{r})$, $\rho(\mathbf{r})$, and $\alpha(\mathbf{r}, \omega)$ as follows:

$$V(\mathbf{r}) = \omega^2\left(\frac{1}{c_0^2} - \frac{1}{c^2(\mathbf{r})}\right) + \sqrt{\rho(\mathbf{r})}\nabla^2\left(\frac{1}{\sqrt{\rho(\mathbf{r})}}\right) - i2\omega\frac{\alpha(\mathbf{r}, \omega)}{c(\mathbf{r})}. \quad (15)$$

In this algorithm and in Eq. (15), a monochromatic mode of operation, ~$\exp(-i\omega t)$, and a homogeneous background medium with velocity c_0 and without absorption ($\alpha_0 \equiv 0$) are assumed.

Since the experimental data used for the reconstruction depend on the angles of wave incidence and scattering, they naturally fit the circular scheme of tomographic data acquisition in a real experiment. The scatterer function can be determined at any fixed point of space independently of its values at other points. Such a locality of the solution is convenient for use in practical applications and, in particular, for problems of medical tomography. The domain of the algorithm's applicability turned out to be much wider than was presumed initially by the authors, although it has limitations connected with the conditions of providing the necessary accuracy of the solution [16, 17].

An opportunity to reconstruct the scatterers down to small details by the Grinevich–Novikov algorithm is illustrated below by an example of sufficiently strong centrosymmetric scatterers with different values of the contrast of small-scale details and their width (some results of simulation are briefly described in [18]). The condition of central symmetry of scatterers was used only at the stage of the formation of simulated scattering data to reduce computation time. However, in the case of scatterer reconstruction using the Grinevich–Novikov algorithm, the condition of symmetry was not used at all. In the numerical simulation, it was assumed that $\lambda_0 = 16$ length discretization units and the size of the simulation area was $16\lambda_0 \times 16\lambda_0$.

A scatterer with a fine structure in the form of a central cavity is shown in Figs. 4a and 4b in the range $x, y \in [-4\lambda_0, 4\lambda_0]$. The function $\operatorname{Re} V(\mathbf{r})$ consists of a large-scale part of Gaussian shape with a half-width $d_1 = 2\lambda_0$ at the level $1/e$ and with the amplitude value corresponding to the velocity contrast $\Delta c_1/c_0 = 0.2$ relative to the background value. A narrow cavity of Gaussian shape, half-width $d_2 = \lambda_0/8$ at the level $1/e$, and amplitude value corresponding to the negative contrast $\Delta c_2/c_0 = -0.04$ occurs at the center of the large-scale inhomogeneity (Fig. 4c). The function $\operatorname{Im} V(\mathbf{r})$ is a "plateau." The scatterer is sufficiently strong: an additional phase shift along the central section is $\Delta\psi \approx 1.16\pi$, and the total absorption along this section leads to a decrease in amplitude by a factor of ≈6.58.

The high strength of the scatterer is evidenced by the result of reconstructing $\hat{V}_{\text{born}}(\mathbf{r})$ in the approximation of single scattering (Fig. 4f), where neither the amplitude scale nor the characteristic details of the true function $V(\mathbf{r})$ are reproduced correctly. At the same time, estimate $\hat{V}(\mathbf{r})$ obtained using the Grinevich–Novikov algorithm (Figs. 4d, 4e) adequately reproduces the large-scale part of the scatterer (both refraction and absorption parts). However, the amplitude of the reproduced cavity turned out to be understated. The cause is as follows. The local value of the velocity contrast for

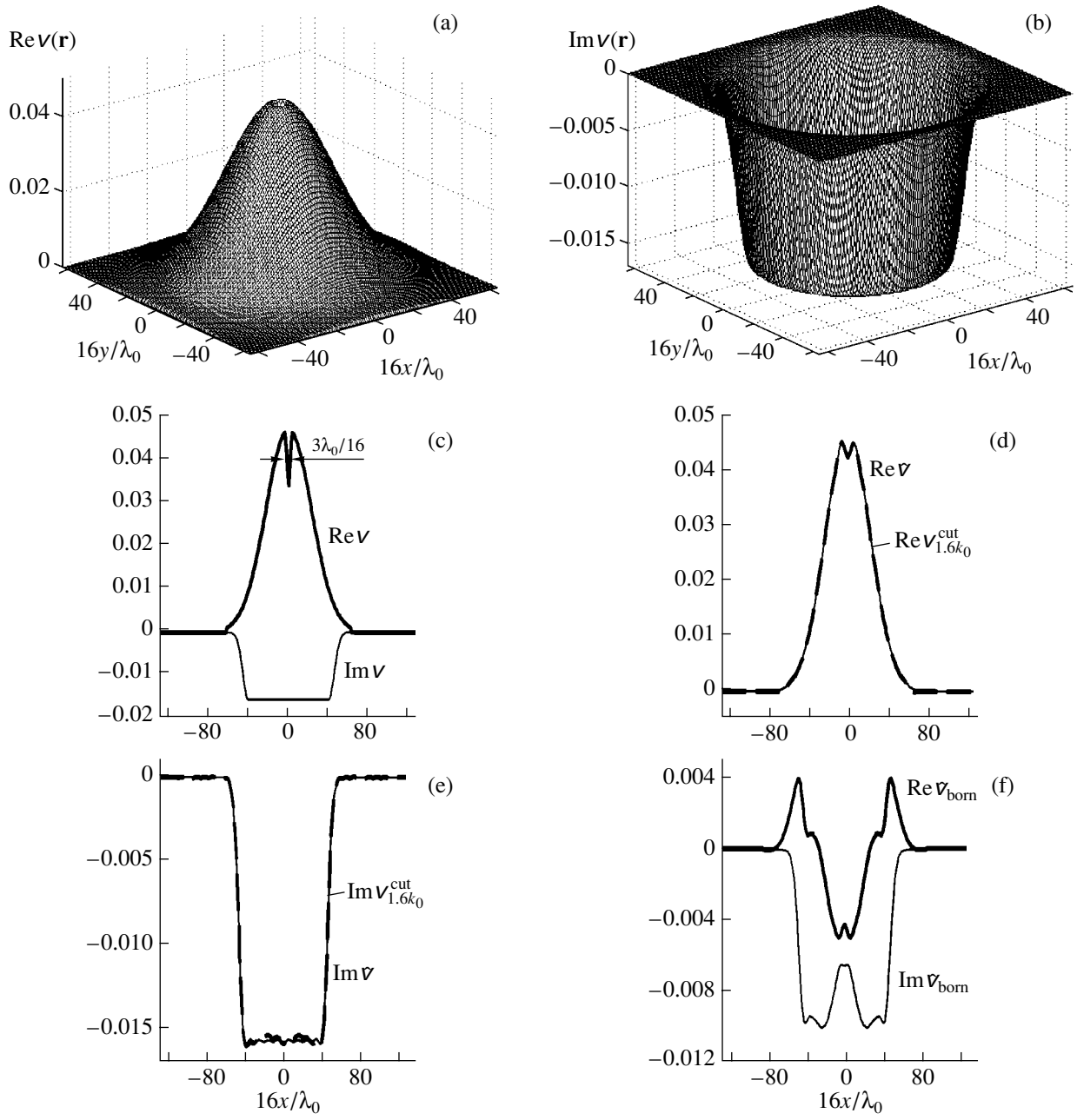

Fig. 4. Large-scale strong refractive–absorbing scatterer (the relative velocity contrast is $\Delta c_1/c_0 = 0.2$, the additional phase shift is $\Delta\psi \approx 1.16\pi$, the half-width at a level of $1/e$ is $d_1 = 2\lambda_0$, and the amplitude decrease due to absorption in the scatterer is by a factor of 6.6) with a fine structure in the form of a central cavity (a velocity contrast of $\Delta c_2/c_0 = -0.04$ and a half-width of $d_2 = \lambda_0/8$). The general form of the (a) real and (b) imaginary parts of the true scatterer and (c) their central sections. The central sections of the (d) real and (e) imaginary parts of the scatterer: the shape of the true scatterer after limiting the frequencies of its spatial spectrum by a circle with a radius of $1.6k_0$ (the thin line is for $v^{\text{cut}}_{1.6k_0}$); the scatterer reconstructed in the absence of noise taking into account the multiple scattering (the thick dashed line is for $\hat{v}$). (f) The central section of the scatterer reconstructed in the Born approximation.

the large-scale inhomogeneity at the site of the central small-scale cavity is $\Delta c_1/c_0 = 0.2$, which corresponds to the local values of the velocity $\bar{\bar{c}} = 1.2c_0$ and the wave number $\bar{\bar{k}} = k_0/1.2$. Therefore, to determine the reconstruction quality of the fine structure, function $\hat{v}(\mathbf{r})$ was compared with function $v^{\text{cut}}_{1.6k_0}(\mathbf{r})$ of a true scatterer with a spatial spectrum in which all components $\tilde{v}(|\vec{\boldsymbol{\xi}}|)$ at the frequencies $|\vec{\boldsymbol{\xi}}| \geq 2\bar{\bar{k}} \approx 1.6k_0$ are zero (Figs. 4d, 4e). It is also possible to see the scatterer, which is a

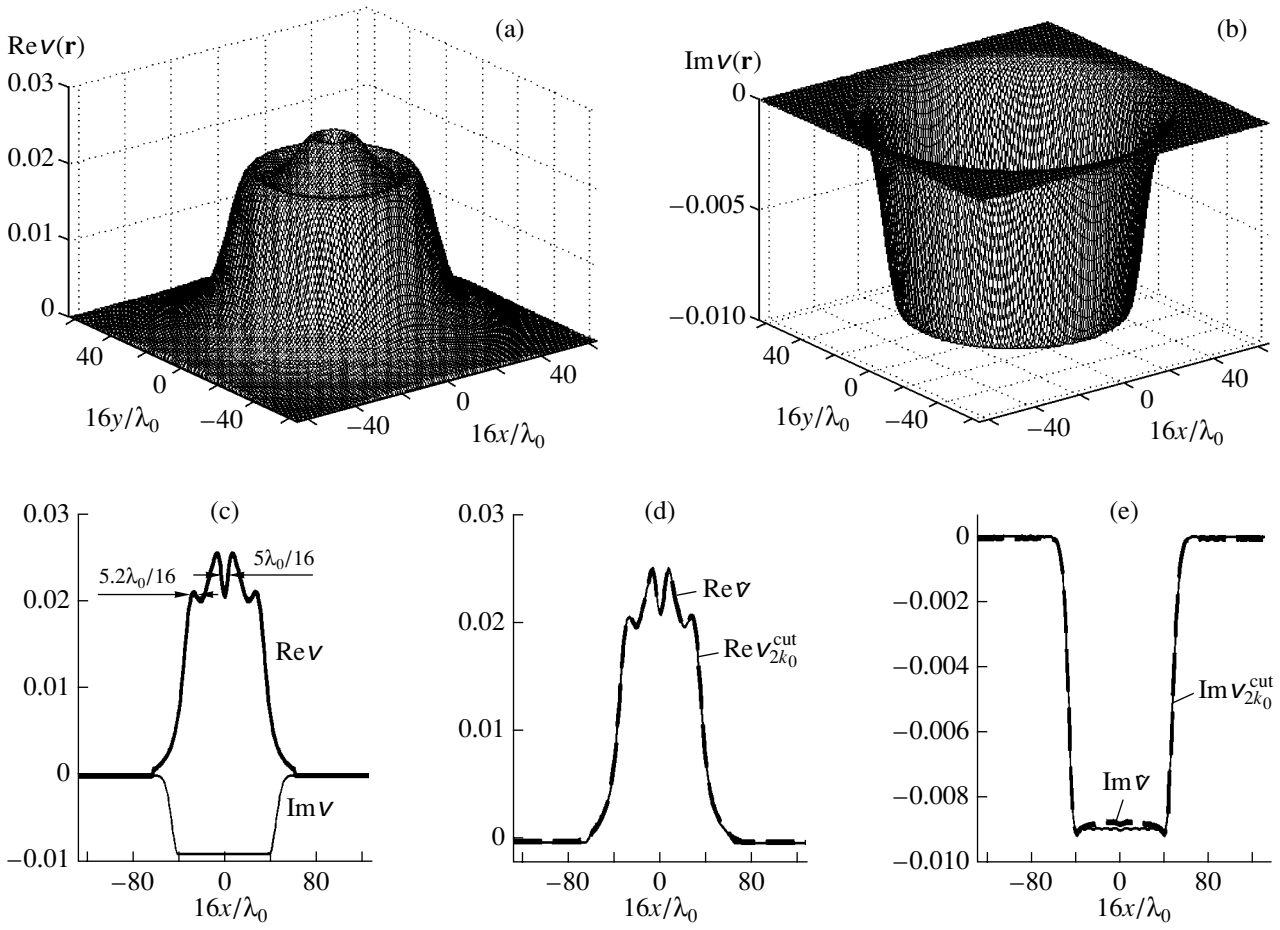

Fig. 5. Large-scale refractive–absorbing scatterer of intermediate strength (the relative velocity contrast is $\Delta c_1/c_0 = 0.1$, the additional phase shift is $\Delta\psi \approx 0.62\pi$, the half-width at the level of $1/e$ is $d_1 = 2\lambda_0$, and the amplitude decrease due to absorption in the scatterer is by a factor of 2.9) with a fine structure in the form of a central cavity (a velocity contrast of $\Delta c_2/c_0 = -0.02$ and a half-width of $d_2 = \lambda_0/4$) and an external circular wall (a velocity contrast of $\Delta c_3/c_0 = 0.03$ and a half-width of $d_3 = \lambda_0/2$). The general form of the (a) real and (b) imaginary parts of the true scatterer and (c) their central sections. The central sections of the (d) real and (e) imaginary parts of the scatterer: the shape of the true scatterer after limiting the frequencies of its spatial spectrum by a circle with a radius of $2k_0$ (a thin line is for $V_{2k_0}^{\text{cut}}$) and the scatterer reconstructed in the absence of noise taking into account the multiple scattering (the thick dashed line is for $\hat{V}$).

weak scatterer against the background of the homogeneous medium with wave number $\overline{\overline{k}}$. The result of its reconstruction by the algorithm coincides in shape with function $V_{1.6k_0}^{\text{cut}}(\mathbf{r})$. Then, proceeding from the comparison of $\hat{V}$ and $V_{1.6k_0}^{\text{cut}}$, one can see that the small-scale structure of the strong scatterer under consideration is reconstructed against an unknown large-scale contrast background with the resolution quality comparable with the reconstruction quality of the same small-scale structure in the Born approximation against a known background with wave number $\overline{\overline{k}}$.

In the case of the scatterer presented in Figs. 5a and 5b, the fine structure is represented simultaneously by a central cavity and a narrow external circular wall. The largest contrast and half-width at level $1/e$ for the large-scale inhomogeneity are equal to $\Delta c_1/c_0 = 0.1$ and $d_1 = 2\lambda_0$. The same parameters for the cavity are equal to $\Delta c_2/c_0 = -0.02$ and $d_2 = \lambda_0/4$; therefore, the total width of the cavity is $\approx 5\lambda_0/16$ at half of its depth (Fig. 5c). The central section of the wall has a Gaussian shape with a half-width of $d_3 = \lambda_0/2$ at the level $1/e$ and the amplitude value corresponding to the contrast $\Delta c_3/c_0 = 0.03$.

The additional phase shift is $\Delta\psi \approx 0.62\pi$, and the attenuation of the wave amplitude is by a factor of ≈ 2.9. The result of scatterer reconstruction in the single scattering approximation is similar to the one given in Fig. 4f; i.e., $\hat{V}_{\text{born}}(\mathbf{r})$ differs greatly from the true func-

tion $v(\mathbf{r})$. If multiple scattering is taken into account, the reconstruction result $\hat{v}(\mathbf{r})$ almost does not differ from the function $v_{2k_0}^{\text{cut}}(\mathbf{r})$ (Figs. 5d, 5e), which in this case is close to the initial function $v(\mathbf{r})$. Thus, both the circular wall and the central cavity are reproduced correctly.

Hence, the Grinevich–Novikov algorithm reliably reproduces the fine structure of a scatterer (details with a linear dimension of $\geq\lambda_0/3$) in the presence of unknown large-scale (several λ_0) inhomogeneities, which are also reconstructed by the algorithm. The use of the single scattering approximation in the reconstruction of such a scatterer leads to a strong distortion of the whole structure. The application of the Grinevich–Novikov algorithm provides a high quality of the fine structure resolution, which is not inferior to the reconstruction quality of this structure alone in the single scattering approximation against a known homogeneous background. The quality of the simultaneous reconstruction of large- and small-scale structures by this algorithm (which does not encounter the problem of convergence) is comparable to the reconstruction quality achieved with the iterative procedure.

In closing, we note that the initial statement and characteristics of the two-step iteration algorithm and those of the Grinevich–Novikov algorithm differ significantly. Namely, the two-step algorithm fundamentally needs the pulsed mode of data acquisition at its first step. Therefore, it uses an array of finite dimensions, for which the concept of propagation time makes sense. At the same time, the Grinevich–Novikov algorithm initially uses the data on the scattering of plane waves in the monochromatic mode, for which the concept of propagation time simply does not exist. Data in the form of the scattering amplitude can be obtained from physically feasible schemes of measurement by the secondary recalculation of real physical measurements. The difference between the two algorithms is the basic reason why the comparison of their efficiency in application to the same model object encounters considerable difficulties in numerical solution of direct model problems.

Thus, the quality of scatterer reconstruction by the two-step algorithm and the Grinevich–Novikov algorithm seems comparable. The expediency of using one of these algorithms is determined by the fundamental technical aspects of a specific problem.

ACKNOWLEDGMENTS

This work was supported by the Russian Foundation for Basic Research, project no. 01-02-16282, and by grant no. NSh-1575.003.2 from the President of Russian Federation.

REFERENCES

1. M. P. André, H. S. Janée, P. J. Martin, *et al.*, Int. J. Imaging Syst. Technol. **8** (1), 137 (1997).
2. V. A. Burov, S. N. Sergeev, S. A. Morozov, and O. D. Rumyantseva, Biomed. Tekhnol. Radioélektron., No. 3, 5 (2002).
3. V. A. Burov and O. D. Rumyantseva, Akust. Zh. **49**, 590 (2003) [Acoust Phys. **49**, 496 (2003)].
4. P. P. Parkhomenko, M. F. Karavaĭ, E. G. Sukhov, *et al.*, RF Patent No. 2,145,797 (23 June 1999).
5. A. J. Devaney and M. L. Oristaglio, Phys. Rev. Lett. **51** (1), 237 (1983).
6. M. P. André, H. S. Janée, G. P. Otto, *et al.*, Acoust. Imaging **22**, 151 (1996).
7. B. K. P. Horn, Proc. IEEE **66** (5), 551 (1978).
8. B. K. P. Horn, Proc. IEEE **67** (12), 1616 (1979).
9. V. A. Burov and O. D. Rumyantseva, Akust. Zh. **40**, 41 (1994) [Acoust. Phys. **40**, 34 (1994)].
10. V. A. Burov, A. L. Konyushkin, and O. D. Rumyantseva, Akust. Zh. **43**, 463 (1997) [Acoust. Phys. **43**, 395 (1997)].
11. V. A. Burov, A. L. Konjushkin, and O. D. Rumyantseva, Acoust. Imaging **25**, 109 (2000).
12. P. G. Grinevich and S. V. Manakov, Funkts. Anal. Pril. **20** (2), 14 (1986) [Funct. Anal. Appl. **20** (2), 94 (1986)].
13. R. G. Novikov, Teor. Mat. Fiz. **66** (2), 234 (1986) [Theor. Math. Phys. **66** (2), 154 (1986)].
14. R. G. Novikov, J. Funct. Anal. **103**, 409 (1992).
15. V. A. Burov and O. D. Rumyantseva, Akust. Zh. **39**, 793 (1993) [Acoust. Phys. **39**, 419 (1993)].
16. A. V. Bogatyrev, V. A. Burov, S. A. Morozov, *et al.*, Acoust. Imaging **25**, 65 (2000).
17. A. V. Bogatyrev, S. N. Vecherin, and S. A. Morozov, in *Proceedings of X Session of the Russian Acoustical Society* (GEOS, Moscow, 2000), Vol. 1, p. 141; http://www.akin.ru/Docs/Rao/Ses10/Di3.PDF.
18. V. A. Burov, S. A. Morozov, and O. D. Rumyantseva, Acoust. Imaging **26**, 231 (2002).

Translated by M. Lyamshev

Acoustical Physics, Vol. 49, No. 6, 2003, pp. 638–646. Translated from Akusticheskiĭ Zhurnal, Vol. 49, No. 6, 2003, pp. 751–760.

Long-Range Sound Propagation in the Central Part of the Barents Sea

R. A. Vadov

Andreev Acoustics Institute, Russian Academy of Sciences, ul. Shvernika 4, Moscow, 117036 Russia

e-mail: vadov@akin.ru

Received October 15, 2002

Abstract—The data of the experiments on long-range propagation of explosion-generated and tonal sound signals, which had been performed in different years in the central part of the Barents Sea in summertime conditions, are used to analyze the space structure of the sound field intensity, to estimate the attenuation coefficient due to the sound energy loss in the bottom sediments, and to determine the frequency dependence of this coefficient. A comparison of the data on the long-range propagation of explosion-generated signals is performed between two experiments carried out on the same 230-km-long path crossing the Central Basin of the Barents Sea, several years in succession. The two experiments differ in the propagation conditions: in the first experiment, a near-bottom sound channel extends along the entire path, and in the second experiment, the path crosses a frontal zone characterized by fairly complex variations of the sound speed field. Calculations are carried out to show that the specific behavior of the frequency dependence of attenuation can be explained by the power-law frequency dependence (with an exponent of 1.4) of the sound absorption in the water-saturated upper layer of the bottom sediments. It is also shown that the difference in the decay laws obtained for the sound field levels in the two experiments is caused by the difference in the corresponding hydrological conditions. *© 2003 MAIK "Nauka/Interperiodica".*

The specificity of long-range sound propagation in the Barents Sea is determined by the substantial variability of the environment. This variability is governed not only by the seasonal changes in the vertical temperature profiles but also by the time-varying fields of water currents, the rough bottom relief, and the complex structure of the upper sediment layers of the seafloor [1–4].

On several expeditions of the research vessels of the Acoustics Institute, studies of the specific features of the sound field in the Barents Sea were carried out. This paper presents the results of analyzing the data of several experiments on long-range sound propagation, which were carried out in summer in the region of the Central Basin with sea depths of 250–350 m.

Before or after each experiment, the hydrological characteristics of the path were surveyed. The vertical profiles of temperature and salinity (electrical conductivity) in the water bulk were measured at different points of the path. In one of the experiments, samples of the bottom material (columns 30–60 cm in depth) were taken at three points along the 230-km-long path. The samples consisted of viscous gray-green silt. The sea state was no higher than Beoufort 3–4 during the experiment, and the wind speed was 7–8 m/s.

In the studies of the sound field intensity in the Barents Sea, both tonal and explosion-generated signals were used. By analogy with a deep sea, the following intensity parameters of the sound field are used to characterize the propagation in a shallow sea: the attenuation coefficient, the propagation anomaly, and the transition distance. However, in view of the specificity of sound propagation in shallow-water regions, the aforementioned parameters need to be somewhat amended.

In a deep ocean, the attenuation means the range dependence of the mean level of the sound field under the influence of sound attenuation and scattering in the water medium. For a shallow sea, along with the geometric spread, absorption, and volume scattering, the bottom-caused losses (the reflection and scattering of sound from the bottom roughness and the penetration of sound energy into the sea floor) play an important role in sound field decay. Such losses lead to an additional level decrease, which follows an exponential law. As a rule, the attenuation coefficient serves to describe these losses in the experimental decay laws determined for the sound field in a shallow sea. In contrast to the attenuation coefficient in the water medium, we call the aforementioned quantity effective attenuation coefficient, β_{eff}.

In a deep sea, the propagation anomaly is defined for water rays as the excess of the sound field level produced by some source in the sea water over the level produced by the same source in a homogeneous boundless space with the absorption coefficient of the sea medium. By analogy, the propagation anomaly in a shallow sea means the excess of the sound field level produced by some source in the sea water over the level produced by the same source in a homogeneous boundless space with the absorption coefficient β_{eff} that char-

1063-7710/03/4906-0638$24.00

acterizes the actual features of the sound propagation in the region at hand.

Thus, the decay law of the sound field in shallow water can be described as

$$I = \frac{I_0}{R^2} A(R) \times 10^{-0.1\beta_{\text{eff}} R}, \quad (1)$$

where I_0 is the sound field intensity produced by the sound source at a unit distance from it in a homogeneous boundless medium.

The propagation medium (the shallow sea) is represented by a water layer overlying the bottom material. If one excludes the sound intensity loss caused by the attenuation, the sound field decay at long ranges will follow the cylindrical law, and the propagation anomaly will change in proportion to the distance: $A(R) = kR$. The quantity $1/k$ is usually called the transition distance (R_0). For distances $R \gg R_0$, by substituting the anomaly expressed in terms of the transition distance into Eq. (1), we obtain the expression for the sound field decay in the layer:

$$I = \frac{I_0}{RR_0} \times 10^{-0.1\beta_{\text{eff}} R}.$$

In view of the aforementioned definitions of the main intensity characteristics of the sound field, we developed a technique to measure them in the Barents Sea.

In experimenting with frequencies in the kilohertz frequency band, we used a towed sound source that consisted of a set of cylindrical piezoceramic transducers mounted within the towed body. The transmitting vessel traveled at a speed of 3 knots away from the receiving vessel or toward it. A continuous noise signal (in a 1/3-octave band) was transmitted. At the receiving vessel, the signal was continuously recorded with the reference to the distance between the vessels (at long ranges) or to the distance between the transmitting and receiving systems (at short ranges). The stability of the transmitted signal was monitored by measuring the level of the electric signal applied to the transducer.

As raw data for estimating the attenuation, the experimental sound field decay obtained on a path of up to 24 km was used. The attenuation coefficient was determined from the deviation of the range-dependent sound field level from the cylindrical law at long distances ($R \gg R_0$, with R_0 of about 300 m). In addition to the experimental sound field decay, the data on transducer calibration performed in the deep sea were used to estimate the transition distance and the propagation anomaly.

Figure 1 shows the decay of the sound field level experimentally measured at a frequency of 3.15 kHz with source and receiver depths of 100 and 150 m, respectively. At the time of the experiment, a near-bottom sound channel was present in the sea: a negative sound speed gradient (with different absolute values at

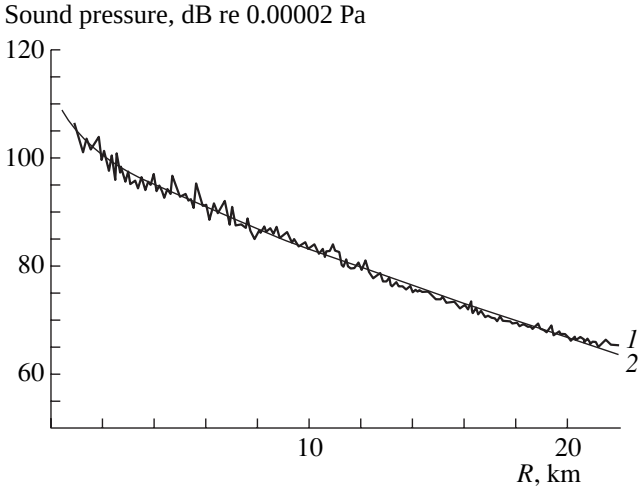

Fig. 1. Decay of the sound field level at a frequency of 3.15 kHz. The depths of the source and the omnidirectional receiver are 100 and 150 m, respectively: (*1*) experiment and (*2*) cylindrical spread + exponential attenuation (β_{eff} = 1.4 dB/km) approximating the experimental decay law.

different depths) was observed within the entire sea depth. The vertical sound speed profiles $c(z)$ recorded by the receiving vessel in this experiment are presented in Fig. 2 (the profiles were measured every 8 h). The sea depth in the region of the experiment was 280–300 m. By analyzing the experimental decay laws of the sound field, the following values of the attenuation coefficients β_{eff} were obtained: 0.95, 1.4. and 1.8 dB/km at 1.6, 3.15, and 4.0 kHz, respectively. The scatter in the values of β_{eff} estimated from the sound level decays at different horizons (150, 50, and 15 m) was less than 10%. The experimental estimates of the transition distance were within 200–300 m.

In one of the experiments, a vertical receiving antenna array was used in addition to omnidirectional receivers. With this array, the angular structure of the sound field was measured. Figure 3 shows a fragment of the record of the angular field structure measured at distances of 0.9 to 4.0 km from the signal source deployed to a depth of 150 m. The record consists of a sequence of the angular spectra recorded at the array output as the distance to the reception point continuously varied. The center of the receiving array was at a depth of 100 m. The vertical width of the array directivity pattern was about 2° (at the 0.7 level). Up to distances of 3.4–3.6 km, a good resolution of the signals arriving at different angles was observed. At distances greater than 3.6 km, the resolution failed. According to the calculations, there are no purely water-path rays (rays that do not touch the bottom and/or the surface) at such distances. The experimental data show that only water-path rays can be well resolved by the array. In the bottom and surface reflections, the signal loses its coherence and in-phase summation at the array becomes impossible.

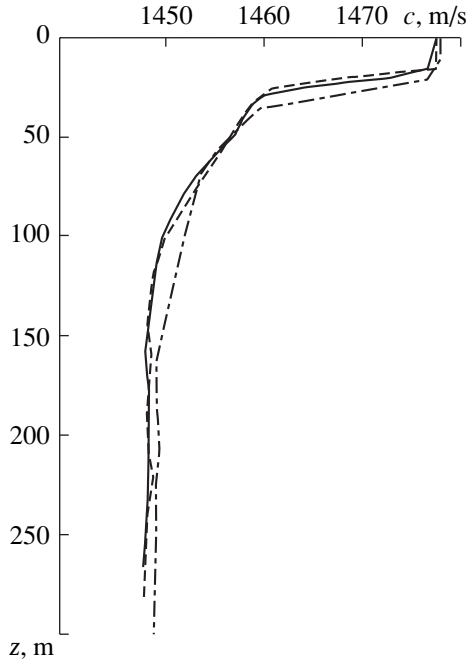

Fig. 2. Vertical sound speed profiles measured in one of the experiments in the central part of the Barents Sea.

In experimenting with low frequencies, we used an electromagnatic sound source that could not be towed. At different distances (up to 125 km) from the source, which was at a depth of 100 m, the vertical structure of the sound field was measured. These experiments were performed with tonal transmissions. Figure 4 illustrates the measured vertical structure of the sound field at a frequency of 16 Hz.

At a distance of 125 km from the source, the maximal propagation anomaly (25 dB) corresponding to a frequency of 16 Hz was observed at depths within 150–200 m. The difference between the maximal and minimal sound levels reached 15–20 dB. The vertical spatial period of interference increased as the distance from the source increased. The interference period decreased in inverse proportion to the increasing frequency.

To estimate the decay law of the low-frequency sound field, the sound levels were averaged in energy over the entire depth interval under study. From the deviation of the decay laws of the average sound levels from the cylindrical law, we found the values of β_{eff}, which proved to be 0.07, 0.08, 0.1, and 0.125 dB/km at 16, 32, 63, and 125 Hz, respectively. The low-frequency sound source was calibrated in a deep sea six days after the acoustic experiments. With the calibration data, we recalculated the sound field levels to the propagation anomalies and determined the transition distance R_0, which proved to be equal to 300 m. The scatter in the values of R_0 was no higher than 20–30% at all frequencies.

The experiment on the long-range propagation of the explosion-generated signals in the Barents Sea was performed in summertime (the second half of July), twice in different years on the same path. The receiving vessel drifted 500 km northeast of Murmansk. The transmitting vessel went a heading of 330° off the receiving one. The total length of the path was about 240 km. The path crossed the Central Basin from southeast to northwest. The sea depth varied from 210–220 to 340–350 m along the path. The bottom relief on the path is shown in Fig. 5c, as obtained in the echosounder survey carried out during the acoustic experiment. Explosive charges were detonated at a depth of 100 m. The signals were received by omnidirectional systems deployed at different depths. At the moment of explosion, the distance between the vessels was measured from the difference in the propagation times of the acoustic and radio signals.

The measurements of the profiles $c(z)$ were carried out with an ISTOK-3 instrument, before and after the first experiment. A near-bottom sound channel was present on the entire path in the first experiment. In the second experiment, the hydrological survey of the path was performed with the use of expendable TZO-2 thermoprobes, simultaneously with the explosions. Twelve thermoprobes were dropped at equal intervals along the path. At several points of the path, after the acoustic experiments, check measurements of the salinity and temperature were performed using bathometers. At dis-

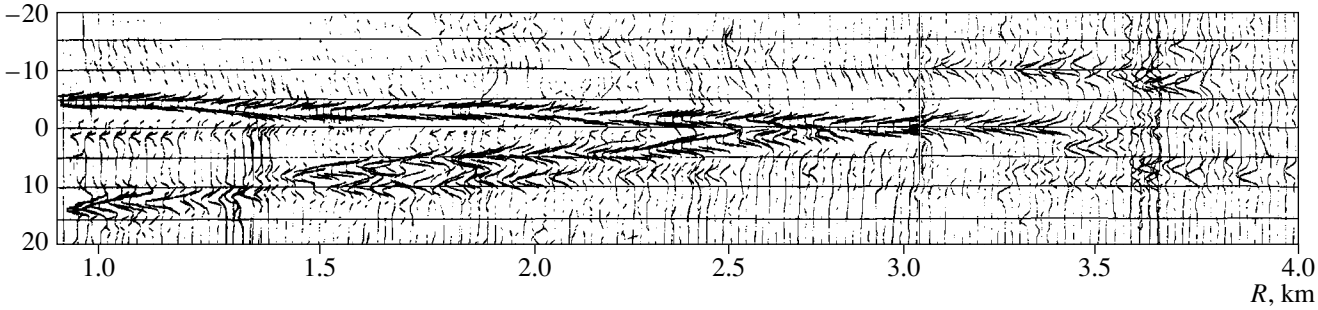

Fig. 3. Angular structure of the sound field measured at distances of 1–4 km by a vertical antenna array with its center at a depth of 100 m. The source depth is 150 m. The transmitted signal is a 2-octave noise with a central frequency of 3 kHz.

tances of 50–150 km from the reception point, the path crossed a frontal zone, i.e., the boundary of the cold polar waters. In this transition zone, the sound speed field was rather complex; this fact was reported previously by other researchers [5, 6]. The propagation conditions south and north of the frontal zone were noticeably different. The main difference consisted in the position of the minimum in the sound speed profile. For the southern waters, a near-bottom sound channel is characteristic. In the northern waters, the axis of the underwater sound channel was at a depth of 50–100 m. Figures 5a and 5b illustrate the sound speed field along the path for the experiments under discussion.

In the first experiment, the hydrological conditions were characterized by a negative sound speed gradient from surface to bottom, with a sound speed minimum at the bottom. At distances greater than 10–15 km, the signal propagating along the path was multiply reflected from the bottom. The time structure of the explosion-generated signal received at different distances from the source has the shape typical for such propagation conditions (Fig. 6a). Separate elementary (single-ray) signals can hardly be extracted from the total multiray signal. The signal begins with a sharp increase in level and then reaches its maximum, after which a smooth decrease down to the noise level follows. Near the source, the grazing angles of the reflected rays vary from 3°–4° to 89°–90° at the bottom. The upper limit of the grazing angles decreases in distance due to the loss at the bottom reflections. As the grazing angle grows, the bottom reflection coefficient decreases and the number of reflections per unit distance increases. The first signals to arrive at the receiver are those propagating along flat rays with small grazing angles near the bottom and small numbers of bottom reflections. The last signals to arrive are those propagating along steep rays with large grazing angles and large numbers of bottom reflections. Studenichnik [7] attempted to estimate the difference in the angular dependences of the bottom reflection coefficient at different frequencies from the dependence of the signal duration on frequency, which, in its turn, was obtained from the spectral analysis of the explosion-generated signal. In our experiments, no such difference was observed.

The signal loses its coherence at the bottom reflections. However, according to the experiments with the explosion-generated signals, the complex shape of the signal spectrum, which is caused by the interaction of the shock wave and the first gas-bubble oscillation, does not vanish up to the ultimate distance (240 km in our case). Figure 6b shows the spectrum of the signal received 30 km from the source. For a two-pulse signal, the complex shape of the spectrum can be seen in the entire frequency band.

With the explosions as signal sources, the following quantity serves as the characteristic of the sound field that is equivalent to the signal energy within the frequency band Δf: $E_f = \int_0^T p_f^2(t)dt$, where T is the duration of the explosion-generated signal and $p_f(t)$ is the sound pressure normalized to the frequency band Δf.

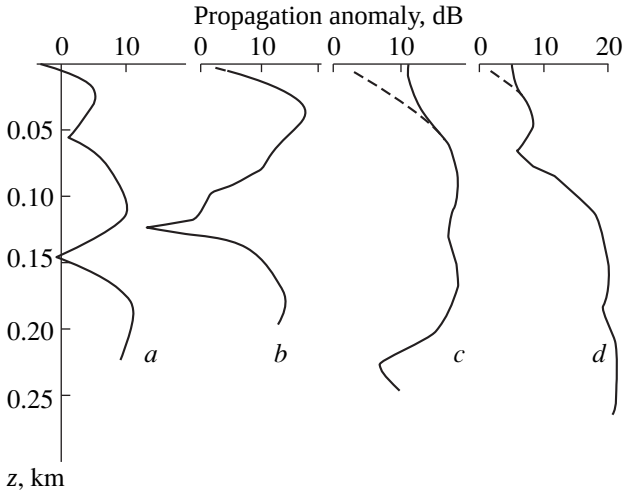

Fig. 4. Vertical structure of the sound field produced by a source positioned at a depth of 100 m. The distances are (*a*) 2; (*b*) 8; (*c*) 42; and (*d*) 86 km. The frequency of the transmitted tonal signal is 16 Hz.

In processing the energy spectrum of the explosion-generated signals received at different distances from the source, we obtained the experimental decay laws of the sound field at different frequencies. Figure 7 illustrates the decays obtained at 100, 200, and 400 Hz, with the receiver at a depth of 150 m. The values of β_{eff} obtained from the data of the first experiment are summarized in Table 1.

These values were determined from the sound field decays at the 100-m and 150-m horizons. The difference between the two resulting sets of data is insignificant: about 20% at low frequencies and less than 3–5% at high frequencies of the band under study. When the frequency changes from 100 to 1000 Hz, the values of β_{eff} change by a factor of as little as 2–2.5. The attenuation coefficients β_{eff} experimentally obtained at 125 Hz agree well with the value (0.125 dB/km) found from studying the vertical structure of the sound field produced by a low-frequency transmitting transducer at the same frequency. These studies of the vertical structure were carried out in the same region.

The last column of Table 1 contains the coefficients of sound absorption in the waters of the Barents Sea. These values are calculated with allowance for the low-frequency relaxation associated with boron in sea water. The calculation is based on the formulas proposed in [8] with the parameters specified as follows: $t = -0.5$°C, $S = 34.5$‰, and pH = 7.95. As one would expect, the experimental values of β_{eff} are by a factor of

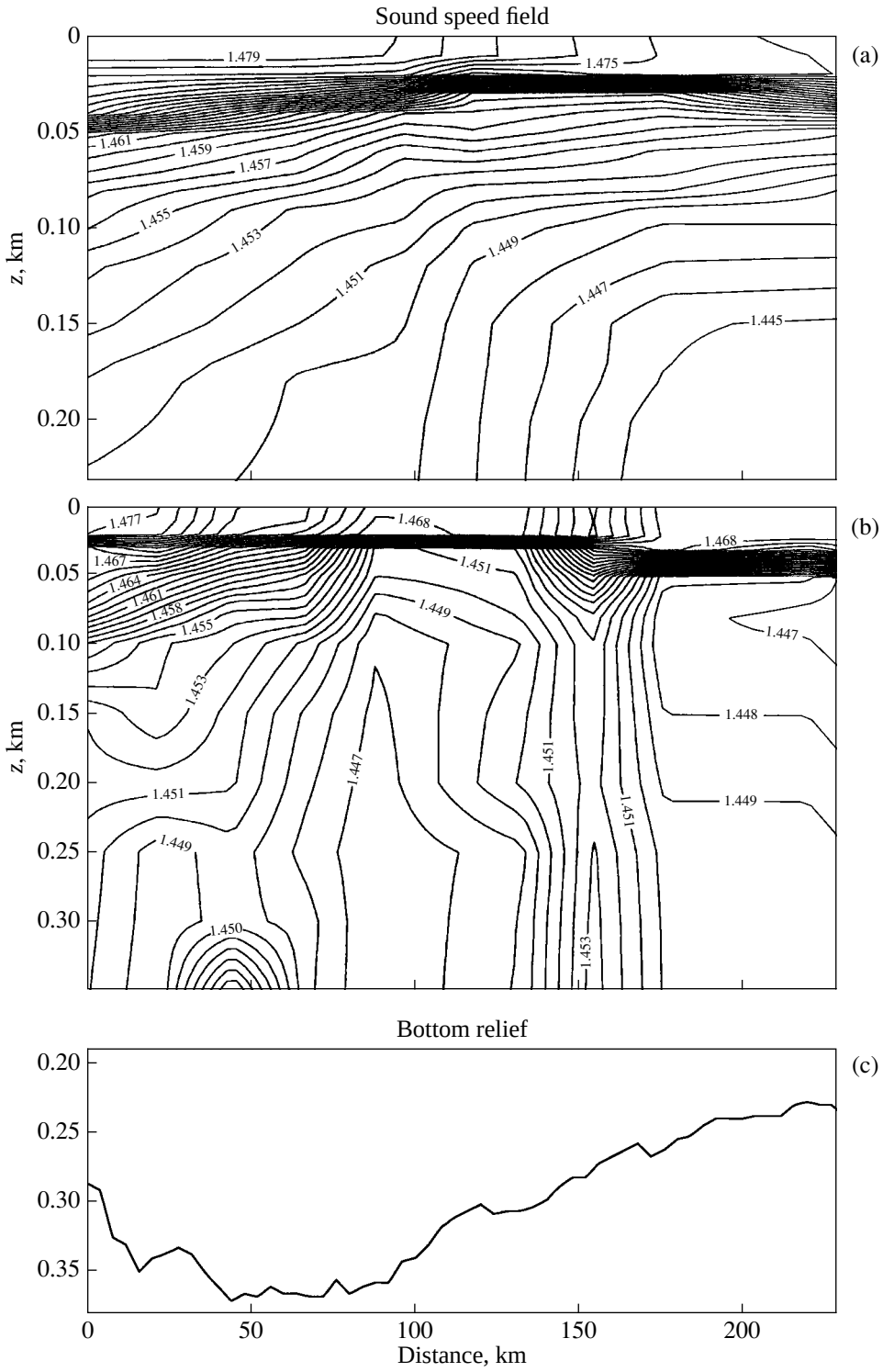

Fig. 5. Sound speed fields obtained in hydrological surveys of the path in (a) the first and (b) the second experiments and (c) the bottom relief obtained by echo sounding on the propagation path of the explosion-generated signals.

several tens higher than the absorption coefficient. The effective attenuation coefficient is almost fully governed by the loss of the sound energy in the bottom reflections.

A somewhat unordinary frequency dependence of the coefficient β_{eff} is worth mentioning. From 300 Hz to 1 kHz, the values of β_{eff} are nearly frequency-independent ($\beta_{eff} \sim 0.3$ dB/km). The decrease in frequency from

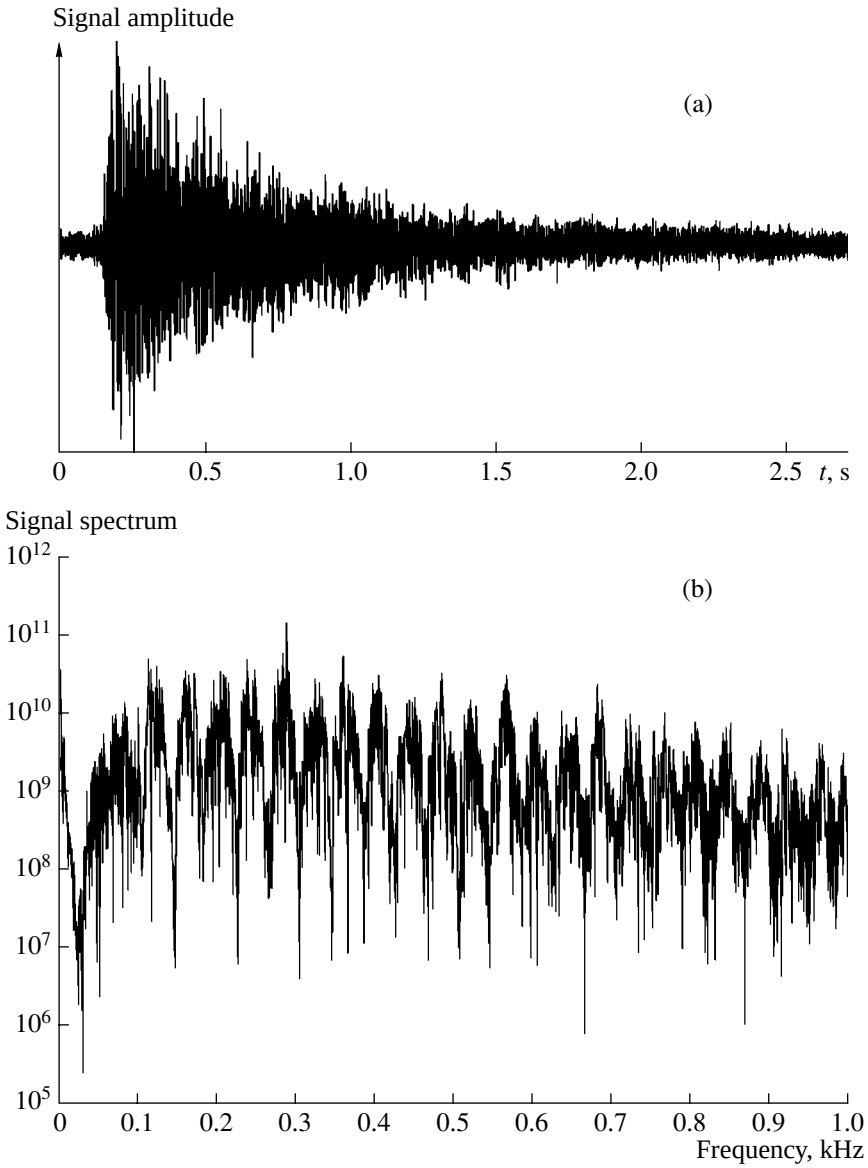

Fig. 6. Time structure of (a) the explosion-generated signal received at a distance of 30 km and (b) its spectrum.

300 to 100 Hz leads to the decrease in β_{eff} down to 0.13–0.17 dB/km (i.e., by a factor of about 2). To find the reason for such a peculiar frequency dependence, we performed a number of calculations with the use of the wave-method computer code developed by Avilov [9]. The calculations were carried out for noise signals (in 1/3-octave frequency bands) with allowance for the bottom relief (the data on echo sounding were used) for six profiles $c(z)$ (the data on hydrological surveys were used) and a three-layer bottom model (according to the archive data, two layers overlying a half-space) by neglecting the shear waves. In accordance with the aforementioned technique, we used the calculated sound field to determine the effective attenuation coefficient, whose frequency dependence was compared with the experimental data.

The calculations led to an interesting result. As the frequency increased, β_{eff} also increased, reached its maximum, and then smoothly decreased. With the 5-m thickness of the upper water-saturated sediment layer, the maximum corresponded to a frequency of about 200 Hz. A decrease in the thickness of this layer shifted the maximum towards higher frequencies. With the 3-m thickness, the maximum occurred at a frequency of about 300 Hz.

In the calculations, the absorption coefficient of the sediments was assumed to be proportional to the frequency. The loss coefficient was specified to be frequency-independent. However, the experimental data on the frequency dependence of the absorption in sediments lead to a power law with the exponent varying from 0.7 to 1.3 [10]. Theoretical studies [11–13] of the

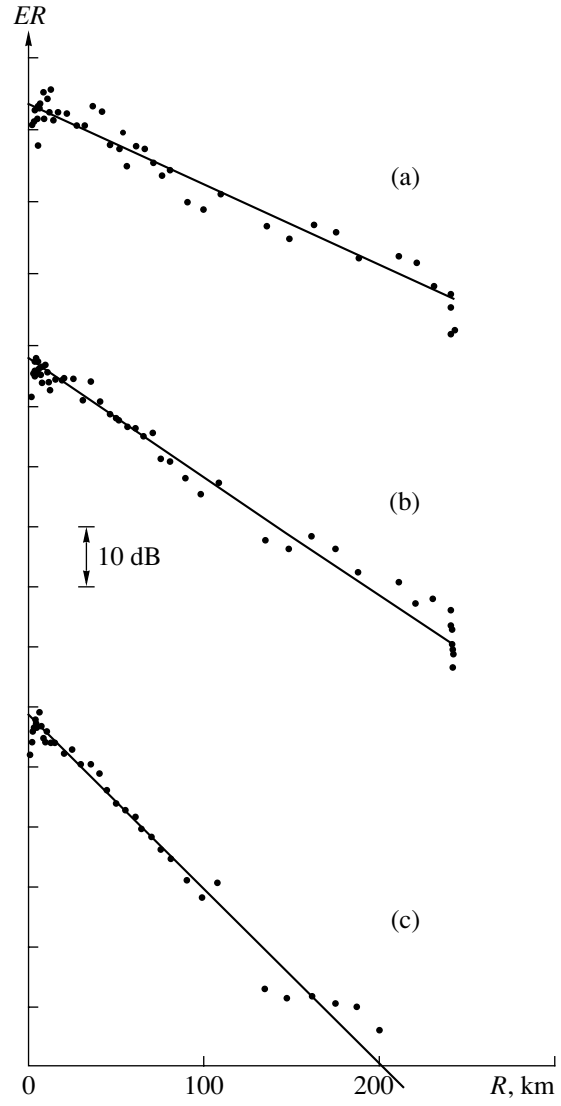

Fig. 7. Experimental decay laws obtained for the sound field levels of explosion-generated signals in the first experiment at the frequencies (a) 100; (b) 200; and (c) 400 Hz. The explosion and reception depths are 100 and 150 m, respectively.

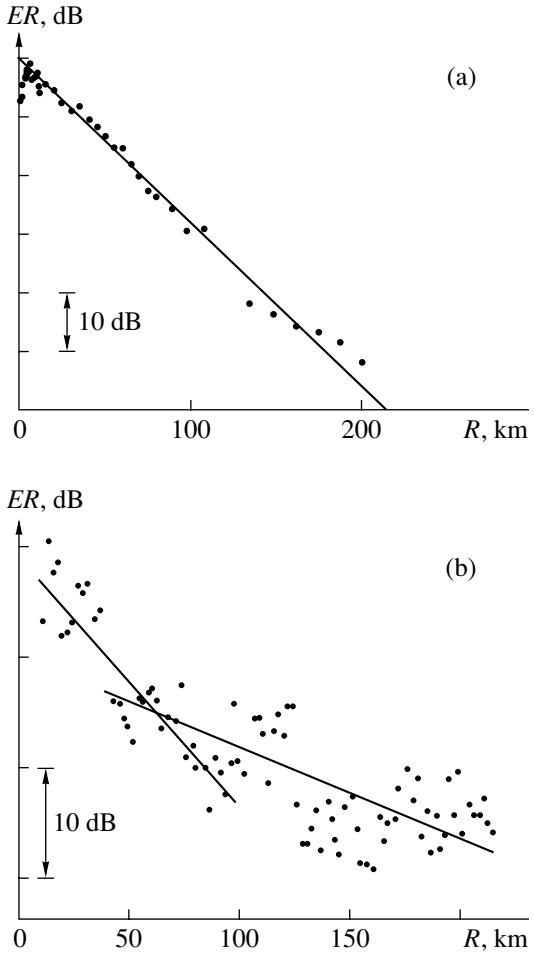

Fig. 8. Experimental decay laws obtained for the sound field levels of explosion-generated signals in (a) the first and (b) the second experiments at a frequency of 315 Hz. The explosion and reception depths are 100 and 150 m, respectively.

sound absorption in water-saturated sediments and suspensions allow the exponent to vary from 0.5 to 2.

By specifying a value of 1.4 for the exponent in the power-law frequency dependence of sound absorption in the upper water-saturated layer, we achieved a flattening of the β_{eff} curve at frequencies higher than 300 Hz, although it remained decreasing at lower frequencies. Thus, agreement between the experimental and calculated frequency dependences of β_{eff} was attained.

In forming the frequency dependence of attenuation, the bottom relief plays an important part. This can be verified by performing similar calculations for a flat bottom with the same characteristics of the sediments. For a flat bottom with a sea depth of 300 m, the calculation yields a monotonic frequency-proportional increase in the attenuation coefficient at frequencies higher than 300 Hz, such a behavior being noticeably different from the experimental frequency dependence.

In the calculations, the upper water-saturated sediment layer was characterized by range-independent parameters: a layer thickness of $h_1 = 3$ m, a sediment density of $\rho_1 = 1.5$ g/cm^3, a sound speed in sediments of $c_1 = 1450$ m/s, and an absorption of $\beta_1 = af^{1.4}$, where $a = 0.95$ dB/km kHz$^{1.4}$. For the second layer, the layer thickness was specified to change on two initial fractions of the path, from 100 to 10 m at the distances 0–60 km and from 10 to 50 m at 110–140 km, and to be constant on the two remaining fractions, 10 m at 60–110 km and 50 m at 140–230 km. Other parameters were as follows: $\rho_2 = 2.0$ g/cm^3, $c_2 = 1700$ m/s, and a loss coefficient of $\delta_2 = 0.02$. For the underlying halfspace, the following parameter values were specified:

ρ_3 = 2.2 g/cm^3, c_3 = 2300 m/s, and δ_3 = 0.006. The parameters of the second layer and the underlying halfspace corresponded to the archive data (with small variations in the loss coefficients). With the accepted bottom model, the calculated effective attenuation coefficient differed from the experimental one by 30–50% (the calculation led to lower values than the experiment). Perhaps some variations in the parameter values could result in a better agreement. However, we did not consider this problem in the present work, although, nowadays, many studies [14, 15] are known to deal with developing geoacoustic models for the bottom of a shallow sea on the basis of acoustic measurements.

In the second experiment, the initial part of the path, about 50 km in length, was also characterized by a negative gradient of the sound speed from surface to bottom, with the sound velocity minimum near the bottom. However, at distances greater than 50 km from the reception point, a weak underwater sound channel occurred on certain fractions of the path. This channel was formed by masses of polar water occupying depths from 50–100 m to bottom. Deeper than 50–200 m, a positive sound speed gradient close to hydrostatic was observed.

The decay of the sound field and, in particular, the values of β_{eff} strongly depend on the vertical sound speed profile. Thus, the difference in the experimental values of β_{eff} obtained on the two path fractions, north and south of the frontal zone, can quantitatively characterize the difference in the corresponding propagation conditions. Figure 8 compares the experimental decay laws observed in the (a) first and (b) second experiments at a frequency of 315 Hz and a reception depth of 150 m. The data of the second experiment exhibit an increased scatter of the experimental values and an evident kink in the decay curve 60–80 km from the reception point, while no such kink occurs in the data of the first experiment. The values of β_{eff} determined for distances of 10–100 km (south of the frontal zone) and 60–230 km (north of the southern zone boundary) are summarized in Table 2.

The values of β_{eff} differ by a factor of 2–2.5 for these two path fractions. At the same time, the difference in the values of β_{eff} obtained in the first experiment and on the southern path fraction of the second experiment is no greater than 20–30%.

With the hydrological environment of the second experiment, the calculations were carried out using the same computer code by Avilov. The bottom model accepted for the first experiment was also used for the second one, because both experiments were performed on the same path. The main objective of the calculations consisted in estimating the role of the frontal zone in the formation of the different sound field decay laws observed in the two experiments. As in the experiment, the calculated sound field decays corrected for the cylindrical spread exhibit changes in the steepness of decay. When determined from the calculations for distances of 70–100 km to the end of the path, the sound attenuation proved to be 2–4 times lower than that determined from the calculations corresponding to the first experiment. This difference agrees well with the experimental data.

Table 1. Experimental values of β_{eff} obtained for the Barents Sea in the first experiment with explosive sound sources at a depth of 100 m

Frequency, Hz	β_{eff}, dB/km, a reception depth of 100 m	β_{eff}, dB/km, a reception depth of 150 m	Sound absorption, dB/km
80	0.160	–	0.0003
100	0.167	0.126	0.0004
125	0.179	0.135	0.0007
160	0.183	0.153	0.0011
200	0.202	0.187	0.002
250	0.268	0.215	0.003
315	0.292	0.280	0.004
400	0.307	0.326	0.007
500	0.301	0.296	0.01
630	0.277	0.306	0.015
800	0.310	0.301	0.02
1000	0.311	0.291	0.03

Table 2. Attenuation coefficient (dB/km) obtained from the data of the second experiment with explosive sound sources for two path fractions, south and north of the frontal zone

Frequency, Hz	South of the frontal zone		North of the frontal zone	
	Reception depth 50 m	Reception depth 150 m	Reception depth 50 m	Reception depth 150 m
63	0.155	0.135	0.063	0.050
80	0.135	0.155	0.074	0.048
100	0.160	0.150	0.071	0.054
125	0.145	0.175	0.078	0.060
160	0.175	0.195	0.078	0.069
200	0.180	0.200	0.088	0.075
250	0.215	0.230	0.110	0.073
315	0.240	0.240	0.125	0.079
400	0.265	0.245	0.130	0.078
500	0.290	0.260	0.150	0.084
630	0.315	0.240	–	–
800	0.340	0.245	–	–
1000	0.380	0.250	–	–

In conclusion, let us summarize the main results.

—For the summertime conditions of the central part of the Barents Sea, the experimental data on the sound attenuation associated with the loss due to the bottom

reflections are obtained for the frequency band of 16–4000 Hz.

—The specific character of the frequency dependence obtained for the low-frequency attenuation can be explained by assuming a power-law frequency dependence of the absorption coefficient in the upper water-saturated sediment layer with an exponent equal to 1.4. The calculations reveal the important role of the bottom relief in the formation of the frequency dependence of attenuation.

—The data of two experiments with explosive sound sources, which were carried out on the same path in different years, illustrate a possible year-to-year variability of the propagation conditions. In the second experiment, the path crossed the frontal zone corresponding to the transition from southern to northern waters with the near-bottom and underwater sound channels, respectively. The data of hydrological surveys testified to the complex structure of the frontal zone.

—The vertical structure of the sound field exhibited an complex shape caused by interference, with the interference period decreasing when the frequency increases and increasing when the distance increases.

—The transition distances determined at low frequencies (tens of hertz) and at high frequencies (several kilohertz) agree well with each other.

—With the use of a vertical receiving antenna array, the arrival direction can be determined with confidence only for the water-path signals, which undergo no bottom reflections.

ACKNOWLEDGMENTS

This work was supported by the Russian Foundation for Basic Research, project nos. 01-02-16636 and 01-05-64711.

REFERENCES

1. V. F. Sukhoveĭ, *Seas of the Global Ocean* (Gidrometeoizdat, Leningrad, 1986).
2. B. S. Zalogin and A. N. Kosarev, *Seas* (Mysl', Moscow, 1999).
3. M. V. Klenova, in *Oceanographic Encyclopedia* (Gidrometeoizdat, Leningrad, 1974).
4. M. V. Klenova, in *Present-Day Sediments of Seas and Oceans* (Akad. Nauk SSSR, Moscow, 1961), pp. 419–436.
5. N. M. Adrov and I. V. Smolyar, in *Abstracts of All-Union Seminar on Oceanological Fronts in Northern Seas: Characteristics, Methods of Investigation, and Models* (Akad. Nauk SSSR, Moscow, 1989), p. 3.
6. J. F. Lynch, G. Jin, R. Pavlovicz, *et al.*, J. Acoust. Soc. Am. **99**, 803 (1996).
7. N. V. Studenichnik, Akust. Zh. **42**, 134 (1996) [Acoust. Phys. **42**, 119 (1996)].
8. R. A. Vadov, Akust. Zh. **46**, 624 (2000) [Acoust. Phys. **46**, 544 (2000)].
9. K. V. Avilov, Akust. Zh. **41**, 5 (1995) [Acoust. Phys. **41**, 1 (1995)].
10. E. L. Hamilton, in *Physics of Sound in Marine Sediments*, Ed. by L. Hampton (Plenum, New York, 1974; Mir, Moscow, 1977).
11. M. A. Biot, J. Acoust. Soc. Am. **28**, 168 (1956); J. Acoust. Soc. Am. **28**, 179 (1956).
12. R. D. Stoll, in *Physics of Sound in Marine Sediments*, Ed. by L. Hampton (Plenum, New York, 1974; Mir, Moscow, 1977).
13. E. M. Hovem, in *Bottom-Interacting Ocean Acoustics*, Ed. by W. Kuperman and F. Jensen (Plenum, New York, 1981; Mir, Moscow, 1984).
14. A. I. Belov, in *Proceedings of the VIII School–Seminar of Academician L. M. Brekhovskikh on Acoustics of the Ocean* (GEOS, Moscow, 2000), p. 81.
15. P. Pignot and N. R. Chapman, J. Acoust. Soc. Am. **110**, 1338 (2001).

Translated by E. Kopyl

Acoustical Physics, Vol. 49, No. 6, 2003, pp. 647–652. Translated from Akusticheskiĭ Zhurnal, Vol. 49, No. 6, 2003, pp. 761–767.

Diffraction of Light by an Acoustic Wave with Three Frequency Components

A. V. Vershubskiĭ and V. N. Parygin[†]

Moscow State University, Vorob'evy gory, Moscow, 119992 Russia

e-mail: parygin@osc162.phys.msu.su

Received November 19, 2002

Abstract—Collinear light diffraction by three-frequency sound is investigated theoretically. The amplitude distributions of transmitted and diffracted light waves along the cell are calculated for different amplitudes of sound signals. The dependence of the intensity of principal diffraction peaks on the frequency difference between acoustic signal components is studied for different amplitude ratios of these components. It is shown that the character of this dependence for a wave being in synchronism differs substantially from that for two other waves characterized by detuning. The dependence of the amplitudes of principal and parasitic diffraction peaks on the efficiency of acoustooptical interaction is investigated. It is demonstrated that parasitic sideband components in diffracted light can play a considerable role if the diffraction efficiency is sufficiently high and exceeds 80%. *© 2003 MAIK "Nauka/Interperiodica".*

INTRODUCTION

The basis for the phenomenon of acoustooptical interaction is the photoelastic effect, i.e., the variation of the refractive index of a medium under an elastic stress. As a result, an acoustic wave propagating in an optically transparent medium constitutes a phase diffraction grating moving with the velocity of sound. Being transmitted through an acoustic field, light is diffracted by the inhomogeneities of the refractive index. An important area of practical application of acoustooptical interaction is the design of information processing systems, where acoustooptical devices are used for real-time processing of microwave signals. Depending on the intended application, several types of acoustooptical devices have been developed: deflectors, modulators, filters, processors, etc. [1–5].

The theory of acoustooptical interaction for monochromatic waves is developed in sufficient detail. It not only describes the diffraction of light by a plane sound wave [6, 7] but also takes into account bounded three-dimensional divergent beams [8, 9]. However some acoustooptical devices (especially systems for optical information processing) use nonmonochromatic sound beams [10]. Since an acoustooptical cell is a nonlinear element with respect to an acoustic signal, the spectrum of diffracted light proves to be enriched with combination frequencies of acoustic signals. This substantially restricts the dynamic range of acoustooptical devices. Proklov and Chesnokov [11] theoretically studied the diffraction of light by multifrequency sound with a pronounced nonlinearity of photoelasticity. They demonstrated that, in some cases, the presence of two different kinds of nonlinearity provides an opportunity to suppress the sideband signals and, thus, to expand the dynamic range of a device.

One of the most important acoustooptical devices widely used for optical data processing is a spectrum analyzer for radio signals [3]. In this device, the signal to be analyzed is fed to a piezoelectric transducer and propagates in the form of a sound signal in an acoustooptical medium. Light from a laser source is diffracted by ultrasound, so that each spectral component of the acoustic wave produces a diffracted light beam with its own propagation direction. This provides an opportunity to judge the spectral composition of the initial signal.

All characteristics of a spectrum analyzer are usually calculated from the conditions of light diffraction by a harmonic acoustic wave. However, this approach is valid only for a linear acoustooptical device. Real acoustooptical interaction is nonlinear, even if it is possible to ignore the acoustic and optical nonlinearities of the medium. The specific acoustooptical nonlinearity is related to multiple light scattering by sound and is most pronounced in the case of light diffraction by a multifrequency sound signal.

This paper is devoted to the characteristic features of light diffraction by a multifrequency signal, which is represented by a three-frequency acoustic beam as an example. The fundamental need to consider a three-frequency signal is determined by the fact that, in the case of a two-frequency signal, it is impossible to evaluate the real dynamic range of a device, because for any arbitrary amplitude values of the two spectral acoustic components, true diffraction peaks will always be higher than parasitic ones. In the case of a three-frequency signal, it is possible to reduce the amplitude of

[†] Deceased.

1063-7710/03/4906-0647$24.00

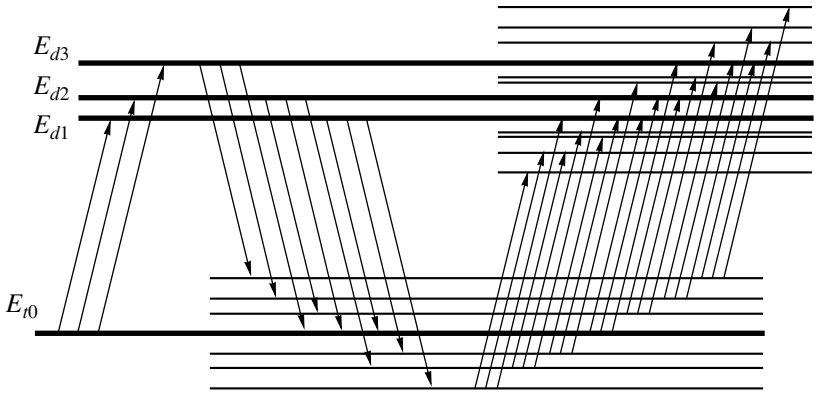

Fig. 1. Diagram of light diffraction by a three-frequency acoustic signal. The lines indicate the levels of the principal and sideband frequencies; the arrows show possible transitions due to light scattering by sound.

the third component relative to the parasitic sideband components.

THEORY OF THREE-FREQUENCY ACOUSTOOPTICAL INTERACTION

Let us consider the propagation of a light beam in an acoustooptical cell along the x axis in the presence of sound traveling in the same direction. The electric field vector $\vec{E}$ in a medium perturbed by sound propagation must satisfy the wave equation [12]

$$\mathrm{curl}\,\mathrm{curl}\vec{E} + \frac{1}{c^2}\frac{\partial^2}{\partial t^2}\varepsilon_0\vec{E} = -\frac{1}{c^2}\frac{\partial^2}{\partial t^2}\Delta\varepsilon\vec{E}, \qquad (1)$$

where ε_0 is the dielectric permeability tensor of the medium in the absence of sound and $\Delta\varepsilon$ is the variation of the tensor ε_0 due to the sound propagation.

When a multifrequency signal is fed to the input of an acoustooptical cell, a sound wave of the following form is generated in the crystal by the piezoelectric transducer:

$$u = \sum_{m=1}^{N} A_m \cos(\Omega_m t - K_m x), \qquad (2)$$

where A_m, K_m, and Ω_m are the amplitude, wave number, and frequency of a partial sound wave. In this paper, we consider the case of light diffraction by an acoustic wave consisting of three partial waves with close frequencies. In this situation, ignoring the attenuation, we reduce Eq. (2) to the form

$$u = A_1\cos\Phi_1 + A_2\cos\Phi_2 + A_3\cos\Phi_3, \qquad (3)$$

where $\Phi_i = \Omega_i t - K_i x$.

Because of the nonlinearity of acoustooptical diffraction, the interaction of sound wave (3) with light incident upon the cell will result in the propagation of a set of transmitted and diffracted waves with combination frequencies in the crystal. Restricting our consideration to the third-order nonlinearity, we obtain seven transmitted and twelve diffracted waves with their own frequencies. Here, we examine the case where one of the partial waves is in synchronism (i.e., it satisfies the Bragg condition exactly) and two other waves are detuned relative to this condition. The detuning parameters η can be determined from the expressions

$$\begin{aligned} k_t + K_1 &= k_d \\ k_t + K_2 &= k_d + \eta_1 \\ k_t + K_3 &= k_d + \eta_2, \end{aligned} \qquad (4)$$

where k_t and k_d are the wave numbers of the incident and diffracted light waves, $\eta_1 = K_2 - K_1$, and $\eta_2 = K_3 - K_1$. Here and below, the index t belongs to the incident component and the index d, to the diffracted component.

The diagram in Fig. 1 illustrates the specific features of light diffraction by a three-frequency signal. As the result of single scattering, three diffracted light beams with frequencies of $\omega + \Omega_1$, $\omega + \Omega_2$, and $\omega + \Omega_3$ are formed, where ω is the incident light frequency. Each of these beams can be rescattered by any of the three acoustic components. As a result, light waves with close frequencies of $\omega - \Omega_1 + \Omega_2$, $\omega - \Omega_1 + \Omega_3$, $\omega + \Omega_1 - \Omega_3$, $\omega + \Omega_2 - \Omega_3$, $\omega + \Omega_3 - \Omega_2$, and $\omega + \Omega_1 - \Omega_2$ appear in addition to the incident light with frequency ω. Each of these partial waves in turn can be scattered by any of the three sound components. This leads to the appearance of nine additional diffracted beams, which lie near the three principal peaks and can be identified by a spectrum analyzer as additional frequency components of the signal under analysis. The basic method of selecting true signal components from parasitic ones relies on the fact that the amplitudes of the parasitic components are smaller. However, the application of this method limits the dynamic range of the spectrum analyzer.

The table complements the diagram of light scattering given in Fig. 1. It describes the basic characteristics

Basic characteristics of each of the partial light waves propagating in the cell in the case of three-frequency acoustooptical interaction with allowance for nonlinearity no higher than the third-order one

Amplitude of the corresponding light wave	Wave number	Frequency shift relative to ω	Parameter of detuning relative to k_t or k_d	Amplitudes of acoustic components
E_{t0}	k_t	0		
E_{t1}	$k_t + K_1 - K_3$	$\Omega_1 - \Omega_3$	$-\eta_2$	A_1A_3
E_{t2}	$k_t + K_2 - K_3$	$\Omega_2 - \Omega_3$	$\eta_1 - \eta_2$	A_2A_3
E_{t3}	$k_t + K_1 - K_2$	$\Omega_1 - \Omega_2$	$-\eta_1$	A_1A_2
E_{t4}	$k_t + K_2 - K_1$	$\Omega_2 - \Omega_1$	η_1	A_1A_2
E_{t5}	$k_t + K_3 - K_2$	$\Omega_3 - \Omega_2$	$\eta_2 - \eta_1$	A_2A_3
E_{t6}	$k_t + K_3 - K_1$	$\Omega_3 - \Omega_1$	η_2	A_3A_1
E_{d1}	$k_t + K_1 = k_d$	Ω_1		A_1
E_{d2}	$k_t + K_2 = k_d + \Delta K_2$	Ω_2	η_1	A_2
E_{d3}	$k_t + K_3 = k_d + \Delta K_3$	Ω_3	η_2	A_3
E_{d4}	$k_d - \Delta K_3$	$2\Omega_1 - \Omega_3$	$-\eta_2$	$A_1A_3A_1$
E_{d5}	$k_d + \Delta K_2 - \Delta K_3$	$\Omega_1 - \Omega_3 + \Omega_2$	$\eta_1 - \eta_2$	$A_1A_3A_2$
E_{d6}	$k_d - \Delta K_2$	$2\Omega_1 - \Omega_2$	$-\eta_1$	$A_1A_2A_1$
E_{d7}	$k_d + \Delta K_2 - \Delta K_3$	$2\Omega_2 - \Omega_3$	$2\eta_1 - \eta_2$	$A_2A_3A_2$
E_{d8}	$k_d - \Delta K_2 + \Delta K_3$	$\Omega_1 - \Omega_2 + \Omega_3$	$\eta_2 - \eta_1$	$A_1A_2A_3$
E_{d9}	$k_d + 2\Delta K_2$	$2\Omega_2 - \Omega_1$	$2\eta_1$	$A_2A_1A_2$
E_{d10}	$k_d + \Delta K_2 + \Delta K_3$	$\Omega_2 - \Omega_1 + \Omega_3$	$\eta_1 + \eta_2$	$A_2A_1A_3$
E_{d11}	$k_d + 2\Delta K_3 - \Delta K_2$	$2\Omega_3 - \Omega_2$	$2\eta_2 - \eta_1$	$A_3A_2A_3$
E_{d12}	$k_d + 2\Delta K_3$	$2\Omega_3 - \Omega_1$	$2\eta_2$	$A_3A_1A_3$

of each of the partial waves propagating in the acoustooptical cell. Each of these waves is characterized by its own wave number, frequency shift with respect to the incident light beam, detuning parameter, and also amplitudes of acoustic components by which the consequent scattering occurred.

As is well known, in the case of collinear diffraction, the optical field in the region of interaction of light and sound can be represented as a sum of incident and diffracted beams, which in the case of cubic nonlinearity of interaction (i.e., in the case under study) can be represented as

$$E(x, t) = \sum_{i=0}^{6} E_{ti}(x, t) + \sum_{j=1}^{12} E_{dj}(x, t). \qquad (5)$$

Substituting Eq. (5) into wave equation (1) and then equating the coefficients of equal frequencies, we obtain a set of equations that connects the amplitudes of transmitted and diffracted waves:

$$\frac{dE_{t0}}{dx} = \frac{q_1}{2}E_{d1} + \frac{q_2}{2}E_{d2}e^{j\eta_1 x} + \frac{q_3}{2}E_{d3}e^{j\eta_2 x}$$

$$\frac{dE_{t1}}{dx} = \frac{q_1}{2}E_{d1} + \frac{q_7}{2}E_{d4}e^{-j\eta_2 x} + \frac{q_8}{2}E_{d5}e^{j(\eta_1-\eta_2)x}$$

$$\frac{dE_{t2}}{dx} = \frac{q_2}{2}E_{d2}e^{j\eta_1 x} + \frac{q_8}{2}E_{d5}e^{-j(\eta_1-\eta_2)x} + \frac{q_{10}}{2}E_{d7}e^{j(2\eta_1-\eta_2)x}$$

$$\frac{dE_{t3}}{dx} = \frac{q_1}{2}E_{d1} + \frac{q_9}{2}E_{d6}e^{-j\eta_1 x} + \frac{q_8}{2}E_{d8}e^{j(\eta_2-\eta_1)x}$$

$$\frac{dE_{t4}}{dx} = \frac{q_2}{2}E_{d2}e^{j\eta_1 x} + \frac{q_{11}}{2}E_{d9}e^{2j\eta_1 x} + \frac{q_8}{2}E_{d10}e^{j(\eta_1+\eta_2)x}$$

$$\frac{dE_{t5}}{dx} = \frac{q_3}{2}E_{d3}e^{j\eta_2 x} + \frac{q_8}{2}E_{d8}e^{j(\eta_2-\eta_1)x} + \frac{q_{12}}{2}E_{d11}e^{j(2\eta_2-\eta_1)x}$$

$$\frac{dE_{t6}}{dx} = \frac{q_3}{2}E_{d3}e^{j\eta_2 x} + \frac{q_8}{2}E_{d10}e^{j(\eta_1+\eta_2)x} + \frac{q_{13}}{2}E_{d12}e^{2j\eta_2 x}$$

$$\frac{dE_{d1}}{dx} = -\frac{q_1}{2}E_{t0} - \frac{q_4}{2}E_{t1}e^{-j\eta_2 x} - \frac{q_6}{2}E_{t3}e^{-j\eta_1 x}$$

$$\frac{dE_{d2}}{dx} = -\frac{q_2}{2}E_{t0} - \frac{q_6}{2}E_{t4}e^{j\eta_1 x} - \frac{q_5}{2}E_{t2}e^{-j(\eta_2-\eta_1)x} \qquad (6)$$

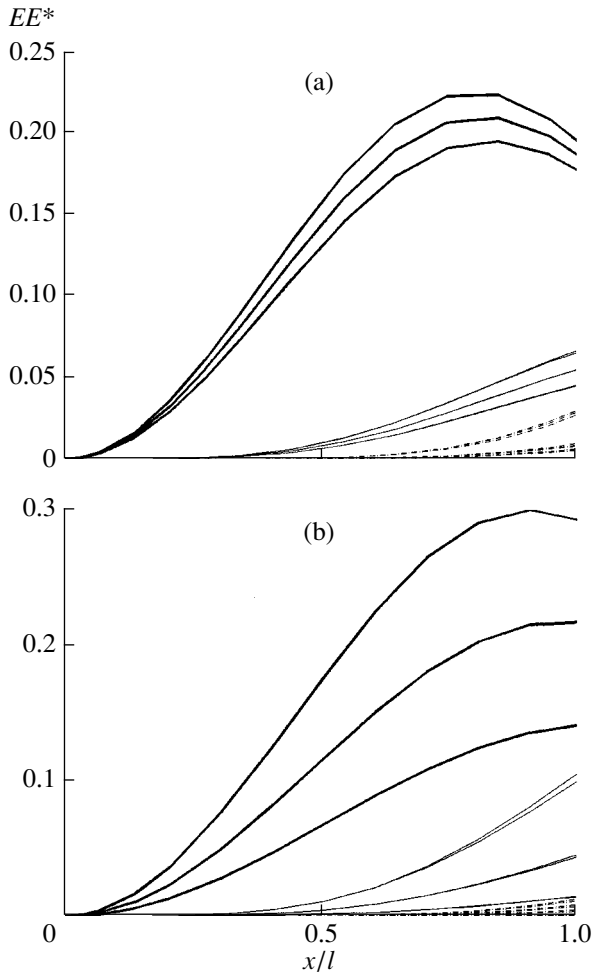

Fig. 2. Distribution of light wave amplitudes along the cell for different ratios between the amplitudes of sound signal components. The thick, thin, and dot-and-dash lines correspond to the wave amplitudes at principal frequencies, at combination frequencies in transmitted light, and at combination frequencies in diffracted light, respectively. (a) $A_1 : A_2 : A_3 = 1 : 0.95 : 0.9$; (b) $A_1 : A_2 : A_3 = 1 : 0.8 : 0.6$. $\eta_1 l = 0.1$; $\eta_2 l = 0.15$.

$$\frac{dE_{d3}}{dx} = -\frac{q_3}{2}E_{t0} - \frac{q_4}{2}E_{t6}e^{-j\eta_2 x} - \frac{q_5}{2}E_{t5}e^{-j(\eta_1-\eta_2)x}$$

$$\frac{dE_{d4}}{dx} = -\frac{q_4}{2}E_{t1}e^{-j\eta_2 x}$$

$$\frac{dE_{d5}}{dx} = -\frac{q_4}{2}E_{t1}e^{-j\eta_2 x} - \frac{q_5}{2}E_{t2}e^{-j(\eta_2-\eta_1)x}$$

$$\frac{dE_{d6}}{dx} = -\frac{q_6}{2}E_{t3}e^{-j\eta_1 x}$$

$$\frac{dE_{d7}}{dx} = -\frac{q_5}{2}E_{t2}e^{-j(\eta_2-\eta_1)x}$$

$$\frac{dE_{d8}}{dx} = -\frac{q_6}{2}E_{t3}e^{-j\eta_1 x} - \frac{q_5}{2}E_{t5}e^{-j(\eta_1-\eta_2)x}$$

$$\frac{dE_{d9}}{dx} = -\frac{q_6}{2}E_{t4}e^{j\eta_1 x}$$

$$\frac{dE_{d10}}{dx} = -\frac{q_6}{2}E_{t4}e^{j\eta_1 x} - \frac{q_4}{2}E_{t6}e^{j\eta_2 x}$$

$$\frac{dE_{d11}}{dx} = -\frac{q_5}{2}E_{t5}e^{-j(\eta_1-\eta_2)x}$$

$$\frac{dE_{d12}}{dx} = -\frac{q_4}{2}E_{t6}e^{-j\eta_2 x}.$$

Here, $q_1 = E_i A_1$, $q_2 = E_i A_2$, $q_3 = E_i A_3$, $q_4 = E_i A_1 A_3$, $q_5 = E_i A_2 A_3$, $q_6 = E_i A_1 A_2$, $q_7 = E_i A_1^2 A_3$, $q_8 = A_1 A_2 A_3$, $q_9 = E_i A_1^2 A_2$, $q_{10} = E_i A_2^2 A_3$, $q_{11} = E_i A_2^2 A_1$, $q_{12} = E_i A_3^2 A_2$, and $q_{13} = E_i A_3^2 A_1$.

DISCUSSION OF THE RESULTS

System of equations (6) was used to calculate the amplitude distribution of light waves along the cell for various amplitude ratios between the components of the sound signal. The results of calculation are presented in Fig. 2. The length of the interaction region was selected to provide a complete energy transfer from wave E_{t0}. The detuning values η_1 and η_2 determined by Eqs. (4) weakly influence the qualitative results obtained for the distribution of light amplitudes and only reduce the energy transfer to the diffraction peak. Therefore, in the calculation at hand, they were assumed to be small.

In the case of almost equal amplitude values of the acoustic components (Fig. 2a), the intensities of principal diffraction peaks reach approximately 20% of the incident light intensity. The share of parasitic peaks in the incident light is 3–7%, and in the diffracted light, 3%. Thus, the dynamic range of the spectrum analyzer in the case of a high efficiency of diffraction is about 10 dB. If the difference in amplitude of the analyzed signal is large (Fig. 2b), the dynamic range slightly increases. From the character of the amplitude distribution of light waves, one can see that the parasitic amplitudes in the diffraction peak grow along the interaction length much faster than the principal ones. Therefore, it is necessary to reduce the diffraction efficiency at least twice to obtain a noticeable increase in the dynamic range of the spectrum analyzer.

Figure 3 presents the intensity dependences of the principal diffraction peaks $E_{di}E_{di}^*$ ($i = 1, \ldots, 3$) on the quantity ηl for the case of almost equal amplitudes of acoustic signal components $A_1 \approx A_2 \approx A_3$ (Fig. 3a) and for widely different amplitudes (Fig. 3b). As one can see from Fig. 3, the character of the dependence for a wave being in synchronism (curves *1*) differs substantially from that observed for two other waves characterized by detunings η_1 and η_2 (curves *2* and *3*). This is connected with the energy redistribution between

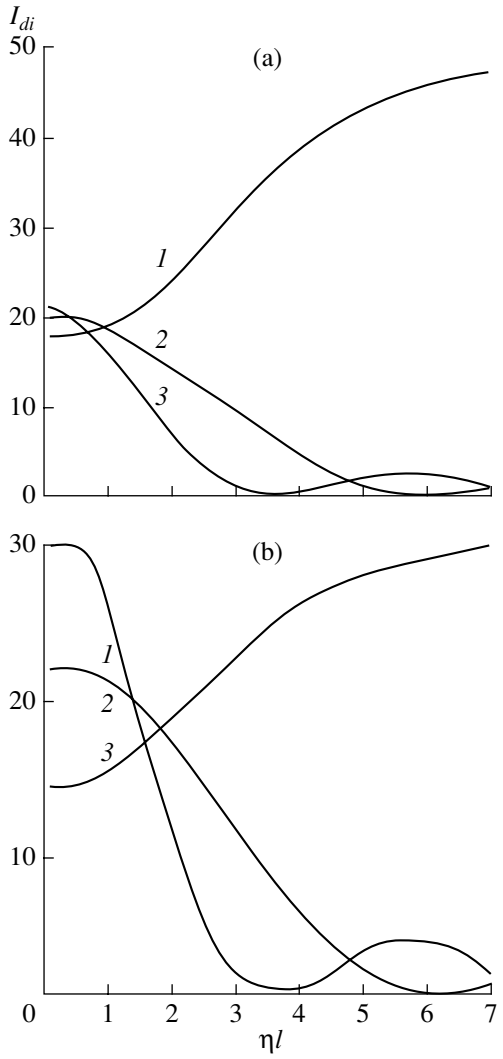

Fig. 3. Intensity of the principal diffraction peaks $E_{di}E_{di}^*$ ($i = 1, \ldots, 3$) versus the quantity ηl for (*1*) the wave being in synchronism, (*2*) the wave with the detuning η_1, and (*3*) the wave with the detuning η_2. (a) $A_1 \approx A_2 \approx A_3$; (b) $A_1 : A_2 : A_3 = 1 : 0.8 : 0.6$. $\eta_2 = 1.5\eta_1$.

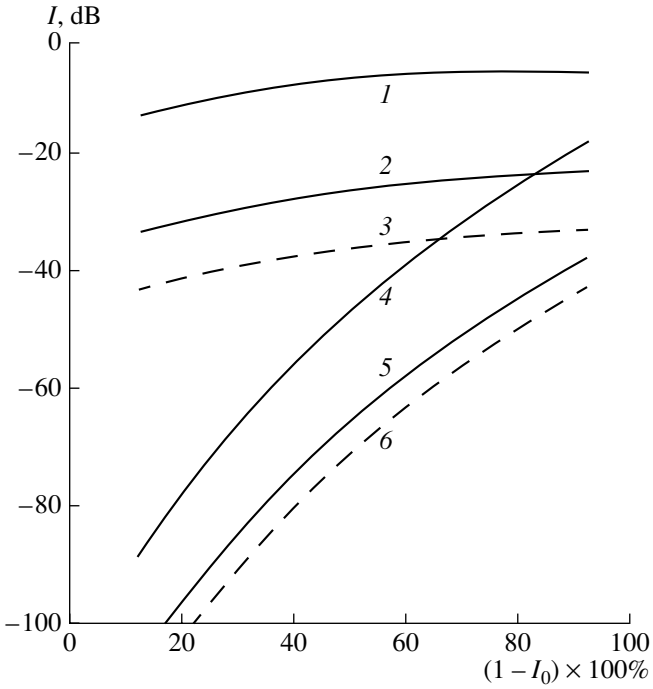

Fig. 4. Intensity of the principal and parasitic diffraction peaks versus the efficiency of acoustooptical interaction.

waves in the diffraction peak. For waves E_{d2} and E_{d3}, the curves have the shape characteristic of a common transmission function of an acoustooptical filter, i.e., with a principal peak and sidelobes. Naturally, the width of the principal transmission lobe is greater for the wave with a smaller ΔK. For wave E_{d1}, the curve displays a monotonic increase due to the energy decrease in two components of the useful signal. Comparing the curves in Figs. 3a and 3b, we note that the width and the position of the sidelobe in the transmission curves of detuned waves E_{d2} and E_{d3} almost do not change. However, in the case of the wave being in synchronism, the relative increment of intensity is greater when the amplitudes of the acoustic signal components are almost equal. It is worth noting that the total intensity of the three diffracted waves of fundamental frequencies decreases with increasing ηl despite the reduction in the total intensity of parasitic sideband components. This is connected with the general reduction in the diffraction efficiency in the case of a fixed length of the region of acoustooptical interaction; i.e., more and more energy is retained in the incident light beam. Naturally, this effect is most pronounced in Fig. 3b, because in this case the intensities of parasitic sideband components were initially smaller.

The dynamic range of acoustooptical spectrum analyzers is determined by the difference between the levels of true and parasitic components in the diffracted light under investigation. Therefore, it is necessary to calculate the dependence of the amplitudes of principal and parasitic diffraction peaks on the efficiency of acoustooptical interaction. The results of the corresponding calculation are given in Fig. 4. Curve *1* in this figure demonstrates the intensity of the principal diffraction peaks as a function of diffraction efficiency in the case of equal amplitudes of all three spectral components of the acoustic signal. Curves *4* and *5* determine the intensity limits of parasitic peaks. As the diffraction efficiency decreases, these peaks corresponding to the waves of combination frequencies decrease much more rapidly than the principal peaks. This fact provides an opportunity to obtain a dynamic range greater than 60 dB at a diffraction efficiency of 20%.

Curve *2* in Fig. 4 corresponds to a 20-dB reduction of the amplitude of the third acoustic component in comparison with the two others. In this case, at a large

efficiency of acoustooptical interaction, the third component of the useful signal is smaller than some parasitic peaks. In this situation, it is impossible to reveal this component in analyzing the signal under investigation. If the reduction of the amplitude of the third acoustic component is 30 dB (curve *3* in Fig. 4), this component can be revealed only by a further reduction in the diffraction efficiency down to 60%. It is interesting to note that the range of the values of parasitic peaks changes only at its lower boundary, which drops with decreasing amplitude A_3 down to curve *6*. The upper boundary of the range of parasitic peaks does not depend on the amplitude of the third acoustic component.

CONCLUSIONS

The study described above demonstrated that parasitic sideband components that occur in diffracted light can play a significant role if the diffraction efficiency is sufficiently high and exceeds 80%. A fundamental opportunity to considerably reduce the amplitudes of parasitic peaks of an acoustooptical spectrum analyzer was demonstrated in [13]. It was suggested to perform preliminary distortion of the input signal fed to the analyzer with the aim to compensate the cubic nonlinearity of its characteristic. In this way, the dynamic range of a spectrum analyzer could be broadened by no less than 20 dB.

One more way to separate the true components of an acoustic signal from parasitic ones can be proposed. For this purpose, one can use the difference in the rates of decrease in the amplitudes of true and parasitic components of diffracted light with the variation of the amplitude of the signal under analysis. If the input signal amplitude is reduced to 0.7 dB from the initial value in the course of measurement, the intensity of the principal peaks will drop by 3 dB and the intensity of the peaks of combination waves, by 9 dB. Thus, the diffracted light components that decrease rapidly with decreasing input signal amplitude are parasitic and should not be taken into account in analyzing the radiofrequency signal fed to the input of an acoustooptical spectrum analyzer.

In practice, it is also necessary to take into account the presence of permanent noise due to the light scattering by inhomogeneities within and at the surface of the crystal forming the acoustooptical cell. This noise determines the minimum amplitude level of the input signal. Usually, this level is –60 to –70 dB of the maximum level of the input signal. Therefore, the suppression of the sideband parasitic components below the noise level is useless, and the optimal reduction of the diffraction efficiency for choosing the operational range of the analyzer corresponds to the reduction of parasitic peaks down to the noise level in the system.

REFERENCES

1. A. Korpel, *Acousto-Optics* (Marcel Dekker, New York, 1988; Mir, Moscow, 1993).
2. Xu Jieping and R. Stroud, *Acousto-Optic Devices* (Wiley, New York, 1992).
3. V. I. Balakshiĭ, V. N. Parygin, and E. L. Chirkov, *Physical Foundations of Acoustooptics* (Radio i Svyaz', Moscow, 1985).
4. V. N. Parygin, A. V. Vershubskiĭ, and K. A. Kholostov, Zh. Tekh. Fiz. **70** (8), 91 (2000) [Tech. Phys. **45**, 1045 (2000)].
5. V. D. Voloshinov, Opt. Eng. **31** (10), 2089 (1992).
6. C.-W. Tarn, R. S. Huang, and C.-W. Hsieh, Appl. Opt. **37**, 7496 (1998).
7. Chieu D. Tran and Geng-Chen Huang, Opt. Eng. **38** (7), 1143 (1999).
8. V. N. Parygin and A. V. Vershubskiĭ, Opt. Spektrosk. **82** (1), 138 (1997) [Opt. Spectrosc. **82**, 125 (1997)].
9. V. N. Parygin, A. V. Vershubskiĭ, and Yu. G. Rezvov, Akust. Zh. **47**, 29 (2001) [Acoust. Phys. **47**, 22 (2001)].
10. F. W. Windels, V. I. Pustovoit, and O. Leroy, Ultrasonics **38**, 586 (2000).
11. V. V. Proklov and V. N. Chesnokov, Fiz. Tverd. Tela (St. Petersburg) **36**, 3268 (1994) [Phys. Solid State **36**, 1739 (1994)].
12. V. N. Parygin, A. V. Vershubskiĭ, and S. V. Petrov, Izv. Ross. Akad. Nauk, Ser. Fiz. **64**, 2377 (2000).
13. V. N. Parygin and A. V. Vershubskiĭ, Radiotekh. Élektron. (Moscow) **47** (10), 1293 (2002).

Translated by M. Lyamshev

Acoustical Physics, Vol. 49, No. 6, 2003, pp. 653–661. Translated from Akusticheskiĭ Zhurnal, Vol. 49, No. 6, 2003, pp. 768–777.

Investigation of the Sound Field Structure in the Ocean with a Deep-Water Reception

O. P. Galkin and L. V. Shvachko

Andreev Acoustics Institute, Russian Academy of Sciences, ul. Shvernika 4, Moscow, 117036 Russia

e-mail: bvp@akin.ru

Received October 15, 2002

Abstract—The results of studying the angular and energy structures of a sound field at great depths (880 and 1100 m) with the emission of pseudonoise signals (a frequency range of 1–4 kHz) in the upper layers of the ocean below the velocline (at a depth of 200 m) are presented. The results refer to two ocean regions characterized by the presence of a single-axis deep-water sound channel. The sound field structure at great depths is compared with that recorded at the source depth. The experimental data for the first two convergence zones are compared with the calculations by the ray method. A conclusion is made that, on the whole, the basic regularities of the field structure at great depths are adequately described by the ray theory. However, the spatial positions of the convergence zones observed in the experiment differ from those predicted by the ray calculations. Moreover, a closer examination of the field characteristics shows that the parameters of the angular and energy structures noticeably deviate from the calculated values. © *2003 MAIK "Nauka/Interperiodica".*

It is well known that the basic features of the sound field structure, which are observed in oceanic waveguides, strongly depend on the hydrological conditions of the region and on the relative positions of the source and the receiver. In deep-water oceanic regions, a sound field is more frequently formed in the conditions characterized by the presence of a single-axis underwater sound channel. For the latter, the characteristic feature is the clearly defined zonal structure of the sound field in the form of a sequence of shadow and convergence zones. Precisely in these conditions typical of regions with sound velocity profiles $c(z)$ of tropical and subtropical types, most field investigations of the angular and energy structure of the sound fields were carried out [1–3]. The bulk of experimental data was obtained with the source and receiver positions in the 500-m-thick upper layer of the waveguide. However, in several regions of the ocean, the sound field structure was also measured at much greater depths (from 800 to 2000 m). It should be noted that all experiments were carried out with the research vessels of the Acoustics Institute by using a transmitting–receiving system specially designed under the supervision of A.M. Dymshchits at the Morfizpribor Central Research Institute.

The experiments were carried out using broadband pseudonoise signals. In the upper oceanic layers (up to several hundreds of meters), the signal reception was realized by both omnidirectional hydrophones and two identical vertical 40-m-long flexible arrays with an external diameter of 5 cm. They were lowered into the water through trunks made along the ship diametral in the bottom of the receiving research vessel. Each array contained 296 hydrophones united into 74 phase centers. Owing to the nonequidistant arrangement of the hydrophones, it was possible to measure signal arrival angles in the vertical plane in a wide (3-octave) frequency range (0.5–4.0 kHz) with almost identical resolution (2°–2.5°) owing to the difference in the length of the array segments. After amplification in a special bathysphere located in the immediate vicinity of the upper part of the array, the signals from all 74 phase centers were transmitted to the receiving ship, where they were recorded and subjected to the necessary processing. For studying the angular structure of the sound field at great depths, a special deep-water vertical array was manufactured in the form of a 10-m-long hard girder. It was lowered not through the trunks but from the shipboard with a specially developed high-frequency single-core cable. For transmitting multichannel information to shipboard, a packing system was used. To compare the angular field structures simultaneously measured in the upper oceanic layers and at great depths, the arrangement of the hydrophones on the hard girder and their number corresponded to the central parts of the vertical flexible arrays. In this case, the angular resolution of the deep-water array for noise signals with an average frequency of f_{av} = 3.15 kHz was also ~2.5°. The deep-water array was used for measurements to a depth of 2000 m.

The experiments described below were performed with the use of two research vessels that lay to. From the transmitting ship, a broadband, almost omnidirectional, sound source was lowered through a special trunk to a depth of about 200 m. At the receiving ship, the signals were received by the flexible arrays down to a depth of 600 m, and at greater depths, by the deep-water array. The measurements were carried out with a

1063-7710/03/4906-0653$24.00

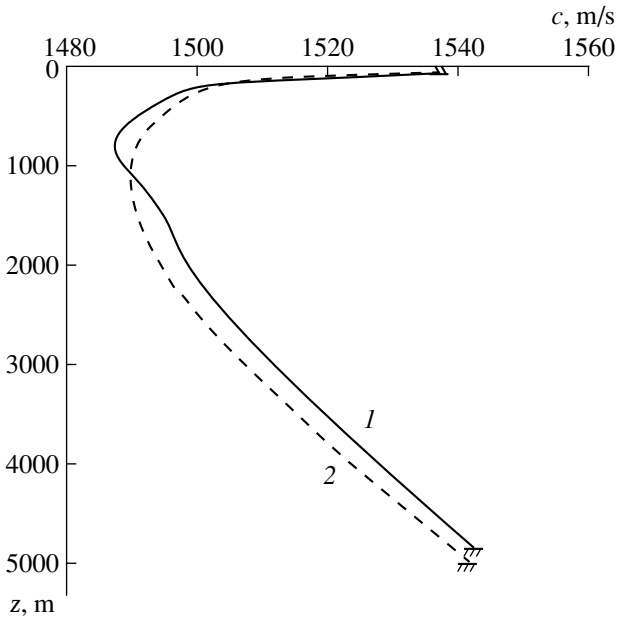

Fig. 1. Sound velocity profiles $c(z)$ in (*1*) the Quiana region of the Atlantic Ocean (solid line) and (*2*) the Central Basin of the Indian Ocean (dotted line).

slow and continuous variation of the distance between the corresponding points by means of the transmitting ship motion against the drift and the free drift of the receiving ship. The distance between the source and the receiving arrays (but not between the ships, as is usually done in many oceanic experiments) was determined every minute with specially developed hardware [4]. For this purpose, in the system of unique (international) time, short pulses of high intensity were added to the continuous pseudonoise signal. At the receiving ship, after the determination of the signal arrival angles in the vertical plane and propagation time of pulses over the corresponding rays, the distance to the source was calculated.

Studies of the angular and energy structure of the sound field at great depths and comparison of this information with the field structure simultaneously measured at depths close to that of the source (~200 m) were carried out in various regions of the ocean. The maximum distances where the measurements were carried out correspond to the two first convergence zones (~120–130 km). In the Mediterranean Sea, the deep-water reception was realized at a depth of ~1500 m; in the Indian Ocean: in the region of the Central Basin, at a depth of ~1100 m, and in the West-Australian Basin, at a depth of ~2000m; in the Atlantic Ocean: near the Canary Islands, at a depth of ~1400 m, near the Cape Verde Islands, at a depth of 800 m, and also in some other regions.

The field structure at great depths was investigated in most detail in the Quiana region of the Atlantic Ocean (off the coast of Brasil) with the deep-water receiving system positioned at a depth of 880 m, near the axis of the underwater sound channel. For this region, the sound velocity profile is shown by a solid line in Fig. 1. As is seen, the velocline with a high negative gradient of the sound velocity was observed in the test region at depths from 50 to 200 m. In a single-axis sound channel, the sound field character is mainly determined by the difference in the sound velocities at the emission and reception depths. The experiment was carried out with the emission of a noise signal in the frequency range 1–4 kHz at a depth of 200 m and with the reception at depths of 190 m (the center of one of the flexible arrays) and 880 m (the center of the deep-water array). As was noted above, the test track covered the two first convergence zones. In general, the sound field structure at both depths is quite adequately described by a ray pattern (note that, for the frequencies considered, the sound field calculations by the ray and wave codes give almost identical results [5–7]). So, while at a reception depth of 190 m the sound field was mainly formed by the signals turning in the upper oceanic layers, at a reception depth near the channel axis, i.e., ~880 m, it was generated by the signals arriving at steeper angles. This is confirmed by the experimental angular structure of the water signals (arriving without reflections from the waveguide boundaries) in the first convergence zone (Figs. 2a, 2b) for the aforementioned depths of reception. Distance r in kilometers is represented by the abscissa and the arrival angles α in degrees, by the ordinate. The "+" sign corresponds to the signals arriving at the reception point from above, and the "–" sign, to signals arriving from below. The dots indicate the experimental data, and the solid lines, the calculations. As follows from Fig. 2a, the angular structure of the field at a reception depth of 190 m has the pattern typical of the case when the sound velocity difference between the emission and reception depths is small. The pattern is formed by four congruences of rays with signal arrival angles from –12.5° to +12.5°, including the zero angle. At a depth of 880 m, because of the great difference in the sound velocity at the source and reception depths ($\Delta c \cong 16.2$ m/s), these ray congruences are shifted upwards and downwards along the α axis, toward greater (in magnitude) arrival angles. As a result, the signals with arrival angles close to zero are absent in the angular spectra. According to the calculated curve $\alpha(r)$ in Fig. 2b, the field generated by the water signals near the axis of the sound channel is formed by two clearly separated congruences of rays with the arrival angles $8° \le |\alpha| \le 15°$. Note that comparison of the experimental and calculated data (Figs. 2a, 2b) shows that the experimental points fit well the curves α for both depths of reception. However, the experimental points are present also at distances that are nearer than the calculated head of the convergence zone. The signals corresponding to these points are recorded r = 4–5 km nearer than the calculated distance. It should be noted, however, that the first water signals recorded in the experiments are very weak: their

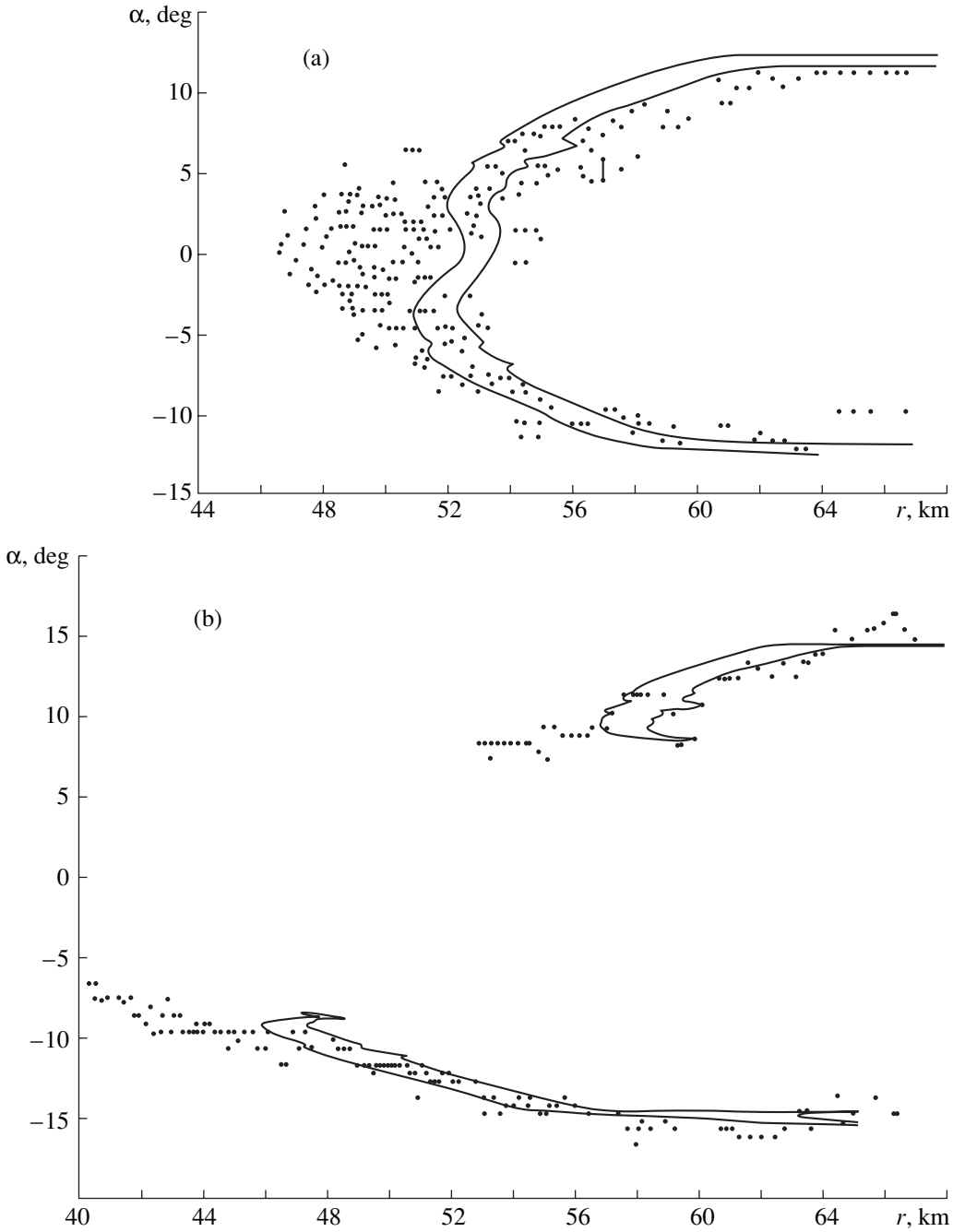

Fig. 2. Angular structure of the sound field in the first convergence zone observed in the Quiana region with an emission depth of 200 m and a reception depth of (a) 190 and (b) 880 m.

focusing factor F is close to 0.01–0.02. Therefore, Figs. 2a and 2b cannot serve for judging the degree of disagreement between the experimental and calculated head of the convergence zones.

The comparison of the field energy structure recorded with omnidirectional reception at a depth of 190 m and at the channel axis (880 m) for pseudonoise signals in the 1/3-octave band with the mean frequency f_{av} = 3.15 kHz is shown in Figs. 3a and 3b. Here, the field structure at the channel axis is also presented for the signals within the lower frequency range with f_{av} = 1.25 kHz. In all curves, distance r in kilometers is represented by the abscissa and the signal intensity I in decibels, by the ordinate; the level 0 dB is taken to be the field level at r = 1 km from the source for the spherical law of propagation. The solid lines correspond to experimental data $I_{exp}(r)$; the thin dashed lines, to the calculation results $I_{cal}(r)$; and the thin dot-and-dash

lines, to the spherical law with allowance for the attenuation equal 0.14 dB/km for f = 3.15 kHz and 0.04 dB/km for f = 1.25 kHz. From these data it follows that the experimental energy structure of the total field at both reception depths agrees well with the experimental angular structure shown in Figs. 2a and 2b. Indeed, for the upper reception depth, the convergence zone is the insonified segment of the track 15–16 km in length, where the maximum of the signal intensity is at distances from 50 to 52 km. At a depth of 880 km, the convergence zone 22–23 km in length consists of two parts with enhanced signal intensity, which correspond to separate ray congruences in the ray structure. These parts are separated by the track segment where the signal level is noticeably lower. For both segments of the convergence zone, the maximum value of the sound intensity is lower than that in the upper oceanic layers. So, while the maximum value of the transmission anomaly at a depth of 190 m is 23 dB for a frequency of f_{av} = 3.15 Hz (Fig. 3a), at a depth of 880 m it does not exceed 16 dB. Thus, the difference in the signal focusing factor at a depth close to that of the source and at the sound channel axis (ΔA_{max}) is ~7 dB.

For the signals with a frequency of f_{av} = 1.25 kHz, the energy structure of sound intensity I_{exp} at the channel axis (Fig. 3c) retains the basic features of I for signals with f_{av} = 3.15 kHz. However, one should notice a lower level of focusing in the caustics (A_{max} = 13–14 and 15 dB for the first and second parts of the zone, respectively). As the experimental data shows, the quantity ΔA_{max} retains almost the same value (~7 dB). Some differences are also observed in the fine structure of the sound field. They are caused by the smoother character of curve I due to the large period of interference for this frequency range.

From comparison of the experimental and calculated energy characteristics (Figs. 3a–3c), it follows that curves $I_{exp}(r)$ and $I_{cal}(r)$ are similar to one another but are shifted by Δr in distance. If we determine the head of the convergence zone from the rapid increase in the intensity of the received signals when the signal focusing factor exceeds unity, then the head of the zone in the experiment is nearer to the source at both depths by a quantity Δr equal ~2 km for a reception depth of 190 m and 2.5–3.0 km for a reception depth of 880 m. In the latter case, the value of the shift Δr is almost equal to both initial and terminal segments of the convergence zone. Thus, the disagreement between the experimental and calculated values of the head of the zone at the channel axis is somewhat greater than in the upper oceanic layers.

The estimates obtained for quantity Δr are close to the maximum values recorded in various regions of the ocean. The difference between experimental and calculated data, Δr, in hydrological conditions of the tropical type $c(z)$ usually exceeds Δr obtained in the subtropical conditions.

In the case of omnidirectional signal reception, the interference effects appear in the energy structure of the sound field, especially at the channel axis (Figs. 3b and 3c), where the number of arriving signals is somewhat smaller than that at the upper reception depth. It is of interest to compare these data with the energy structure of the field measured using the directional reception in the vertical plane. Figure 4a exhibits the intensity, $I_\alpha(r)$, of individual signals of frequency f_{av} = 3.15 kHz. They are received near the sound channel axis and arrive at the point of reception along the first convergence zone from below at the angles $\alpha = -(8°–15°)$ and from above at angles of $\alpha = 8°–15°$ (points and circles in the curve, respectively). The level corresponding to the spherical law of propagation is denoted by a thin dot-and-dash line; it allows one to estimate the transmission anomaly of the signals spanned by a lobe ~2.5° in width. The calculated head of the zone for the signals arriving from below is denoted in the curve by the vertical thick line *1*, while the head of the zone and end of the zone for the signals arriving from above, by the straight lines *2* and *3*, respectively. From the data of Fig. 4a, it is clear that the range of distances (40–69 km) in which the water signals were received is noticeably greater than the calculated range (46–64 km); i.e., the signals were recorded not only nearer to the source but also farther than predicted by the ray theory.

The most interesting segment in Fig. 4a corresponds to the initial range of distances at the head of the convergence zone, and this segment is presented in more detail in Fig. 4b. Here, signal intensity $I_\alpha(r)$ with directional reception (curve *2*) is compared with the field intensity I with omnidirectional reception (curve *1*). It is seen that the character of the curves is almost the same beginning from the distance ~42.6 km. The field intensity reaches its maximum value at a distance of 44 km for both kinds of reception (Fig. 4b). With directional reception, the maximum transmission anomaly does not differ from that obtained with omnidirectional reception.

Consider now the results of studying the field structure in the second convergence zone. Figure 5 exhibits the experimental and calculated data for the signal reception at a depth of the sound channel axis (~880 m). Figure 5a presents the range dependence of the angular structure, $\alpha(r)$, of the water pseudonoise signals with f_{av} = 3.15 kHz (the points represent the experiment, and the curves represent the calculation). Figures 5b and 5c present the energy structure of the sound field with omnidirectional reception for signals with f_{av} = 3.15 kHz and f_{av} = 1.25 kHz, respectively (the solid line refers to the experiment, and the dotted line, to the calculation). It is seen that the angular structure of the field has the same basic features noted in discussing the results for the first zone. First, the signals arrive with grazing angles that agree with the calculation, and, second, the angular range where the signals are absent is the same. The basic difference is that the disagreement between

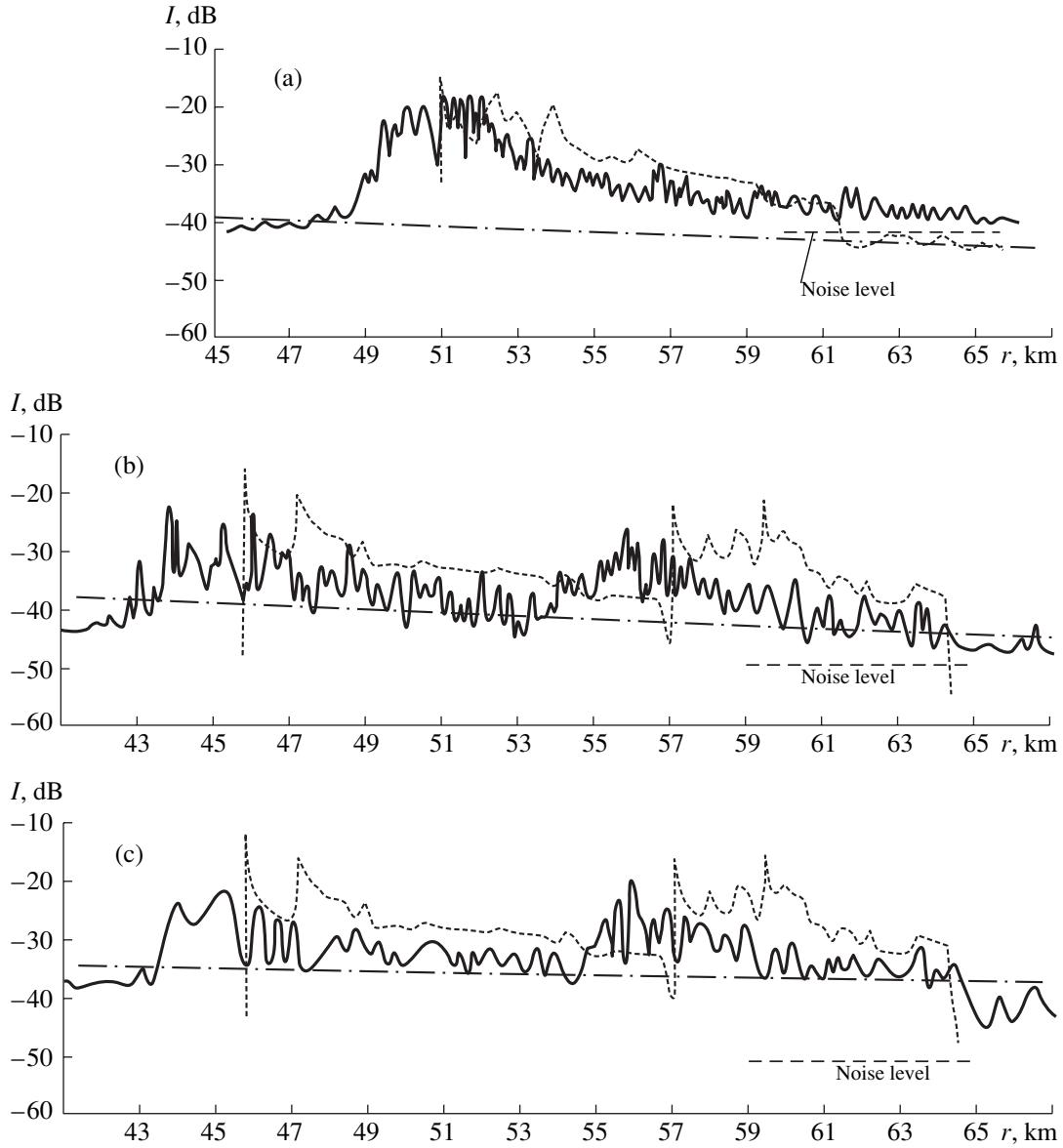

Fig. 3. Energy structure of the sound field in the case of omnidirectional reception in the first convergence zone (Quiana region): the emission depth is 200 m; the reception depth is (a) 190 and (b, c) 880 m; f_{av} = (a, b) 3.15 and (c) 1.25 kHz.

the experimental and calculated positions of the head of the convergence zone is much greater. In the first zone, this shift was 2.5–3.0 km, and in the second zone, it was ~3.0–3.5 km for the first part of the zone and 4.0–4.5 km in its second part.

The calculated energy structure of the field in the second convergence zone differs from the experimental one much more than the field structure in the first zone does. This fact is confirmed by the dependences $I(r)$ (Figs. 5b, 5c) obtained with omnidirectional reception for both frequency ranges, as well as by the variation of $I_\alpha(r)$ with distance at directional reception for f = 3.15 kHz (Fig. 5b). Here, the points denote the signals recorded at the head of the zone (they arrived at the point of reception from below), and the circles denote the signals in the second part of the zone; they arrived at the point of reception from above. From these dependences it follows that the energy structure of the field in the second convergence zone, as well as in the first zone, consists of two parts separated by an interval with a lower sound intensity. This is clearly seen in dependence $I_\alpha(r)$ at the directional reception. In this case, the transmission anomaly (A) reaches –(10–12) dB near the middle of the zone at a distance of $r \cong 104$ km for a frequency of f_{av} = 3.15 kHz. At the same time, with omnidirectional reception at the same distances, the transmission anomaly increased up to + 5 dB (mainly due to the bottom reflected signals), but for signals with f_{av} = 1.25 kHz it was somewhat smaller ($A \sim 0$ dB). For the total range of distances presented in the curves, the

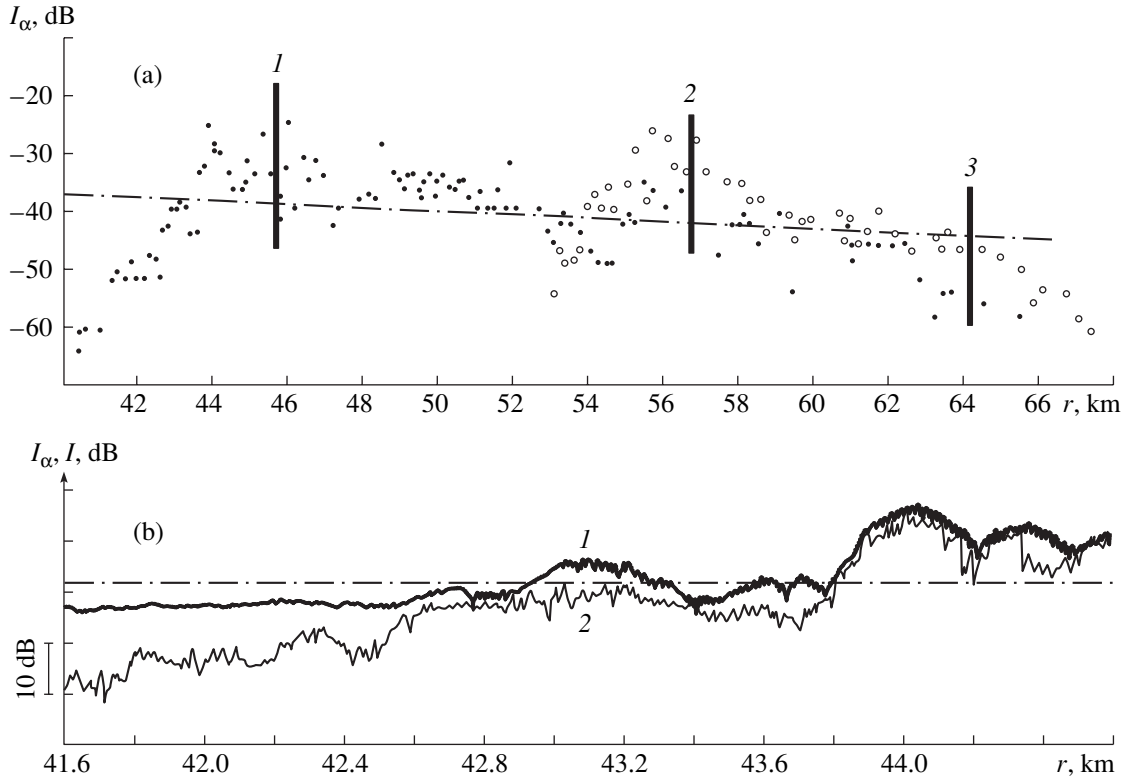

Fig. 4. Energy structure of the sound field near the underwater sound channel axis in the first convergence zone (Quiana region): the emission depth is 200 m, the reception depth is 880 m, and f_{av} = 3.15 kHz; variations of the signal intensity (a) in the case of the directional reception within the whole length of the zone and (b) in the case of the (*1*) omnidirectional and (*2*) directional reception at the zone head.

maximum values of the transmission anomaly (A_{max}) with omnidirectional reception of the signals with f_{av} = 3.15 kHz reach +16 dB (at the head of the zone) and +15 dB (at the end of the zone). For signals of frequency f_{av} = 1.25 kHz, the corresponding data are almost 16 dB and 17 dB, respectively. With directional reception of the signals with f_{av} = 3.15 kHz (Fig. 5b), A_{max} was equal to the maximum transmission anomaly with omnidirectional reception (the first part of the zone) or deviated from it by no more than 1–2 dB (the second part of the convergence zone). According to the results of the investigations in the second convergence zone at a depth of 190 m, which are not presented in this paper, the difference in the signal focusing near the depths of emission (200 m) and the channel axis (880 m) is ΔA_{max} ~ 7–8 dB. Thus, for both convergence zones, the value of ΔA_{max} is almost the same.

The results of studying the sound field structure at large depths, which were obtained in the Quiana region, can be compared with those obtained in the Central Basin of the Indian Ocean. The experiments were carried out with the same technique and the same measuring system. The test region was characterized by profile $c(z)$ of the tropical type shown in Fig. 1 by the dotted line. As seen from Fig. 1, profiles $c(z)$ are almost identical in the subsurface layer (to a depth of ~200 m) of the Quiana region and the Central Basin; in addition, their negative gradients of the sound velocity are very close to one another in both cases. Some differences in the profiles appear in deeper layers directly below the velocline. In the Indian Ocean, the sound channel axis lies almost 200 m below that in the Quiana region. At depths more than 2500 m, the sound velocity gradients are almost identical, although their absolute values $c(z)$ are different [8].

The results of studying the sound field structure in the first convergence zone in the Central Basin of the Indian Ocean are presented in Fig. 6 for a source located at a depth of 200 m, for a reception depth of 1100 m. The first of the curves (Fig. 6a) corresponds to the angular structure of the pseudonoise signal with a frequency of f_{av} = 3.15 kHz, and the other two, to the energy structure of the field with omnidirectional reception of the signals with f_{av} = 3.15 kHz (Fig. 6b) and f_{av} = 1.25 kHz (Fig. 6c). As was noted above, when the corresponding points are at different depths, the angular structure is mainly determined by the difference in sound velocity Δc at the depths of the source and receiver. For the conditions of the Indian Ocean, Δc was ~12.5 m/s, and it was ~16.2 m/s for the conditions of the Quiana region. This determines some differences in the angular structure of the sound field as well. So,

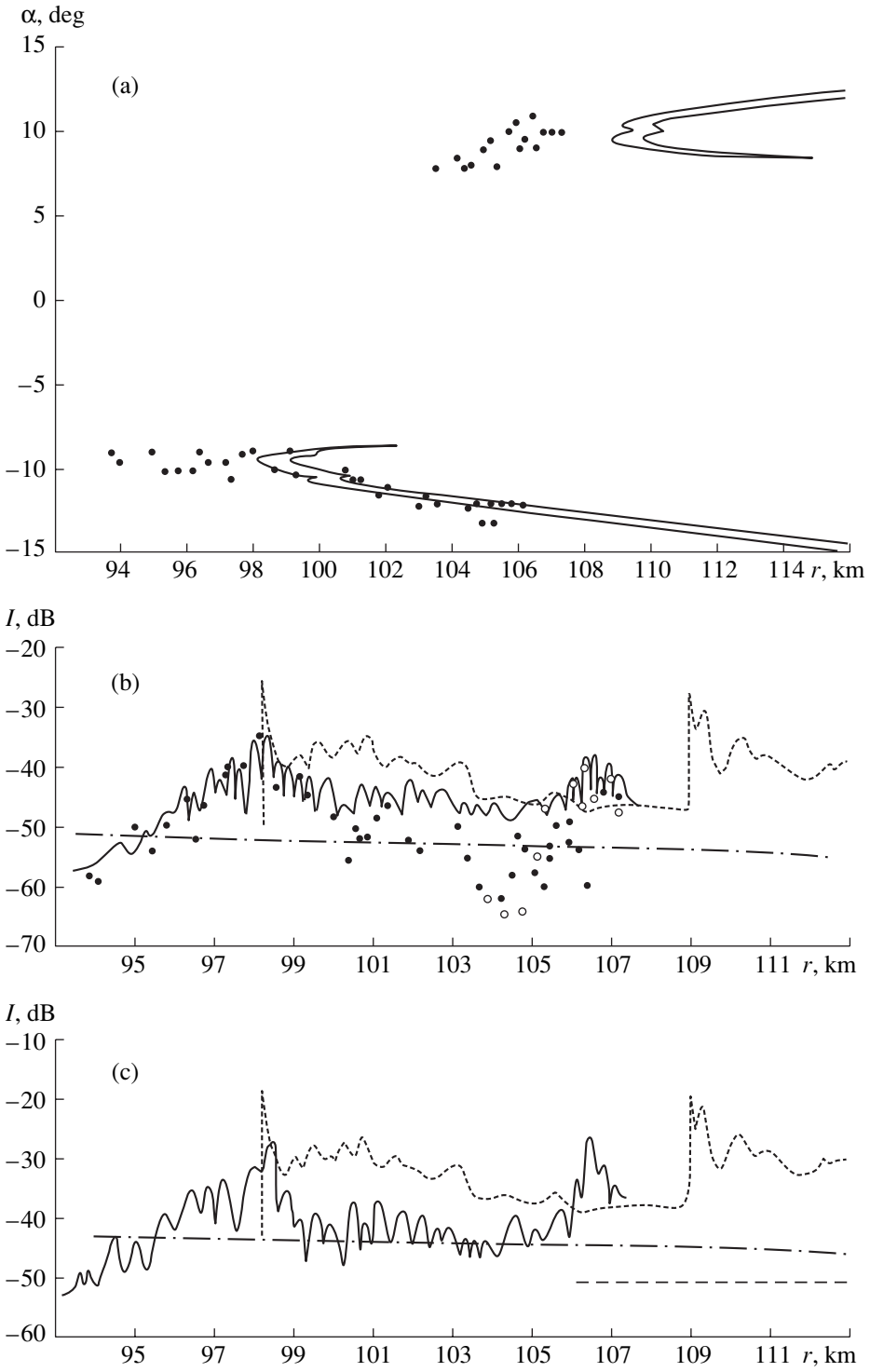

Fig. 5. Sound field structure in the second convergence zone (Quiana region): the emission depth is 200 m and the reception depth is 880 m; (a) the angular structure, f_{av} = 3.15 kHz; (b) the energy structure at the omnidirectional (the solid line) and directional (dots) reception, f_{av} = 3.15 kHz; (c) the energy structure at the omnidirectional reception, f_{av} = 1.25 kHz.

according to Fig. 6a, the congruences of rays forming the first and second parts of the convergence zone had minimum arriving angles of 7° (7° ≤ |α| ≤ 15°) rather than 8°, which led to a smaller angular sector where the signals were absent, as compared to the previous experiment. The first convergence zone in the Indian Ocean, as in the Quiana region consisting of two parts, was located 2 km farther from the sound source. The second part of the zone (formed by the signals arriving from below) was much farther from its first part (formed by

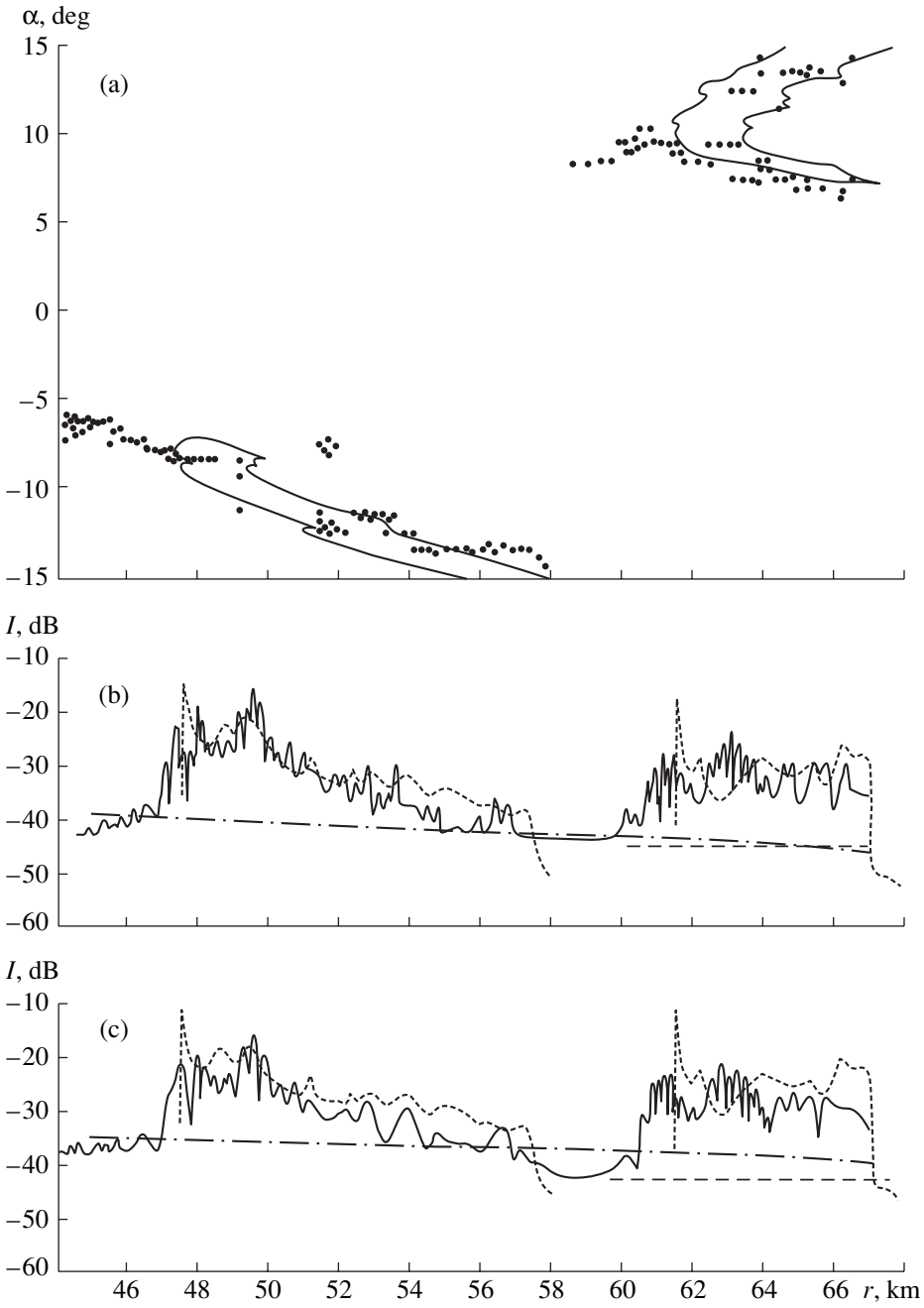

Fig. 6. Sound field structure in the first convergence zone (the Central Basin of the Indian Ocean): the emission depth is 200 m and the reception depth is 1100 m; (a) the angular structure, f_{av} = 3.15 kHz; (b, c) the energy structure at the omnidirectional reception, f_{av} = (b) 3.15 and (c) 1.25 kHz.

the signals arriving from above) than in the previous experiment (14 and 11 km, respectively). As is seen from Fig. 6a, the experimental data satisfactorily agree with the calculated dependences of the signal arrival angles on the distance, $\alpha(r)$. However, in this region, the rather weak water signals were first recorded several kilometers before the head of the convergence zone given by the calculation. As for the energy characteristics of the field (see Figs. 6b and 6c), the experimental range dependences $I(r)$ of the total field intensity for both frequency ranges have almost the same structure as in the Quiana test region: the zone is clearly separated into two parts by an interval of lower intensity. However, the maximum levels of the sound field are much higher than in the previous test region. According to Figs. 6b and 6c, the maximum values of the transmission anomaly, A_{max}, reached 22 and 19 dB, respectively, at a reception depth of 1100 m in the first and second

parts of the convergence zone for the signals with f_{av} = 3.15 kHz, and 20 and 17 dB for the signals with f_{av} = 1.25 kHz; these values are much higher than in the Quiana region. The higher signal intensity was recorded also at a depth of 200 m, which is equal to the emission depth. The maximum values of the transmission anomaly, A_{max}, at omnidirection reception were ~26 and 24 dB for the signals with f_{av} =3.15 and 1.25 kHz, respectively. In this test region, the difference in the maximum values of the transmission anomaly at depths of 200 and 1100 m was $\Delta A \cong 7$ dB (in the second part of the zone).

The agreement between the experimental and calculated energy structure in this region was much better than in the previous one. From Figs. 6b and 6c, one can see that the experimental data (solid line) and the calculations (dotted line) are close in both the form of the dependence $I(r)$ and the total level of the received signals within almost the whole convergence zone. The shift of the head of the zone to the source relative to the calculated position was much smaller in the Indian Ocean than that in the Quiana region, and it was only ~0.8 km for f_{av} = 3.15 kHz and ~0.6 km for f_{av} = 1.25 kHz.

Such discrepancies between the experimental and theoretical data for the position of the first head of the zone at great depths are smallest among all results obtained in the test regions specified at the beginning of the paper. Note that all calculations of the sound field characteristics were carried out with allowance for Earth curvature [1], which makes it possible to correct the theoretical positions of the convergence zones relative to the sound source.

Summarizing the results described above, we make the following conclusions.

The angular and energy structures of the sound field in the frequency range 1–4 kHz, which were obtained experimentally in different regions of the ocean (the Mediterranean Sea, the central and southern regions of the Atlantic Ocean, the Central and West-Australian Basins of the Indian Ocean), correspond in general to the main ray laws of sound propagation in a single-axis sound channel when the reception occurs at great depths (from 800 to 2000 m) and the emission of pseudonoise signals, in the upper oceanic layers (190–200 m).

The signal focusing in convergence zones with the deep-water reception is noticeably weaker (from 14 to 22 dB) than the focusing obtained with the reception near the emission depth (22–26 dB). The difference in the maximum values of the transmission anomaly in the convergence zones observed at a reception depth close to the emission depth, as well as at much greater depths, is usually about 5–7 dB.

Specific characteristics of the angular and energy structures largely depend on the difference in the sound velocities at the source and receiver depths. This difference determines the angular sector of signal absence (signals propagate without reflections from waveguide boundaries) around the zero arrival angle, as well as the length of the low-intensity interval that separates the convergence zones in two parts.

In actual oceanic conditions, the convergence zones are located nearer to the sound source than predicted by calculations, even with allowance for Earth curvature (for the first zone, by 0.6–2.5 km). Fine elements of the sound field structure, in particular, the angular spectrum and the field intensity variations along the convergence zone, which were observed in the experiments, noticeably deviate from the corresponding calculated parameters, this deviation being somewhat greater for the deep-water reception as compared to the reception in the upper oceanic layers.

ACKNOWLEDGMENTS

This work was supported by the Russian Foundation for Basic Research, project nos. 00-02-17694 and 00-15-98496.

REFERENCES

1. O. P. Galkin, in *Acoustics of the Ocean: State of the Art*, Ed. by L. M. Brekhovskikh and I. B. Andreeva (Nauka, Moscow, 1982), pp. 92–106.
2. O. P. Galkin, L. V. Shvachko, and E. A. Kharchenko, in *Acoustics in the Ocean* (Nauka, Moscow, 1992), pp. 114–127.
3. O. P. Galkin, E. A. Kharchenko, and L. V. Shvachko, Akust. Zh. **46**, 325 (2000) [Acoust. Phys. **46**, 274 (2000)].
4. A. E. Vedeneev, O. P. Galkin, I. S. Rogozhkin, and L. M. Filippov, Vopr. Sudostr., Ser. Akust., No. 15, 122 (1982).
5. K. P. Bongiovanni and W. L. Siegmann, J. Acoust. Soc. Am. **100**, 3033 (1996).
6. K. V. Avilov, O. P. Galkin, A. E. Lenets, *et al.*, in *Proceedings of the 9th School–Seminar of Academician L. M. Brekhovskikh on Acoustics of the Ocean* (GEOS, Moscow, 2002), p. 37.
7. D. M. Fromm, M. D. Collins, and G. V. Norton, J. Acoust. Soc. Am. **108**, 2562 (2000).
8. V. N. Stepanov, *The Global Ocean: Dynamics and Properties of Waters* (Znanie, Moscow, 1974).

Translated by Yu. Lysanov

Acoustical Physics, Vol. 49, No. 6, 2003, pp. 662–667. Translated from Akusticheskiĭ Zhurnal, Vol. 49, No. 6, 2003, pp. 778–784.

Computer Modeling of Sound Fields in the Ocean with Fine-Structured Inhomogeneities

V. S. Gostev, O. E. Popov, and R. F. Shvachko

Andreev Acoustics Institute, Russian Academy of Sciences, ul. Shvernika 4, Moscow, 117036 Russia

e-mail: bvp@akin.ru

Received December 16, 2002

Abstract—The results of a computer modeling of sound propagation in the ocean with fine-structured inhomogeneities are presented. The modeling was performed using a wave code based on the wide-angle approximation, which allows one to estimate the effects of sound field perturbations. These effects include the insonification of the geometric shadow zones and the abnormal attenuation of low-frequency sound in the course of its propagation in an oceanic waveguide. Calculations clearly demonstrate that the fine-structured inhomogeneities of the sound velocity considerably affect the sound propagation in the ocean. *© 2003 MAIK "Nauka/Interperiodica".*

Modern computer technologies allow one to use wave codes for computing the energy characteristics of the sound field of a kilohertz range in the shadow zones of the deep ocean on the condition that the sound velocity profile is given with the discreteness corresponding to the scales of the fine-structured inhomogeneities along both vertical and horizontal coordinate axes. The use of such codes allows one to estimate the intensity of the shadow zone insonification and the additional attenuation of low-frequency sound in the underwater sound channel as functions of the scales and intensity of the fine structure of the sound velocity over a wide range of these variable quantities.

The modeling of the fine structure of the sound velocity field depending on only the vertical coordinate (a plane-layered medium) was carried out on the basis of experimental data for the fine-structured inhomogeneities of the sound velocity [1, 2]. The direct measurements of the sound velocity in the sea medium were carried out in various regions of the ocean with a spatial resolution of about 1.5 m to a depth of ~3 km. A cyclic sound velocity meter with a sensitivity of $\sim 10^{-6}$ units of the refractive index was used. The measured sound velocity profile was processed by an averaging cosine-filter with a half-width of 30 m. As a result, the profile of the mean sound velocity was determined. The latter was subtracted from the measured profile, and the high-frequency components of the vertical distribution of the sound velocity were obtained. In what follows, the sliding energy spectra of the high-frequency component of the sound velocity profile were computed with a 200-m long window of analysis at a step of 100 m. To increase the stability of the estimates of the spectral density of sound velocity fluctuations, the spectra obtained were subjected to a sliding averaging over ten adjacent frequencies.

Figure 1 exhibits an example of such processing of the sound velocity profiles in the tropical part of the Pacific Ocean (18°13′ S, 163°50′ W). On the left, Fig. 1 presents the depth dependence of the average sound velocity $\bar{c}(z)$ obtained as a result of filtering the sounding data by a cosine filter. In the middle, the dependence of the high-frequency component of the sound velocity on depth, $\delta c(z) = c(z) - \bar{c}(z)$, is shown. On the right, the sliding energy spectra of the sound velocity fluctuations, which were obtained from 200-m segments of the high-frequency component, are presented. The spectra are plotted on double logarithmic scales. The quantity $\log E_c(k_z)$ is plotted along the ordinate axis [$E_c(k_z)$ in units of m^3/c^2 is the energy spectrum of the sound velocity fluctuations]. The quantity $\log k_z$ is represented by the abscissa (where $k_z = 2\pi/\lambda_z$ is the wave number and λ_z is the wavelength of the inhomogeneity, expressed in meters). To determine the total level of the spectra, the horizontal line on the vertical axis should be matched with the horizontal line near the ordinal number of a corresponding spectrum. This line also marks the depth (axis on the left) of the middle of the high-frequency component segment subjected to spec-

1063-7710/03/4906-0662$24.00 © 2003 MAIK "Nauka/Interperiodica"

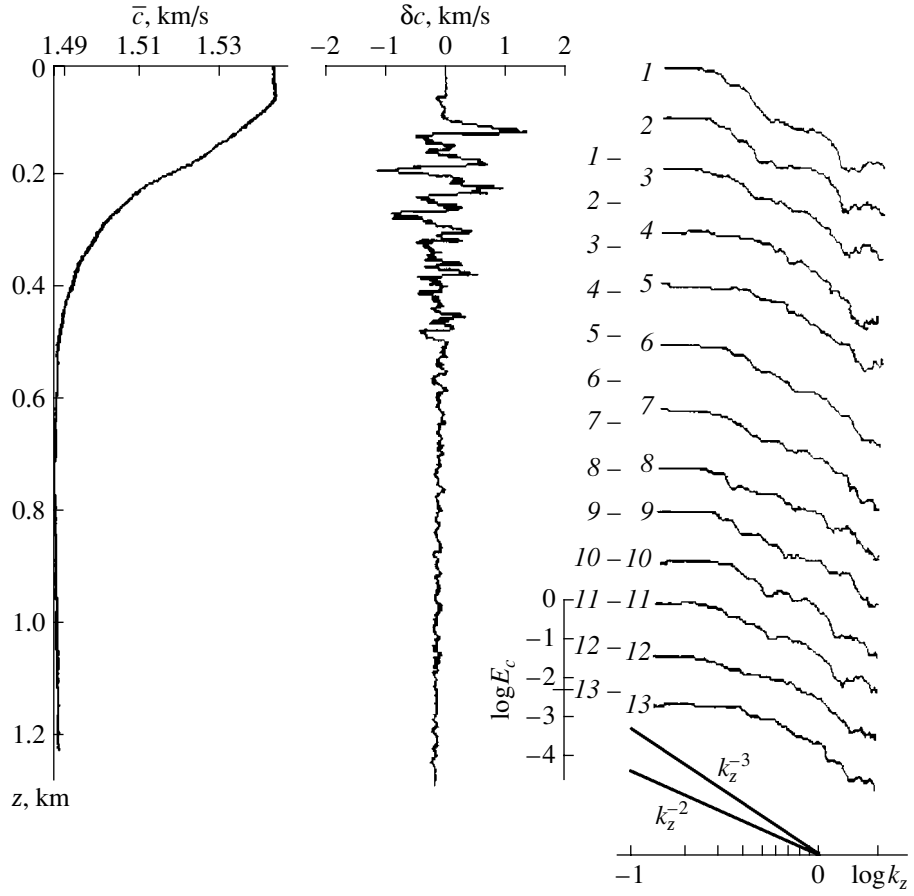

Fig. 1. Results of the statistical processing of the measured vertical distribution of the sound velocity.

tral processing. The straight lines show the behavior of k_z^{-2} and k_z^{-3}. It is easy to verify that all experimental spectra in the range of scales 3–30 m follow (on the average, with rare exceptions) the power law of the decay k_z^{-n} (where n is within 2–3); in most cases, $n = 2$.

To obtain quantitative estimates of the dependence of the spectral density levels of the fine-structured fluctuations on depth, readings of the values of $E_c(k_z)$ for $k_z = 2\pi/\lambda_z = 1$ m^{-1} ($\log k_z = 0$) were taken at each realization. Thus, for each depth, the constant C_c characterizing the intensity of the fine-structured inhomogeneities was found from the equation $E_c(k_z) = C_c^2 k_z^{-2}$.

To model the fine-structured fluctuations of the sound velocity, $\delta c(z)$, near the average vertical distribution, a white gaussian noise $x(z)$ is generated by a computer and then subjected to filtering using a filter that provides for decay of the spectral power of the filtered process $y(z)$ by the power law $E \sim k^{-2}$. The resulting random process $y(z)$ is then multiplied by the normalization factor σ, which is determined as the ratio of the rms values of experimentally measured fluctuations $\delta c(z)$ at a certain depth z and the fluctuations of y ($\sigma = \sigma_c(z)/\sigma_y$), and by the function $f(z)$, which takes into account the decrease in $\sigma_c(z)$ with depth. In field conditions, the greatest values of $\sigma_c(z)$ are observed at depths of the velocline and the thermocline. Below the underwater channel axis, the inhomogeneities of the fine structure, as a rule, degenerate [1]. The decrease in $\sigma_c(z)$ with depth is adequately described by the exponential function

$$f(z) = \begin{cases} 0 & \text{for } z \le z_0 \\ \exp(-(z - z_0)/d) & \text{for } z > z_0, \end{cases}$$

where z_0 is the thickness of the subsurface mixed layer and d is a constant on the order of the thermocline thickness, which characterizes the decrease in the fluctuation levels with depth.

As stated above, a code was developed for specifying the sound velocity fluctuations near the average vertical distribution because of fine-structured inhomogeneities. Figure 2 exhibits the fluctuations modeled by

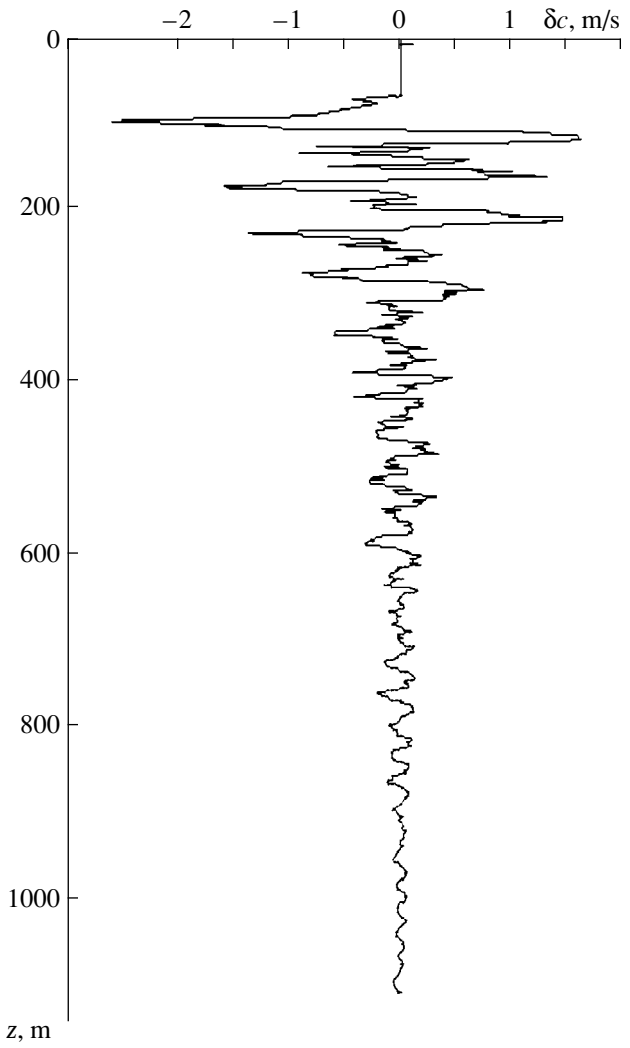

Fig. 2. Computer modeling of the fine-structured fluctuations of the sound velocity about the average vertical distribution.

the algorithm $\delta c(z) = \sigma y(z)\exp(-(z - z_0)/d)$ for d = 400 m and z_0 = 70 m.

For sound field calculations, Avilov's wave code was used [3], which realizes the method of the wide-angle parabolic equation. This code allows one to calculate the sound fields for an almost arbitrary two-dimensionally inhomogeneous sound velocity field, as well as to investigate by numerical modeling the variety of the effects of the fine-structured inhomogeneities on the sound propagation.

Figure 3 shows the vertical sound velocity distribution at a finite number of depths (Fig. 3a), which is usually preset in such calculations, and a fragment of the same distribution to which the fluctuation component from Fig. 2 is added (Fig. 3b).

The introduction of the fine-structured component (the medium retains its plane-layered character) leads to a significant change in the process of sound propagation, namely, to the known effect of sound penetration into the shadow zone [4–6]. To demonstrate this effect, a sound field with a frequency of 600 Hz was computed up to a distance of 105 km for the smooth vertical distribution of the sound velocity presented in Fig. 3a and for the vertical distribution with the fine-structured component at depths from 70 to 800 m (Fig. 3b). In both cases, the sea bottom was assumed to be a liquid half-space. In order to minimize the bottom reflection, which in our case is noise, the sound velocity in the half-space was assumed to be equal to that in the waveguide at the maximum depth. The results of relevant calculations of the sound field amplitudes are shown in Figs. 4a and 4b in certain shades of gray. One can see that the introduction of the fine-structured component generates a sound field reradiated from thin high-gradient interlayers of the sound velocity and this field propagates into the shadow zones, where it considerably increases the field level relative to that calculated for the smooth profile. It is also seen that the convergence zone gives rise to an additional sound field that is rereflected at distances about 60 km in the range of velocline depths where the fine-structured inhomogeneities are most pronounced. This additional field propagates into the second shadow zone, which can lead to an increase in the field level at distances of about 90 km as the second convergence zone is approached. This fact is confirmed by Fig. 4. It is significant that such a modeling of the effect of fine-structured perturbations of the sound velocity profile on the sound propagation provides the possibility not only of obtaining a qualitative picture but also of estimating this effect quantitatively. For example, in the case under consideration, the introduction of the fine-structured perturbation into the sound velocity profile increases the sound field level in the shadow zone by 20 dB or even more (Fig. 5).

The effect of the fine-structured inhomogeneities on the sound propagation also manifests itself in prereverberation [7], as well as in the additional attenuation of low-frequency sound. If, for estimating the insonification of the shadow zone, a plane-layered model of the fine-structured inhomogeneities is applicable, then, for estimating the additional attenuation, it is necessary to preset uncorrelated random components of the sound velocity profile at spatial intervals corresponding to the horizontal correlation radius of the inhomogeneities. In this case, the finite half-width of the scattering pattern, as well as the leakage of the sound energy over steep angles exceeding the trapping angle of the underwater sound channel, are provided. To this end, the uncorrelated components, $\delta c(z)$, were generated by the above method in the necessary number at depths from the surface to a depth of 800 m. These components were then summarized with a constant average vertical distribution of the sound velocity. Every resulting profile was related to a certain distance at regular intervals along

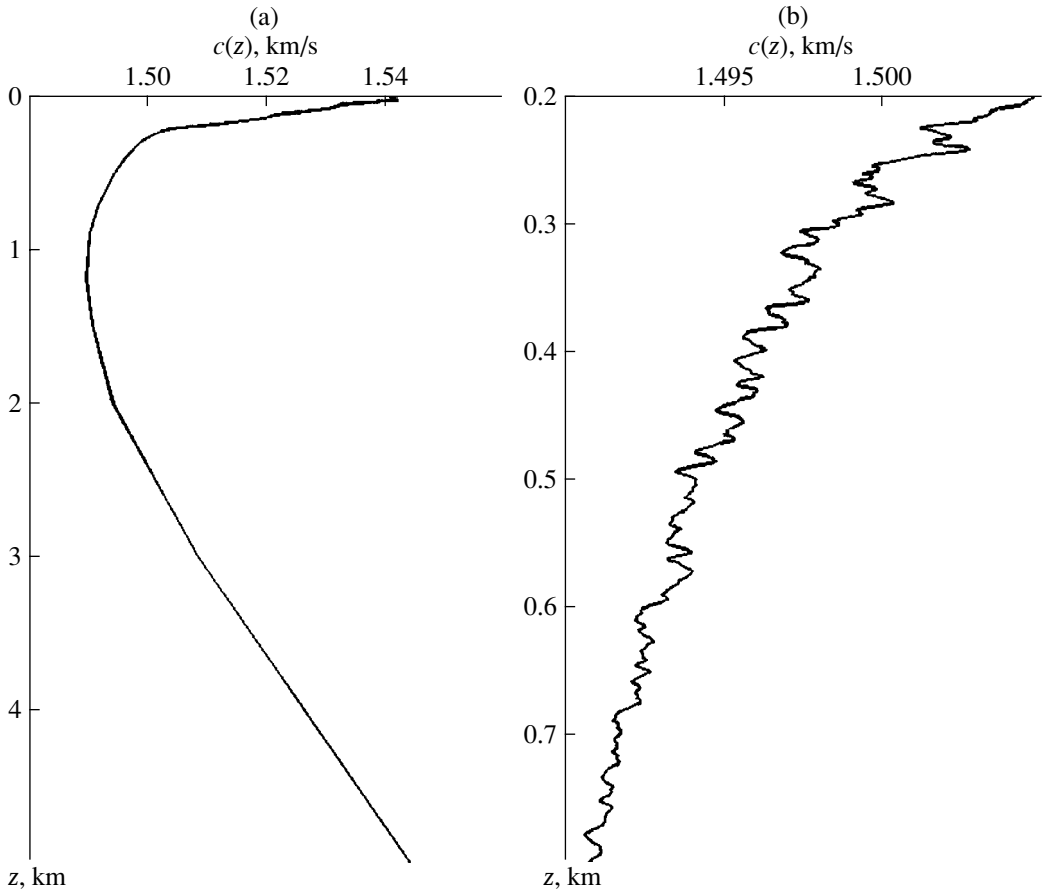

Fig. 3. (a) Average vertical distribution of the sound velocity and (b) the vertical distribution of the sound velocity with allowance for the fine-structured component.

the propagation track. For a test calculation, 400 profiles were given at 1-km intervals along the track. The average vertical distribution of the sound velocity in the waveguide was chosen to be bilinear. The sound velocity at the surface and the bottom (the depth was 3.0 km) was equal to 1524 m/s and 1500 m/s at the channel axis (a depth of 1.0 km). The length of the propagation track was 400 km. The correlation radius of the inhomogeneities along depth was about 20 m. Thus, the anisotropy coefficient (the ratio of the horizontal scale, 1 km, to the vertical one, 20 m) of the fine-structured inhomogeneities was on the order of 50. In both cases, the sea bottom was assumed to be a water half-space with the sound velocity equal to that in the waveguide at a depth of 3000 m.

The calculations of the sound field were performed for a harmonic source operating at a frequency of 25 Hz at a depth of 300 m. In the first case, the calculations were performed for a track with the smooth vertical sound velocity distribution (a plane-layered ocean without fine-structured inhomogeneities) and in the second case, with fine-structured inhomogeneities modeled as described above. Figure 6 exhibits the results of calculations. The upper plot demonstrates the sound field level in shades of gray, and the lower plot, the decay of the total sound energy (averaged over the vertical section at every step of calculations) in the channel (in dB) without considering the cylindrical divergence.

From Fig. 6 it follows that the additional attenuation caused by the introduction of the fine-structured inhomogeneities has a steplike character with a periodicity of the zonal structure of the sound field. A steep decrease in the total sound energy in the channel takes place at distances where the sound energy is most amplified at near-bottom depths in the regions of its leakage into the bottom. Sound scattering by fine-structured inhomogeneities in subsurface layers contributes to the leakage of sound energy into the bottom, which leads to additional attenuation of the sound field (the difference between curves *1* and *2* in Fig. 6). At a frequency of 25 Hz, the additional attenuation was found

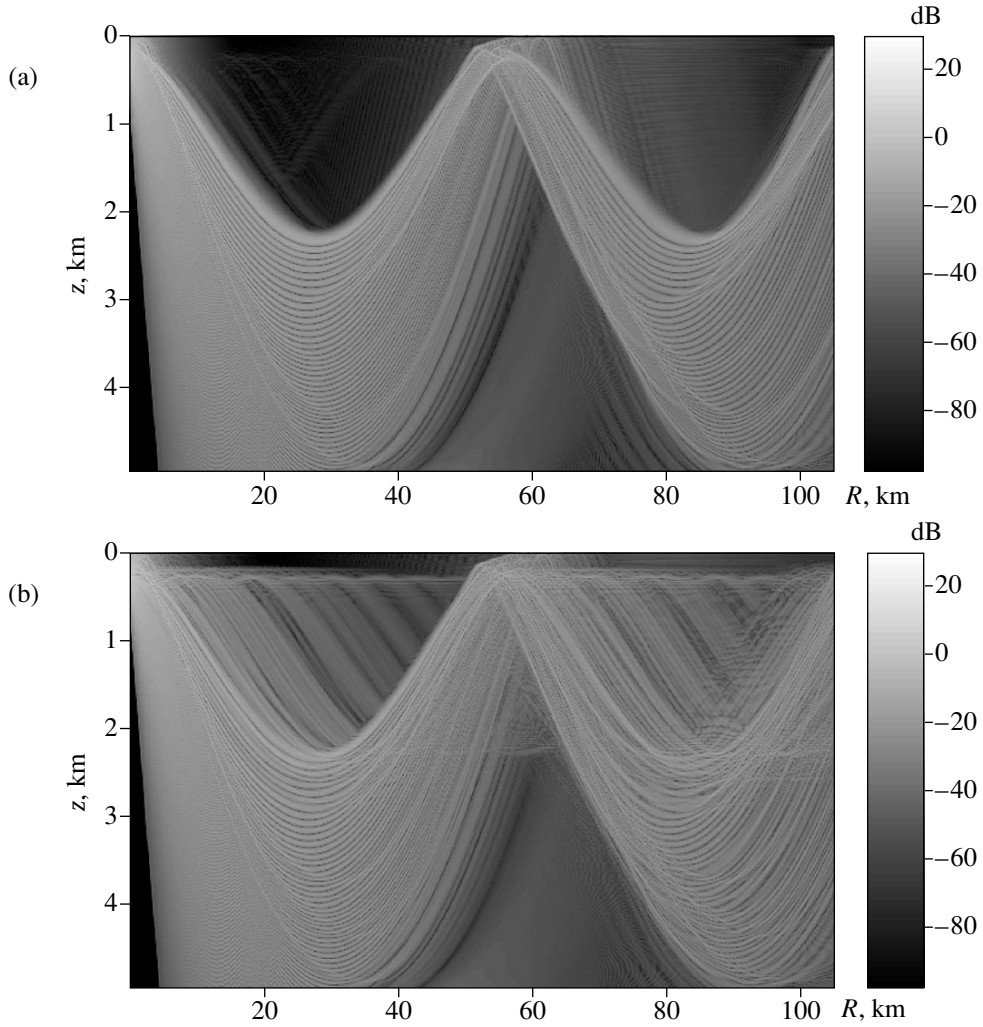

Fig. 4. Results of the sound field calculation from the vertical distribution of the sound velocity without the fine structure (the upper plot) and with allowance for the fine-structured component (the lower plot). The source depth is 300 m.

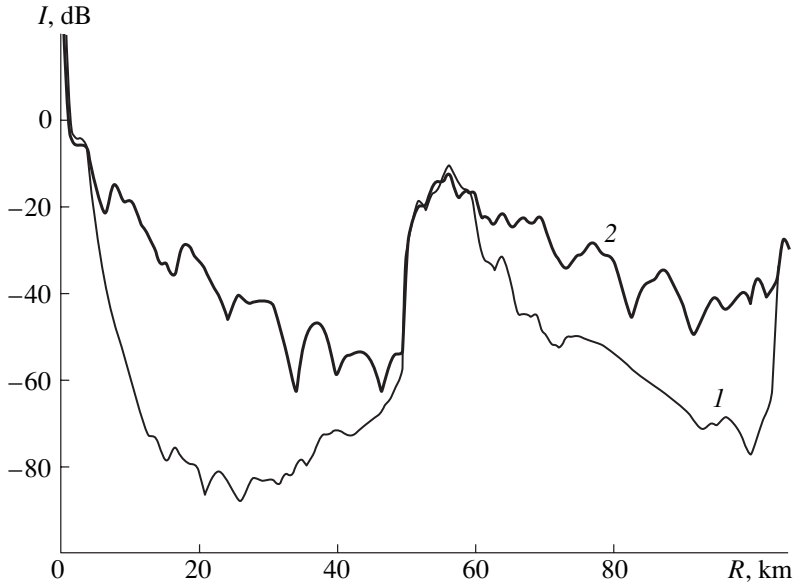

Fig. 5. Horizontal runs of the sound field at a depth of 300 m: the calculation for the average vertical sound distribution (*1*) without the fine structure and (*2*) with allowance for the fine-structured component.

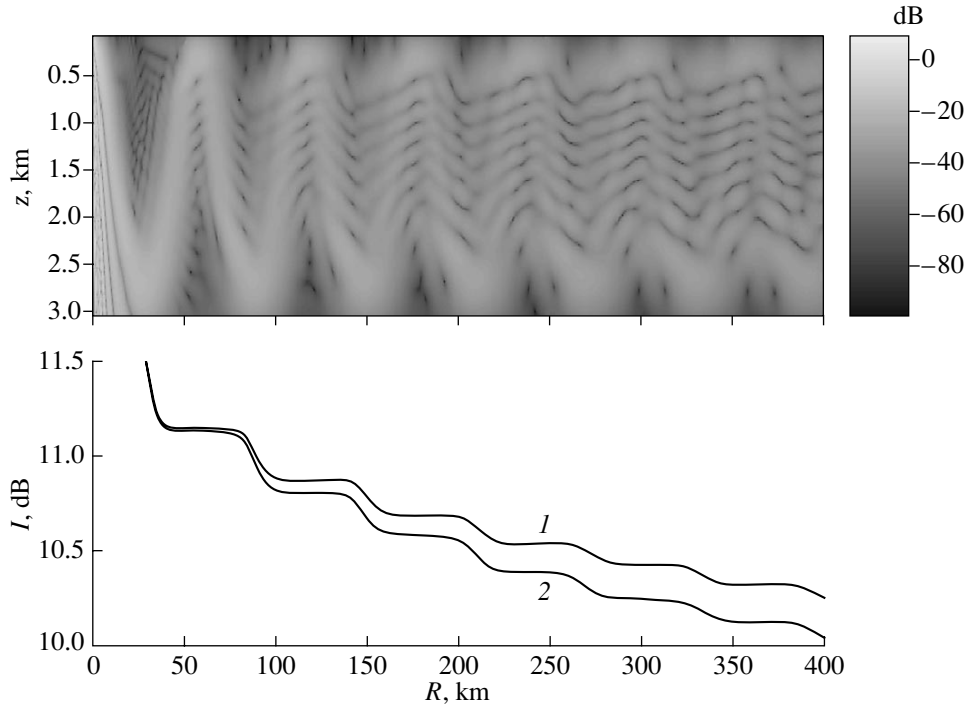

Fig. 6. Additional sound attenuation (*2*) in the case of the propagation through a waveguide with fine-structured inhomogeneities in comparison with (*1*) the case of a waveguide with a smooth sound velocity profile.

to be 0.3 dB per 400 km (0.75 dB per 1000 km), which agrees well with the experimental data.

REFERENCES

1. V. S. Gostev and R. F. Shvachko, in *Problems of the Ocean Acoustics*, Ed. by L. M. Brekhovskikh and I. B. Andreeva (Nauka, Moscow, 1984), pp. 153–164.
2. V. S. Gostev, N. G. Potylitsin, and R. F. Shvachko, in *Proceedings of XI All-Union Acoustic Conference* (Akust. Inst. Akad. Nauk SSSR, Moscow, 1991), Sect. D, p. 109.
3. K. V. Avilov, Akust. Zh. **41**, 5 (1995) [Acoust. Phys. **41**, 1 (1995)].
4. V. S. Gostev and R. F. Shvachko, Akust. Zh. **47**, 623 (2001) [Acoust. Phys. **47**, 540 (2001)].
5. V. S. Gostev and R. F. Shvachko, in *Proceedings of the IX Scientific School–Seminar of Academician L. M. Brekhovskikh on Acoustics of the Ocean* (GEOS, Moscow, 2002), p. 120.
6. K. V. Avilov, A. V. Mikryukov, and O. E. Popov, in *Proceedings of the IX Scientific School–Seminar of Academician L. M. Brekhovskikh on Acoustics of the Ocean* (GEOS, Moscow, 2002), p. 41.
7. V. S. Gostev and R. F. Shvachko, Akust. Zh. **45**, 857 (1999) [Acoust. Phys. **45**, 774 (1999)].

Translated by Yu. Lysanov

Acoustical Physics, Vol. 49, No. 6, 2003, pp. 668–676. Translated from Akusticheskiĭ Zhurnal, Vol. 49, No. 6, 2003, pp. 785–793.

Acoustic Attenuation in the Layers of a Microwave Transducer at the Excitation of Longitudinal and Shear Elastic Waves by a Piezoelectric of the 6*mm* Symmetry Class

M. A. Grigor'ev, A. V. Tolstikov, and Yu. N. Navrotskaya

Chernyshevski State University, Saratov, ul. Astrakhanskaya 83, Saratov, 410026 Russia

e-mail: magrig@sgu.ssu.runnet.ru

Received June 28, 2002

Abstract—An electroacoustic transducer in the form of a piezoelectric of the 6*mm* symmetry class with an arbitrary orientation of the sixfold axis and with two finite-thickness metal electrodes is considered taking into account the acoustic attenuation in the transducer layers. A system of equations is obtained to determine the impedance of the transducer, the radiation resistances for shear and longitudinal waves, the power ratio of these waves in the acoustic line, and the transformation factors for transverse and longitudinal waves. The effect of attenuation on the characteristics of a specific transducer operating in the 15-GHz frequency range is numerically analyzed. *© 2003 MAIK "Nauka/Interperiodica".*

INTRODUCTION

In this paper, we consider a microwave electroacoustic transducer in the form of a three-layer piezoelectric element (metal–piezoelectric–metal) based on a piezoelectric crystal of the 6*mm* symmetry class (ZnO, CdS) with an arbitrary orientation of the sixfold symmetry axis. Unlike the case considered in our previous publication [1], we now analyze the effect of acoustic attenuation in the layers of such a transducer. Transducers of this kind may be used, for example, in acoustooptical devices operating in the short-wave region of the microwave frequency range [2] or in acoustic delay lines. To design the latter with an acceptable attenuation of signals in the short-wave region of the microwave frequency range requires the use of shear elastic waves, the attenuation of which in certain crystals ($Y_3Al_5O_{12}$, $MgAl_2O_4$, etc.) is much weaker than that of longitudinal waves. Shear elastic waves can be obtained using piezoelectric films deposited in vacuum at an oblique incidence of molecules on the surface of an acoustic line. In our previous experiments [3], we excited shear elastic waves in $MgAl_2O_4$ at a frequency of 36.5 GHz by a ZnO film with an oblique molecular structure. A serious difficulty arising in the development of efficient transducers for the short-wave region of the microwave frequency range is the acoustic attenuation in their layers.

In the literature, one can find many publications concerned with different problems of electroacoustic transducers exciting bulk elastic waves (see, e.g., [4–7]). However, we did not encounter any publications analyzing the effect of acoustic attenuation in a multilayer transducer.

The model considered in this paper is shown in Fig. 1. It consists of (*4*) an acoustic line extending to infinity along the x_3' axis, (*1*, *3*) two metal electrodes across which an alternating voltage of microwave frequency is applied, and (*2*) a piezoelectric placed between the electrodes and oriented so that the x_2 axis of the crystal coordinate system is perpendicular to the plane of the drawing and the x_3 axis makes an angle θ with the normal $\vec{n}$ to the end of the acoustic line. The choice of this orientation of the piezoelectric does not lead to any loss of generality owing to the isotropy of

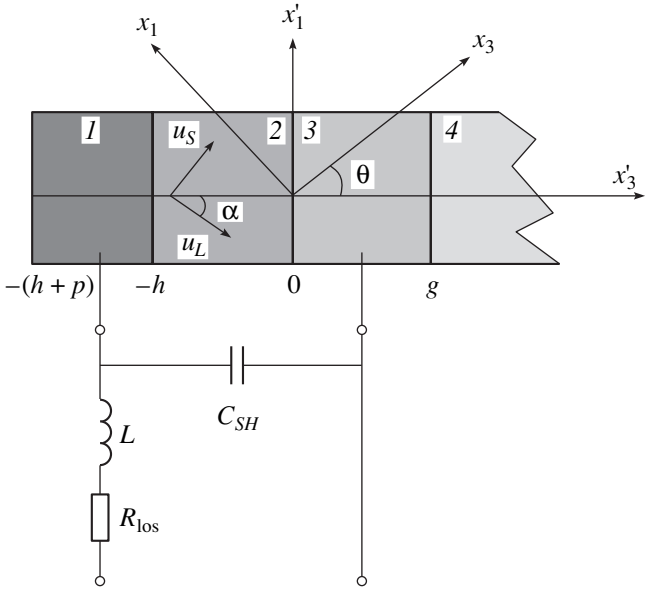

Fig. 1. Piezoelectric transducer under consideration.

1063-7710/03/4906-0668$24.00 © 2003 MAIK "Nauka/Interperiodica"

the elastic properties of hexagonal crystals in the plane perpendicular to the sixfold axis. We assume that the metal electrodes and the acoustic line are either isotropic or crystalline with their longitudinal normals oriented along the x_3' axis. We also assume that the conductivity of the piezoelectric and the dielectric loss in it are equal to zero.

A piezoelectric element incorporated into a microwave circuit possesses a frequency-dependent impedance whose active component absorbs electromagnetic power. The power is spent for the excitation of acoustic waves (both longitudinal and shear) in the acoustic line, as well as for the loss.

The efficiency of the transducer as a whole, including the exciting system, is characterized by the electroacoustic transformation coefficient η:

$$\eta = P_{ac}/P_+, \tag{1}$$

where P_{ac} is the power of the excited acoustic wave and P_+ is the power of the direct electromagnetic wave in the line supplying the energy to the transducer. Since

$$P_{ac} + P_{los} = P_+(1 - |\Gamma|^2), \tag{2}$$

where P_{los} is the loss power and $|\Gamma|$ is the absolute value of the reflection coefficient in the line, we obtain

$$\eta = (1 - |\Gamma|^2)\frac{R_{rad}}{R_{rad} + R_{los}}. \tag{3}$$

Here, R_{rad} is the active radiation resistance of the piezoelectric element and R_{los} is the loss resistance.

The quantity $|\Gamma|$ can easily be determined if we know the load impedance Z_L in some cross section of the line characterized by the wave impedance Z_0:

$$|\Gamma| = \frac{|Z_L - Z_0|}{|Z_L + Z_0|}. \tag{4}$$

Here, Z_L is determined as the result of the transformation of the transducer impedance and the loss resistance by the exciting system. In Fig. 1, the piezoelectric element is connected to an LCR circuit, which connects the transducer to the transmission line. The circuit consists of a parasitic shunt capacitance C_{SH}, inductance of the connecting lead L, and its active resistance R_{los}. Thus, at the first step, it is necessary to calculate the impedance of the piezoelectric element: $Z(\omega) = R(\omega) + jX(\omega)$.

AMPLITUDES OF ELASTIC WAVES IN THE PIEZOELECTRIC

In the general case, an alternating electric field directed along the x_3' axis, which coincides with the normal $\vec{n}$, excites quasi-longitudinal and quasi-transverse elastic waves in the piezoelectric, so that these waves are polarized in the plane of the drawing (see Fig. 1).

Taking into account that the transverse dimensions of real transducers are much greater than the thickness of their layers, we set $\partial/\partial x_1' = \partial/\partial x_2' = 0$. Then, the equations describing the electromechanical processes in the piezoelectric take the form

$$\rho\partial^2 u_i/\partial t^2 = \partial T_{i3}/\partial x_3', \tag{5}$$

$$T_{i3} = c_{i33l}'\partial u_l/\partial x_3' - e_{3i3}'E_3, \tag{6}$$

$$D_3 = e_{3l3}'\partial u_l/\partial x_3' + \varepsilon_{33}'E_3, \tag{7}$$

$$\partial D_3/\partial x_3' = 0, \tag{8}$$

where u_i is the ith component of the displacement vector ($i = 1, 3$); T_{i3} is a component of the elastic stress tensor; E_3 is the strength of the alternating electric field directed along the x_3' axis; c', e', and ε' are the components of the elastic constant, piezoelectric constant, and dielectric constant tensors, respectively, in the x_1', x_2', x_3' coordinate system rotated through an angle θ about the x_2 axis; ρ is the density of the piezoelectric; and D_3 is the electric displacement vector component, which, according to Eq. (8), is independent of the coordinate.

We assume that the acoustic attenuation weakly affects the sound velocities. Then, for the quasi-longitudinal and quasi-transverse waves in the piezoelectric, we can use the dependences of the velocities and polarization directions on angle θ that were obtained for the case without attenuation [8]:

$$v_{LS}^2 = \frac{\dot{c_{55}} + \dot{c_{33}}}{2\rho} \pm \sqrt{\left(\frac{\dot{c_{55}} - \dot{c_{33}}}{2\rho}\right)^2 + \left(\frac{\dot{c_{35}}}{2\rho}\right)^2}, \tag{9}$$

$$\tan 2\alpha = 2\dot{c_{35}}/(\dot{c_{35}} - \dot{c_{55}}),$$

where

$$\begin{aligned} \dot{c_{55}} &= c_{55}' + (e_{35}')^2/\varepsilon_{33}', \\ \dot{c_{35}} &= c_{35}' + e_{35}'e_{33}'/\varepsilon_{33}', \\ \dot{c_{33}} &= c_{33}' + (e_{33}')^2/\varepsilon_{33}'. \end{aligned} \tag{10}$$

Here, subscripts L and S refer to quasi-longitudinal and quasi-transverse waves, respectively, and α is the angle characterizing the direction of the displacement vectors (see Fig. 1). In the expressions presented above, we used the matrix notations for the components of the stiffness tensor and the piezoelectric constant tensor.

To take into account the acoustic attenuation in all media forming the transducer, we introduce complex propagation constants. For the piezoelectric, we have

$$\Gamma_{S,L} = \beta_{S,L} - j\alpha_{S,L}, \tag{11}$$

where $\beta_{S,L}$ are the wave numbers for L or S waves: $\beta_{S,L} = \omega/v_{S,L}$ (ω is the circular frequency) and $\alpha_{S,L}^{(2)}$ are

the attenuation coefficients, which depend on the frequency f according to the law

$$\alpha_{S,L} = A_{S,L} f^2 \tag{12}$$

(here, $A_{S,L}$ are the attenuation constants expressed in $1/(\text{Hz}^2\ \text{m})$ units). For other media, in which only pure elastic modes can exist, we have

$$\Gamma_i^{(k)} = \beta_i^{(k)} - j\alpha_i^{(k)}, \tag{13}$$

where superscript (k) indicates the number of the medium ($k = 1, 3, 4$) and subscript i indicates the direction of the displacement vector of the wave: $i = 1$ along the x_1' axis (a transverse wave) and $i = 3$ along the x_3' axis (a longitudinal wave). The wave numbers and the attenuation coefficients are expressed as

$$\begin{aligned} \beta_i^{(k)} &= \omega/v_i^{(k)}, \\ \alpha_i^{(k)} &= A_i^{(k)} f^2. \end{aligned} \tag{14}$$

In the piezoelectric bounded on two sides, direct and inverse elastic waves must simultaneously take place:

$$u_L = B_L^+ \exp(-j\Gamma_L x_3') + B_L^- \exp(j\Gamma_L x_3'), \tag{15}$$

$$u_S = B_S^+ \exp(-j\Gamma_S x_3') + B_S^- \exp(j\Gamma_S x_3'), \tag{16}$$

where B_L^+, B_S^+, B_L^-, and B_S^- are the complex amplitudes of direct and inverse quasi-longitudinal and quasi-transverse waves at $x_3' = 0$.

The amplitudes of the displacement vector components, to which the L and S waves contribute, can be represented in the form

$$u_1^{(2)}(x_3') = u_L(x_3')\sin\alpha + u_S(x_3')\cos\alpha \tag{17}$$

$$u_3^{(2)}(x_3') = u_L(x_3')\cos\alpha - u_S(x_3')\sin\alpha. \tag{18}$$

The quantities $B_{S,L}^{+,-}$ can be determined from the boundary conditions of continuity for the elastic stress and displacement components or, in the case of a free boundary, the condition of zero elastic stress at the boundary. To determine the electric impedance, it is sufficient to know only the amplitudes of the waves that occur in the piezoelectric. For this purpose, we need four equations, which can be obtained using the definition of the acoustic impedance. For waves propagating along the x_3' axis with displacements along the x_i' axis, the acoustic impedance can be expressed as

$$Z_i^{(k)}(x_3') = -\frac{T_{i3}^{(k)}(x_3')}{u_i^{(k)}(x_3')}, \tag{19}$$

where $u_i^{(k)}$ is the ith component of the displacement vector in the kth medium.

In the piezoelectric, the quantity $u_i^{(k)}$ is formed as the sum of the projections of displacements in L and S waves on the corresponding coordinate axes (see Eqs. (17) and (18)), while in all other media, this quantity directly represents the displacements of either longitudinal or shear waves. The equality of the displacement components, as well as the elastic stress components, at the boundary between two media allows us to assume that the acoustic impedances are also equal. For media bordering the piezoelectric, it is easy to preliminarily determine these impedances for both longitudinal and transverse waves. Then, the conditions set at the boundaries of the piezoelectric take the form

$$T_{i3}^{(2)}(-h) + Z_i^{(1)}(-h)\, j\omega u_i^{(2)}(-h) = 0 \tag{20}$$

$$T_{i3}^{(2)}(0) + Z_i^{(3)}(0)\, j\omega u_i^{(2)}(0) = 0. \tag{21}$$

To determine the impedance $Z_i^{(1)}(-h)$ in layer *1* at the piezoelectric boundary $x_3' = -h$ for a wave with the displacement along the ith coordinate, one should take into account that, at the free boundary $x_3' = -(h + p)$, the total acoustic impedance is equal to zero. Thus, layer *1* represents a segment of a short-circuited acoustic waveguide with attenuation, for which the impedance is expressed as

$$Z_i^{(1)}(-h) = -Z_{0i}^{(1)} \tanh(j\Gamma_i^{(1)} p). \tag{22}$$

Here, p is the thickness of medium *1* (the upper layer) and $Z_{0i}^{(1)}$ is the complex acoustic wave impedance of medium *1* for transverse ($i = 1$) or longitudinal ($i = 3$) waves. For the medium of number k, according to Eqs. (13) and (19), the quantity $Z_{0i}^{(k)}$ has the form

$$Z_{0i}^{(k)} = \rho^{(k)} v_i^{(k)} (1 - j v_i^{(k)} \alpha_i^{(k)}/\omega). \tag{23}$$

Here, $v_i^{(k)}$, $\rho^{(k)}$, and $\alpha_i^{(k)}$ are the velocity of sound, the density, and the attenuation coefficient for the kth medium.

In a similar way, one can determine impedance $Z_i^{(3)}(0)$ in medium *3* at the other piezoelectric boundary $x_3' = 0$. For a chosen wave ($i = 1$ or 3), medium *3* serves as an impedance transformer loaded with the acoustic wave impedance of the acoustic line (for transverse or longitudinal waves). In the presence of attenuation, the desired quantity is expressed as

$$Z_i^{(3)}(0) = Z_{0i}^{(3)} \frac{Z_{0i}^{(4)} \cosh(j\Gamma_i^{(3)} g) + Z_{0i}^{(3)} \sinh(j\Gamma_i^{(3)} g)}{Z_{0i}^{(3)} \cosh(j\Gamma_i^{(3)} g) + Z_{0i}^{(4)} \sinh(j\Gamma_i^{(3)} g)}, \tag{24}$$

where the complex wave impedance $Z_{0i}^{(4)}$ is determined by Eq. (23) for $k = 4$.

Now, we substitute Eqs. (22) and (24) and the stress tensor components $T_{i3}^{(2)}(0)$ and $T_{i3}^{(2)}(-h)$ determined from Eqs. (6) and (7) into Eqs. (20) and (21). Introducing the normalized complex amplitudes

$$b_{\mathrm{L,S}}^{\pm} = B_{\mathrm{L,S}}^{\pm}\varepsilon'_{33}\omega/jD_3 \tag{25}$$

and taking into account Eqs. (17) and (18), we obtain a system of four inhomogeneous linear equations, which determines the quantities b_{L}^{+}, b_{L}^{-}, b_{S}^{+}, and b_{S}^{-}. The elements of the matrix of this system have the form

$$a_{11} = \exp(j\Gamma_{\mathrm{L}}h)\left[\frac{\Gamma_{\mathrm{L}}}{\omega}(\dot{c}_{35}\tan\alpha + \dot{c}_{33}) - Z_3^{(1)}(-h)\right],$$

$$a_{12} = -\exp(-j\Gamma_{\mathrm{L}}h)\left[\frac{\Gamma_{\mathrm{L}}}{\omega}(\dot{c}_{35}\tan\alpha + \dot{c}_{33}) + Z_3^{(1)}(-h)\right],$$

$$a_{13} = \exp(j\Gamma_{\mathrm{S}}h)\left[\frac{\Gamma_{\mathrm{S}}}{\omega}(\dot{c}_{35} - \dot{c}_{33}\tan\alpha) + Z_3^{(1)}(-h)\tan\alpha\right],$$

$$a_{14} = -\exp(-j\Gamma_{\mathrm{S}}h)\left[\frac{\Gamma_{\mathrm{S}}}{\omega}(\dot{c}_{35} - \dot{c}_{33}\tan\alpha) - Z_3^{(1)}(-h)\tan\alpha\right],$$

$$a_{21} = \exp(j\Gamma_{\mathrm{L}}h)\left[\frac{\Gamma_{\mathrm{L}}}{\omega}(\dot{c}_{55}\tan\alpha + \dot{c}_{53}) - Z_1^{(1)}(-h)\tan\alpha\right],$$

$$a_{22} = -\exp(-j\Gamma_{\mathrm{L}}h)\left[\frac{\Gamma_{\mathrm{L}}}{\omega}(\dot{c}_{55}\tan\alpha + \dot{c}_{53}) + Z_1^{(1)}(-h)\tan\alpha\right],$$

$$a_{23} = \exp(j\Gamma_{\mathrm{S}}h)\left[\frac{\Gamma_{\mathrm{S}}}{\omega}(\dot{c}_{55} - \dot{c}_{53}\tan\alpha) - Z_1^{(1)}(-h)\right],$$

$$a_{24} = -\exp(-j\Gamma_{\mathrm{S}}h)\left[\frac{\Gamma_{\mathrm{S}}}{\omega}(\dot{c}_{55} - \dot{c}_{53}\tan\alpha) + Z_1^{(1)}(-h)\right],$$

$$a_{31} = \left[\frac{\Gamma_{\mathrm{L}}}{\omega}(\dot{c}_{35}\tan\alpha + \dot{c}_{33}) - Z_3^{(3)}(0)\right],$$

$$a_{32} = -\left[\frac{\Gamma_{\mathrm{L}}}{\omega}(\dot{c}_{35}\tan\alpha + \dot{c}_{33}) + Z_3^{(3)}(0)\right],$$

$$a_{33} = \left[\frac{\Gamma_{\mathrm{S}}}{\omega}(\dot{c}_{35} - \dot{c}_{33}\tan\alpha) + Z_3^{(3)}(0)\tan\alpha\right],$$

$$a_{34} = -\left[\frac{\Gamma_{\mathrm{S}}}{\omega}(\dot{c}_{35} - \dot{c}_{33}\tan\alpha) - Z_3^{(3)}(0)\tan\alpha\right],$$

$$a_{41} = \left[\frac{\Gamma_{\mathrm{L}}}{\omega}(\dot{c}_{55}\tan\alpha + \dot{c}_{53}) - Z_1^{(3)}(0)\tan\alpha\right],$$

$$a_{42} = -\left[\frac{\Gamma_{\mathrm{L}}}{\omega}(\dot{c}_{55}\tan\alpha + \dot{c}_{53}) + Z_1^{(3)}(0)\tan\alpha\right],$$

$$a_{43} = \left[\frac{\Gamma_{\mathrm{S}}}{\omega}(\dot{c}_{55} - \dot{c}_{53}\tan\alpha) - Z_1^{(3)}(0)\right],$$

$$a_{44} = -\left[\frac{\Gamma_{\mathrm{S}}}{\omega}(\dot{c}_{55} - \dot{c}_{53}\tan\alpha) + Z_1^{(3)}(0)\right].$$

The constant terms b_1, b_2, b_3, and b_4 are determined by the formulas

$$b_1 = b_3 = \frac{e'_{33}}{\cos\alpha}, \quad b_2 = b_4 = \frac{e'_{35}}{\cos\alpha}.$$

The normalized amplitudes $b_{\mathrm{L,S}}^{\pm}$ obtained as a result of solving this system can be used to calculate the electric impedance of the transducer and the electroacoustic transformation factor, as well as to determine the optimal angles θ, at which mainly shear or mainly longitudinal waves are excited in the acoustic line.

IMPEDANCE OF THE PIEZOELECTRIC ELEMENT

The impedance of the piezoelectric element can be determined in the quasi-static approximation [1]:

$$Z(\omega) = \frac{\int_{-h}^{0} E_3 dx'_3}{j\omega D_3 S} = \frac{\int_{-h}^{0}\left(D_3 - e'_{35}\dfrac{\partial u_1}{\partial x'_3} - e'_{35}\dfrac{\partial u_3}{\partial x'_3}\right)dx'_3}{j\omega\varepsilon'_{33}D_3 S},$$

where S is the area of the transducer.

Dividing this expression by the capacitive resistance of the piezoelectric element $X_0 = h/\omega\varepsilon'_{33}S$ and substituting Eqs. (15)–(18) and (25) into it, we perform the integration to obtain the normalized impedance of interest:

$$\frac{Z(\omega)}{X_0} = -j + \frac{1}{\varepsilon'_{33}v_{\mathrm{S}}\Gamma_{\mathrm{S}}h}\{e_{\mathrm{L}}[b_{\mathrm{L}}^{+}(e^{j\Gamma_{\mathrm{L}}h} - 1) + b_{\mathrm{L}}^{-}(e^{-j\Gamma_{\mathrm{L}}h} - 1)] + e_{\mathrm{S}}[b_{\mathrm{S}}^{+}(e^{j\Gamma_{\mathrm{S}}h} - 1) + b_{\mathrm{S}}^{-}(e^{-j\Gamma_{\mathrm{S}}h} - 1)]\}, \tag{26}$$

where $e_{\mathrm{L}} = e'_{35}\sin\alpha + e'_{33}\cos\alpha$ and $e_{\mathrm{S}} = e'_{35}\cos\alpha - e'_{33}\sin\alpha$ [3].

The second term in Eq. (26) is a complex quantity whose real part is the normalized active resistance consuming the microwave power. The latter, according to its physical meaning, is the sum of the powers of the transverse and longitudinal elastic waves excited in the acoustic line and the power scattered in the layers of the piezoelectric element due to the acoustic attenuation. In relation to these powers, the active component of the impedance can be represented as the sum of three terms,

$$R = R_{\mathrm{rad,S}} + R_{\mathrm{rad,L}} + R_{\mathrm{los}},$$

where $R_{\mathrm{rad,S}}$ is the radiation resistance for transverse waves, $R_{\mathrm{rad,L}}$ is the radiation resistance for longitudinal waves, and R_{los} is the loss resistance.

RADIATION RESISTANCE

To determine the radiation resistances, we use the condition of equal displacements at the boundaries of medium *3*.

At $x_3' = 0$, we have

$$(B_S^+ + B_S^-)\cos\alpha + (B_L^+ + B_L^-)\sin\alpha = u_{1+}^{(3)}(0) + u_{1-}^{(3)}(0), \quad (27)$$

$$-(B_S^+ + B_S^-)\sin\alpha + (B_L^+ + B_L^-)\cos\alpha = u_{3+}^{(3)}(0) + u_{3-}^{(3)}(0), \quad (28)$$

and at $x_3' = g$, we have

$$u_{1+}^{(4)}(g) = u_{1+}^{(3)}(g) + u_{1-}^{(3)}(g) = u_{1+}^{(3)}(g)(1 + \gamma_1^{(3)}(g)), \quad (29)$$

$$u_{3+}^{(4)}(g) = u_{3+}^{(3)}(g) + u_{3-}^{(3)}(g) = u_{3+}^{(3)}(g)(1 + \gamma_3^{(3)}(g)), \quad (30)$$

where $\gamma_1^{(3)}(g)$ and $\gamma_3^{(3)}(g)$ are the reflection coefficients for shear and longitudinal waves, respectively:

$$\gamma_{1,3}^{(3)} = \frac{Z_{01,3}^{(3)} - Z_{01,3}^{(4)}}{Z_{01,3}^{(3)} + Z_{01,3}^{(4)}}. \quad (31)$$

We use formula (31) for the reflection coefficient to express the complex amplitudes of reflected waves on the right-hand sides of Eqs. (27) and (28) through the amplitudes of the direct waves. Then, we determine $u_{1+}^{(3)}$ and $u_{3+}^{(3)}$ and substitute them into Eqs. (29) and (30). Changing to normalized displacements (see Eq. (25)), we arrive at the following expressions for the amplitudes of elastic waves excited in the acoustic line:

$$u_{1+}^{(4)}(g) = jD_3\frac{(b_S^+ + b_S^-)\cos\alpha + (b_L^+ + b_L^-)\sin\alpha}{\exp(j\Gamma_1^{(3)}g) + \gamma_1^{(3)}\exp(-j\Gamma_1^{(3)}g)} \times \frac{(1 + \gamma_1^{(3)})}{\varepsilon_{33}'\omega s}, \quad (32)$$

$$u_{3+}^{(4)}(g) = jD_3\frac{-(b_S^+ + b_S^-)\sin\alpha + (b_L^+ + b_L^-)\cos\alpha}{\exp(j\Gamma_3^{(3)}g) + \gamma_3^{(3)}\exp(-j\Gamma_3^{(3)}g)} \times \frac{(1 + \gamma_3^{(3)})}{\varepsilon_{33}'\omega s}. \quad (33)$$

These formulas allow us to determine the powers of the transverse and longitudinal acoustic waves excited in the acoustic line:

$$P_S = \frac{\omega^2|u_{1+}^{(4)}|^2}{2}\mathrm{Re}(Z_{01}^{(4)}) \quad (34)$$

$$P_L = \frac{\omega^2|u_{3+}^{(4)}|^2}{2}\mathrm{Re}(Z_{03}^{(4)}). \quad (35)$$

The same powers can be expressed via the radiation resistances $R_{\mathrm{rad,S}}$ and $R_{\mathrm{rad,L}}$ and the displacement current density in the piezoelectric, $j_{\mathrm{dis}} = j\omega D_3$:

$$P_S = \frac{\omega^2|D_3|^2}{2}s^2R_{\mathrm{rad,S}}, \quad (36)$$

$$P_L = \frac{\omega^2|D_3|^2}{2}s^2R_{\mathrm{rad,L}}. \quad (37)$$

Now, by equating the right-hand sides of Eqs. (34) and (36) and also the right-hand sides of Eqs. (35) and (37), we obtain the formulas for calculating the radiation resistances $R_{\mathrm{rad,S}}$ and $R_{\mathrm{rad,L}}$:

$$R_{\mathrm{rad,S}} = \frac{|1 + \gamma_1^{(3)}|^2\mathrm{Re}(Z_{01}^{(4)})|(b_S^+ + b_S^-)\cos\alpha + (b_L^+ + b_L^-)\sin\alpha|^2}{(\varepsilon_{33}'\omega)^2 s|\exp(j\Gamma_1^{(3)}g) + \gamma_1^{(3)}\exp(-j\Gamma_1^{(3)}g)|^2}, \quad (38)$$

$$R_{\mathrm{rad,L}} = \frac{|1 + \gamma_3^{(3)}|^2\mathrm{Re}(Z_{03}^{(4)})|-(b_S^+ + b_S^-)\sin\alpha + (b_L^+ + b_L^-)\cos\alpha|^2}{(\varepsilon_{33}'\omega)^2 s|\exp(j\Gamma_3^{(3)}g) + \gamma_3^{(3)}\exp(-j\Gamma_3^{(3)}g)|^2}. \quad (39)$$

POWER RATIO P_S/P_L

From the formulas obtained above, we can easily calculate the power ratio of the shear and longitudinal waves excited in the acoustic line:

$$M(\theta) = \frac{P_S}{P_L} = \frac{R_{\mathrm{rad,S}}(\theta)}{R_{\mathrm{rad,L}}(\theta)}. \quad (40)$$

The quantity M depends on the angle θ between the sixfold axis of the piezoelectric and the normal to the end of the acoustic line. This allows us to determine the optimal orientation of the piezoelectric at which either shear or longitudinal wave excitation will predominate.

TRANSFORMATION FACTOR

Let us calculate the electroacoustic transformation factor defined by Eq. (1). We assume that the electro-

magnetic power is supplied from the generator to the piezoelectric element through a double-wire line with a given wave impedance Z_0. The generator has an alternating electromotive force E and is matched with the line. The latter condition means that the internal resistance of the generator is equal to the wave impedance of the line. In this case, the power carried by the direct wave is equal to the power transferred to the matched load: $P_+ = P_{CL} = |E|^2/8Z_0$. A parasitic capacitance C_{SH} is connected in parallel to the piezoelectric element (see Fig. 1), and the lead with an active resistance R_{los} and inductance L is connected to it in series.

In this configuration, the transmission line is loaded with the load impedance

$$Z_L = \frac{Z}{(1 + j\omega C_{SH} Z)} + j\omega L + R_{LOS},$$

where Z is the impedance of the piezoelectric element (see Eq. (26)).

The complex amplitude of the current flowing through the piezoelectric element is determined as

$$I_P = \frac{E}{(Z_0 + Z_L)(1 + j\omega C_{SH} Z)}.$$

Then, the power of the shear wave excited in the acoustic line is

$$P_S = \frac{|I_P|^2}{2} R_{rad,\,S},$$

and the transformation factor in the case of the transverse wave excitation will have the form

$$\eta_S = \frac{P_S}{P_{CL}} = \frac{4R_{rad,\,S} Z_0}{\left|(Z_0 + Z_L)(1 + j\omega C_{SH} Z)\right|^2}. \qquad (41)$$

A similar expression can be obtained for the longitudinal wave excitation (η_L) by replacing $R_{rad,\,S}$ in Eq. (41) with the quantity $R_{rad,\,L}$.

DISCUSSION: RESULTS OF THE NUMERICAL ANALYSIS

Below, we consider the case of the transverse wave excitation by an Al–ZnO–Al piezoelectric element mounted on a $Y_3Al_5O_{12}$ acoustic line with the [110] orientation along the x_3' axis (see Fig. 1). The necessary piezoelectric and dielectric constants for ZnO are taken from the literature [8]. The values of the density and the velocities of longitudinal and transverse waves for Al are taken from [9]. As tentative data for choosing the acoustic attenuation coefficients in the layers of the piezoelectric element, we used the experimental results reported in [10] and also some data from [9]. The calculations were performed for the frequency range from 10 to 20 GHz. The thicknesses of layers *1–3* (see Fig. 1) were 0.032, 0.09, and 0.048 μm, respectively. These values were chosen so as to obtain the maximal transformation factor for a shear wave at a frequency of approximately 15 GHz.

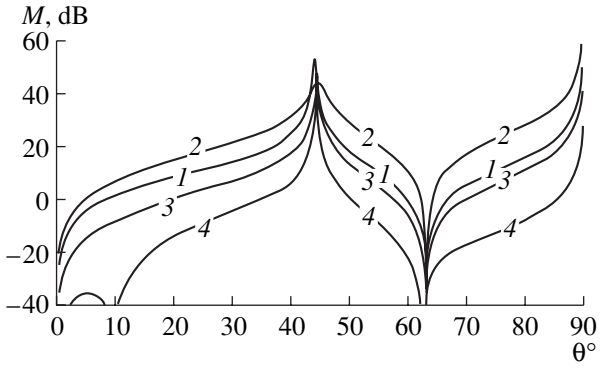

Fig. 2. Dependences of the quantity $M = P_S/P_L$ on angle θ without acoustic attenuation in the layers of the piezoelectric element for different frequencies: (*1*) 11, (*2*) 14, (*3*) 17, and (*4*) 20 GHz.

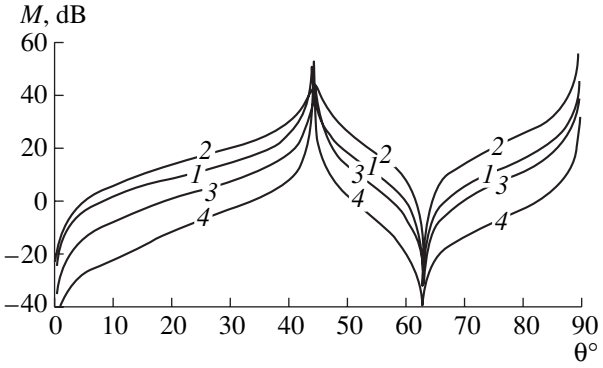

Fig. 3. Same as in Fig. 2 with allowance for the acoustic losses. The preset values of the attenuation coefficients correspond to f = 10 GHz: for the ZnO piezoelectric, α_S = 1.24 dB/μm{α_L = 2.48 dB/μm}; for Al, α_1 = 4.0 dB/μm {α_3 = 6.4 dB/μm}; and for $Y_3Al_5O_{12}$, $\alpha_1 = 5 \times 10^{-3}$ dB/μm {$\alpha_3 = 10^{-4}$ dB/μm}.

Figure 2 presents a family of dependences of ratio M on angle θ. The curves were obtained from calculations by Eqs. (38)–(40), without taking into account the attenuation, for several frequencies indicated in the figure caption. Figure 3 shows similar dependences obtained with allowance for the attenuation. The chosen values of the attenuation coefficients are specified in the figure caption.

The behavior of the curves noticeably depends on frequency. At a given limitation of quantity M from below, the allowable range of angles θ strongly depends on f. If, for the excitation of a shear wave, we preset $M \geq 20$ dB, then, in the absence of attenuation, angle θ can be varied within 28°–55° at f = 14 GHz and only within 43°–45° at f = 20 GHz. In the case of longitudinal wave excitation, a similar situation takes place with the only difference being that the wider range of allowable angles θ occurs at a frequency of 20 GHz (~60°–67°)

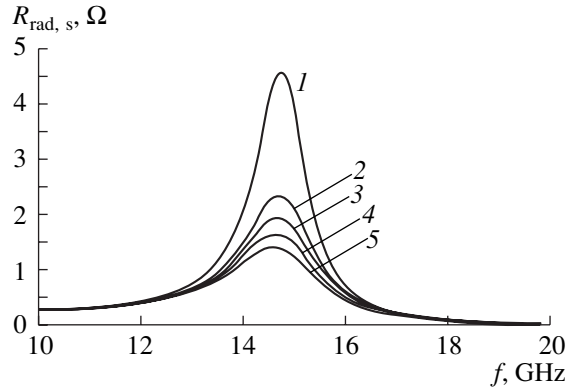

Fig. 4. Frequency dependences of the radiation resistance $R_{rad, S}$ at θ = 44.6° for different attenuations: (*1*) without attenuation; (*2–5*) the attenuation coefficients at *f* = 10 GHz are α_S = (*2*) 0, (*3*) 1.24, (*4*) 2.48, and (*5*) 3.72 dB/μm; {α_L = (*2*) 0, (*3*) 2.48, (*4*) 4.96, and (*5*) 7.44 dB/μm}; for shear waves $\alpha_1^{(1)} = \alpha_1^{(3)}$ = 4 dB/μm; for longitudinal waves, $\alpha_3^{(1)} = \alpha_3^{(3)}$ = 6.4 dB/μm. The diameter of the piezoelectric element is 0.05 mm.

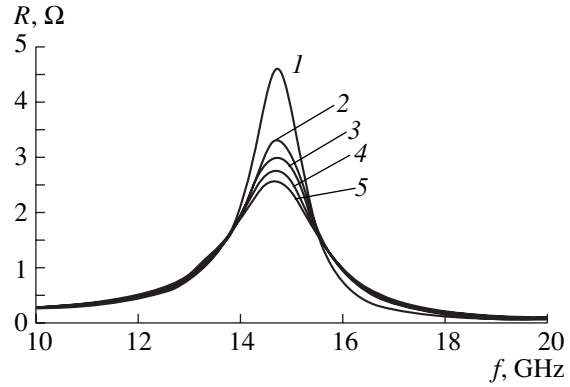

Fig. 5. Frequency dependences of the active impedance component of the piezoelectric element, *R*(*f*), for different acoustic attenuations in its layers: (*1*) the case without attenuation and (*2–5*) the cases corresponding to those specified in Fig. 4.

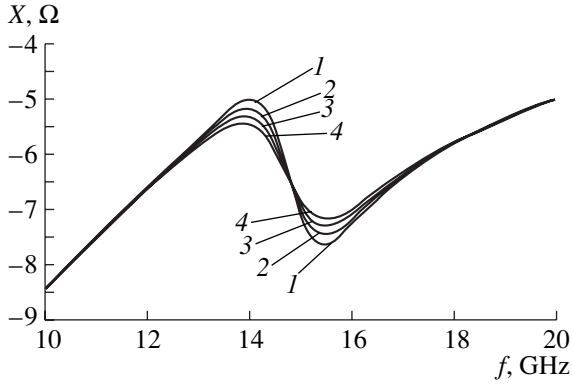

Fig. 6. Frequency dependences of the reactive impedance component of the piezoelectric element, *X*(*f*), for different acoustic attenuations in its layers: curves *1–4* correspond to the attenuation coefficients specified in Fig. 4 for curves *2–5*, respectively.

rather than at 14 GHz (62°–64°). The inclusion of attenuation caused the most pronounced changes in curves *2* and *4* (see Fig. 3): curve *2* was shifted downwards, and curve *4*, upwards. The other two curves remained practically unchanged. As a result, the interval of allowable angles was somewhat narrowed for the transverse wave excitation at a frequency of 14 GHz and it somewhat widened at a frequency of 20 GHz. In the case of the longitudinal wave excitation, the same changes in the curves caused corresponding changes in the intervals of allowable angles.

The positions of the extrema of the curves on the θ axis are practically the same for different frequencies. In the frequency band from 11 to 14 GHz, the optimal angle for the shear wave excitation increases from 43.85° to 44.75°, and when the frequency *f* increases further to 20 GHz, the optimal angle decreases to 44.35°. The inclusion of attenuation (Fig. 3) does not introduce any considerable changes into this behavior of the optimal angle. The extreme values of *M* also differ for different frequencies *f*. For example, at θ ≈ 44°–45°, the maximal values of *M* corresponding to the frequencies specified in Fig. 2 are 51.6, 44.1, 58.5, and 56.4 dB. The inclusion of attenuation (see Fig. 3) leads to a slight decrease in these values: 51.0, 44.0, 53.2, and 51.7. A similar situation occurs in the vicinity of θ ≈ 63°, where the attenuation most strongly reduces the depth of the valleys in the curves obtained for 17 and 20 GHz: instead of –42.6 and –59.6 dB, the depths become equal to –39.1 and –38.3 dB.

Figure 4 shows the results of calculating the radiation resistance $R_{rad, S}(f)$ by Eq. (38) for the case of the transverse wave excitation (θ = 44.6°) with allowance for the attenuation in all media of the piezoelectric element. Four different cases of acoustic absorption in the piezoelectric were considered with a single set of parameters used for the upper layer and the underlayer. Curve *1* corresponds to the absence of attenuation in all media. One can see that an increase in attenuation leads to a decrease in $R_{rad, S}$. Curve *2* in Fig. 4 corresponds to the case when the longitudinal wave attenuation in ZnO at a frequency of 10 GHz is close to the value measured in the experiment [5]. As for the transverse waves, no experimental data on their attenuation in thin layers can be found in the literature. We took this attenuation to be two times smaller than the longitudinal wave attenuation. The inclusion of such an attenuation resulted in a considerable decrease in the maximal radiation resistance: by more than 50%.

The effect of the acoustic attenuation in the layers of a piezoelectric element on the impedance of this element is illustrated by the curves calculated by Eq. (26). Figure 5 presents the frequency dependences of the active impedance component *R*(*f*) for different attenuations in the piezoelectric for a single model of acoustic losses in all other layers. Curve *1* corresponds to the case when the attenuation is absent in all layers. The reactive impedance component *X*(*f*) is represented by

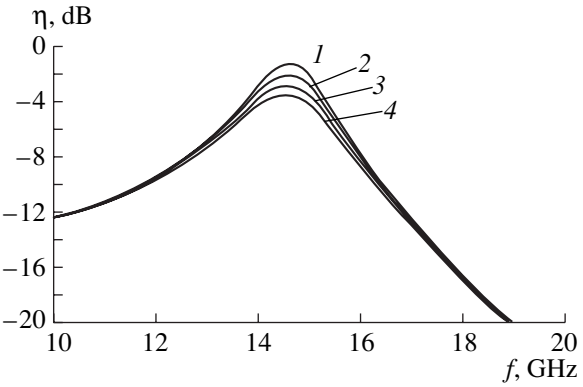

Fig. 7. Frequency dependences of the electroacoustic transformation factor $\eta_S(f)$ in the case of the transverse wave excitation for different attenuations in the piezoelectric and without attenuation in all other layers. Curves *1–4* correspond to the coefficients α_S and α_L specified in Fig. 4 for curves *2–5*, respectively. The wave impedance of the transmission line is 8.9 Ω.

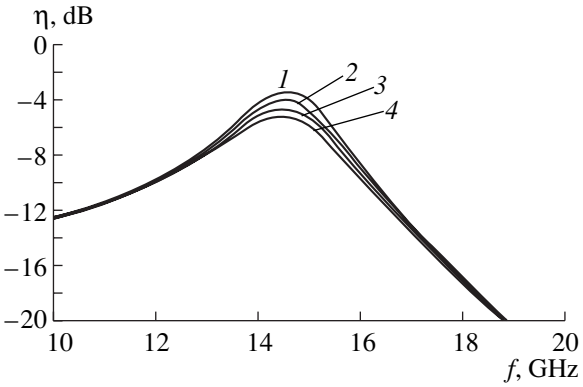

Fig. 8. Same as in Fig. 7 with allowance for the attenuation in the underlayer and the upper layer. The attenuation coefficients $\alpha_1^{(1)}$, $\alpha_1^{(3)}$, $\alpha_3^{(1)}$, and $\alpha_3^{(3)}$ are the same as those in Fig. 4.

similar curves in Fig. 6. First of all, we note that, as one would expect, curve $R(f)$ obtained in the absence of acoustic attenuation coincides with the corresponding curve $R_{\text{rad, S}}(f)$ at $\theta = 44.6°$ (see curves *1* in Figs. 4 and 5). An increase in attenuation leads to a decrease in R, but the corresponding decrease in $R_{\text{rad, S}}$ occurs faster, which agrees well with physical considerations. As for the component $X(f)$, it is also affected by the acoustic attenuation in the layers of the piezoelectric element. When the frequency varies, the quantity $X(f)$ oscillates around the value of the capacitive resistance $1/\omega C_0$, where C_0 is the static capacitance of the piezoelectric element. The peak-to-peak amplitude of these oscillations decreases as the attenuation in the layers grows, which is illustrated by the curves shown in Fig. 6.

The main characteristic of a transducer is the frequency dependence of transformation factor $\eta_S(f)$ or $\eta_L(f)$. To reveal the effect of acoustic attenuation on this dependence, we assumed that the diameter of the piezoelectric element was 0.05 mm, the absolute value of its impedance was ~8.9 Ω, $\theta = 44.6°$, and the wave impedance of the transmitting line was $Z_0 = 8.9$ Ω. The latter value of Z_0 is optimal, providing the maximal value of η_S in the absence of any matching devices. In this case, an almost purely shear wave should be excited. Figures 7 and 8 show the dependences $\eta_S(f)$ calculated by Eq. (41) for different attenuations in the layers. The values of the attenuation coefficients are indicated in the figure captions. In Fig. 7, the attenuation in only the piezoelectric layer is taken into account, while Fig. 8 presents the curves obtained with allowance for the attenuation in all other media as well. One can see that an increase in attenuation leads to a decrease in the transformation factor. However, for the chosen values of the attenuation coefficients, this decrease is relatively small: within 2–3 dB. Note that a decrease in η_S is observed only near the curve maximum, while the ends of the curves are practically unaffected by attenuation.

CONCLUSIONS

In this paper, we obtained the formulas for calculating the characteristics of a piezoelectric transducer that consists of a piezoelectric of the 6*mm* symmetry class with an arbitrary orientation of the sixfold axis and two metal electrodes of finite thickness. The formulas take into account the acoustic attenuation in the layers of the transducer. Depending on the orientation of the piezoelectric, such a transducer can excite shear or longitudinal elastic waves. The results of the numerical analysis show that, at a frequency of ~15 GHz, the acoustic attenuation in the layers of the transducer plays an important role. The radiation resistance of a transducer made on the basis of ZnO with Al electrodes and operating in the shear wave excitation mode decreases by 50 to 55% under the effect of attenuation, while the transformation efficiency decreases by 2 to 3 dB. A further increase in frequency will undoubtedly lead to a greater decrease in the efficiency of the transducer.

The results reported in this paper may be used in the design of efficient transducers for elastic waves in the short-wave region of the microwave frequency range.

REFERENCES

1. M. A. Grigor'ev, S. S. Kuryshov, and A. V. Tolstikov, Akust. Zh. **36**, 255 (1990) [Sov. Phys. Acoust. **36**, 139 (1990)].
2. V. V. Petrov, M. A. Grigor'ev, and A. V. Tolstikov, Opt. Spektrosk. **89**, 505 (2000) [Opt. Spectrosc. **89**, 463 (2000)].
3. M. A. Grigor'ev, B. D. Zaĭtsev, and V. N. Shevchik, Fiz. Tverd. Tela (Leningrad) **18**, 3708 (1976) [Sov. Phys. Solid State **18**, 2162 (1976)].

4. T. L. Rhyne, IEEE Trans. Ultrason. Ferroelectr. Freq. Control **43** (6), 1136 (1996).
5. Hashimoto Ken-ya and Yamaguchi Masatsune, IEEE Trans. Ultrason. Ferroelectr. Freq. Control **48** (5), 1181 (2001).
6. C. Bacon, E. Guilliorit, and B. Hosten, J. Acoust. Soc. Am. **110**, 1398 (2001).
7. M. A. Grigor'ev, A. V. Tolstikov, and Yu. N. Navrotskaya, Akust. Zh. **48**, 187 (2002) [Acoust. Phys. **48**, 155 (2002)].
8. N. F. Foster, G. A. Coquin, G. A. Rozgonyi, and F. A. Vannata, IEEE Trans. Sonics Ultrason. **15** (1), 28 (1968).
9. G. Kino, *Acoustic Waves: Devices, Imaging, and Analog Signal Processing* (Prentice Hall, Englewood Cliffs, N.J., 1987; Mir, Moscow, 1990).
10. M. A. Grigor'ev, B. D. Zaĭtsev, and A. V. Tsibin, Pis'ma Zh. Tekh. Fiz. **5** (1), 50 (1979) [Sov. Tech. Phys. Lett. **5**, 20 (1979)].

Translated by E. Golyamina

Acoustical Physics, Vol. 49, No. 6, 2003, pp. 677–681. Translated from Akusticheskiĭ Zhurnal, Vol. 49, No. 6, 2003, pp. 794–798.

Acoustical Method of Studying the Growth and Collapse of a Vapor Bubble in Boiling

B. M. Dorofeev and V. I. Volkova

Stavropol State University, ul. Pushkina 1, Stavropol, 355009 Russia

e-mail: stavsu@stavsu.ru

Received July 17, 2002

Abstract—A new method is proposed for determining the characteristics of the dynamics of the vapor bubble volume variation from the parameters of the sound pulse generated by this bubble. The accuracy of the method is estimated, and its application is illustrated by a specific example. © *2003 MAIK "Nauka/Interperiodica".*

It is well known that the maximum (on the order of hundreds of MW/m^2) heat flow density can be obtained in surface boiling of a subcooled liquid, which is therefore used in heat exchangers (at nuclear plants, in aircraft and rocket industry, in microwave electronics, and so on). However, the design of these systems is based on approximate semiempirical formulas, because the study of the physics of boiling is far from complete. The relevant issues of fundamental importance that remain insufficiently studied experimentally include the dynamics of the volume variation of a vapor bubble.

Previously, experimental studies of the dynamics of growth and collapse of vapor bubbles were carried out with the use of high-speed filming (for example, in [1, 2] at a rate of 15000 and 22000 frames per second). Analysis of data obtained in this way is performed by discrete images of a bubble in separate frames of the film. The behavior of the bubble during the intervals between the frames remains unclear. In addition, for a bubble of irregular shape, the calculation of instantaneous volumes of the bubble is quite laborious and leads to considerable errors (on the order of ten percent).

A simpler method is the photometric method of super-high-speed continuous recording of the variation of the linear dimension of a vapor bubble by using a photomultiplier tube [3–6] (in these experiments, the sound pressure produced by a bubble was simultaneously recorded). The determination of the change in the bubble volume by this method is only possible for a spherical bubble.

In this paper, we propose a new sound-measurement method for determining the vapor bubble characteristics and studying the dynamics of its volume variation, which is free of the aforementioned drawbacks. This method can also be used with experimental systems, providing a direct input of the measured data into a computer for processing with the help of modern information technologies.

We begin considering the mechanism of growth and collapse of a vapor bubble in a local boiling on a flat surface. In this case, temperature T_l of the main body of liquid, except for a thin layer near the surface, is lower than saturation temperature T_{sat}. At the beginning, the bubble grows inside this layer of a "hot" liquid whose temperature is higher than T_{sat}. Under the action of the growing bubble, the adjoining layer of "hot" liquid rises. Due to the evaporation, the thickness of this layer above the bubble and near its sides decreases and finally becomes equal to zero. From this point on, two processes proceed simultaneously: the evaporation near the base of the bubble continues and the condensation on its upper part and, later, near its sides begins. As the bubble grows, the area of its interphase surface at the boundary with the "cold" liquid (with a temperature lower than T_{sat}) increases. This results in an increase in the velocity $\dot{V}_-$ of condensation, which approaches the velocity $\dot{V}_+$ of evaporation.

The growing bubble sets in motion the surrounding liquid. After $\dot{V}_-$ and $\dot{V}_+$ become equal, its volume continues to grow due to the motion of the liquid under its inertia. Therefore, after reaching its maximum size, the bubble becomes mechanically (vapor pressure p_v is smaller than the pressure in liquid $p_{l\infty}$) and thermally ($\dot{V}_- > \dot{V}_+$) nonequilibrium. As a result, it begins to degrade, entraining the surrounding liquid. After pressures p_v and $p_{l\infty}$ become equal, the liquid moving under its own inertia compresses the bubble. Then, p_v sharply increases, which can lead to the formation of a shock wave [6]. The maximum height of the bubble is approximately by an order of magnitude greater than the thickness of the hot liquid layer. Consequently, during the whole time of collapse, the major part of the interphase surface of the bubble borders on the cold liquid and, hence, the evaporation process does not play a significant part.

1063-7710/03/4906-0677$24.00

According to the above physical model, the following formula was derived to describe the dynamics of the radius variation of a spherical vapor bubble [7]:

$$\frac{R}{R_m} = \frac{1 - \exp(-\alpha t/t_m) - (\alpha t/t_m)\exp(-\alpha)}{1 - (1+\alpha)\exp(-\alpha)}, \quad (1)$$

where R_m and t_m are the maximum radius and time of bubble growth and constant α must satisfy the boundary condition

$$1 - \exp(-\alpha\tau/t_m) - (\alpha\tau/t_m)\exp(-\alpha) = 0 \quad (2)$$

(τ is the lifetime of the bubble).

Dependences (1) and (2) are based on the following equations: first, the heat balance equation (the resulting heat flow determined by the processes of evaporation and condensation is equal to the difference of heat flows into and out of the bubble); second, the formula of the vapor bubble's growth in the body of a uniformly superheated liquid, which was obtained in [8] by solving the nonstationary heat conduction equation; and third, the formula of the bubble's collapse at a constant volume of vapor condensed from a unit surface per unit time [6].

Since in Eqs. (1) and (2) the radius and the time are expressed on a relative scale, in their derivation the cofactors of the initial relations involving constant coefficients, physical constants, and similarity criterions are reduced. Consequently, Eqs. (1) and (2) should remain valid for the boiling of a subcooled liquid under various conditions. This conclusion is confirmed quantitatively in [7] by the results of experiments carried out with the use of a high-speed filming.

Two equations of hydrodynamic sound generation are known. The first is the Rayleigh equation

$$p = \frac{\rho'(R^2\ddot{R} + 2R\dot{R}^2)}{r}, \quad (3)$$

where p is the generated alternating pressure, ρ' is the density of the liquid, R is the current radius of a spherical bubble, and r is the distance from the bubble center to the point of pressure determination. As is shown in [9], relation (3) is a consequence of the Cauchy–Lagrange integral and holds for all points of the region of the potential liquid motion. The Rayleigh equation is often used as a basic equation in nonlinear acoustics (for instance, in [10]). The second equation ([11–13] and others) has the form

$$p = \frac{\rho'\ddot{V}}{4\pi r} \quad (4)$$

(V is the current volume of the bubble). Both Eqs. (3) and (4) are valid within the nonwave zone $R \ll r \ll \lambda$ (λ is the sound wavelength) and are mathematically equivalent in the case of a spherical bubble. However, these equations can also be used in other cases, because the shape of a sound source that is small compared to r has no effect on the sound pressure generated by it [14]. In this case, in Eq. (3) R is the radius of an equivalent (of equal volume) spherical bubble.

From Eqs. (1) and (3), we obtain the formula of hydrodynamic sound generation under the conditions of a boiling subcooled liquid:

$$p = \frac{K\rho' R_m^3 (1-b-ac)\lfloor 2(b-c)^2 - b(1-b-ac)\rfloor}{r t_m^2}, \quad (5)$$

where $K = \alpha^2/[1-(1+\alpha)c]^3$, $a = \alpha t/t_m$, $b = \exp(-a)$, and $c = \exp(-\alpha)$.

The calculation of the pair of curves $R(t)$ and $p(t)$ performed in [7] by formulas (1), (2), and (5) showed that these curves agree quantitatively with the results of combined experiments [4–6] in which the variations of the radius of a spherical bubble and the sound pressure generated by it were simultaneously recorded by a photomultiplier tube and a hydrophone in the form of paired oscillograms.

Formulas (1), (2), and (5) are used as the basis for the proposed acoustical method. In this method, according to Eq. (5), we solve the inverse problem of determining the characteristics t_m, α, and R_m of the dynamics of the bubble radius variation (Eq. (1)) from the parameters of the sound pulse generated by the bubble.

The bubble successively generates positive, negative, and positive pressures with amplitudes of P_{m^1}, P_{m^2}, and P_{m^3} (Fig. 1). The change in sign and the termination of pressure generation takes place at instants t_1, t_2, and τ. The aforementioned quantities are the amplitude and time parameters of the sound pulse that are used in the calculations.

The specially developed technique consists in the application of the following approximate formulas derived from Eqs. (2) and (5) and by calculations:

(i) for calculating the time of bubble growth,

$$t_{m*} = \frac{t_1 + t_2}{2}; \quad (6)$$

(ii) for finding constant α by a numerical method in four ways (α_*, α_1, α_2, and α_{12}),

$$1 - \exp(-\alpha_*\tau/t_{m*}) - (\alpha_*\tau/t_{m*})\exp(-\alpha_*) = 0, \quad (7)$$

$$2(b_1 - c_1)^2 - b_1(1 - b_1 - a_1c_1) = 0 \quad (8)$$

($a_1 = \alpha_1 t_1/t_{m*}$, $b_1 = \exp(-a_1)$, and $c_1 = \exp(-\alpha_1)$),

$$2(b_2 - c_2)^2 - b_2(1 - b_2 - a_2c_2) = 0 \quad (9)$$

($a_2 = \alpha_2 t_2/t_{m*}$, $b_2 = \exp(-a_2)$, and $c_2 = \exp(-\alpha_2)$) and

$$\alpha_{12} = \frac{\alpha_1 + \alpha_2}{2}; \quad (10)$$

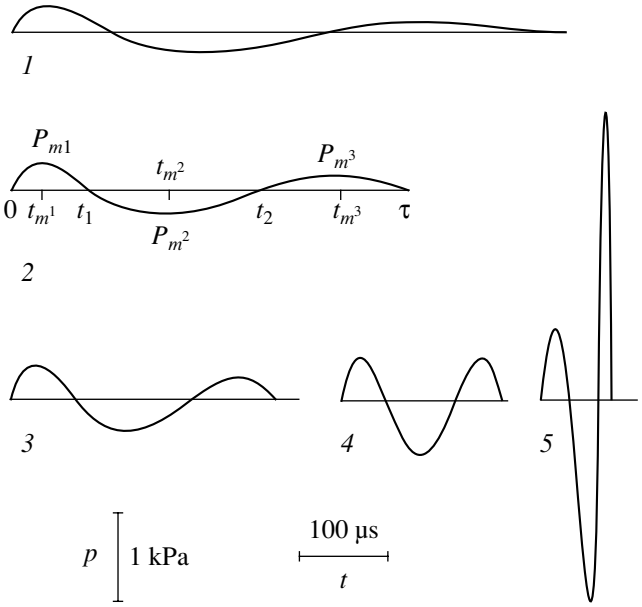

Fig. 1. Sound pulses generated by vapor bubbles for various degrees of subcooling of the liquid (Table 1).

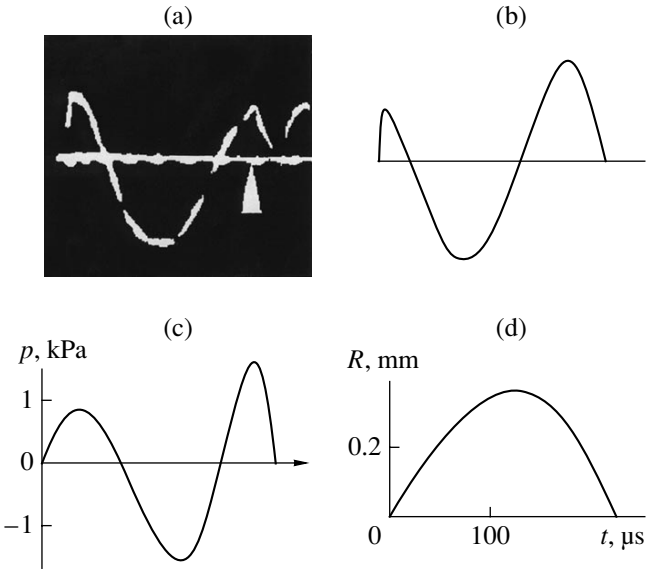

Fig. 2. Determination of the dynamics of the bubble radius variation from the sound pulse generated by this vapor bubble: (a–c) the sound pulse and (d) the radius variation.

(iii) and for computing the maximum radius of the bubble,

$$R_{m*}^3 = -\frac{rt_{m*}P_{m^2}[1 + (1 + \alpha_{12})c_{12}]}{\alpha_{12}^2 c_{12}\rho'} \qquad (11)$$

($c_{12} = \exp(-\alpha_{12})$).

Table 1 shows the data borrowed from [15], which allow us to corroborate the suggested technique. In Table 1, $\Delta T_s = T_{sat} - T_l$ and ρ' are the subcooling and density of the liquid; R_m, t_m, and τ are the microcharacteristics of the bubble. The constant α is calculated from boundary condition (2). Table 1 also contains the times t_1, t_2 and the amplitude P_{m^2} of the negative pressure generated by the bubble (r = 13 mm), which are determined in calculating the sound pulses (Fig. 1) by formula (5).

The results of evaluating the accuracy of formulas (6)–(11) are given in Tables 2 and 3, which include the values calculated by these formulas with relative errors for each of the five bubbles and the mean absolute values of relative errors.

The analysis of errors (Tables 2 and 3) testifies that the suggested technique is practically applicable. The errors of formulas (6) and (11) for determining t_m and R_m are on the order of one percent and the errors of formulas (7) and (10) for determining α are on the order of three percent.

A rigorous solution of this problem requires complicated calculations. In this case, in Eqs. (8) and (9), t_{m*} is replaced by t_m, and α_1 and α_2 are replaced by α. By repeatedly applying in turn the two relations obtained in this way, it is possible to calculate the exact values of t_m and α by the method of successive approximations. Then, by varying t in Eq. (5), the time t_{m^1}, t_{m^2}, or t_{m^3} corresponding to the maxima of P_{m^1}, P_{m^2}, or P_{m^3}, respectively (Fig. 1), is found with the aim of determining the exact value of R_m by this formula. Since the errors of the simpler calculations described above are sufficiently small, the rigorous solution, as a rule, is unnecessary.

Table 1

No.	ΔT_s, K	ρ', kg/m^3	R_m, mm	t_m, μs	τ, μs	α (16)	t_1, μs	t_2, μs	P_{m^2}, Pa
1	15.6	970	0.51	244	600	0.951	117	375	−248
2	32.2	980	0.44	190	450	0.812	94.0	289	−276
3	54.4	990	0.38	138	300	0.445	71.9	206	−379
4	70.2	996	0.32	90	180	0.015	49.7	130	−616
5	86.0	999	0.27	50	80	−2.028	33.2	66.2	−2350

Table 2

No.	t_{m*}, μs	δ_t, %	α_* (7)	δ_*, (7)	α_1 (8)	δ_1, %
1	246	0.82	0.919	–3.36	1.005	5.68
2	192	1.05	0.781	–3.82	0.847	4.31
3	139	0.72	0.428	–3.82	0.471	5.84
4	89.9	–0.11	0.015	0	0.015	0
5	49.7	–0.60	–1.933	4.68	–2.142	–5.62
Mean values		0.66		3.14		4.29

Table 3

No.	α_2 (9)	δ_2, %	α_{12} (10)	δ_{12}, %	R_m, mm	δ_R, %
1	0.840	–11.7	0.923	–2.94	0.519	1.76
2	0.691	–14.9	0.769	–5.30	0.446	1.36
3	0.385	–13.5	0.428	–3.82	0.382	0.53
4	0.015	0	0.015	0	0.320	0
5	–1.826	9.96	–1.984	2.17	0.278	2.96
Mean values		10.0		2.85		1.32

Now, we illustrate the use of the proposed technique by a specific example. First of all, we will specify the conditions of experiments [3].

The boiling of a degassed water of temperature T_l = (300.9 ± 2.5) K occurred on a nichrome wire of length 2.0 and diameter 0.1 mm. Before the experiment began, the wire was raised to red heat in air (by an electric current through the wire) and then immersed in the liquid. When the current flowing through the wire was low, vapor bubbles appeared on the wire one after another (the intervals between the appearance of bubbles were much longer than their lifetime).

The bubble generating sound was at the center of a spherical vessel 306 mm in diameter. Under these conditions, not only the direct waves but also the once-reflected wave were spherically symmetric. A hydrophone was located at a distance of 6.5 mm from the center of the vessel. The time interval of recording the sound pressure unaffected by the reflected wave was (204 ± 2) μs.

Figure 2a displays the oscillogram of a sound pulse generated by a single bubble. The second beam of the oscilloscope represents the time axis. The 25-μs time mark generator is turned on. The distances between the time marks increase toward the end of the oscillogram, which indicates that the sweep is nonlinear. Beginning from the eighth time mark, the pulse becomes distorted because of the effect of the once-reflected wave on the hydrophone in addition to the direct wave (the sound reflection occurs with the loss of a half-wave). In spite of the indicated features, this oscillogram is quite informative from the point of view of applying the proposed acoustical method.

From the oscillogram shown in Fig. 2a, one can see that t_1 = 75 μs and t_2 = 175 μs (the third and seventh time marks, respectively). The results of calculations by Eqs. (6), (8), and (2) ($\alpha = \alpha_1$) are as follows: t_{m*} = 125 μs, α_1 = –0.752, and τ = 225 μs. For the amplitude of negative pressure P_{m^2} = –1.6 kPa, from Eq. (11) it follows that R_{m*} = 0.4 mm ($\alpha_1 = \alpha_{12}$, r = 6.5 mm, and ρ' = 1000 kg/m^3).

Figure 2b shows the sound pulse calculated by Eq. (5) with consideration for the nonlinearity of the sweep (the distorted time in arbitrary units is $t_* = k_1 t + k_2 t^2$, where $k_1 = 2.5 \times 10^{-2}$ arb. un./μs and $k_2 = 6.0 \times 10^{-4}$ arb. un./μs^2). This plot is presented for convenience of comparison with the recorded pulse (Fig. 2a). The comparison testifies to the reasonable reliability of the results.

Figures 2c and 2d show the undistorted sound pressure and the bubble radius variation with time, calculated by Eqs. (5) and (1). Thus, the three measured parameters of the sound pulse, namely, t_1, t_2, and P_{m^2}, allowed us to determine the characteristics t_m, α, τ, and R_m and then to reproduce the whole pulse and represent the dynamics of the vapor bubble radius variation (both of them on a real scale).

REFERENCES

1. G. G. Treshchev, in *Heat Transfer at High Thermal Loads and Other Special Conditions*, Ed. by A. A. Armand (Gosénergoizdat, Moscow, 1959), pp. 51–68.

2. F. Schmidt, J. Robinson, and R. Skapura, in *Proceedings of 4th International Heat Transfer Conference* (1970), Vol. 5, No. 1.8.
3. B. M. Dorofeev and I. S. Sologub, in *Research in the Physics of Boiling* (Stavropol. Gos. Pedagog. Inst., Stavropol, 1975), No. 3, pp. 34–41.
4. B. M. Dorofeev, Teplofiz. Vys. Temp. **23** (5), 586 (1985) [High Temp. **23** (3), 479 (1985)].
5. B. M. Dorofeev, Doctoral Dissertation in Physics and Mathematics (Stavropol, 1994).
6. B. M. Dorofeev and V. I. Volkova, Teplofiz. Vys. Temp. **38** (5), 842 (2000) [High Temp. **38** (5), 814 (2000)].
7. B. M. Dorofeev, Teplofiz. Vys. Temp. **40** (3), 475 (2002) [High Temp. **40** (3), 437 (2002)].
8. B. M. Dorofeev and N. A. Poddubnaya, Teplofiz. Vys. Temp. **37** (5), 841 (1999) [High Temp. **37** (5), 814 (1999)].
9. L. I. Sedov, *A Course in Continuum Mechanics*, 4th ed. (Nauka, Moscow, 1984; Wolters–Noordhoff, Groningen, 1972), Vol. 2.
10. A. O. Maksimov, Akust. Zh. **48**, 805 (2002) [Acoust. Phys. **48**, 713 (2002)].
11. L. D. Landau and E. M. Lifshitz, *Mechanics of Continuous Media* (GITTL, Moscow, 1954).
12. M. A. Isakovich, *General Acoustics* (Nauka, Moscow, 1973).
13. *Taschenbuch der Techischen Akustik*, Ed. by M. Heckl and H. A. Müller (Springer, Berlin, 1975; Sudostroenie, Leningrad, 1980).
14. E. Skudrzyk, *The Foundations of Acoustics: Basic Mathematics and Basic Acoustics* (Springer, New York, 1971; Mir, Moscow, 1976), Vol. 2.
15. B. M. Dorofeev and V. I. Volkova, in *Acoustics at the Threshold of the XXI Century: Proceedings of VI Session of the Russian Acoustical Society* (Moscow State Univ. of Mines, Moscow, 1997), p. 276.

Translated by A. Svechnikov

Acoustical Physics, Vol. 49, No. 6, 2003, pp. 682–687. Translated from Akusticheskiĭ Zhurnal, Vol. 49, No. 6, 2003, pp. 799–805.

Wideband Focused Film Transducer for Optoacoustic Tomography

A. N. Zharinov, A. A. Karabutov, V. V. Kozhushko, I. M. Pelivanov, V. S. Solomatin, and T. D. Khokhlova

International Laser Center, Moscow State University, Vorob'evy gory, Moscow, 119992 Russia
e-mail: aak@sasha.phys.msu.su

Received December 2, 2002

Abstract—The response of a focused film transducer to wideband acoustic signals is studied both theoretically and experimentally. The transducer has the form of a narrow PVDF strip placed on a concave cylindrical surface. A software package is developed for calculating the impulse transient response functions depending on the position of the point source of spherical waves. The experiments are performed using laser thermooptical sources of acoustic spherical wave pulses excited by a pulsed diode-pumped Nd:YAG laser. The theoretical and measured temporal profiles of signals recorded by the transducer are shown to be in good agreement for the source positioned near the transducer's focus. For this region, a transducer sensitivity map is investigated. For the case of the source positioned at the focus of the transducer, the absolute value of the transducer sensitivity is 8 μV/Pa. © *2003 MAIK "Nauka/Interperiodica"*.

Laser optoacoustic tomography is one of the most promising new methods for diagnoses of biological tissues. The most straightforward and, as it seems now, the most important of its applications is the early diagnosis of mammary gland cancer [1, 2]. In this case, it is necessary to visualize a light-absorbing object, which is several millimeters in size and is buried several centimeters deep in a light-scattering medium. A model of such a system [2] uses a Q-switched Nd:YAG laser as a source of the probe radiation, a fiber-optic guiding system, and a 32-channel piezoelectric antenna constructed on the basis of a 110-μm-thick PVDF film. Piezoelectric elements 3×12.7 mm in size were spaced 4 mm apart on an arc of a radius of 60 mm. Experiments performed on phantoms, ex vivo and in vitro, demonstrated a high contrast of the image and a sufficiently high resolution (~1 mm) in the image plane [2]. However, the resolution in the direction perpendicular to the image plane, being determined by the length of the piezoelectric element and the depth of the object, was 15 to 20 mm, which can hardly be regarded as satisfactory.

This paper addresses a focused, rather than a planar, film transducer, which will improve the resolution in the direction perpendicular to the image plane. The transducer has the form of a narrow rectangular PVDF strip fixed on a concave cylindrical surface (Fig. 1). Its geometrical parameters (curvature radius R_0, length l, width h, and thickness d) are primarily determined by the task to be accomplished by the tomographic study.

The purpose of this paper is to investigate, both theoretically and experimentally, the impulse transient response of the wideband cylindrical transducer described above and to construct a sensitivity map for the region near the focus. The solution of this problem is necessary for determining the parameters and developing the optimal design of a wideband antenna array for the laser optoacoustic tomography of biological objects.

Optoacoustic tomography uses temporal profiles of ultrasonic signals; it is therefore reasonable to study the impulse transient response, rather than the frequency response, of the piezoelectric transducers. Calculating the response of a finite-size damped transducer to a

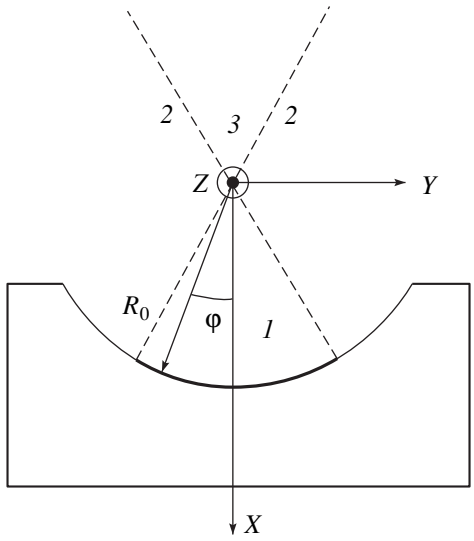

Fig. 1. Schematic diagram of a piezoelectric transducer.

1063-7710/03/4906-0682$24.00 © 2003 MAIK "Nauka/Interperiodica"

short spherical-wave pulse is a complex problem which can only be solved numerically. Therefore, it is important to develop simplified numerical methods that would nevertheless give results close to exact solutions.

We will study two kinds of impulse transient response functions. The first one, which we will further refer to as the *impulse response*, is the response of a planar transducer to a plane wave in the form of a δ pulse incident normally to the surface. This response function allows for the finite bandwidth of the transducer associated with its design. The other response function, which we will further refer to as the *point-source response*, is the response of a finite-aperture piezoelectric element (perhaps, with a curvilinear surface) to a spherical-wave δ pulse as a function of the source position. In this case, we disregard the finiteness of the piezoelectric element's bandwidth.

To calculate the point-source response of a transducer with an arbitrary aperture, one can use the Rayleigh integral [3–5]:

$$h(r, t) = \int_S \frac{\delta\left(t - \frac{|\mathbf{r}_0 - \mathbf{r}_1|}{c}\right)}{2\pi|\mathbf{r}_0 - \mathbf{r}_1|} dS, \quad (1)$$

where S is the transducer surface, $\mathbf{r}_0$ is the position vector of the source, and $\mathbf{r}_1$ is the position vector of the element of the surface S.

Physically, formula (1) means that the response at a certain instant is proportional to the area covered on the transducer's surface by the spherical wave over an infinitesimal time interval. Integral (1) can be calculated analytically if the transducer's surface is, for example, a planar polygon. However, in most cases, the point-source response can only be calculated numerically. Planar finite apertures have been studied in sufficient detail (see, e.g., [3–5]). Algorithms optimized in terms of speed have been proposed in [5].

Let us represent the surface of the piezoelectric transducer as a combination of a finite number of small elementary planar apertures. When calculating the Rayleigh integral, their area should be directly related to the time quantization interval, so that, in this small time interval, the acoustic wave front travels a distance on the transducer surface that is much smaller than the distance between the source and the transducer. Therefore, the elementary surface covered by the wave can approximately be regarded as a planar surface. Then the approach employed in [3–5] can be used to calculate the point-source response of the focused transducer. The response function was calculated for sources located near the focus. This region is of the most interest, because it must be characterized by maximum sensitivity. The angle between the line that connects the source with an element of the aperture and the normal to this element is no wider than 12°, which is much smaller than the critical angle for a planar longitudinal wave incident from the liquid onto the surface of an organic glass [6] (acoustic impedances of PVDF and organic glass are close). Thus, the wave transmission coefficient will vary over all points considered by no more than 3% of the maximum value. The transformation of the longitudinal wave into the shear wave on the surface can also be neglected, because the incidence angle is small. Although the approach proposed is approximate, it allows us to determine the main characteristics of the focused recording of acoustic pulses produced by sources located near the transducer's focus.

To calculate the point-source response, we used the cylindrical coordinates (the Z axis coincides with the axis of the cylinder on which the transducer resides, and the origin is at the transducer's focus, i.e., the point where the symmetry axis and the Z axis intersect) (Fig. 1).Then, the position vectors of the point source and of the transducer's surface element are (r_0, φ_0, z_0) and (R_0, φ, z), respectively. Here, R_0 is the curvature radius of the cylindrical surface, φ varies within the angle $\mp\varphi_0 = \pm(l/2R_0)$, and Z varies within the width of the film $\mp h/2$. In these notations, the Rayleigh integral takes the form

$$h(t, r_0, \varphi_0, z_0) = \int_{-\varphi_0}^{\varphi_0} d\varphi \int_{-h/2}^{h/2} dz R_0 \times \frac{\delta\left(t - \frac{\sqrt{r_0^2 + R_0^2 + (z - z_0)^2 - 2R_0 r_0 \cos(\varphi - \varphi_0)}}{c}\right)}{2\pi\sqrt{r_0^2 + R_0^2 + (z - z_0)^2 - 2R_0^2 r_0 \cos(\varphi - \varphi_0)}}, \quad (2)$$

where c is the phase velocity of sound in the medium. The point-source response function is nonzero only on the time interval $[t_{min} = R_{min}/c, t_{max} = R_{max}/c]$, where R_{min} and R_{max} are the distances from the source to the nearest and farthest aperture elements.

Figure 2 shows the theoretical point-source responses of a cylindrically focused piezoelectric transducer. For the source located at the focus, the response has the form of the delta function, because we calculate the response function assuming that the transducer bandwidth is infinite. For a source located nearer than the focus (curve *1* in Fig. 2 and region *1* in Fig. 1), the spherical wave first arrives at the elementary surface region of the transducer whose normal passes through the source, and later, at the transducer edges. Therefore, the point-source response has a sharp leading edge (Fig. 2), which corresponds to the instant the wave reaches the piezoelectric element, followed by a negative slope in accordance with the decrease in the area covered by the plane wave on the transducer surface; finally, the response has a sharp trailing edge, which occurs when the spherical wave reaches the transducer's edges. For a source located behind the focus (curve *3* in Fig. 2 and region *3* in Fig. 1), the behavior

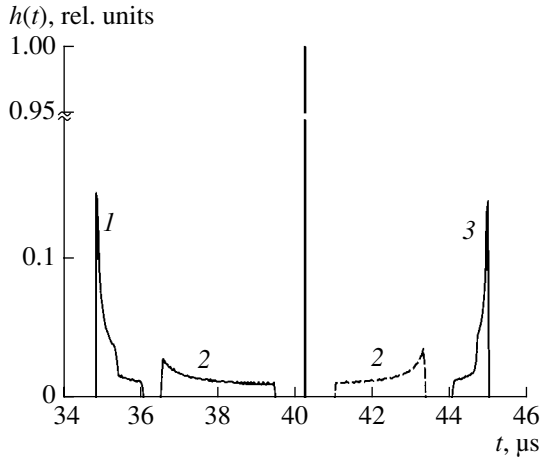

Fig. 2. Impulse responses to a point source located in different space regions (refer to curve numbers) shown in Fig. 1. The central peak is the response to the source located at the focus of the transducer with a coverage angle of 60°.

is the reverse: the leading edges correspond to the instants when the wave arrives at the transducer's edges, the response increases with time, and the sharp trailing edge occurs when the wave leaves the transducer.

For a source lying outside the transducer's coverage angle (region *2* in Fig. 1), the point-source response will take sufficiently long time, the wave being capable of reaching the transducer earlier (solid line *2* in Fig. 2), as well as later (dotted line *2* in Fig. 2), than the wave that comes from the focus. The leading edge corresponds to the instant the wave reaches the near edge of the piezoelectric element, and the trailing edge, to the instant the wave reaches the far edge. The relative levels of the leading and trailing edges depend on whether the source lies above or below the focus. Because the wave in this case travels along the piezoelectric element, the response will be weaker than that for sources located in region *1* or *3*. This is quite natural for a sharply focused transducer and corresponds to high-resolution optoacoustic tomography.

To experimentally study the point-source response functions, we used a setup comprising a pulsed diode-pumped Nd:YAG laser (model LCS-DTL-324Q from LaserCompact Co. Ltd, Russia) with a pulse length of τ_L = 8 ns and a pulse repetition rate of 500 Hz. Its radiation was guided through a fiber to the source of the optoacoustic signal in the form of a 20-μm-thick black polyethylene film placed into the immersion liquid (distilled water). Because the acoustic impedance of polyethylene is close to the impedance of water, the system could be considered as acoustically homogeneous. The footprint of the laser beam on the film surface was 1 mm in diameter, and the laser pulse energy was 70 to 80 μJ. The electric signal was amplified by a preamplifier and recorded by a Tektronix TDS220 oscilloscope with averaging over 128 realizations, providing a >40-dB dynamic range.

In our experiment, the strip of the piezoelectric element was l = 60 mm long, h = 1 mm wide, and d = 110 μm thick and had a curvature radius of R_0 = 60 mm. The substrate was made of organic glass, because its acoustic impedance is close to the impedance of PVDF. The organic glass was 80 mm thick, which provided measurements with a more than 60-μs-wide time window. The theoretical bandwidth of the transducer at points 1/e was from 50 kHz to 3.5 MHz. The optoacoustic source was moved across the surface of the piezoelectric transducer in two coordinates with the help of micrometer screws (in Cartesian coordinates X and Y (Fig. 1)).

The impulse responses considered above were obtained under the assumption that the transducer bandwidth was infinite and that the pulse had the form of a delta function. In the experiments, the received bandwidth was finite and the excitation pulse was described by a short unipolar burst. Therefore, to compare the experimental responses with those calculated theoretically, we convolved point-source response (2) with the optoacoustic spherical wave waveform and with the impulse response of the planar piezoelectric element. As we noted above, when calculating the Rayleigh integral, the time quantization interval Δt was chosen so that the front of the acoustic wave traveled a distance on the transducer's surface that is much shorter than the distance between the source and the transducer. Therefore, the elementary surface covered within time Δt was approximately considered as a planar surface. It was thus assumed that, at each time instant, the spherical wave from the point source is incident on the planar finite transducer surface. Since our study refers to the region near the transducer's focus, the dependence of the wave transmission coefficient on the incident angle and the mode transformation effects were neglected.

The open-circuit relative complex spectral sensitivity of the film transducer at frequency f is proportional to the difference between the particle displacements at the edges of the piezoelectric element [7]:

$$S(f) = A\int_0^d \frac{\partial \xi}{\partial x} dx, \qquad (3)$$

where ξ is the particle displacement, d is the PVDF thickness, and A is a constant that depends on the longitudinal piezoelectric modulus and permittivity of the film.

The impulse response of the planar transducer is the inverse Fourier transform of the function $S(f)$. We calculated it by the modified matrix method [8]. The method relies on the pressure and particle velocity continuity conditions for individual harmonics at the interfaces of the multilayer structure, which yield the frequency spectra of the pressure and particle velocity in

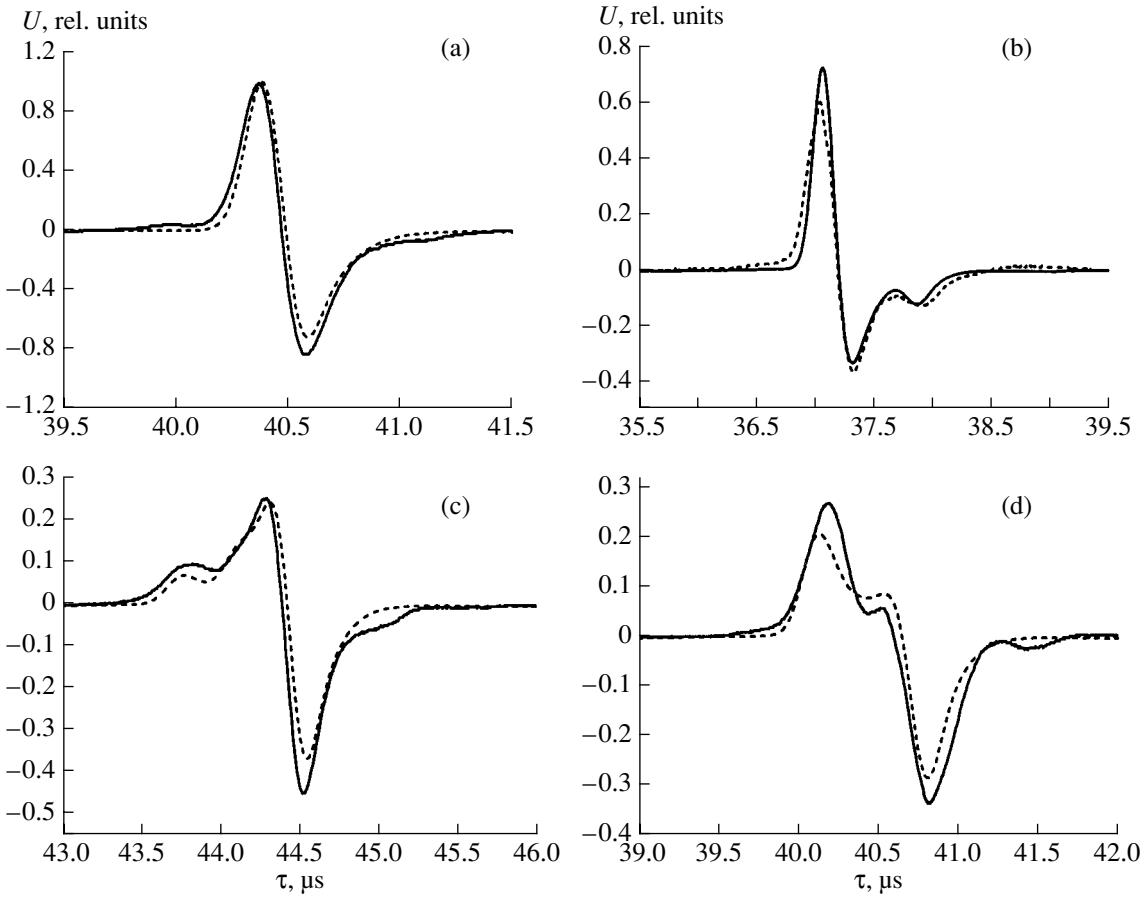

Fig. 3. Experimental (solid lines) and theoretical (dotted lines) temporal profiles of optoacoustic signals recorded by the transducer for a spherical wave source located (a) at the focus, (b) in region *1*, (c) in region *3*, and (d) in region *2*.

any layer. The transducer is designed so that the PVDF is sandwiched between water and organic glass half-spaces. Its relative complex spectral sensitivity can be expressed analytically as

$$S(f) = A\frac{i2z_2c_2/(2\pi f)(2z_2 - i2z_2\sin(2\pi fd/c_2) - 2z_3\cos(2\pi fd/c_2))}{(z_1 + z_2)(z_2 + z_3)\exp(i2\pi fd/c_2) + (z_1 - z_2)(z_2 - z_3)\exp(-i2\pi fd/c_2)}, \quad (4)$$

where z_1, z_2, and z_3 are the acoustic impedances of water, PVDF, and organic glass, respectively, and c_2 is the velocity of sound in PDVF. Because the laser pulse is short relative to the time taken by the wave to travel through the heat release region, the shape of the excited optoacoustic signal depends on the geometry of the heat release region alone [9, 10]. In our case, the shape of the optoacoustic signal at the transducer was defined by the energy distribution over the laser beam footprint and could, to the first approximation, be assumed equal to the derivative of the Gaussian pulse with the spectrum limited (at the 1/*e* points) by a frequency of f_{max} = 4 MHz.

In the experiment, we recorded the signals received by the transducer versus time for various positions of the optoacoustic source on the *XY* plane (Fig. 3). Figure 3a shows the calculated and measured temporal profiles for the source placed at the transducer's focus. In this case, the duration of the response function will be minimal (see Fig. 2), because the spherical wave front arrives at all elements of the transducer aperture at the same time and its effect on the recorded signal profile will also be minimal. The theoretical and experimental optoacoustic signals were normalized by the amplitude of the pulse produced by the source placed at the focus. The optoacoustic signal consists of a compression phase and a longer rarefaction phase, this structure being explained by the specific features of the transducer's impulse response. The experimental temporal profiles of signals are seen to be in good agreement with the theoretical ones. The absolute low-frequency

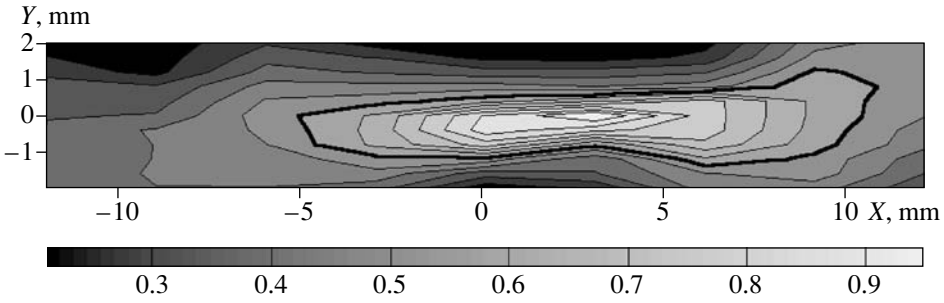

Fig. 4. Experimentally measured transducer's sensitivity map. The thick line outlines the region where the amplitude of the integral of the optoacoustic signal is greater than 0.5 of its maximum value.

sensitivity of the transducer measured for this particular source position was 8 μV/Pa.

Figure 3b shows the calculated and measured profiles of signals received by the focused transducer from the source located in region *1* (Fig. 1). The point-source response function determines temporal profiles of the signals recorded. Therefore, the signal amplitude in the compression phase is greater than that at the rarefaction phase. For the source located in region *3*, the maximum of the response function is observed when the wave front arrives at the farthest aperture element whose normal passes through the source. At first, the acoustic signal arrives at the edge points of the aperture, while the normal component appears at the last moment, which gives a clear-cut minimum in the total resultant signal; i.e., the amplitude in the rarefaction phase is greater than that in the compression phase (Fig. 3c).

When the source is in region *2*, the optoacoustic signal spreads over the time interval between t_{min} and t_{max} (Fig. 3d). For sources located in regions *1* and *3*, the signal amplitude is greater than for those in region *2* at the same *X*, because the wave front simultaneously arrives at the aperture elements that are symmetric about the normal. For a particular *X* coordinate, the signal is maximal when the source is at the *X* axis. In each of the regions, the time taken by the wave front to travel over the aperture increases with the displacement from symmetry axis *X*, which expectedly reduced the relative response. When the source moves along the *Z* axis, the region dependences remain the same with the only difference being that the travel time over the film along the *Z* axis is taken into account, which reduces the relative level of the response.

To determine the transducer's sensitivity region, the following measurements were carried out. With the help of micrometric screws, the optoacoustic source was moved in the *Y* and *X* directions with a step of 0.4 and 0.3 mm, respectively. The acoustic signals recorded by the transducer were integrated, and their maximum values were determined and put on the map. This procedure was used, because it is an integral of the far-field optoacoustic pulse that carries information about the distribution of the heat sources in the medium, i.e., about the spatial distribution of absorbing inhomogeneities [10]. The above procedure allows us to determine the transducer's spatial sensitivity region and to estimate the possibility of reconstructing positions and sizes of real sources. Figure 4 shows a 4 × 24-mm region with the transducer's focus at the center. The experimental results validate the preliminary theoretical estimates; i.e., the transducer's sensitivity rapidly varies in the *Y* direction and rather slowly varies in the *X* direction. The region where the amplitude of the integral is greater than 0.5 of its maximum value (it is outlined by a thick line in Fig. 4) is confined to a pearlike zone with its base facing the antenna.

Thus, this paper reports on the theoretical and experimental studies of a wideband focused PVDF transducer. The point-source impulse response functions of a cylindrically focused transducer are theoretically calculated for various source positions in the imaging plane. The temporal profiles of the transducer responses to optoacoustic signals produced by a pulsed source of spherical waves whose frequency spectrum was limited to a band (at the 1/*e* points) with f_{max} = 4 MHz are measured. The absolute sensitivity of the transducer for the source placed at its focus is 8 μV/Pa. Based on the experimental data, the transducer's sensitivity map is constructed. It is shown that the transducer's sensitivity region is confined to a 2 × 15-mm region (at a level of 0.5). The agreement between the calculated and measured responses of the focused piezoelectric element testifies to the applicability of the approximate model used for solving the problem. The theoretical and experimental results obtained in this work will be used in designing an antenna array for optoacoustic tomography.

ACKNOWLEDGMENTS

This work was supported by the Russian Foundation for Basic Research, project nos. 01-02-16539 and 02-02-08008.

REFERENCES

1. R. A. Kruger, D. R. Reinecke, and G. A. Kruger, Med. Phys. **26** (9), 1832 (1999).

2. V. G. Andreev, A. A. Karabutov, S. V. Solomatin, *et al.*, Proc. SPIE **3916**, 36 (2000).
3. P. R. Stepanishen, J. Acoust. Soc. Am. **70**, 1176 (1981).
4. V. G. Andreev, A. A. Karabutov, A. E. Ponomaryov, and A. A. Oraevsky, Proc. SPIE **4618**, 153 (2002).
5. J. A. Jensen, J. Acoust. Soc. Am. **105**, 3266 (1999).
6. I. N. Kanevskiĭ, *Focusing of Sonic and Ultrasonic Waves* (Nauka, Moscow, 1977).
7. G. Kino, *Acoustic Waves. Devices, Imaging, and Analog Signal Processing* (Prentice Hall, Englewood Cliffs, N.J., 1987; Mir, Moscow, 1990).
8. A. A. Karabutov, V. V. Kozhushko, I. M. Pelivanov, and G. S. Mityurich, Akust. Zh. **47**, 890 (2001) [Acoust. Phys. **47**, 721 (2001)].
9. L. M. Lyamshev, *Laser Thermooptical Excitation of Sound* (Nauka, Moscow, 1989).
10. V. É. Gusev and A. A. Karabutov, *Laser Photoacoustics* (Nauka, Moscow, 1991).

Translated by A. Khzmalyan

Acoustical Physics, Vol. 49, No. 6, 2003, pp. 688–694. From Akusticheskiĭ Zhurnal, Vol. 49, No. 6, 2003, pp. 806–813.

Time Reversal Self-Adaptive Focusing in Anisotropic Elastic Solid Medium[1]

Bixing Zhang, Chenghao Wang, and Minghui Lu

Institute of Acoustics, The Chinese Academy of Sciences, 100080, Beijijng, People's Republic of China

e-mail: zhbx@mail.ioa.ac.cn

Received July 15, 2002

Abstract—In this paper, the time reversal method in an anisotropic elastic solid is theoretically studied for the first time. The transversely isotropic anisotropic medium (6*mm* crystal structure) is modeled as the anisotropic elastic solid. A unidirectional glass-reinforced epoxy-fiber is chosen as the material of the 6*mm* anisotropic medium. The time reversal acoustic field is numerically investigated by the ray approximation method. The focused acoustic field has different characteristics in different directions. The focused field is also symmetrical about the principal axes. It is found that the width of the principal lobe of the focused acoustic field reaches the minimum in the maximum group velocity direction and reaches the maximum in the minimum group velocity direction. The relation of the time reversal acoustic field to the parameters of the anisotropic medium is also studied in detail. © *2003 MAIK "Nauka/Interperiodica".*

INTRODUCTION

Time Reversal (TR) is a novel method of self-adaptive focusing which does not require a priori knowledge about the properties and structures of the media and the transducer. The sound beams can be bent and the focusing points can be defocused in the inhomogeneous media. This phenomenon can create phase aberrance and image distortion. The TR method can overcome this difficulty and realize the refocusing. This has been proved in theory and experiment [1–13].

However, the focusing beams can be also defocused by the anisotropy. The focusing beam that is determined to be focused on some point will not be focused on the predetermined focusing point because the propagation velocity is related to the propagation direction. Different focusing results will be obtained in different propagation directions. The self-adaptive focusing in the anisotropy is more difficult and more complicated than that in isotropy. Many people have studied the TR self-adaptive focusing in isotropy, but the TR works in anisotropy have not yet been seen.

In this paper, the TR self-adaptive focusing in the anisotropy is investigated. At first, the theoretical formulation about the anisotropy and TR method is reviewed. Then, the numerical simulation results are given and analyzed.

THEORETICAL FORMULATION

A semi-infinite anisotropic medium which is a nonpiezoelectric 6*mm* crystal structure is considered. It is also assumed that the angle between the crystallographic axis of the 6*mm* material and the free surface is equal to φ. Two Cartesian coordinate systems (x, y, z) whose x and y axes are on the free surface and (x', y', z') oriented along the crystallographic axis are adopted, respectively. The y and y' axes are superposed on the free surface. The anisotropic 6*mm* material is in the range $z \geq 0$ and the region $z < 0$ is the vacuum. Only two-dimensional wave propagation is considered in this paper (i.e., the acoustic field is not related to the y coordinate). The transmission transducer array is on the free surface and extends to infinity along the y direction. The center of the transmission transducer array is on the origins of the Cartesian coordinate systems (x, y, z) and (x', y', z'). The configuration of the medium is shown in Fig. 1.

A. Acoustic Wave in Anisotropy

The modulus matrix of the 6*mm* material in $z \geq 0$ is constant in Cartesian coordinate system (x', y', z'):

$$C = \begin{pmatrix} c_{11} & c_{12} & c_{13} & 0 & 0 & 0 \\ c_{12} & c_{11} & c_{13} & 0 & 0 & 0 \\ c_{13} & c_{13} & c_{33} & 0 & 0 & 0 \\ 0 & 0 & 0 & c_{44} & 0 & 0 \\ 0 & 0 & 0 & 0 & c_{44} & 0 \\ 0 & 0 & 0 & 0 & 0 & c_{66} \end{pmatrix}, \quad (1)$$

where $c_{66} = (c_{11} - c_{12})/2$. There are only five elastic moduli in the medium.

It is convenient to use Cartesian coordinate system (x, y, z). The modulus matrix of Eq. (1) should be trans-

[1] This article was submitted by the authors in English.

formed to the system (x, y, z). It can be written in the form

$$C' = \begin{pmatrix} c'_{11} & c'_{12} & c'_{13} & 0 & c'_{15} & 0 \\ c'_{12} & c'_{22} & c'_{23} & 0 & c'_{25} & 0 \\ c'_{13} & c'_{23} & c'_{33} & 0 & c'_{35} & 0 \\ 0 & 0 & 0 & c'_{44} & 0 & c'_{46} \\ c'_{15} & c'_{25} & c'_{35} & 0 & c'_{55} & 0 \\ 0 & 0 & 0 & c'_{46} & 0 & c'_{66} \end{pmatrix}, \quad (2)$$

where

$$c'_{11} = c_{11}\cos^4\varphi + c_{33}\sin^4\varphi + 2(c_{13} + 2c_{44})\sin^2\varphi\cos^2\varphi,$$

$$c'_{12} = c_{12}\cos^2\varphi + c_{13}\sin^2\varphi,$$

$$c'_{13} = c_{13}\cos^4\varphi + c_{13}\sin^4\varphi + (c_{13} + c_{33} - 4c_{44})\sin^2\varphi\cos^2\varphi,$$

$$c'_{15} = [(c_{13} + 2c_{44} - c_{11})\cos^2\varphi + (c_{33} - c_{13} - 2c_{44})\sin^2\varphi]\sin\varphi\cos\varphi, \quad c'_{22} = c_{11},$$

$$c'_{23} = c_{12}\sin^2\varphi + c_{13}\cos^2\varphi,$$

$$c'_{25} = (c_{13} - c_{12})\sin\varphi\cos\varphi,$$

$$c'_{33} = c_{11}\sin^4\varphi + c_{33}\cos^4\varphi + 2(c_{13} + 2c_{44})\sin^2\varphi\cos^2\varphi,$$

$$c'_{35} = [(c_{13} + 2c_{44} - c_{11})\sin^2\varphi + (c_{33} - c_{13} - 2c_{44})\cos^2\varphi]\sin\varphi\cos\varphi,$$

$$c'_{44} = c_{44}\cos^2\varphi + c_{66}\sin^2\varphi,$$

$$c'_{46} = (c_{44} - c_{66})\sin\varphi\cos\varphi,$$

$$c'_{55} = c_{44}\cos^2 2\varphi + (c_{11} + c_{33} - 2c_{13})\sin^2\varphi\cos^2\varphi,$$

$$c'_{66} = c_{44}\sin^2\varphi + c_{66}\cos^2\varphi.$$

Then, the Christoffel equation can be obtained:

$$\Omega = \left|\Gamma_{ij} - \rho V^2\delta_{ij}\right| = \Omega_1\Omega_2 = 0, \quad (3)$$

where

$$\Omega_1 = c'_{44}\cos^2\theta + c'_{66}\sin^2\theta + c'_{46}\sin 2\theta - \rho V^2, \quad (4)$$

$$\Omega_2 = \begin{vmatrix} c'_{55}\cos^2\theta + c'_{11}\sin^2\theta + c'_{15}\sin 2\theta - \rho V^2 & c'_{15}\sin^2\theta + c'_{35}\cos^2\theta + (c'_{13} + c'_{55})\sin\theta\cos\theta \\ c'_{15}\sin^2\theta + c'_{35}\cos^2\theta + (c'_{13} + c'_{55})\sin\theta\cos\theta & c'_{33}\cos^2\theta + c'_{55}\sin^2\theta + c'_{35}\sin 2\theta - \rho V^2 \end{vmatrix}; \quad (5)$$

here θ is the angle between the radius vector of the field point and the z axis. Let $\xi = \theta - \varphi$, the propagation phase velocities of the quasi-P and quasi-S waves be

$$\begin{cases} V_p^2 = \dfrac{1}{2\rho}[c_{11}\sin^2\xi + c_{33}\cos^2\xi + c_{44} + \sqrt{[(c_{11} - c_{44})\sin^2\xi - (c_{33} - c_{44})\cos^2\xi]^2 + (c_{13} + c_{44})^2\sin^2 2\xi}], \\ V_{s1}^2 = \dfrac{1}{2\rho}[c_{11}\sin^2\xi + c_{33}\cos^2\xi + c_{44} - \sqrt{[(c_{11} - c_{44})\sin^2\xi - (c_{33} - c_{44})\cos^2\xi]^2 + (c_{13} + c_{44})^2\sin^2 2\xi}], \end{cases} \quad (6)$$

and the phase velocity of the pure S wave be

$$V_{s2}^2 = (c_{44}\cos^2\xi + c_{66}\sin^2\zeta)/\rho. \quad (7)$$

It is easy to obtain the slowness surfaces, ray surfaces, and normal surfaces of the quasi-P, quasi-S, and pure S waves by Eqs. (4)–(7). It can be seen that the propagation velocities of the quasi-P, quasi-S, and pure S waves are related the orientation of the radius vector relative to the crystallographic axis.

The displacement field in the medium can be obtained by the christoffel equation. It can be written as the following form in the k_x wavenumber domain

$$\begin{pmatrix} U_x \\ U_y \\ U_z \end{pmatrix} = \begin{pmatrix} e^{ik_{z1}z} & e^{ik_{z2}z} & 0 \\ 0 & 0 & e^{ik_{z3}z} \\ a_1 e^{ik_{z1}z} & a_2 e^{ik_{z2}z} & 0 \end{pmatrix} \begin{pmatrix} K_1 \\ K_2 \\ K_3 \end{pmatrix}, \quad (8)$$

where

$$a_i = -\frac{c'_{11}k_x^2 + c'_{55}k_{zi}^2 + 2c'_{15}k_x k_{zi} - \rho\omega^2}{c'_{15}k_x^2 + c'_{35}k_{zi}^2 + (c'_{13} + c'_{55})k_x k_{zi}}, \quad i = 1, 2, \quad (9)$$

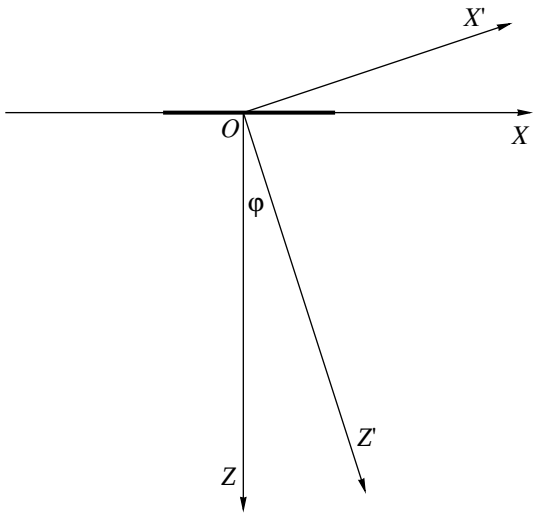

Fig. 1. The geometrical configuration of the medium.

and k_{zi} represent the wavenumbers in the (i = 1, 2, 3) direction of quasi-P, quasi-S, and pure S waves, respectively.

The stress components can be obtained:

$$\begin{pmatrix} \tau_{xz} \\ \tau_{yz} \\ \tau_{zz} \end{pmatrix} = \begin{pmatrix} \Delta_1 & \Delta_2 & 0 \\ 0 & 0 & \Delta_5 \\ \Delta_3 & \Delta_4 & 0 \end{pmatrix} \begin{pmatrix} iK_1 e^{ik_{z1}z} \\ iK_2 e^{ik_{z2}z} \\ iK_3 e^{ik_{z3}z} \end{pmatrix}, \tag{10}$$

where $\Delta_1 = c'_{15}k_x + c'_{35}k_{z1}a_1 + c'_{55}(k_{z1} + k_x a_1)$, $\Delta_2 = c'_{15}k_x + c'_{35}k_{z2}a_2 + c'_{55}(k_{z2} + k_x a_2)$, $\Delta_3 = c'_{13}k_x + c'_{33}k_{z1}a_1 + c'_{35}(k_{z1} + k_x a_1)$, $\Delta_4 = c'_{13}k_x + c'_{33}k_{z1}a_2 + c'_{35}(k_{z1} + k_x a_2)$, $\Delta_5 = c'_{44}k_{z3} + c'_{46}k_{z1}k_x$. So, it is obtained by Eqs. (8) and (10) that

$$\begin{pmatrix} U_x \\ U_y \\ U_z \end{pmatrix} = -i \begin{pmatrix} e^{ik_{z1}z} & e^{ik_{z3}z} & 0 \\ 0 & 0 & e^{ik_{z3}z} \\ a_1 e^{ik_{z1}z} & a_2 e^{ik_{z2}z} & 0 \end{pmatrix} \times \begin{pmatrix} \Delta_4/\Delta & 0 & -\Delta_2/\Delta \\ -\Delta_3/\Delta & 0 & \Delta_1/\Delta \\ 0_3 & 1/\Delta_5 & 0 \end{pmatrix} \begin{pmatrix} \tau_{xz} \\ \tau_{yz} \\ \tau_{zz} \end{pmatrix}_{z=0}, \tag{11}$$

where $\Delta = \Delta_1\Delta_4 - \Delta_2\Delta_3$. If only the stress component $z = 0$ is excited in the range $[-l/2, l/2]$ at the free surface τ_{zz}, i.e.,

$$\tau_{zz}\big|_{z=0} = \int_{-l/2}^{l/2} e^{-ik_x x}dx = \frac{2}{k_x}\sin\frac{k_x l}{2}. \tag{12}$$

Therefore,

$$\begin{cases} U_x(x,z) = \dfrac{1}{2\pi}\displaystyle\int_{-\infty}^{\infty} U_x(k_x,z)e^{ik_x x}dk_x \\ = \displaystyle\int_{-\infty}^{\infty} \frac{i}{\pi k_x \Delta}\sin\frac{k_x l}{2}(\Delta_2 e^{ik_{z1}z} - \Delta_1 e^{ik_{z2}z})e^{ik_x x}dk_x, \\ U_z(x,z) = \dfrac{1}{2\pi}\displaystyle\int_{-\infty}^{\infty} U_z(k_x,z)e^{ik_x x}dk_x \\ = \displaystyle\int_{-\infty}^{\infty} \frac{i}{\pi k_x \Delta}\sin\frac{k_x l}{2}(a_1\Delta_2 e^{ik_{z1}z} - a_2\Delta_1 e^{ik_{z2}z})e^{ik_x x}dk_x. \end{cases} \tag{13}$$

The corresponding displacement components of the compression wave are

$$\begin{cases} U_x^p(x,z) = \displaystyle\int_{-\infty}^{\infty} \frac{i\Delta_2}{\pi k_x \Delta}\sin\frac{k_x l}{2}e^{i(k_x x + k_{z1}z)}dk_x, \\ U_z^p(x,z) = \displaystyle\int_{-\infty}^{\infty} \frac{ia_1\Delta_2}{\pi k_x \Delta}\sin\frac{k_x l}{2}e^{i(k_x x + k_{z1}z)}dk_x. \end{cases} \tag{14}$$

The integrals in Eq. (14) can be given by the ray approach method for the far field:

$$\begin{cases} U_x^p(x,z) = g_x(r,\theta)e^{i(\omega r/V_g + \pi/4)}, \\ U_z^p(x,z) = g_z(r,\theta)e^{i(\omega r/V_g + \pi/4)}, \end{cases} \tag{15}$$

where $g_x(r,\theta) = \sqrt{\dfrac{2}{\pi r f\cos\theta}}\dfrac{\Delta_2}{k_x\Delta}\sin\dfrac{k_x l}{2}$, $g_z(r,\theta) = a_1 g_x(r,\theta)$, $f = \left|\dfrac{d^2 k_{z1}}{dk_x^2}\right|$, $g_x(r,\theta)$ and $g_z(r,\theta)$ are named as the directional factors in x and z axes, and the saddle point condition is determined by

$$\frac{dk_{z1}}{dk_x} = -\tan\theta. \tag{16}$$

It is indicated in Eqs. (15) and (16) that the compression wave propagates as its group velocity V_g instead of the phase velocity V_p. The signal received by the receiver is the information about the group velocity [14].

B. Time Reversal Field

It is assumed that the transducer has M array elements. The acoustic field radiated by the nth array element (n = 1, 2, …, M) can be written in the following form in the time domain

$$U_n(\mathbf{r}_n, t) = g(\mathbf{r}_n)f(t - \tau_n), \tag{17}$$

where $\tau_n = r_n/V_n$ represents the propagation time from the nth element to the receiver point. $g(\mathbf{r}_n)$ is the directional factor in the x or z axis. The total field excited by all elements of the transducer at the receiver point is

$$U(\mathbf{r}, t) = \sum_{n=1}^{M} U_n(\mathbf{r}_n, t) = \sum_{n=1}^{M} g(\mathbf{r}_n) f(t - \tau_n). \quad (18)$$

The acoustic waves excited by different array element arrive at the receiver point at different times. They can't be superposed coherently and formed a widened pulse. If the time signal of the each element is reversed

$$U_n(\mathbf{r}_n, T - t) = g(\mathbf{r}_n) f(T - t - \tau_n), \quad (19)$$

where T is a long time. This reversal signal is normalized with a maximum of 1 and is then retransmitted by the same array element

$$f_n^{TR}(t) = \frac{g(\mathbf{r}_n)}{|g(\mathbf{r}_n)|} f(T - t - \tau_n), \quad (20)$$

so the total field is

$$U^{TR}(\mathbf{r}', t) = \sum_{n=1}^{M} \frac{g(\mathbf{r}_n)}{|g(\mathbf{r}_n)|} g(\mathbf{r}_n') f(T - t + \tau_n' - \tau_n). \quad (21)$$

If $\mathbf{r}' = \mathbf{r}$, it is easy to see that

$$U^{TR}(\mathbf{r}, t) = \left[\sum_{n=1}^{M} |g(\mathbf{r}_n)|\right] f(T - t). \quad (22)$$

This demonstrates that the waves radiated by the different element arrive at the receiver synchronously and coherently superpose. The acoustic field is refocused to the original point.

NUMERICAL SIMULATION

In this section, the numerical results are given. The unidirectional glass-reinforced epoxy fiber is chosen as the material for the anisotropic medium [15]. This material has 6*mm* anisotropy. The elastic constants and the density of this material are given in Table 1. The corresponding values of the kind of isotropic material are also given as the comparison analyses. In the numerical simulation, the signals received are the displacement components of the quasi-P wave in the z axis. The transmission pulse is a sine packet with a periodicity of 10 [7, 8]. The frequency is 1 MHz.

Table 1. The values of elastic constants and the densities of the materials. (The units of elastic constants and densities are 10^{10} N/m^2 and kg/m^3, respectively)

Materials	c_{11}	c_{12}	c_{13}	c_{33}	c_{44}	ρ
Epoxy fiber	2.58	2.42	0.70	6.01	0.49	1900
Isotropy	6.01	5.03	5.03	6.01	0.49	1900

The slowness surfaces, ray surfaces, and normal surfaces of the quasi-P, quasi-S, and pure S waves of this material are shown in Fig. 2. Fig. 2b is important for this paper because the information received concerns the group velocity. It can be seen that the group velocity reaches a maximum of $\sqrt{c_{33}/\rho}$ in the direction $\xi = 0$ (i.e., $\theta = \varphi$) and reaches a minimum of $\sqrt{c_{11}/\rho}$ in the direction $\xi = 90°$ (i.e., $\theta = 90° + \varphi$).

It is assumed that the length of the transducer array is in the range [–0.5, 0.5] in the numerical simulation; i.e., the length of the transducer is $L = 0.1$ m, the transducer is divided into 64 array elements. In the first step of TR, 64 array elements of the transducer transmit a sine packet wave, respectively. Figure 3a displays the displacement components U_z^p of the quasi-P wave received at point R ($x = 0$, $z = 0.4$ m) in the case that φ and θ are both equal to zero. It shows that the quasi-P waves radiated by different elements reach R at different times. In the second step of TR, the above signals are reversed and retransmitted simultaneously by each element. In this time, the displacement z components received at the same point R are shown in Fig. 3b. It is clearly shown that the signals radiated by the different

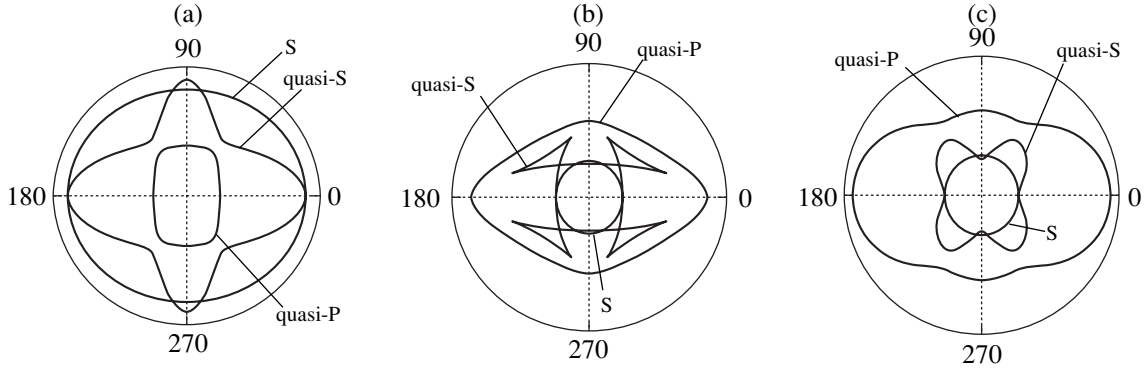

Fig. 2. The slowness surfaces (a), ray surfaces (b), and normal surfaces (c) of the quasi-P, quasi-S, and pure S waves of the unidirectional glass-reinforced epoxy fiber.

Table 2. The values of focusing gain in some focusing points

	φ = 0°			φ = 90°		
(x_0, y_0)	(0, 0.4)	(0.02, 0.4)	(0.04, 0.4)	(0, 0.4)	(0.02, 0.4)	(0.04, 0.4)
Focusing gain	14.4 dB	13.4 dB	12.4 dB	11.0 dB	10.4 dB	10.8 dB

elements arrive synchronously in phase. They are enhanced by each other and refocused. After TR, the signals from the different elements superpose coherently. Figure 3c gives the waveforms in the case that all of the elements transmit the signals synchronously before and after TR. It can be concluded that the coherent peak of the signal after TR is more enhanced. The good effect of self-adaptive focusing is obtained.

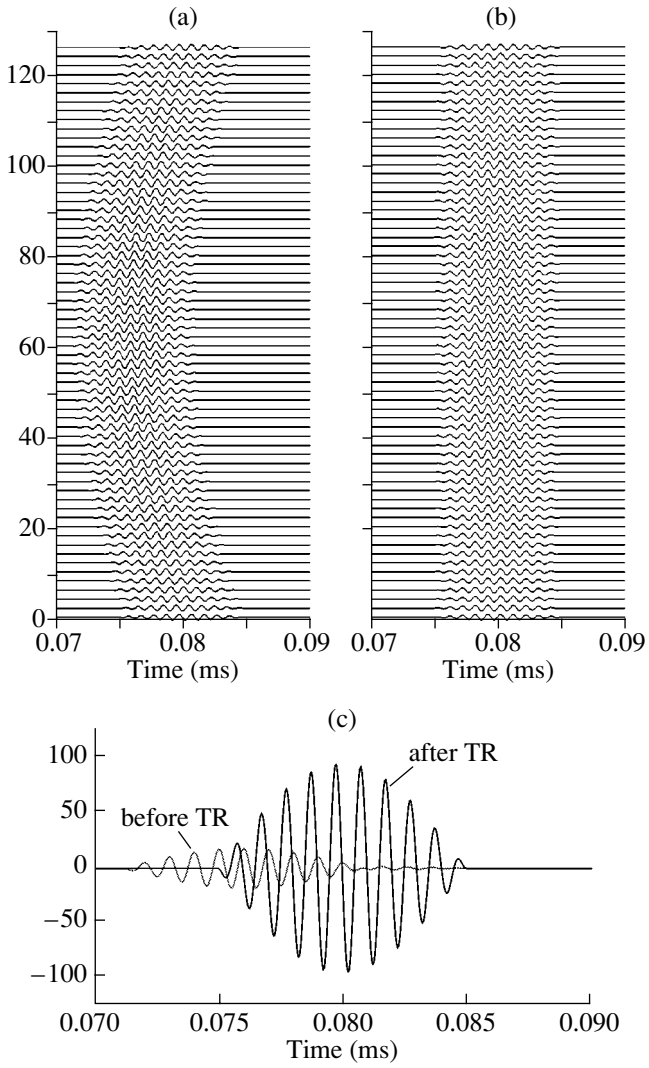

Fig. 3. Displacement components U_z received at point (0, 0.4). (a) Signals received when 64 elements are excited respectively in the first. (b) Signals received when 64 reversed signals are retransmitted respectively after TR. (c) Signals received when 64 elements are excited simultaneously before and after TR.

It is convenient to adopt the focusing gain

$$G = 20\log\frac{\mathrm{Max}[P^{TR}(t)]}{\mathrm{Max}[P(t)]}, \tag{23}$$

where $\mathrm{Max}[P(t)]$ and $\mathrm{Max}[P^{TR}(t)]$ are the maximums of the signals received before and after TR. Let g_M be the maximum of the time series of Eq. (18); the focusing gain can be written in the following form by Eq. (22):

$$G = 20\log\left[\frac{1}{g_M}\sum_{n=1}^{M}|g(\mathbf{r}_n)|\right]. \tag{24}$$

So, for Fig. 3, it is easy to see that the focusing gain is equal to 14.4 dB.

The focusing gain is related to the distance from the focusing point to the transducer. In general, the greater the distance from the focusing point to the transducer, the less the focusing gain. The focusing gain is also related to the orientation of the focusing point. Table 2 gives the values of the focusing gains at some points of the anisotropic medium.

The time reversal acoustic field near the focusing point is investigated. The results are shown in Fig. 4. Curves *1* and *2* represent the field distribution in the cases when the focusing points are (0, 0.4) and (0.04, 0.4), respectively. The focused acoustic field in the corresponding isotropic medium is also depicted in Fig. 4a (curves *3* and *4*).

It is easy to see that the focusing effect in the *x* direction is much better than that in the *z* direction. It is known that the width of the principal lobe of the TR acoustic field along the longitudinal axis in the isotropic medium is longer than that along the transverse axis. In the anisotropic medium, there not only exist the above results, which are the same as those in the isotropic medium, but the width of the main lobe in the transverse (*x*) axis is less than that in the longitudinal (*z*) axis. This is because the propagation velocity is related to the propagation direction. It is not difficult to see that the displacement component U_z reaches the maximum in the *z* direction. This makes the acoustic field more effectively focused along the *x* axis.

Figures 4c and 4d are for φ = 90°. In this case, the group velocity in the *z* axis is equal to $\sqrt{c_{11}/\rho}$, which is less than that in the *x* axis. It can be found from Figs. 4c and 4d that the width of the main lobe of the focused acoustic field is bigger than that in φ = 0. That is, the width of the main lobe of the focused acoustic field is different in different directions in the anisotropic

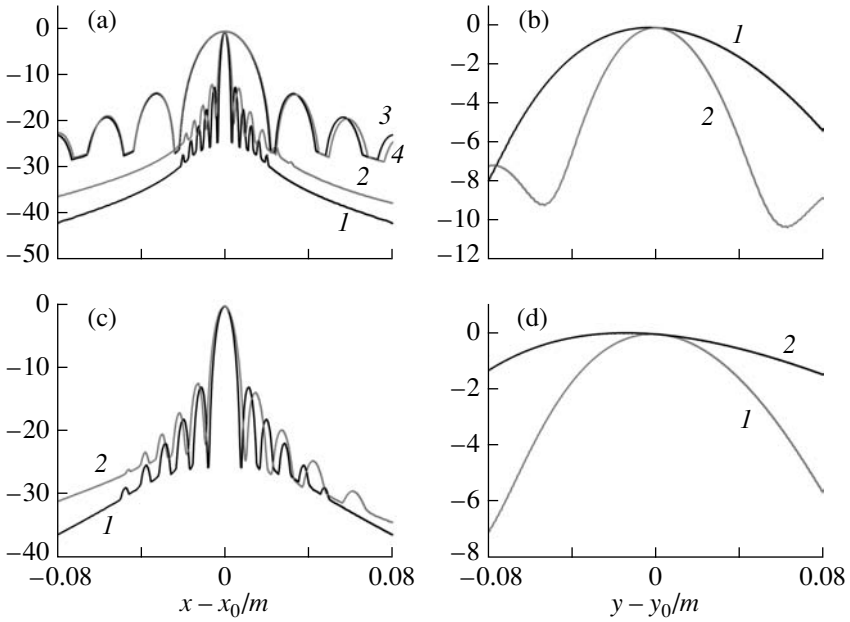

Fig. 4. Time reversal acoustic field along the x [(a) and (c)] and *z* [(b) and (d)] axes. The curves *1* and *2* represent the field distribution in the cases that the focusing points are (0, 0.4) and (0.04, 0.4), respectively. The curves *3* and *4* are similar to that of *1* and *2* in isotropy. φ is equal to zero for (a) and (b) and is 90° for (c) and (d).

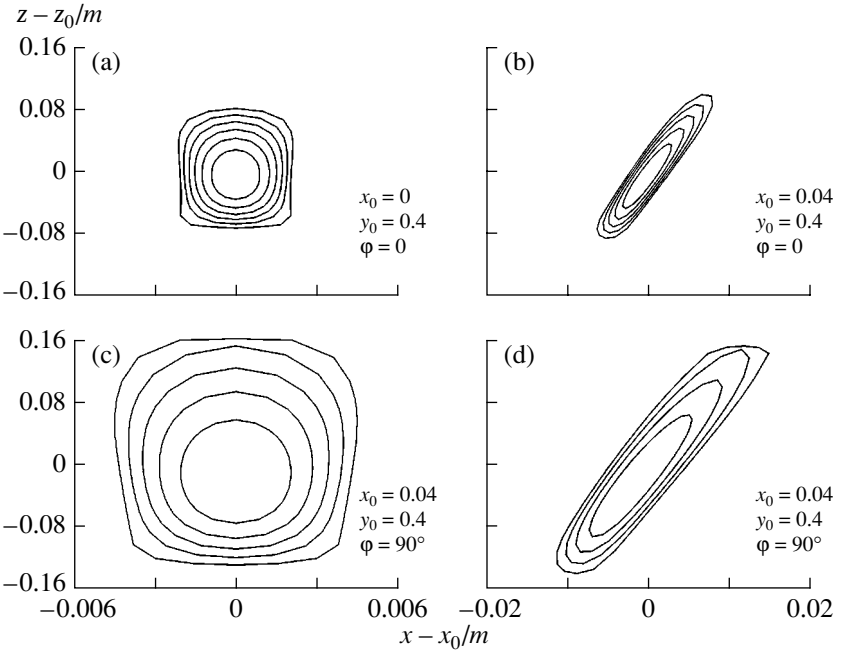

Fig. 5. Isolines of the focused acoustic field.

medium, but the width of the main lobe reaches the minimum in the maximum group velocity direction and reaches the maximum in the minimum group velocity direction.

Curves *1* and *2* in Fig. 4 are for the focusing points (0, 0.4) and (0.04, 0.4), respectively. When the focusing point is not in the *z* axis, the width of the main lobe of the focused field in the *x* axis is bigger than that when the focusing point is in the *z* axis [Figs. 4a, 4c]. However, the width of the main lobe in the *z* axis is bigger than that when the focusing point is in the *z* axis for φ = 90° [Fig. 4d] and less than that when the focusing point is in the *z* axis for φ = 0 [Fig. 4b].

To understand the distribution of the focused acoustic field near the focusing point, the isolines of the focused acoustic field are given in Fig. 5. Figures 5a

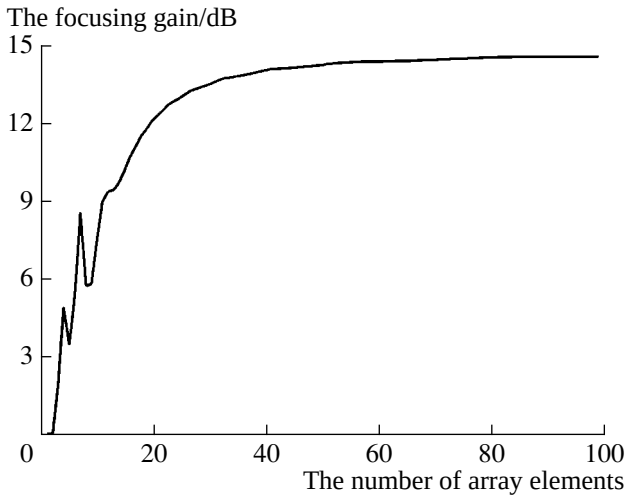

Fig. 6. The relation of the focusing gain to the number of the array elements.

and 5b are for $\varphi = 0$ and 5c and 5d for $\varphi = 90°$, respectively. The focusing points are on the *z* axis in Figs. 5a and 5c and are not on the *z* axis in Figs. 5b and 5d. The closed curves in Fig. 5 from the inner to external circles represent the fart that the focusing gains are equal to –1dB, –2dB, –3dB, –4dB, –5dB, and –6dB, respectively. It is easy to see that the isolines are concentrated in $\varphi = 0$; i.e., the focusing width is minimum in $\varphi = 0$ (i.e., the maximum group velocity direction). This is consistent with the results in Fig. 4. It has been noted that the difference of the distribution range of the isolines between the *x* and *y* axes is more significant. The range of isolines in the *z* axis is about 20 times greater than that in the *x* direction. These characteristics can also be seen in Fig. 4. It can be seen from Figs. 5b and 5d that the isolines are not symmetric about the *x* or *z* axes when the focusing point is not on the *z* axis. One reason is that the radius vector from the transducer to the focusing point is not perpendicular to the transducer array. A similar result can be obtained in the isotropic medium.

Figure 6 displays the relationship of the focusing gain to the number of array elements, which indicates that the focusing gain increases as the number of array elements increase when the number is less than 40. If the number is greater than 40, the focusing gain tends toward a given value as the number increases. Thus, the saturated phenomena could appear in the focusing gain when the number of transducer array elements increases because the transmission pulse has a definite width. These phenomena should appear in the isotropic medium [8].

CONCLUSIONS

Unidirectional glass-reinforced epoxy fiber was chosen as the material for the 6*mm* anisotropic medium. The TR method in this material was theoretically studied for the first time in this paper. The relationship of the TR acoustic field to the parameters of anisotropic medium was analyzed in detail. It was found that the width of the main principal lobe of the focused acoustic field reaches the minimum in the maximum group velocity direction and reaches the maximum in the minimum group velocity direction.

This study on the TR method is very elementary. There remain many problems to be addressed in our future studies. TR self-adaptive focusing in an anisotropic medium is more complicated and more interesting. This paper lays the foundation for further study.

ACKNOWLEDGMENTS

This work was supported by the National Natural Science Foundation of China (10134020).

REFERENCES

1. M. Fink, IEEE Trans. Ultrason. Ferroelectr. Freq. Control **39** (5), 555 (1992).
2. F. Wu, J.-L. Thomas, and M. Fink, IEEE Trans. Ultrason. Ferroelectr. Freq. Control **39** (5), 567 (1992).
3. R. K. Ing and M. Fink, IEEE Trans. Ultrason. Ferroelectr. Freq. Control **45** (4), 1032 (1998).
4. N. Chakroun, M. Fink, and F. Wu, IEEE Trans. Ultrason. Ferroelectr. Freq. Control **42**, 1087 (1995).
5. W. A. Kuperman, W. S. Hodgkiss, and Hee Chen Song, J. Acoust. Soc. Am. **103**, 25 (1998).
6. Hee Chen Song, W. A. Kuperman, and W. S. Hodgkiss, J. Acoust. Soc. Am. **103**, 3234 (1998).
7. Wei Wei and Wang Chenghao, Chin. J. Acoust. **19** (1), 83 (2000).
8. Wei Wei, Liu Chen, and Wang Chenghao, Chin. J. Acoust. **19** (1), 89 (2000).
9. Bixing Zhang, Chenghao Wang, and Minghui Lu, in *Proceedings of 2000 International IEEE Ultrasonics Symposium, San Juan, Puerto Rico, 2000* (IEEE, Piscataway, N.J., 2000), p. 839.
10. L. M. Lyamshev and P. V. Sakov, Akust. Zh. **34**, 127 (1988) [Sov. Phys. Acoust. **34**, 68 (1988)].
11. A. P. Brysev, F. V. Bunkin, L. M. Krutyanskiĭ, *et al.*, Akust. Zh. **43**, 244 (1997) [Acoust. Phys. **43**, 207 (1997)].
12. A. P. Brysev and L. M. Krutyanskiĭ, Akust. Zh. **46**, 447 (2000) [Acoust. Phys. **46**, 382 (2000)].
13. A. P. Brysev, F. V. Bunkin, M. F. Hamilton, *et al.*, Akust. Zh. **49**, 24 (2003) [Acoust. Phys. **49**, 19 (2003)].
14. Wang Chenghao and Chen Dongpei, Chin. J. Acoust. **4** (4), 298 (1985).
15. E. Zimmer and J. R. Cost, J. Acoust. Soc. Am. **47**, 795 (1970).

Acoustical Physics, Vol. 49, No. 6, 2003, pp. 695–699. Translated from Akusticheskiĭ Zhurnal, Vol. 49, No. 6, 2003, pp. 814–819.

Phase Conjugation for Suppressing the Effect of Multipath Propagation on the Result of Active Location

V. A. Zverev

Institute of Applied Physics, Russian Academy of Sciences,
ul. Ul'yanova 46, Nizhni Novgorod, 603950 Russia
e-mail: zverev@hydro.appl.sci-nnov.ru

Received July 17, 2002

Abstract—For an ideal waveguide used as an example, the possibility of suppressing the effect of multipath propagation on the target detection by applying wave conjugation is demonstrated. © *2003 MAIK "Nauka/Interperiodica".*

Under the conditions of multipath signal propagation, the detection of a target by acoustic location is difficult. Instead of the expected target response, a continuous buzz arrives at the receiver, and one can hardly separate the reflection from the object of interest against the background of random variations in the signal level. Formally, multipath propagation in the form of repetitions of the signal and noise does not change the signal-to-noise ratio. Therefore, one may expect that a multipath medium should not noticeably affect the signal detection. Possibly, this is true for a number of important situations. However, there is a wide class of signals for which their shapes, rather than the signal-to-noise ratio, are critical. The signals used in active location belong to this class. Active location is efficient at rather low ratios of the desired signal to the interfering noise if the signal and noise levels are understood as their energies averaged over the same relatively long time interval. If a narrow pulse reflected from the located object is much higher in amplitude than the standard deviation σ of the noise (i.e., the square root of the variance minus the mean value), the pulse is quite pronounced on the noise background in spite of the fact that the time-average energy of the short pulse is much smaller than the time-average energy of the continuous interfering noise.

If pulsed signals are used in the location procedure, the signal detection is based on the prominence of the pulse against the noise background. However, this main difference between signal and noise (the pulse prominence) is lost in the case of pulse propagation in a multipath medium. As an illustration, let us consider the signal propagation in an ideal waveguide. Let the waveguide have reflecting walls, so that a single narrow probing pulse takes the form shown in Fig. 1.

Let us imagine that, in a free medium, the result of location appears as shown in Figs. 2a and 2b. The noise background can be produced by both the additive ambient noise and the reflections. We consider the latter situation. In this case, we deal with the so-called reverberation noise that is characteristic of, e.g., a shallow sea [1]. In the case illustrated in Fig. 2, the pulse reflected from the object to be located is quite pronounced. The ratio of the mean signal level to the mean noise level is equal to –4 dB when averaging is performed over the length of the realization shown in Fig. 2a. At the same time, the maximum signal amplitude shown in the same figure is almost 19 dB higher than σ, which makes the pulse clearly visible. Figure 3 shows the same signals in the case of multipath propagation. The probing signal now has the form similar to that shown in Fig. 1. Each individual pulse of those shown in Fig. 2a is repeated by the extended probing signal. As seen from Fig. 3, the excess of the target-reflected signal shown in Fig. 2a proves to be insufficient in a multipath medium. For the sake of comparison, two cases are illustrated by Fig. 3. In one of these cases, the desired signal is present, and in the other case, it is absent. According to Fig. 3, these cases are nearly indistinguishable, and one cannot decide where the desired signal is actually present. Figure 4 illustrates the same situation as in Fig. 3, but with the reverberation level shown in Fig. 2b, which is by 20 dB lower. In Fig. 4, the signal-to-noise ratio (expressed in energy levels) is now positive and equal to almost 16 dB. Figure 4 shows that the signal manifests itself in its magnitude but not in its shape, which has become noiselike.

The purpose of this paper is to show that, in multipath signal propagation, the phase conjugation can be helpful in detecting the object to be located.

Recently, much attention has been paid to using phase conjugation in acoustics [2]. It was found that acoustics is more suitable for applying the phase conjugation technique than optics [2]. To create a phase-conjugate wave in acoustics, it is not necessary to use dedicated media or a nonlinear transformation of complex amplitudes of the signal to their complex-conjugate values. To implement the phase conjugation in acous-

1063-7710/03/4906-0695$24.00

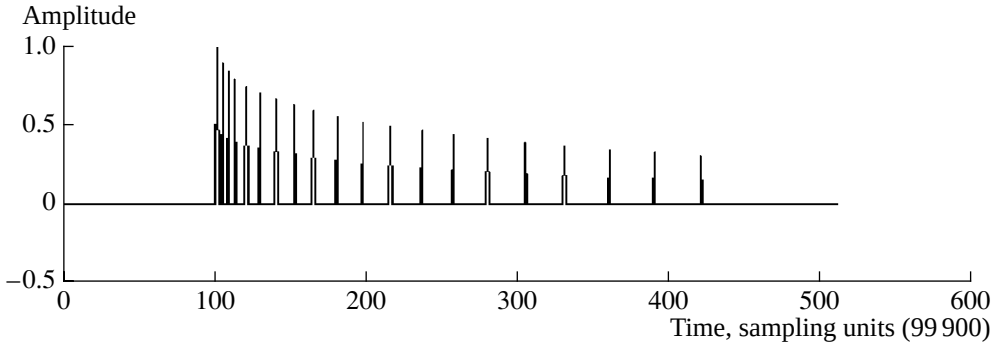

Fig. 1. Sequence of the pulses reflected from the walls of an ideal waveguide, as used in the calculations.

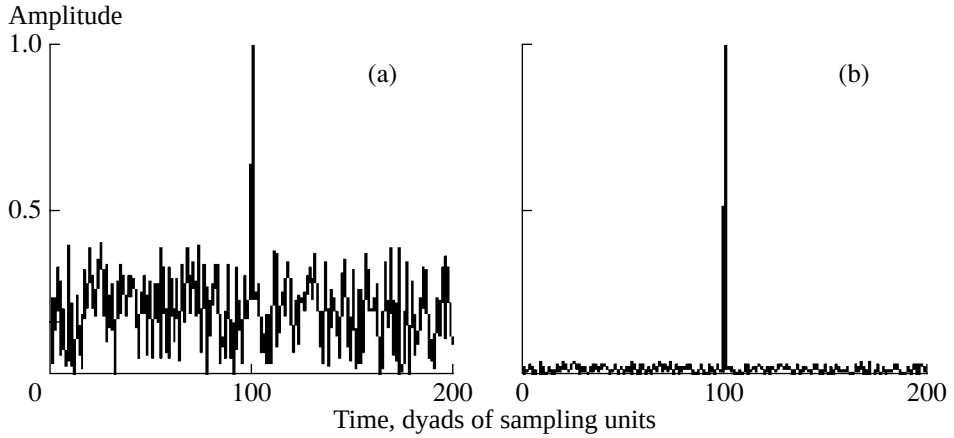

Fig. 2. Results of location in the absence of reflections from the waveguide walls for two reverberation levels: (a) one level is 20 dB higher than (b) the other.

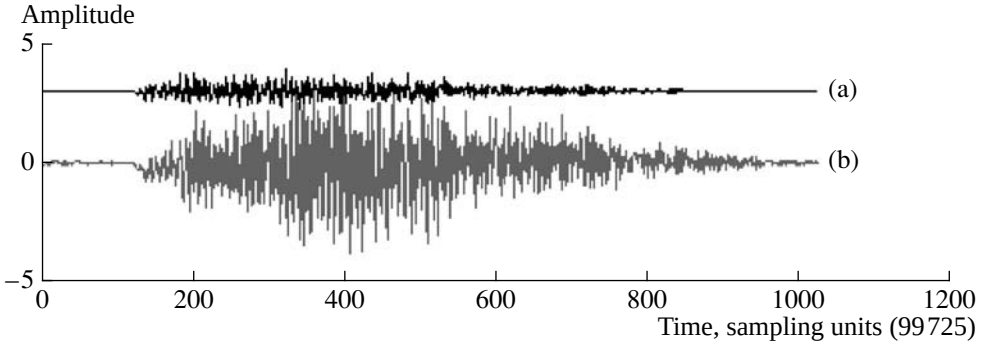

Fig. 3. Results of location in the waveguide (a) in the absence of the object that is clearly visible in Fig. 2 and (b) in the presence of the object. The reverberation level is the same as in Fig. 2a.

tics, it is sufficient to receive the ordinary real-valued sound field (a sequence of short probing pulses, for instance), to save it, and then to send it back to the same medium by applying, first, a time reversal to the signal. As a result of the inverse wave propagation, the same field as was sent initially is formed in the medium. This is true for propagation in a complex medium containing scatterers that can multiply scatter the sound field, in a multipath medium, or in other inhomogeneous media [2]. The aforementioned opportunity was practically implemented in a shallow-sea wave propagation [3–5].

Let us apply the phase conjugation method to reconstruct the shape of a pulsed signal propagating through a multipath medium. To analyze the problem, it is convenient to consider the following simplest example. A sound source that can transmit broadband probing signals for active location is placed at a point A in a multipath medium. The same acoustic system operating as

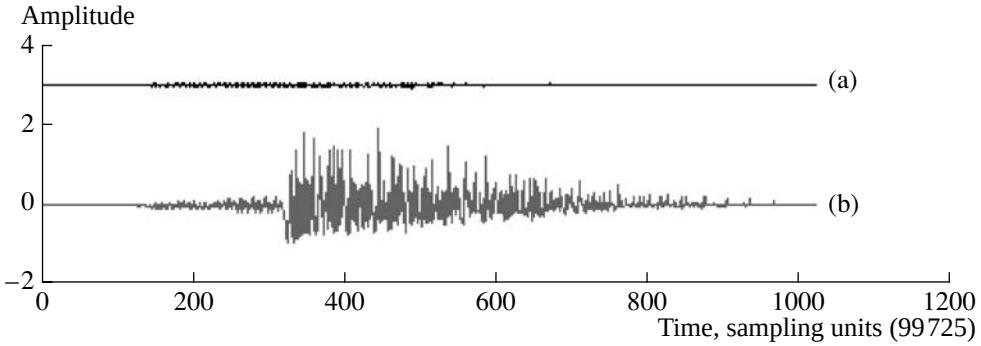

Fig. 4. Results of location in the waveguide (a) in the absence of the object and (b) in the presence of the object. The reverberation level is the same as in Fig. 2b.

the sound source is able to receive the echo signals arriving at point *A* as well. In a multipath medium, such a system can produce the signal patterns shown in Figs. 3 and 4. To noticeably change these patterns, we proceed as follows. Let us emit a short pulsed signal at some point *B* of the medium where the target of interest may appear. This signal will be received at point *A*. The received signal will be distorted by multipath propagation and will have the shape shown in Fig. 1. We denote this signal as *C*. If the signal *C* is inverted in time and then transmitted into the medium again, precisely the same pulse as the initially emitted one will be observed at point *B* [2]. The use of this pulse in the location procedure is advantageous, because the pulse is not distorted by the multipath propagation. Figure 5 shows the wave field produced in the medium as a result of the phase conjugation. This field interacts with the objects of location in the same way as in a free space. The waveguide does not participate in the process at its first stage, which is very important. At the first stage, the phase-conjugation-produced short pulse is multiplied by the reflection pattern shown in Fig. 2. (Further, we use only the pattern shown in Fig. 2a.) According to Fig. 5, the medium is nonuniformly insonified in the phase conjugation process. The signal is focused to yield the maximum magnitude at the distance corresponding to the point from which the short pulse was emitted.

If, at point *B*, the object of location is present at the instant of the pulse's arrival, the reflected signal will have the shape of signal *C*. If no object occurs at point *B*, no response will be obtained. To detect the object at a certain place and at a certain time, one has to distinguish signal *C* from all other signals. To that end, the method of matched filtration can be applied. A filter must be designed whose frequency response is complex-conjugate with signal *C*. Then, at the filter output, at some instant, a narrow pulse is obtained whose duration is inversely proportional to the pulse frequency band [6] and amplitude is determined by the entire signal energy. The short pulse of high amplitude, which occurs at the output of the filter matched with signal *C*, can replace the pulse that serves as an indicator of the object of interest in Fig. 2.

Figure 6 shows the time response of the filter matched with signal *C* for two cases: when the object is present at point *B* and when it is absent.

The calculations were performed using the following formulas. First, the signal propagation through the waveguide was modeled. The pulse was described by the rectangular function $E(t)$ with an amplitude equal to unity at one of the sampling intervals, at $t = 0$. This pulse was repeated in the waveguide at certain intervals determined by distance R between the transmission and reception points (A and B) and by waveguide thickness h. The distance at which the nth pulse reflected by the waveguide walls is observed is expressed as

$$r_n = \sqrt{R^2 + n^2h^2}. \quad (1)$$

The sequence of the pulses shown in Fig. 1 was first formed in the spectral domain. The spectrum of this sequence is determined by the expression

$$G(u) = \sum_n g(u)\exp(-\beta n)\exp\left(i\frac{2\pi}{L}ur_n\right). \quad (2)$$

Here, u is the spatial frequency, β is the attenuation coefficient at the pulse reflections from the waveguide walls, $g(u)$ is the spectrum of a single pulse $E(t)$ that occupies one sampling interval in space, and $L = 512$ is the size of the entire data array. The desired pulse sequence shown in Fig. 1 is determined as the Fourier spectrum of $G(u)$. The values of the parameters were chosen so as to model the propagation of a sound pulse in a shallow sea: $R = 5$ and $h = 0.02$. The interval of sampling in distance was so small that the values of r_n could be described by integer numbers: this interval was by a factor of 20000 smaller than the unit of length. In the figures, the distance is given in units of sampling in length or time minus the number of intervals indicated in the figures. The quantity n was limited by as lit-

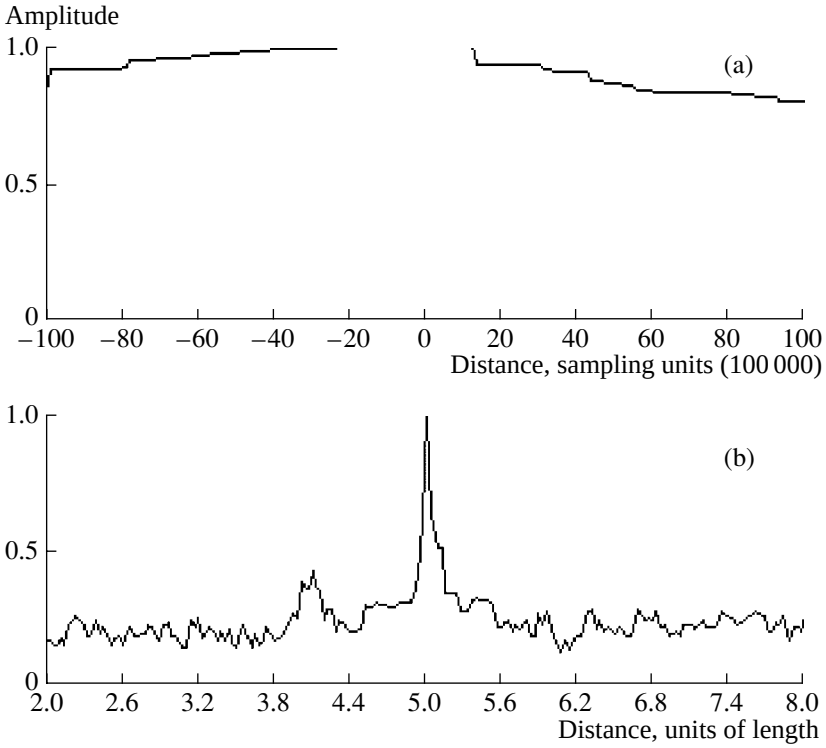

Fig. 5. Distribution of the sound field in the medium as a result of the emission of the signal with phase conjugation.

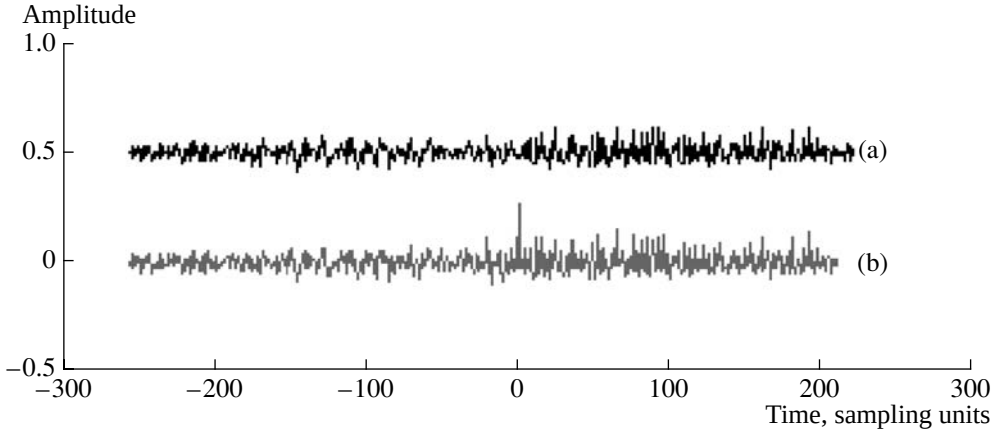

Fig. 6. Results of location with the phase conjugation (a) in the absence and (b) in the presence of the object. The reverberation level is the same as in Fig. 2a.

tle as 20 values. An increase in n to 50 or 100 values has little effect on the results.

The reverberation shown in Fig. 2 was modeled by a set of random numbers $Q(m)$, whose values were uniformly distributed in the interval from 0 to 0.4 (Fig. 2a) or from 0 to 0.04 (Fig. 2b). The reverberation was uniformly distributed over the path with a discreteness of two sampling intervals in distance (0.0001 units of distance), within 200 values of length m with the center at $R = 5$. The object of location positioned at the center of Figs. 2a and 2b had a unit amplitude.

The spectra shown in Figs. 3 and 4 were calculated by the formula

$$U(u) = \sum_n \sum_m Q(m)G(u) \times \exp(-\beta n)\exp\left(i\frac{2\pi}{L}ur_n(m)\right). \quad (3)$$

Here, $Q(m)$ is the signal shown in Fig. 2. For Fig. 3a, this signal is the one shown in Fig. 2a without the central peak. For Fig. 3b, it is the whole signal shown in

Fig. 2a. The quantity $G(u)$ is given by Eq. (2). Function $r_n(m)$ was calculated from Eq. (1) into which the following function $R(m)$ was substituted:

$$R(m) = 5 - 0.0001(m - 100). \quad (4)$$

Figure 4 was obtained in the same manner as Fig. 3, but with the function $Q(m)$ shown in Fig. 2b.

Figure 5 shows the field generated in the medium when the time-inverted signal C is emitted from point A. The field of the signal was determined from its spectrum. The result of the phase conjugation in the medium is obtained by the inverse Fourier transformation of the function

$$K(u) = G(u)\overline{GR(u)}, \quad (5)$$

where function $G(u)$ is determined by Eq. (2). Function $GR(u)$ is also determined by Eq. (2) for the corresponding value of R, and the overbar means complex conjugation. Figure 5a shows the focusing as a function of the ordinal number of the sampling interval on an enlarged scale. As one can see, the focusing weakly affects the calculation results for the distances used in modeling.

The signals shown in Fig. 6 are obtained by using the formula

$$M(u) = \sum_n \sum_m Q(m)g(u) \times \exp(-\beta n)\exp\left(i\frac{2\pi}{L}ur_n(m)\right). \quad (6)$$

This formula differs from Eq. (3) in that it uses a different spectrum of the probing pulse: function $g(u)$ is used instead of $G(u)$. The time response of the matched filter is obtained by the inverse Fourier transformation of function $V(u)$, which is determined as

$$V(u) = G(u)\overline{M(u)}. \quad (7)$$

The efficiency of the proposed technique can be estimated by comparing Figs. 3 and 6. Both figures show the result of location. However, in Fig. 3, the effect of multipath propagation is not suppressed, while in Fig. 6 it is suppressed by the phase conjugation procedure.

The method described above cannot change the ratio of the intensity of the reflected signal to that of reverberation. The only advantage of the method is that it eliminates the effect of multipath propagation on the shape of the received signal. However, this advantage is quite significant. The ratio of the maximal signal amplitude to σ in Fig. 6 differs from that in Fig. 2a by less than 1 dB. This difference and the difference in the signal shapes shown in Figs. 6b and 2a can be explained by the change in the distributions. In Fig. 2a, a uniform distribution is specified within the considered interval of values, while in Fig. 6 the distribution is closer to the normal one.

With the use of the proposed method, an object can be successfully detected at a single point. There can be more than one of such points if the shape of signal C remains unchanged at the other point of interest. At all points where the shape of signal C is the same, the aforementioned procedure provides detection of the object. If the waveguide is cylindrically symmetric and sufficiently homogeneous, the point at which the object produces a narrow response at the matched filter output is transformed to a locus in the form of a circle.

Theoretically, the proposed method of eliminating the reverberation distortions can be implemented by calculating the expected shape of signal C on the basis of the data on the properties of the medium. However, the latter statement is doubtful. The point is that one does not know exactly what should be known about the medium and to what accuracy. That is why the approach based on calculating the shape of the signal C should be rejected without discussion. Then, the remaining way is to directly measure the response of the medium, as described above. In this case, one significant constraint holds: the medium to be studied must be sufficiently stable.

Here, we considered one of the possible types of reverberation, namely, multipath propagation. Other types of reverberation are also possible, for example, the signal reflections from a rough bottom and a rough surface [7]. For these types of reverberation, the proposed method seems to be useless.

ACKNOWLEDGMENTS

I am grateful to V.I. Talanov, A.G. Luchinin, and B.M. Salin for their interest in this work and useful remarks. I am also grateful to the reviewer of this paper for useful recommendations. This work was supported by the Russian Foundation for Basic Research, project nos. 00-15-96741 and 02-02-17056.

REFERENCES

1. B. G. Katsnel'son and V. G. Petnikov, *Acoustics of a Shallow Sea* (Nauka, Moscow, 1997).
2. M. Fink, D. Cassereau, A. Derode, *et al.*, Rep. Prog. Phys. **63**, 1933 (2000).
3. W. A. Kuperman, W. S. Hodgkiss, H. C. Song, *et al.*, J. Acoust. Soc. Am. **103**, 25 (1998).
4. W. Hodgkiss, H. Song, W. Kuperman, *et al.*, J. Acoust. Soc. Am. **105**, 1597 (1999).
5. H. Song, W. Kuperman, W. Hodgkiss, *et al.*, J. Acoust. Soc. Am. **105**, 3176 (1999).
6. L. A. Vaĭnshteĭn and V. L. Zubakov, *Signal Detection against the Background of Random Noise* (Sovetskoe Radio, Moscow, 1960).
7. V. A. Zverev and P. I. Korotin, Akust. Zh. **49**, 75 (2003) [Acoust. Phys. **49**, 62 (2003)].

Translated by E. Kopyl

Acoustical Physics, Vol. 49, No. 6, 2003, pp. 700–703. Translated from Akusticheskiĭ Zhurnal, Vol. 49, No. 6, 2003, pp. 820–823.

Sound Diffraction at Sierpinski Carpet

L. M. Lyamshev† and I. A. Urusovskiĭ

Andreev Acoustics Institute, Russian Academy of Sciences, ul. Shvernika 4, Moscow, 117036 Russia

e-mail: mironov@akin.ru

Received January 22, 2003

Abstract—The sound field scattered by a fractal surface in the form of a Sierpinski carpet is calculated in the framework of the perturbation method. The Sierpinski carpet has an alternating acoustic admittance preset at its squares, which sequentially scale down. It is demonstrated that such a Sierpinski carpet scatters sound almost uniformly in all directions. © *2003 MAIK "Nauka/Interperiodica".*

The problem of obtaining sound scattering from room walls with a spatial distribution of the scattered intensity close to uniform is of interest for architectural acoustics [1–3]. Such a situation is possible when the scattering surface is inhomogeneous due to its roughness or the inhomogeneity of its acoustic properties. Fractal surfaces have such properties. Sound scattering by a fractal surface was examined using the Kirchhoff method in [4]. In this connection, it is also appropriate to mention the papers on the sound scattering at fractal structures in the ocean [5, 6].

The spatial spectrum of the field scattered by an inhomogeneous surface can be sufficiently uniform if two conditions are satisfied.

First, inhomogeneities of opposite signs, for example, inhomogeneities of acoustic admittance of opposite signs, are presented on the surface in approximately equal quantities. In this case, the contributions of inhomogeneities of opposite signs into the mirror reflection almost compensate each other.

Second, the scales of all wave dimensions of the sound frequency band of interest must be presented in the spatial spectrum of inhomogeneities, starting from dimensions on the order of wavelength and down to small wave dimensions.

The Sierpinski carpet will have the aforementioned properties if its inhomogeneities of sequentially decreasing scale have alternating signs.

Geometrically, the construction of the Sierpinski carpet is as follows. An initial square is divided by two lines parallel to one pair of its sides and by two lines perpendicular to them into nine equal squares of smaller size. The central square is separated from them. Another eight squares are divided in the same way into nine squares of smaller scale, and the central squares are separated from them, and so on. A fractal structure is formed in the limit. In this structure, each separated square of a given linear dimension is surrounded by eight separate squares of a thrice smaller linear dimension. In reality, the subdivision of squares ends at a certain step N.

The acoustic Sierpinski carpet is a set of inhomogeneities in the form of squares with sequentially decreasing side lengths H_n, $n = 0, 1, 2, \ldots$, where $H_n = 3^{-n}H$ and H is the side of the central square. The number of squares of the nth scale is equal to 8^n, and the total area of the squares of this scale is $8^n H_n^2 = H^2(8/9)^n$. From this formula, it follows that the total area of the squares of the nth scale slowly decreases with the growth of n and is equal to eight-ninths of the area of the preceding scale. Hence, the first condition of uniformity of the spatial spectrum of scattering can be considered as satisfied. The slowness of changes in the total area of the squares of subsequent scales in the presence of scales of various wave dimensions guarantees that the second uniformity condition of the spatial spectrum of scattering is also satisfied. Let us prove this statement by the example of sound scattering at the Sierpinski carpet, for the squares of which we preset an acoustic admittance in the form $(-1)^n\eta_0$; i.e., the admittance of the squares alternates as the square size decreases.

Consider the diffraction of a plane wave of sound pressure $p_i = \exp[i(k_x^0 x + k_y^0 y - k_z^0 z)]$, where $k_z^0 = \sqrt{k^2 - k_x^{0^2} - k_y^{0^2}}$, in the plane $z = 0$ characterized by the acoustic admittance $\eta(x, y)$. We restrict our consideration to the case $|\eta| \ll 1$, where it is possible to apply the perturbation method by assuming that the total field is expressed as

$$p(x, y, z) = 2\cos(k_z^0 z) + p_1(x, y, z), \quad |p_1| \ll 1.$$

In this case, the boundary condition

$$\partial p/\partial z = -ik\eta p \text{ at } z = 0$$

can be reduced in the first approximation to the form

$$\partial p_1/\partial z = -2ik\eta \exp[i(k_x^0 x + k_y^0 y)] \text{ at } z = 0.$$

† Deceased.

Substituting here the expansions of p and η in terms of the spatial spectra

$$p_1(x, y, z) = \int_{-\infty}^{\infty}\int_{-\infty}^{\infty} A(k_x, k_y) \times \exp[i(k_x x + k_y y + k_z z)]dk_x dk_y, \quad (1)$$

$$\eta(x, y) = \int_{-\infty}^{\infty}\int_{-\infty}^{\infty} B(\kappa_x, \kappa_y) \times \exp[i(\kappa_x x + \kappa_y y + \kappa_z z)]d\kappa_x d\kappa_y, \quad (2)$$

where $k_z = \sqrt{k^2 - k_x^2 - k_y^2}$ and $k_z = \sqrt{\kappa^2 - \kappa_x^2 - \kappa_y^2}$, and taking into account the fact that

$$\eta(x, y)\exp[i(k_x^0 x + k_y^0 y)] = \int_{-\infty}^{\infty}\int_{-\infty}^{\infty} B(\kappa_x - k_x^0, \kappa_y - k_y^0)\exp[i(\kappa_y x + \kappa_y y)]d\kappa_x d\kappa_y,$$

we obtain $A(k_x, k_y) = -\dfrac{2k}{k_z} B(k_x - k_x^0, k_y - k_y^0)$.

In spherical coordinates, the projections of the wave vector in a scattered wave and the radius vector of the observation point take the form

$$k_z = k\cos\chi, \quad k_x = k\sin\chi\cos\psi,$$
$$k_y = k\sin\chi\sin\psi,$$
$$k_z^0 = k\cos\theta_0, \quad k_x^0 = k\sin\theta_0\cos\varphi_0,$$
$$k_y^0 = k\sin\theta_0\sin\varphi_0,$$
$$z = R\cos\theta, \quad x = R\sin\theta\cos\varphi,$$
$$y = R\sin\theta\sin\varphi, \quad R^2 = x^2 + y^2 + z^2.$$

Proceeding from here and taking into account the expressions $dk_x dk_y = |k^2\cos\chi\sin\chi|d\chi d\psi$ and $k_x x + k_y y + k_z z = kR[\sin\chi\sin\theta\cos(\psi - \varphi) + \cos\chi\cos\theta]$, we represent Eq. (1) in the form

$$p_1(x, y, z) = -2k^2 \int_{-(\pi/2) - i\infty}^{(\pi/2) + i\infty} \exp[ikR\cos(\chi - \theta)]|\sin\chi|d\chi \times \int_{-(\pi/2) - i\infty}^{(\pi/2) + i\infty} W(\chi, \psi, \theta_0, \varphi_0) \times \exp\{ikR\sin\chi\sin\theta[\cos(\psi - \varphi) - 1]\}d\psi, \quad (3)$$

where

$$W(\chi, \psi, \theta_0, \varphi_0) = B[k(\sin\chi\cos\psi - \sin\theta_0\cos\varphi_0), k(\sin\chi\sin\psi - \sin\theta_0\sin\varphi_0)].$$

When $kR \gg 1$, it is convenient to use the saddle-point technique to estimate the double integral in Eq. (3) [7]. In the vicinity of the saddle point $\chi = \theta$, $\psi = \varphi$, it is possible to take $\cos(\chi - \theta) \cong 1 - (1/2)(\chi - \theta)^2$ and $\cos(\psi - \varphi) \cong 1 - (1/2)(\psi - \varphi)^2$. Taking into account that $\int_{-\infty}^{\infty}\exp(-i\rho s^2)\,ds = \sqrt{\dfrac{\pi}{i\rho}}$, we determine after integration

$$p_1(\theta, \varphi) = 4\pi i\frac{\exp(ikR)}{R} \times kB[k(\sin\theta\cos\varphi - \sin\theta_0\cos\varphi_0), k(\sin\theta\sin\varphi - \sin\theta_0\sin\varphi_0)].$$

Thus, we have

$$\frac{p_1(\theta, \varphi)}{p_1(\theta_0, \varphi_0)} = \frac{B[k(\sin\theta\cos\varphi - \sin\theta_0\cos\varphi_0), k(\sin\theta\sin\varphi - \sin\theta_0\sin\varphi_0)]}{B(0, 0)}.$$

Coordinates $\{x_n, y_n\}$ of the squares of the nth scale, which surround the square of the $(n-1)$th scale with the coordinates $\{x_{n-1}, y_{n-1}\}$, are connected by the expressions $x_n = x_{n-1} + \nu H_{\nu-1}$ and $y_n = y_{n-1} + \mu H_{\nu-1}$, where ν and μ are the integer numbers acquiring the values $\{-1, 0, 1\}$ so as not to be simultaneously equal to zero. In total, there are eight squares of the nth scale that surround the square of the $(n-1)$th scale for corresponding combinations of ν and μ satisfying the condition $|\nu| + |\mu| \neq 0$. We have

$$\frac{1}{4}\int_{x_n - L_n}^{x_n + L_n} dx \int_{y_n - L_n}^{y_n + L_n} \exp[-i(\kappa_x x + \kappa_y y + \kappa_z z)]dy = S_n\exp\lfloor -i(\kappa_x x_n + \kappa_y y_n + \kappa_z z_n)\rfloor,$$

where $L_n = H_n/2$ and

$$S_n = \frac{\sin(\kappa_x L_n)}{\kappa_x}\frac{\sin(\kappa_y L_n)}{\kappa_y}.$$

One can see that the sum of eight such quantities for eight squares with side H_n, which surround the large square with the center at the point (x_{n-1}, x_{n-1}), is equal to

$$S_n\sum_{\mu}\sum_{\nu}\exp[-i(\kappa_x x_n + \kappa_y y_n + \kappa_z z_n)] = C_n,$$

where

$$C_n = C(\kappa_x H_{n-1}, \kappa_y H_{n-1}),$$
$$C(\alpha, \beta) = 2[\cos\alpha + \cos\beta + \cos(\alpha + \beta) + \cos(\alpha - \beta)].$$

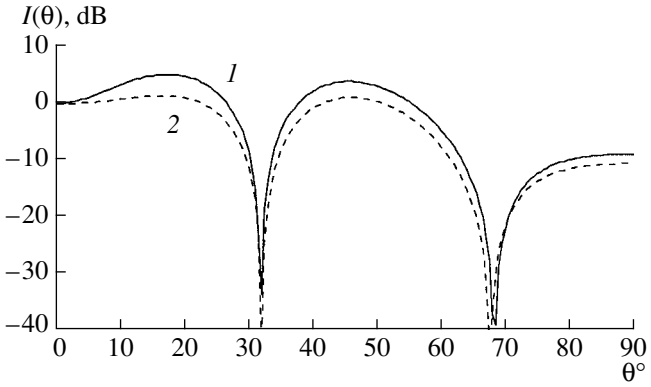

Fig. 1. Relative intensity $I(\theta)$ of a scattered wave (in decibels) in the Fraunhofer zone at $\theta_0 = 0$ and $kH = 9.24$ for $N =$ (*1*) 100 and (*2*) 6 in Eq. (4).

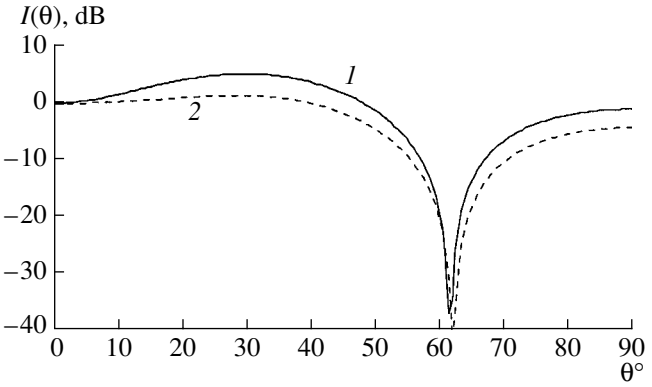

Fig. 2. The same as in Fig. 1 but for $kH = 5.544$.

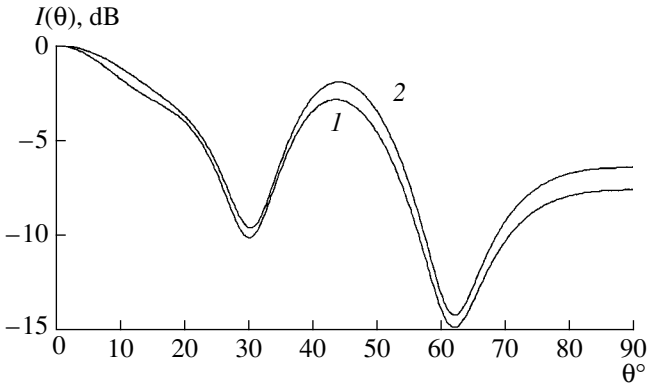

Fig. 3. The same as in Fig. 1 but for an acoustic admittance at the central square equal to $i\eta_0$.

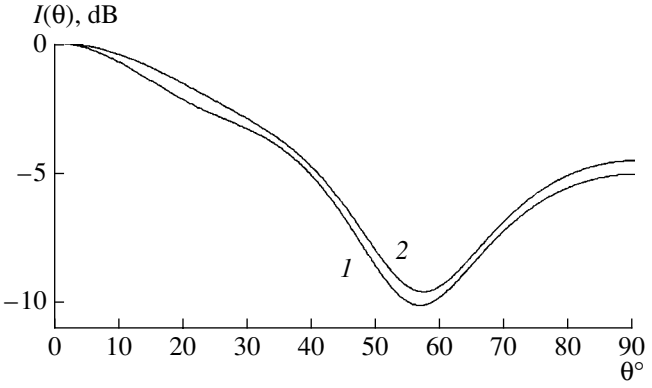

Fig. 4. The same as in Fig. 2 but for an acoustic admittance at the central square equal to $i\eta_0$.

Summarizing the contributions of all squares in the expression for the inverse with respect to Fourier transformation (2)

$$B(\kappa_x, \kappa_y) = \frac{1}{4\pi^2}\int_{-\infty}^{\infty}\int_{-\infty}^{\infty}\eta(x, y) \times \exp[-i(\kappa_x x + \kappa_y y + \kappa_z z)]dxdy$$

of the preset acoustic admittance, we obtain after integration

$$B(\kappa_x, \kappa_y) = \frac{\eta_0}{\pi^2}\left\{S_0 + \sum_{m=1}^{N} S_m(-8)^m \prod_{k=1}^{m}\frac{C_k}{8}\right\}, \quad N \longrightarrow \infty, \tag{4}$$

where

$$B(0, 0) = \frac{\eta_0}{\pi^2}\left(\frac{H_0}{2}\right)^2 \frac{1}{17}\left[9 + 8\left(-\frac{8}{9}\right)^N\right]. \tag{5}$$

Figure 1 presents the relative intensity of a scattered wave $I(\theta) = 20\log(|p_1(\theta, 0)/p_1(0, 0)|)$ (in decibels) at $\theta_0 = 0$ and $kH = 9.24$, which at $H = 1$ m corresponds to a frequency of 500 Hz and a normal incidence of the initial wave. Curve *1* corresponds to a value of $N = 100$ in Eq. (4), and curve *2*, to $N = 6$, i.e., to taking into account the squares up to the hundredth and sixth scales, respectively. As one can see from Fig. 1, the scattered field is rather isotropic in this case except for the directions in the narrow angular ranges near 32° and 68°. Figure 2 shows the function $I(\theta)$ at $\theta_0 = 0$ and $kH = 5.544$, which corresponds to a frequency of 300 Hz for $H = 1$ m. Here, the scattering isotropy is considerably violated only in the vicinity of the angle $\theta = 62°$.

Although the calculations are conducted for the case $|\eta| \ll 1$, one should expect that they stay qualitatively valid also for $|\eta| \approx 1$, when the amplitude of a mirror-reflected wave does not predominate over the scattered field. In a rough approximation, an alternating acoustic

admittance can be realized by a wall relief in the form of alternating bulges and cavities of various scales.

By slightly changing the acoustic admittance at the central square, it is possible to radically reduce the dips in intensity curves $I(\theta)$ in comparison with the curves given in Figs. 1 and 2. For example, exchanging η_0 for $\eta_0 q$ at the central square, we obtain

$$B(\kappa_x, \kappa_y) = \frac{\eta_0}{\pi^2}\left\{S_0 q + \sum_{m=1}^{N} S_m (-8)^m \prod_{k=1}^{m} \frac{C_k}{8}\right\},$$

$$B(0, 0) = \frac{\eta_0}{\pi^2}\left(\frac{H_0}{2}\right)^2\left\{q - 1 + \frac{1}{17}\left[9 + 8\left(-\frac{8}{9}\right)^N\right]\right\},$$

instead of Eqs. (4) and (5). In this case, the curves plotted in Figs. 3 and 4 correspond to a value of $q = i$ instead of the curves given in Figs. 1 and 2.

REFERENCES

1. M. Schroeder, *Fractals, Chaos, Power Laws* (Freeman, New York, 1991; NITs RKhD, Moscow, 2001).
2. M. R. Schroeder, *Number Theory in Science and Communication, with Applications in Cryptography, Physics, Digital Information, Computing, and Self-Similarity*, 3rd ed. (Springer, New York, 1997).
3. T. Wu, T. J. Cox, and Y. W. Lam, J. Acoust. Soc. Am. **108**, 643 (2000).
4. M. B. Luk'yanchenko, in *Physical Acoustics. Wave Propagation and Diffraction: Proceedings of XI Session of the Russian Acoustical Society* (GEOS, Moscow, 2001), Vol. 1, p. 169.
5. Yu. P. Lysanov and L. M. Lyamshev, Dokl. Akad. Nauk **366**, 36 (1999) [Dokl. Phys. **44**, 264 (1999)].
6. E. A. Kopyl, Yu. P. Lysanov, and L. M. Lyamshev, Akust. Zh. **48**, 517 (2002) [Acoust. Phys. **48**, 453 (2002)].
7. M. V. Fedoryuk, *The Saddle-Point Method* (Nauka, Moscow, 1977).

Translated by M. Lyamshev

Acoustical Physics, Vol. 49, No. 6, 2003, pp. 704–710. Translated from Akusticheskiĭ Zhurnal, Vol. 49, No. 6, 2003, pp. 824–831.

Acoustic, Dielectric, and Mechanical Properties of a New Rigid-Rod Poly(heteroarylene)

O. G. Nikol'skiĭ[1], I. I. Ponomarev[2], N. S. Perov[1], and V. A. Martirosov[1]

[1] *Enikolopov Institute of Synthetic Polymeric Materials, Russian Academy of Sciences, Profsoyuznaya ul. 70, Moscow, 117393 Russia*

e-mail: mart@ispm.ru

[2] *Nesmeyanov Institute of Organoelement Compounds, Russian Academy of Sciences, ul. Vavilova 28, Moscow, 117813 Russia*

Received October 28, 2002

Abstract—The structural, relaxational, and stress–strain properties of rigid-rod poly(heteroarylene)s containing high-polarity functional groups in macrochains are studied. The groups are capable of forming strong intermolecular bonds, including those with polar low-molecular substances (residual solvent or water). The acoustic and dielectric spectroscopy methods are used. The properties of a recently obtained poly(heteroarylene)—poly(naphthoyleneimidobenzimidazole)—are studied in detail. It is shown that these rigid-rod polymers can exhibit local and large-scale molecular rearrangements at temperatures considerably lower than the glass transition temperature. The frequency vs. temperature diagram of relaxation transitions is obtained, and the activation energies for these processes are determined. The possible molecular dynamics mechanisms are discussed. *© 2003 MAIK "Nauka/Interperiodica".*

At present, great interest is being shown in studying the structural and physical properties of thermally stable poly(heteroarylene)s (PHAs) because of the broad range of their physicomechanical characteristics at both elevated (up to 673 K) and rather low (helium) temperatures. Apart from the unique mechanical properties, these materials possess limiting (for polymers) thermal, heat, optical, radiative, and chemical stabilities. However, the hitherto existing rigid-rod polymers were insoluble, which hampered their reprocessing. Soluble rigid-rod PHAs have only recently been synthesized. Nevertheless, the data on the structure, molecular dynamics, and macroscopic properties of such polymers are almost lacking in the literature [1, 2]. The correlation between the measured parameters and the chemical structure of these polymers still remains unclear, in spite of a permanent interest in the physical and, specifically, acoustic properties of various polymeric systems [3–6].

The study of unique physical properties of PHAs is necessary primarily for determining their use in industry and technology. Although the acoustic methods of studying the structure and properties of PHAs hold much promise, these methods have not been used so far.

An important feature of the chemical structure of poly(naphthoyleneimide)s is that their structure contains strongly polar groups that not only strengthen the intra- and intermolecular interactions but are also capable of holding many polar low-molecular substances (LMSs), including water and the residual solvent. Due to the active interaction with the functional groups of a polymer, LMSs can affect the system of intermolecular bonds in the polymer and, hence, its structure and its macroscopic properties.

The main purpose of this work was to obtain experimental data that are necessary for establishing the correlation between the microstructure and molecular dynamics of new polymeric materials and their stress–strain, dielectric, and other macroscopic properties. This program was implemented for a new soluble rigid-rod PHA—poly(naphthoyleneimidobenzimidazole) (PNIB)—of the general formula

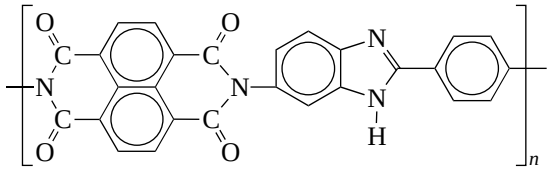

The polymer was prepared by high-temperature polycondensation in organic solvents [7]. According to [7], the Kuhn segment equals 32 ± 1 nm and its molecular weight is higher than 10^5.

It was expected that the combined study of the structural, relaxation, and mechanical properties would allow one, first, to determine the conditions for the appearance of an intense molecular motion in rigid-rod PHAs in their glassy state (for the usual rigid-rod polymers, the molecular mobility in this state is degenerate) and, second, to obtain experimental data necessary to analyze the molecular dynamics mechanism both in the absence and presence of polar low-molecular substances in the polymer bulk and to analyze the mechanism for the formation of an excess free volume after

the removal of LMSs without losing the unique complex of the physicomechanical properties of PHAs.

Films for study were prepared by pouring a reaction solution on a glass substrate, followed by drying at 393–413 K for 10–12 h in vacuum (~1.33 Pa) to a residual phenol content of 15–18 wt %, according to the TGA data.

Some of the starting films were extracted from an acetone–methanol mixture, whereupon they were dried in vacuum under the above conditions with a phenol residual content of no less than 1 wt % (extracted films).

Mechanical tests of the PNIB films were carried out on a 2166 P-5 tensile machine in the tension mode with a velocity of $v = 10^{-4}$ m/s.

Dielectric measurements were made using a multifrequency (50 Hz –100 kHz) P-5083 bridge (Tochelectropribor, Kiev) over the temperature range 80–800 K in air and vacuum (1.33 Pa) on samples with a diameter of 25 mm and a thickness of 0.05 mm.

X-ray structural studies were carried out at temperatures of 193–600 K in the reflection mode on a DRON-3 diffractometer and in the transmission mode on a DRON-1 diffractometer. The plane orientations were determined by photographing X-ray diffraction patterns with a flat-cassette camera of a URS-55 setup. In all cases, CuK_α radiation was used.

The sample densities were measured by the flotation method in a carbon tetrachloride–toluene mixture.

Acoustic measurements were made at low sound frequencies of 100–200 Hz in air and in an inert-gas (argon) flow in the temperature range 80–800 K for samples $24 \times 2 \times 0.05$ mm in size.

For these measurements, we developed a new automated acoustic test bench allowing the properties of polymeric materials to be studied in the resonant vibration mode over a broad range of temperatures and static and dynamic mechanical loads. The tension–compression vibrations proceeded in the presence of controlled static loads.

The functional scheme of the acoustic test bench is shown in Fig. 1a. The bench consisted of the following units: a driving vibrational contour, a measuring vibrational contour, a dynamometric unit, and a unit for setting and controlling temperature.

The basic distinctions between our method and other methods known domestically and abroad are as follows:

(i) the combination of the dilatometric and vibrational methods allowed the substantial improvement of the measurement accuracy;

(ii) the variation of the static and dynamic mechanical loads with simultaneous recording of the coefficient of linear thermal expansion made it possible to identify the nature of molecular motions and determine their correlation with the structure and the physicomechanical properties of a material more accurately; and

(iii) the acoustic properties were studied directly during the course of deformation of a polymeric material.

The acoustic part of the bench was modeled by the simplest system with two degrees of freedom, as shown in Fig. 1b. The equations of motion for it are written as

$$\begin{aligned} m_1\ddot{x}_1 + (k_1^* + k_0^*)x_1 - k_0^* x_2 &= F_1(t), \\ m_2\ddot{x}_2 + (k_b^* + k_0^*)x_2 - k_0^* x_1 &= 0, \end{aligned} \tag{1}$$

where m_1 is the mass of all mobile parts between the sample and the vibrator (the lower clamp, two rods with a system of attaching them to the vibrator membranes, and the membranes themselves); m_2 is the mass of all the mobile parts between the sample and the strain-gage beam (the upper clamp, the rod, and the beam itself); x_1 and x_2 are the displacements from the equilibrium positions of the masses m_1 and m_2, respectively; k_1, k_0, and k_b are the coefficients of elasticity of, respectively, the vibrator, the sample, and the strain-gage beam; and $F_1(t)$ is an external force. In what follows, we restrict ourselves to the analysis of harmonic vibrations. To include the dissipative processes, all coefficients of elasticity will be assumed to be complex and will be marked with asterisk.

Model (1) is analyzed below to obtain the expressions for the components of complex elastic modulus.

Clearly, the vibrations in the system are the sum of natural and forced vibrations. A partial solution to equation (1) is sought in the form

$$x_1 = X_1\exp(i\omega t), \quad x_2 = X_2\exp(i\omega t),$$
$$F_1(t) = F_1\exp(i\omega t),$$

where X_1 and X_2 are the complex amplitudes of mass displacements for m_1 and m_2, respectively. From set (1), one obtains the pair of algebraic equations

$$(k_1^* + k_0^* - \omega^2 m_1)X_1 - k_0^* X_2 = F_1,$$

$$-k_0^* X_1 + (k_b^* + k_0^* - \omega^2 m_2)X_2 = 0.$$

The equation for the natural frequencies ω_1 and ω_2 has the form

$$\begin{vmatrix} k_1^* + k_0^* - \omega^2 m_1 & -k_0^* \\ -k_0^* & k_b^* + k_0^* - \omega^2 m_2 \end{vmatrix} = 0.$$

The terms $k_0^* x_2$ and $k_0^* x_1$ in equation (1) characterize the elastic coupling of the partial systems; one can, therefore, introduce the dimensionless coupling coefficient

$$\gamma = \frac{k_0^{*2}}{(k_1^* + k_0^*)(k_b^* + k_0^*)},$$

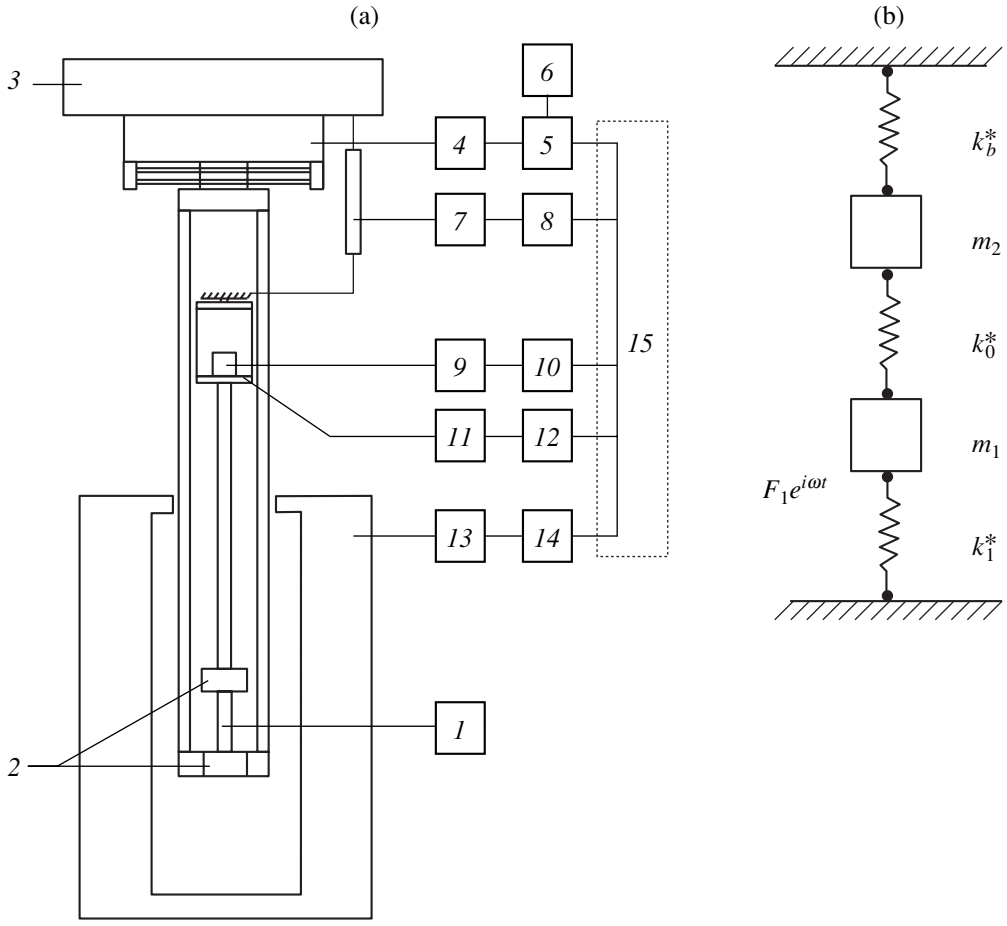

Fig. 1. (a) Functional scheme of the acoustic test bench: (*1*) sample; (*2*) clamps; (*3*) mobile beam; (*4*)–(*6*) dynamometric system for producing harmonic vibrations; (*7*, *8*) displacement measurement system; (*9*, *10*) harmonic vibration detection system; (*11*, *12*) strain-gauge system for the control of static load; (*13*, *14*) temperature control system; and (*15*) data control and processing system. (b) Equivalent scheme of the acoustic test bench.

characterizing the ratio of the mean binding energy to the mean energy in the partial systems. However, for a system with bonding of only a single type (as in our case), one can formulate conditions under which the bonding has only little effect on the vibrations of each of the partial systems. For the elastically coupled systems, this occurs for the γ values satisfying the condition

$$(n_1^2 - n_2^2)^2 \gg 4\gamma n_1^2 n_2^2,$$

where n_1 and n_2 are the partial frequencies.

L.I. Mandelstam analyzed this problem [8] to introduce the concept of associated systems and the association coefficient

$$\sigma = \gamma \frac{2n_1 n_2}{|n_1^2 - n_2^2|}.$$

This coefficient was introduced because the character of interaction of the systems is determined not only by the coupling constant (γ) but also by the proximity of partial frequencies. Consequently, the vibrations can be considered separated if the association (but not bonding) is very weak, i.e., if $\sigma \longrightarrow 0$.

By choosing the parameters of the system in such a way that

$$(k_1^* + k_0^*)(k_b^* + k_0^*) \gg k_0^{*2}$$

and, correspondingly, $n_1 = 60$ and $n_2 = 500$ Hz, one obtains $\sigma < 0.65 \times 10^{-3}$.

The association coefficient as small as that allows the vibrational process for each contour to be treated as proceeding in an isolated system with one degree of freedom. In this case, the expression for the complex acceleration amplitude for m_2 is

$$\bar{a} = \ddot{\bar{X}}_2 = \frac{-F_1 \omega^2}{-\omega^2 + \dfrac{k_b^* + k_0^*}{m_2}}. \qquad (2)$$

After substituting $k_b^* = k_b(1 - i\tan\delta_b)$ and $k_0^* = k_0(1 - i\tan\delta_0)$ in Eq. (2), one has

$$a = -\frac{\omega^2 F_1}{\sqrt{(\omega_2^2 - \omega^2)^2 + (\omega_0^2\tan\delta_0 + \omega_b^2\tan\delta_b)^2}},$$

where $\omega_2^2 = (k_0 + k_b)/m_2$, $\omega_0^2 = k_0/m_2$, and $\omega_b^2 = k_b/m_2$.

Taking into account that, at resonance [8] $\omega \cong \omega_2$ and

$$a_{\text{res}} = -\omega_2^2 F_1/\alpha, \tag{3}$$

where $\alpha = \omega_0^2\tan\delta_0 + \omega_b^2\tan\delta_b$, and, for the detuning $a_{\text{res}}/\sqrt{2}$, one obtains, after denoting $p = \omega^2$, the following equation in p:

$$(2\alpha^2 - \omega_2^4)p^2 + 2\omega_2^6 p + \omega_2^4(\omega_2^4 + \alpha^2) = 0.$$

Solving this equation and denoting $p_1^2 - p_2^2 = 2\Delta\omega\omega_2$, with allowance for $\omega_2^4 \gg 2\alpha^2$, we obtain an expression for the mechanical loss tangent:

$$\tan\delta = \tan\delta_0 = \frac{\omega_2\Delta\omega}{\omega_0^2} - \frac{\omega_b^2}{\omega_0^2}\tan\delta_b. \tag{4}$$

Since $\omega_0^2 = \omega_2^2 - \omega_b^2$, we have:

$$\tan\delta = \frac{\omega_2\Delta\omega}{\omega_2^2 - \omega_b^2} - \frac{\omega_b^2}{\omega_b^2}\tan\delta_b. \tag{5}$$

The dynamic elastic modulus $E' = k_0 l/S$ of the sample, where l is its length and S is its cross-sectional area, is found from the relationship

$$\frac{k_0 + k_b}{m_2} = \omega_2^2 \text{ or } k_0 = m_2(\omega_2^2 - \omega_b^2).$$

As a result, one has

$$E' = \frac{l}{S}(\omega_2^2 - \omega_b^2)m_2$$

and, after measuring the sample density ρ, one obtains the expression for the longitudinal ("rod") sound velocity $c = \sqrt{E'/\rho}$.

The values of k_b, m_2, and $\tan\delta$ were determined by the calibration. To determine k_b and m_2, the relation $1/\omega_2^2 = f(\Delta m)$ was obtained, where Δm is an additive to the mass m_2. By choosing a low-modulus sample and, thereby, satisfying condition $k_b \gg k_0$, one finds the desired k_b and m_2 values from the curve slope and the section on the ordinate axis, respectively. For determining the value of $\tan\delta_2$, samples shaped like steel springs with the working frequency characteristics lying in the range 100–200 Hz were chosen.

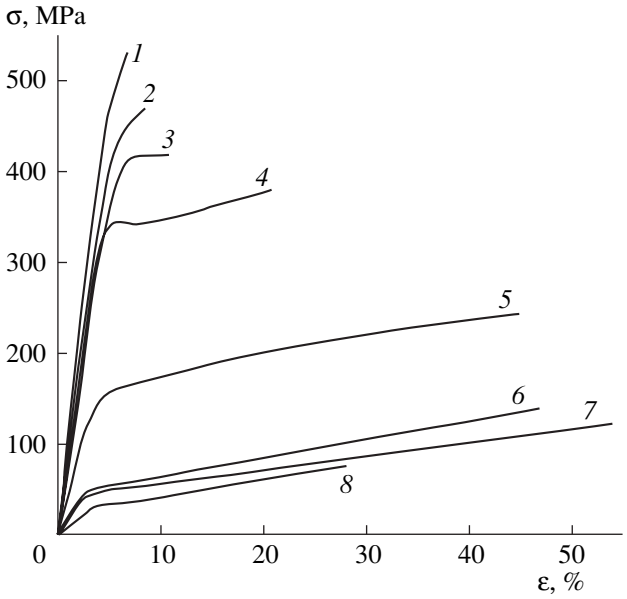

Fig. 2. Stress–strain curves obtained for the PNIB film at temperatures (*1*) 173, (*2*) 223, (*3*) 253, (*4*) 293), (*5*) 373, (*6*) 473, (*7*) 573, and (*8*) 673 K.

The X-ray diffraction patterns of PNIB show ill-defined amorphous halos with $d_1 \sim 0.73$, $d_2 \sim 0.5$, and $d_3 \sim 0.35$ nm. As the temperature was raised to 600 K, the halos were gradually smeared. The subsequent cooling to 193 K did not change the diffraction pattern. The "in-front" and "in-side" X-ray diffraction analyses of the films showed that they were isotropic with an ill-defined planarity.

The stress–strain curves obtained for the starting PNIB films over a broad temperature range are shown in Fig. 2, and the temperature dependences of the breaking strength, ultimate elongation, and Young's modulus are shown in Fig. 3. From these data it is seen that, first, the films possess enhanced strength properties and, second, these properties persist over a broad temperature range (the films retain their workability up to temperatures on the order of 650–670 K).

Mechanical properties as high as those and the retention of their working capacity in a broad temperature range can be due to the structure and the character of molecular mobility in PNIB.

With the aim of revealing a correlation between the molecular dynamics and the macroscopic properties of the films by the acoustic and dielectric relaxation methods, the temperature dependences of the parameters responsible for the relaxation spectrum of this polymer were studied for various film preparation histories.

The temperature dependences of the "rod" sound velocity c and the mechanical loss tangent $\tan\delta$ are shown in Fig. 4 for the extracted films. One can see that,

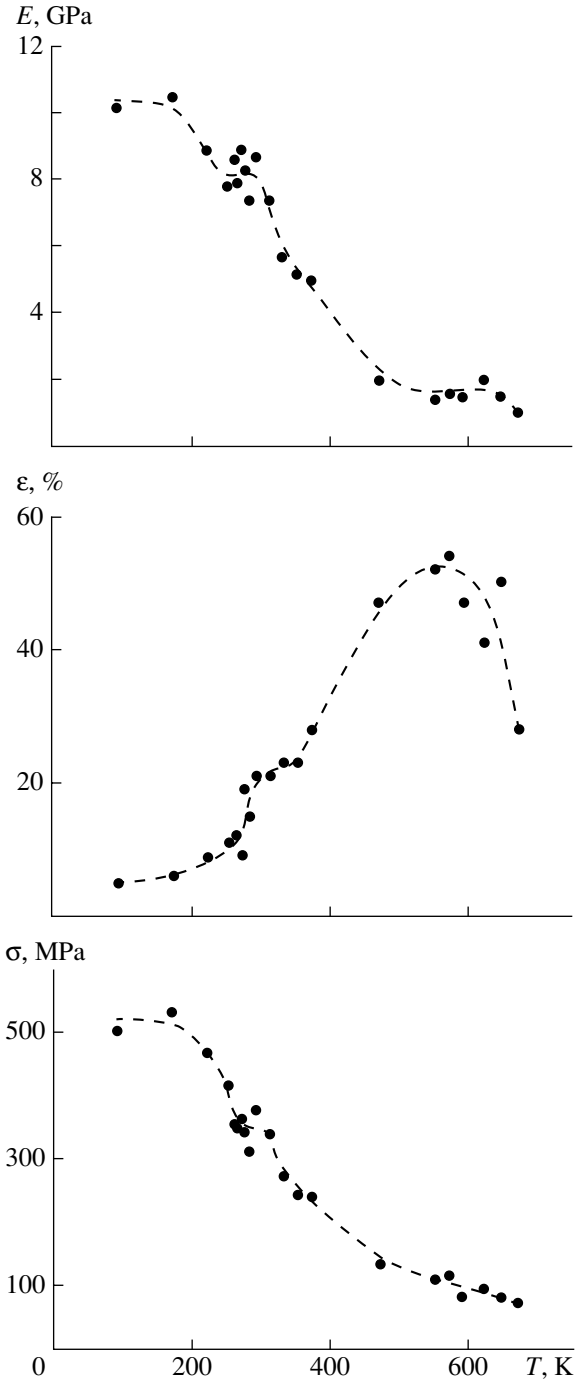

Fig. 3. Temperature dependences of the breaking strength (σ), ultimate elongation (ε), and Young's modulus (*E*) of the PNIB film.

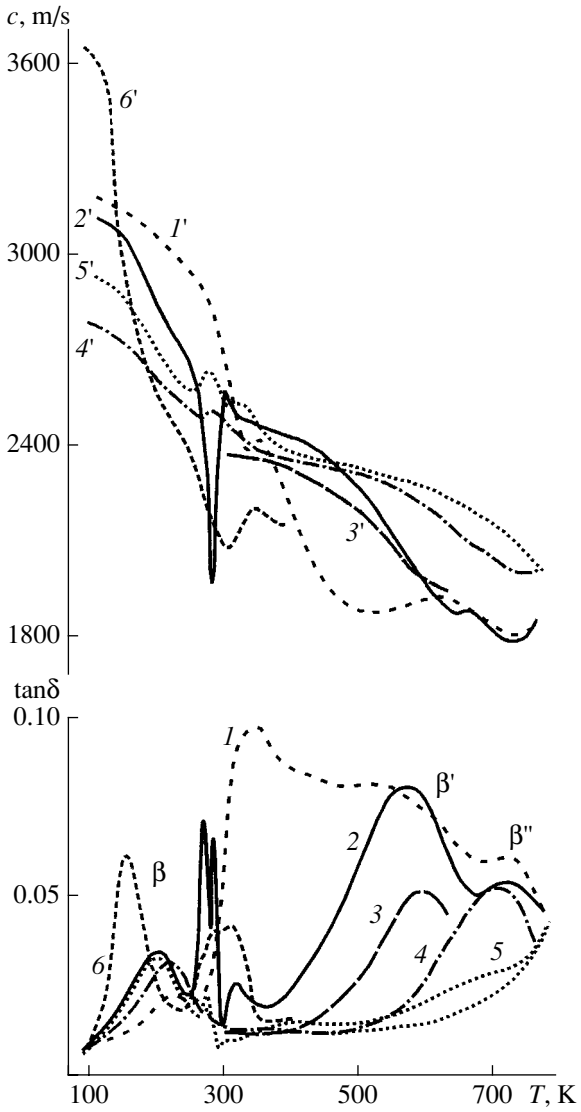

Fig. 4. Temperature dependences of the "rod" sound velocity *c* and the mechanical loss tangent $\tan\delta$ for the PNIB films with different preparation histories: (*1*, *1*') starting film; (*2*, *2*') extracted from LMS; (*3*, *3*') extracted from LMS followed by annealing at 573 K; (*4*, *4*') after annealing at 623 K; (*5*, *5*') after annealing at 773 K (heating and cooling curves are given); (*6*, *6*') after annealing at 623 K and holding in water for one day.

as the temperature increases, the molecular mobility is frozen out near 80 K. We call it the β-relaxation transition (note that we refer the molecular mobility associated with various backbone motional modes of a macromolecule to the group of β-relaxation transitions). The β transition is observed as an inflection in the temperature curve $c(T)$ and as a broad peak with a maximum at ~193 K in the temperature curve $\tan\delta(T)$. Near 273 K, the β transition is interrupted by a region of intense mechanical energy loss. This region (we call it the intermediate loss region) is unrelated to the relaxation, because the dielectric measurements (Fig. 5) show no frequency dependence and, inasmuch as this transition is not observed in the PNIB relaxation spectrum recorded in the cooling regime, it can be assigned to the water desorption from the sample bulk. Above ~373 K, the transition loss region transforms to a broad β' peak with a maximum at ~560 K, corresponding to a monotonic decrease in *c*. The highest-temperature β"

transition is characterized by a maximum of $\tan\delta$ near 730 K.

Since the PNIB glass transition temperature (T_c) exceeds the temperature of the onset of an intense chemical processes in the polymer (thermooxidation destruction), we estimated the value of T_c (at frequencies on the order of 100 Hz) using the well-known Fox equation and the experimental T_{max} values corresponding to the α peaks for a number of copolymers of PNIB with poly(phenylquinoxaline) (PPQ) and for pure PPQ. With allowance for the frequency factor, the resulting value T_c = 775 K is in good agreement with the quasistatic value T_c = 760 K calculated by the known method [9].

The temperature dependences of c and $\tan\delta$ obtained for PNIB allow the conclusion to be drawn that the rigid-rod polymers of this type can exhibit a considerable molecular mobility in the glassy state.

The data on the temperature cycling of the starting PNIB films (Fig. 4), in conjunction with the data on the density and molecular packing coefficients k (table), allow a more precise identification of the different stages observed in the spectra of starting films upon their heat treatment. One can see that, in the two first cycles (T_{max} = 440 and 520 K), the LMS is mainly desorbed, and, upon the subsequent heating, the temperature dependence of $\tan\delta$ virtually coincides with the $\tan\delta$ curve for the extracted PNIB sample. However, in the subsequent heat treatment cycles (T_{max} = 570 and 620 K), the β' peak shifts to higher temperatures and coalesces with the β''-loss region. An increase in T_{max} to 670 K does not change the temperature position of the β'' maximum that, however, irreversibly changes upon heating to 770 K as a result of the limitations posed on the molecular mobility by the chemical structuring (cross-linking) processes.

An analysis of the relaxational data and the densities of the PNIB films studied made it possible to reveal the important role of the polar low-molecular substances in the mechanism of the secondary relaxational transitions of rigid-rod poly(heteroarylene)s containing high-polarity groups in their macrochains.

In addition, it is clear from comparison of the temperature dependences of the ultimate elongation (Fig. 3) and $\tan\delta$ (Fig. 4) of the starting sample that the molecular processes are connected to the deformation properties of the PNIB films. Note also that the molecular mobility has a sizable effect on the character of temperature dependence of the breaking strength and the static elastic modulus of the films (Fig. 3).

Using the acoustic and the dielectric relaxation data for various temperatures (Fig. 5) and the data of quasistatic measurements of dark electrical conductivity, the frequency vs. temperature diagram was constructed for the relaxation transitions and the corresponding activation energies were determined (Fig. 6). One can see that the β process is described by a nearly linear dependence, whose high-temperature extrapolation ($1/T = 0$) gives a preexponential factor on the order of 10^{13} Hz in the relation

$$f = f_0 \exp(E_a/RT), \qquad (6)$$

where f is the frequency, T is the transition temperature, E_a is the activation energy, and R is the universal gas constant. This result, together with a relatively low activation energy of E_a = 50 kJ/mol, allows this transition

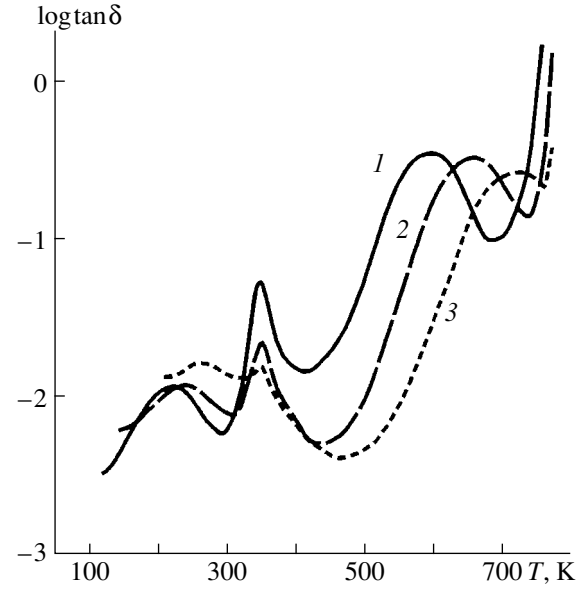

Fig. 5. Temperature dependences of the dielectric loss tangent $\tan\delta$ obtained at frequencies (*1*) 1, (*2*) 10, and (*3*) 100 kHz after heat treatment of PNIB at 673 K.

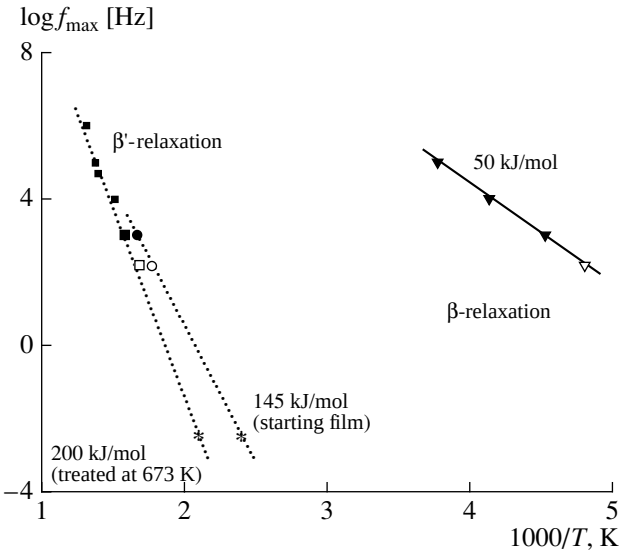

Fig. 6. Frequency vs. temperature diagram of relaxation transitions in PNIB (□, ○, ▽ are acoustic measurements; ■, ●, ▼ are dielectric measurements; and ∗ is electrical conductivity).

The density ρ and the molecular packing coefficient *k* for the PNIB films with different preparation history

Sample	Heat treatment conditions					
	410 K, 12 h		570 K, 15 min		670 K, 15 min	
	ρ, g/cm^3	*k*	ρ, g/cm^3	*k*	ρ, g/cm^3	*k*
Starting	1.409	0.6868	1.432	0.6979	1.442	0.7028
Extracted from low-molecular substances	1.429	0.6965	1.431	0.6974	1.441	0.7023

to be assigned to the local molecular dynamics of chain segments. However, the β' relaxation transition, although occurring below T_c, does not obey the Arrhenius equation, because the dependence $\log f(1/T)$ is extrapolated at $1/T \longrightarrow 0$ to $f = 10^{18}$–10^{20} Hz. One can assume that, for both β' transition and the glass transition process, the activation energy is apparent, so that the transition corresponds to the cooperative motions and does not obey equation (6). Since the values E_a = 200 kJ/mol and $f_0 = 10^{18}$–10^{20} Hz for the β' transition are lower than for the main relaxation transition associated with the glass transition process, one can assume that the β' transition is associated with the less cooperative motions of the macrochain segments than in the glass transition process.

Our studies have shown that the cyclic-chain structure of rigid-rod PHAs; the high molecular weights of PHAs obtained for the first time; and the possibility of simultaneously realizing the dense macromolecule packing, the strong intermolecular interactions (hydrogen bonds and dipole–dipole interactions), and the macromolecule flexibility in a system with the optimal concentration of cyclic rigid-chain fragments determine the specificity and the necessity of a new understanding of the structural organization, molecular dynamics, and the unique combination of the physicomechanical properties of rigid-rod PHAs.

The acoustic studies complemented by the results of dielectric, stress–strain, and other studies have been used to propose a structural approach to the description of the molecular dynamics and an explanation of the unique physicomechanical properties of new polymeric materials based on rigid-rod PHAs. The approach is based on treating these materials as a structurally inhomogeneous polymer–LMS system characterized by the presence of differently ordered (differently packed) regions of fluctuation nature. These regions are formed in the course of system transition from a solution to the glassy state in the presence of an appreciable amount of residual polar LMSs coupled via the strong intermolecular interactions to high-polarity PHA groups. In this case, local and even large-scale molecular rearrangements may occur at temperatures appreciably lower than the glass transition temperature of the system. This approach not only allows the explanation of the reasons for a considerable molecular mobility in the glassy state of the rigid-rod PHAs and the enhanced deformability of their films, together with their unique stress–strain properties, but also substantiates the formation mechanism for the excess free volume upon removing LMSs from such polymers.

ACKNOWLEDGMENTS

This work was supported by the Russian Foundation for Basic Research, project no. 01-02-16762.

REFERENCES

1. Ying-Hung So, Prog. Polym. Sci. **25** (2), 137 (2000).
2. D. J. Jones and J. Roziere, J. Membr. Sci. **185** (1), 41 (2001).
3. G. Busse, I. Yu. Solodov, R. Stoessel, and Yu. Schuetz, Akust. Zh. **48**, 22 (2002) [Acoust. Phys. **48**, 18 (2002)].
4. V. Yu. Zaĭtsev, V. E. Nazarov, and A. E. Shul'ga, Akust. Zh. **46**, 348 (2000) [Acoust. Phys. **46**, 295 (2000)].
5. B. B. Badmaev, O. R. Budaev, and T. S. Dembelova, Akust. Zh. **45**, 610 (1999) [Acoust. Phys. **45**, 541 (1999)].
6. Ya. A. Bordyuk, S. M. Gusakovskiĭ, S. N. Ivanishchuk, and B. S. Kolupaev, Akust. Zh. **44**, 21 (1998) [Acoust. Phys. **44**, 15 (1998)].
7. N. V. Pogodina, N. P. Evlampieva, V. N. Tsvetkov, *et al.*, Dokl. Akad. Nauk SSSR **301** (4), 905 (1988).
8. S. P. Strelkov, *Introduction to the Theory of Oscillations* (GITTL, Moscow, 1950).
9. A. A. Askadskiĭ and Yu. I. Matveev, *Chemical Structure and Physical Properties of Polymers* (Mir, Moscow, 1976).

Translated by V. Sakun

Acoustical Physics, Vol. 49, No. 6, 2003, pp. 711–720. Translated from Akusticheskiĭ Zhurnal, Vol. 49, No. 6, 2003, pp. 832–842.

Sound Field Structure Produced by Tone Sources in the Kurile–Kamchatka Region of the Pacific Ocean with a Surface Channel and Wind Waves

N. V. Studenichnik[†]

Andreev Acoustics Institute, Russian Academy of Sciences, ul. Shvernika 4, Moscow, 117036 Russia
e-mail: vadov@akin.ru

Received November 29, 2002

Abstract—Results of the experimental studies of sound signal propagation in the continental wedge of the northwestern Pacific, near the eastern coast of the Kamchatka Peninsula, are presented. The signals are produced by highly stable tone sources. The experiments are carried out in winter, in the presence of a strong surface sound channel and intense wind waves, at frequencies of 100, 230, and 400 Hz, on a 1000-km-long path. The signal transmission is performed by continuously towing the sound sources at a depth of 50 ± 5 m with a speed of 4.5–5 knots, for 115 hours. The decay of the sound field level with distance is studied as a function of the sea state and the frequency. The results of the experiments, including the sound field decay along the path, are compared with the calculations for different sea states. © *2003 MAIK "Nauka/Interperiodica".*

Extensive studies of the intensity and space-time characteristics of the sound field in the northwestern Pacific were carried out by a number of research groups. The studies were mainly performed in summer and autumn, in the presence of an underwater sound channel in the region (e.g., the studies under the VOSTOK-80 Research Program [1]). In addition, in the period from March 31 to April 5, 1984, the Andreev Acoustics Institute, in cooperation with the Institute of Applied Physics of the USSR Academy of Sciences, the USSR Navy Hydrographic Service, and other organizations, carried out the VOSTOK-84-1 expedition to investigate the sound field structure in the winter-type environment, with a strong surface sound channel and intense wind waves. These investigations, which were preceded by three-year-long preparations, actually continued the VOSTOK-80 Program. They were performed on the same path as the experiments of 1980 [1]. The path, 1000 km in length, was oriented at a great-circle bearing of 120°, off the eastern coastal shelf of the Kamchatka Peninsula. The surface channel extended from the surface to the bottom, with sea depths from 150–200 to 5000 m. The sea state varied from Beoufort 1–2 to 5–6 along the path.

The experiments were intended to study the fine structure of the sound field and the sound intensity decay with distance in a long-range propagation in the surface channel with a wind-perturbed upper boundary. A specific objective was to obtain the space–time and frequency–phase characteristics of the sound field and to investigate their stability in the presence of wind-driven surface waves. This paper presents only the results of studying the intensity characteristics of the sound field.

In the experiments, the research vessels *Pegas* and *Gals* of the USSR Navy Hydrographic Service were used. The former served as the transmitting vessel, while the latter performed the measurements of the hydrological and meteorological parameters of the sea region. The signals were received by a directional antenna array moored at the coastal shelf. As in our previous experiments, the transmitters were continuously towed, and the transmission occurred independently at several frequencies controlled by a single master manipulator. As in the experiments of 1980 [1], we used highly stable tone sources of 100, 230, and 400 Hz. All three sources, along with the reference hydrophone and a depth meter, were mounted on a single frame deployed on a cable from the stern of *Pegas*. At a rated towing speed of 5 knots (2.5 m/s), the depth of the sound sources was within 50 ± 5 m. To form the transmitted signals, we used a dedicated instrument system consisting of master quartz oscillators, a control block, power amplifiers, acoustic transducers, and system for monitoring the transmission parameters. The control block, in addition to the programming unit, allowed us to obtain different transmission regimes. We chose a nearly continuous transmission mode: signals of 500-s duration with 20-s pauses. Every 3 h, an additional mode was switched on: a 100-s alternative operation of three sound sources with a 20-s pause. The transmission level was continuously monitored and maintained within the preset (and measured) limits over the entire experiment. The process of towing and signal transmission continued for five days (115 h). The starting point of signal transmission was closer to the coastline than

[†] Deceased.

the receiving array, at a distance of 5 km from it, on a line that was an extension of the main direction (120°) of the path. In moving along the path, the vessel passed over the receiving system moored at a depth of 200 m, 3 km off the edge of the continental slope, and then proceeded at the chosen course towards the open ocean. The maximal variation of the towing speed was within one knot. Because of the Doppler shifts, the variations of the speed resulted in a frequency instability of the received signals. At a distance of 330–350 km, the transducer began to malfunction, and the transmission was interrupted for 4 h at all frequencies.

The signals were received by separate hydrophones, by vertical hydrophone chains, and, selectively, by individual beams of the directional receiving system. The received signals were recorded by a 14-channel TEAC-50C and a 4-channel type 7003 Bruel&Kjer magnetic tape recorders. Recording was continuously performed for all 115 h of experimentation by four adjacent horizontal beams formed by the analog compensators of the receiving system, by seven vertical hydrophone chains uniformly distributed over the array aperture, and by a single omnidirectional receiver of the same array. At the frequencies used, the vertical chain had a weak vertical directivity and a horizontal directivity pattern close to cardioid. In addition, the signals received by a single hydrophone and by the horizontally narrow array beams were filtered in 3% bands and recorded by the type 1621 Bruel&Kjer chart recorder and by that of the H-100 type.

The bottom relief of the path comprised a short bank with depths of 250–300 m, a steep continental slope of up to 10°, a long plateau with depths of 3000–3500 m at distances of up to 150 km, a deep-water depression of the Kurile–Kamchanka hollow with depths of more than 7000 m, and the abyssal plateau with depths of 5000–5500 m. At distances of 750–950 km, the path crossed the northern branch of the Impair Mounts (the Ten'ga Mount) where the ocean depth decreased to 3000–3500 m. Figure 1 presents samples of the sound speed profiles in the near-surface water layers, the bottom relief obtained in the echo-sounder survey performed by the *Pegas*, and the sound speed field plotted according the data of 26 hydrological measurements carried out by the *Gals*. According to the data shown in this figure, a strong surface sound channel existed on the path, with the minimal sound speed at the ocean surface. The near-surface sound speed varied from 1444 m/s at the reception point to 1458 m/s at distances of 700–1000 km. However, according to [3], the near-surface water layers are saturated with air bubbles at high sea states, and the near-surface sound speed can be considerably lower than that calculated from the measured temperature and salinity: it can reach a value of 1000–1300 m/s. At a transmission depth of 50 m, the sound speed was by 6–15 m/s higher than near the surface, this difference reaching 18 m/s at a reception depth of 200 m. As a result, the angular spectrum of the sound field changed at the end of the path, and a part of the refracted rays with higher characteristic angles (angles of crossing the channel axis) transformed to those with bottom–surface reflections. Therefore, at the end of the path, the angular range of the rays captured by the channel decreased by ±6°–9°, as compared to that at the coastal zone. The bottom rises (up to depths of 3000–3500 m) additionally sharpened the angular spectrum of the refracted components with angles within ±14.7°–21° and reduced the range of the channel-captured rays by ±4°–5°. Naturally, the depletion of the spectrum of the refracted rays by their transformation into bottom–surface reflections led to a decrease in the level of the total sound field and to stronger level decays. With a sea depth of 5000 m and a near-surface sound speed of 1444 m/s, the full range of the captured rays was ±21°, this value decreasing to ±14.7° for a depth of 3000 m and a sound speed of 1458 m/s at the channel axis. The total angular range of the surface-reflected rays was ±5°–21°.

The sea floor strongly varied along the path in its sediment content and geological parameters. In the nearest zone, the bottom material was represented by sand and other coarse-grained sediments with sound speeds by 50–120 m/s higher than in the water and densities of 1.5–2.2 g/cm^3. The continental slope and the deep-water hollow were underlaid by silstone sediments with the sound speed close to that of water near the bottom or even by 10–15 m/s lower than that, the sediment density being 1.30–1.50 g/cm^3. The major part of the region at hand and of the whole path had a sea floor composed of clay and silt with the sound speed by 10–30 m/s lower than in the water and with a density of 1.25–1.45 g/cm^3.

The meteorological situation was rather unstable during experimentation, both in the region as a whole and on individual parts of the path. Periods of relative calm were intermitted with periods of high wind speed due to periodic cyclones with varying wind speeds and directions on different fractions of the path. The weather was monitored from both vessels, which, at different times, were at distances of 50 to 300 km from each other. Northwest and north winds predominated in the region, with speeds varying from 2–5 to 14–20 m/s on different parts of the paths. The downwind direction was predominant with variations of ±60° relative to the direction of the path. In the coastal zone, near the receiving system, the wind speed was less than 3–7 m/s and the sea state was Beoufort 1–3 over the entire experiment. When the signals were transmitted from distances of 0–250 and 550–700 km, the wind speed varied within 3–7 m/s; when these distances were 300–550 and 700–1000 km, the wind speed was 9–14 and 15–20 m/s, respectively. By the time the path end was reached, the sea state increased to Beoufort 5–7.

Experimental data in the form of chart records were used mainly to study the spatial variability of the sound intensity and to determine the decay law for the sound level. The main objective of such studies consisted in

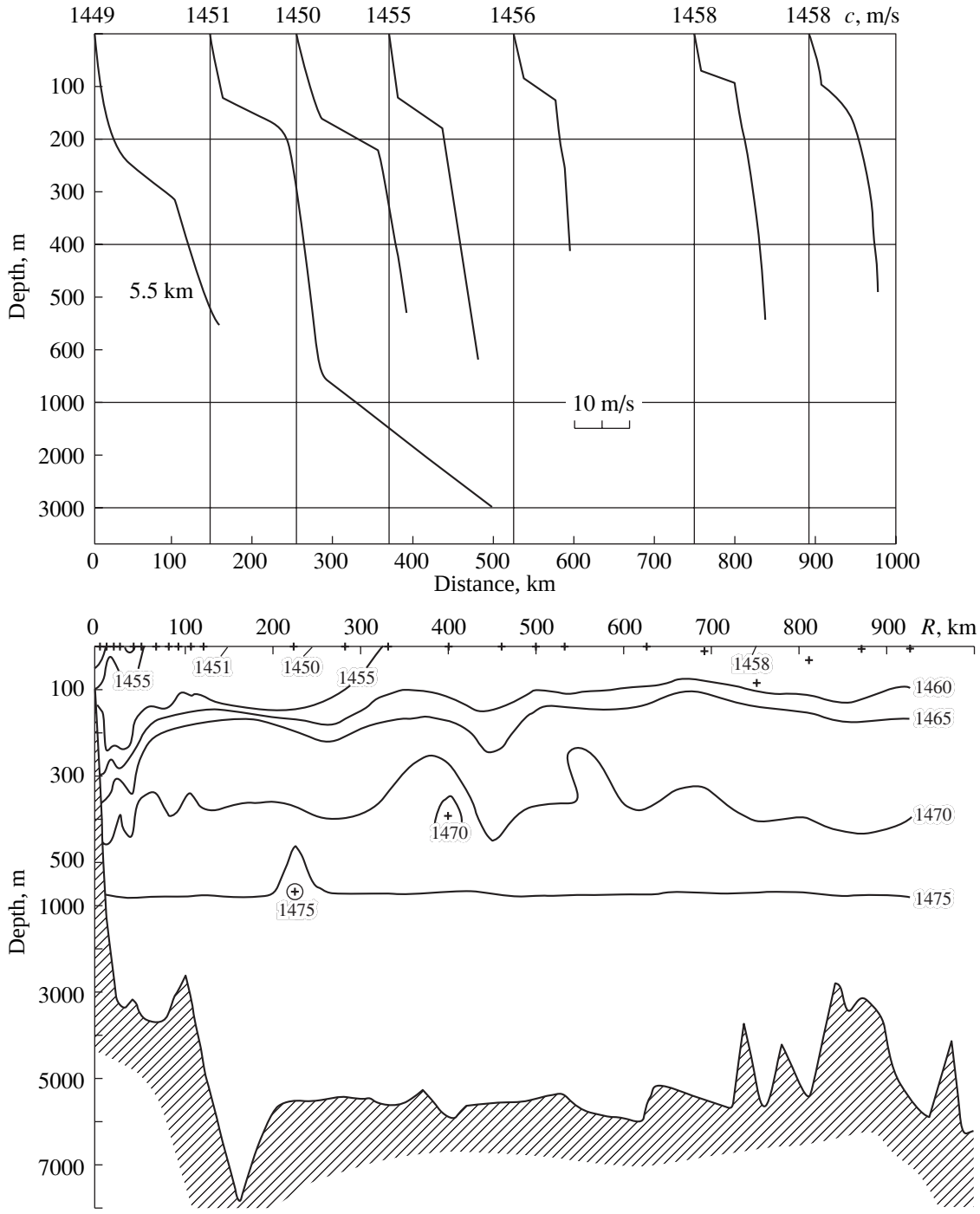

Fig. 1. Bottom relief and sound speed field on the path. The crosses indicate the minimum in the speed of sound (the channel axis), and the solid lines represent the isospeed curves along the path.

revealing the effect of the sea state on the frequency dependence of the sound field. The aforementioned data were also used to qualitatively estimate the frequency–phase stability of the field components. Figure 2 shows 1700-s samples of the signal records at frequencies of 230 and 400 Hz for distances from 160 to 1000 km. These signals were received by the central beam of the array. At shorter distances (up to 200–300 km), the records demonstrate a regular interference structure of the sound field, which is caused by the multipath nature of signal arrivals and depends on the frequency and the speed of the sound source, just as in the summertime experiments of 1980 [1, 2] with an underwater sound channel. The spatial period of interference is about 600 m at 230 Hz and 250–400 m at 400 Hz. The modulation depth reaches 30 dB or more for the near

field (up to 100–200 km) and decreases to zero at ultimate distances. On the other hand, in the surface sound channel with wind waves, a strong irregularity of the intensity envelope caused by interference can be noticed on the whole path, independently of the frequency and the existence of regular interference structure at short distances. At 400 Hz, such an irregularity is well pronounced starting from distances of 100–160 km, with a difference of 10–20 dB between the maximal and minimal levels and a frequency of 0.1–0.2 Hz of the level variations. In the interference maxima, the depth of the high-frequency (0.1–0.2 Hz) modulation is 1–2 dB with a signal-to-noise ratio of 30–40 dB. In the minima, the modulation depth reaches 20–30 dB. The irregularity of the envelope is mainly governed by the surface waves. Other factors of the irregularity can be the waveguide inhomogeneities, the bottom relief in the coastal zone, and the pitch of the towing vessel. However, the effect of the latter factors was not determining in our experiment. At longer distances, especially with stronger winds, the regular low-frequency maxima and minima become smoother or fully vanish, as at 400 Hz, starting from 300–400 km. The field structure becomes similar to that of a noise-like chaotic process without regular phase-dependent summation of the field components. Here, the surface waves predominate with the associated strong prereverberation [4]. At 230 Hz, coherence of individual components is retained up to distances of 600–700 km.

At stronger winds of 12–14 m/s, in addition to the loss of regularity in the phase characteristics of the field components, a noticeable decrease in the total sound level takes place. The decrease is especially pronounced at 400 Hz.: starting at 380 km, the signal-to-noise ratio drops to as little as 10–15 dB. On further continuous signal transmission for 30 hours and increase in the distance from 380 to 650 km, the signal level at the same frequency of 400 Hz does not decrease (or does not remain constant as at 230 Hz): rather, it increases by 5–10 dB. The corresponding signal-to-noise ratio increases up to 20–22 dB. Such a behavior can be explained by the decrease from 12–14 to 5–7 m/s in the wind speed at the transmitting points and by the corresponding decrease in the loss caused by reflection. At distances of 700–1000 km, the wind speed again increased up to 14–20 m/s. The signal level began to rapidly decrease and, at 760 km, the level of the 400-Hz signal reached that of noise. At 230 Hz, a signal-to-noise ratio of 20–25 dB remained up to distances of 900–930 km; it sharply decreased to 5–7 dB at about 1000 km (the final fragment of the record in Fig. 2). At this distance, the experiment was terminated due to rising wind and the risk of losing the sound sources.

To conclude these considerations, it is worth mentioning that, during the experiment, other ships were also present in the region. They caused an additional increase in the noise level. For instance, when a ship passed the traverse of the receiving array and crossed the narrow horizontal beams, the noise level exceeded the signal level by 5–20 dB. This fact can be noticed at distances of 650 km (for the signals of both frequencies) and 930 km (for the 230-Hz signals).

Figure 3 presents the relative decays of the levels of the total sound field at 100, 230, and 400 Hz. At distances from 1 to 300–500 km, the signal levels were measured by a single hydrophone. At longer distances, the signals received by the central array beam were used. The signal levels from different receivers were matched to each other at all frequencies. The distance (in kilometers) is plotted along the abscissa axis (on a logarithmic scale). The ordinate represents the sound level (in decibels). With a single hydrophone, the detection range was 500 km at 100 Hz and less than 350 km at 230 and 400 Hz. In combining the three curves in one plot, the signal levels at different frequencies were normalized to the near field. As the plot shows, the signal intensities on the path and the decay laws substantially depend on frequency. The difference in the levels reaches 10–20 dB. At 100 and 230 Hz and distances 10 to 200 km, the average decay laws are close to the cylindrical law with the transition distances 12 and 5 km, respectively. At 400 Hz, after a sharp decrease of 35 dB (curve *3*) in the signal level in the near field (2 to 10 km), the level does not decrease with distance as the latter increases by a factor of 10, from 10 to 100 km; in contrast, it becomes higher by 5–6 dB. At the distances from 100–200 to 300–400 km, a rather monotonic decrease in the intensity occurs at all frequencies, such behavior being caused by the increase (up to 15–16 m/s) in the wind speed on the path and at the transmission points. In continuous signal transmission on a path fraction of 400 km (from the 300- to 700-km mark), the mean signal levels at all frequencies remained nearly unchanged for 45 h. Moreover, some elevation of the level can be noticed at 400 and 230 Hz. The stability observed in the signal levels can be attributed to the decrease in the wind speed from 14–16 to 4–5 m/s and to the associated decrease in the sea state to Beoufort 2–3. At the end of the path (700–1000 km), the brewing storm and the increase in the wind speed, up to 14–20 m/s, caused a sharp decrease in the signal levels again. Such a decrease is especially pronounced at 230 and 400 Hz. At 400 Hz, the signal amplitude dropped down to the noise level at distances of 700–750 km. At 230 Hz, with a somewhat slower signal decay, the signal-to-noise ratio remained equal to 5–7 dB at the 1000-km mark. It is worth comparing the aforementioned experimental data with those obtained on the same path in summer, with the underwater sound channel and low sea state, at the same frequencies, with the same transmission levels and the same receiving systems. In the summer experiments, the signal-to-noise ratio was 30–40 dB at 1000 km and 15–25 dB at 2100 km, in spite of the 10- to 15-dB decrease in the signal level in the frontal zone produced by the warm waters of the Kuroshio Current and the associated lowering of the channel axis from 150 to 1000 km at dis-

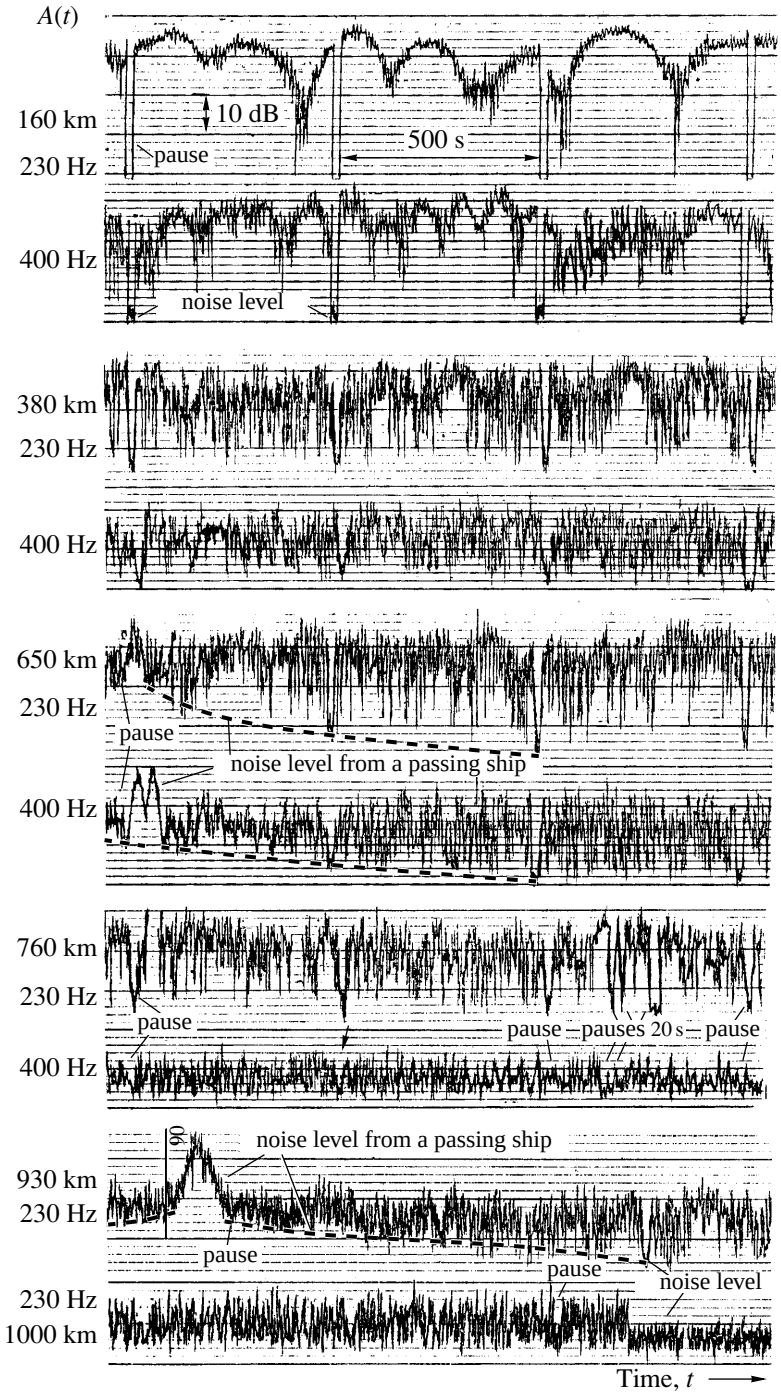

Fig. 2. Fragments of the records of tone signals at the frequencies 230 and 400 Hz; the distances are 160 to 1000 km.

tances of 2000–2100 km from the coastline. At the same time, the coherent components remained quite pronounced in the field structure for characteristic angles within ±9°–14° [1, 2].

The tape-recorded signals allow one to study the spectral characteristics of the field intensity and level decays not only for the total sound field but also for its individual components. To do so, we processed the records obtained from the central array beam by visualizing the signals and imaging the information with narrow-band filtering. As an example, let us consider the data processed at 230 Hz. The signals were processed by V.Ya. Faizov on a PLURIMAT computer. Prior to entering the signals into the computer, they were narrow-band filtered by two Type 1621 Bruel&Kjer filters connected in series. To enter the data, an accelerated

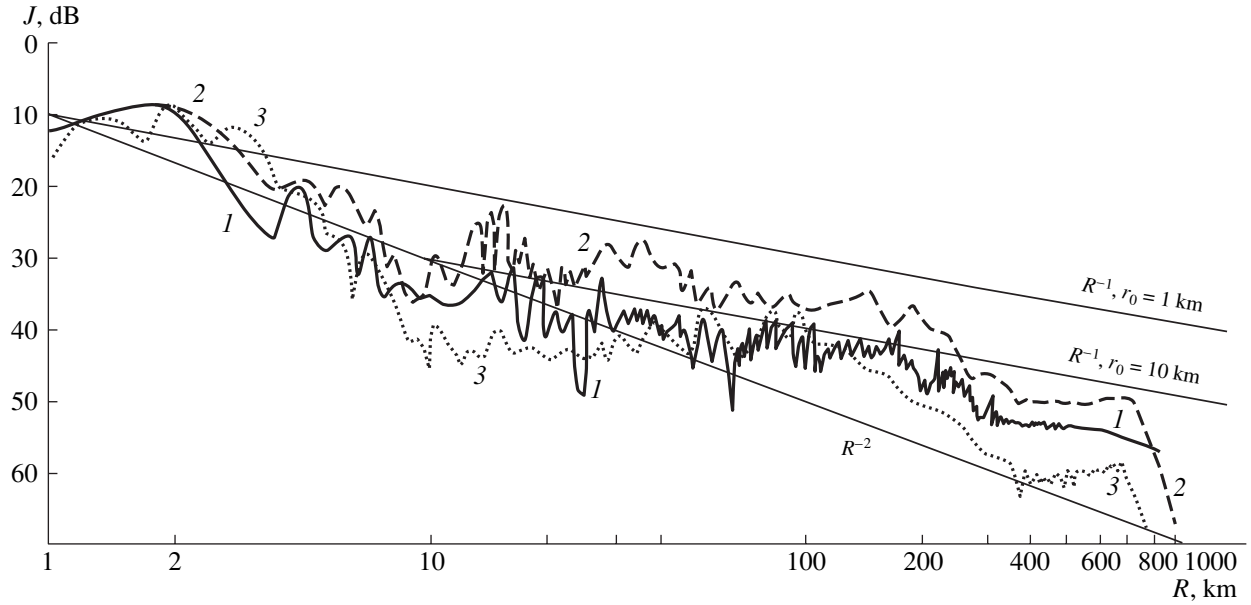

Fig. 3. Decays of the sound field level at the frequencies (*1*) 100, (*2*) 230, and (*3*) 400 Hz. The distance is plotted on a logarithmic scale.

replay of the records was used with an acceleration ratio of 32. The signals were digitized, encoded, and fed to the hard-disk memory of the computer. Since the signal spectra had narrow bands, we could use a much lower sampling frequency than the Kotel'nikov theorem dictates. To produce the desired sampling frequency, the pilot signal of 500 Hz was divided by a factor of 247 with the use of a divider counter circuit. The following sampling parameters were specified: the length of the information block $n = 2048$, the number of quantization levels $N = 2048$, the sampling frequency 2.02429 Hz, and the realization duration $T = 1012$ s (about 17 min). The running spectrum was estimated for time intervals of $T = 1012$ s, into which the total 113-h record was divided. The frequency resolution was $\Delta f = 0.001$ Hz. The FFT procedure was used in estimating the spectrum. To obtain the average estimate, spectral smoothing was performed by using a digital filter of low frequencies. The calculation procedure consisted in an envelope being obtained for each realization; the data were compensated and packed into a single block. The envelope was obtained on the basis of the Hilbert transformation. Upon a number of procedures, each value obtained for the envelope corresponded to a distance interval of 700 m. The values were smoothed within a 10-point window, which corresponds to a distance interval of 7 km. The processed data are presented in Figs. 4a–4c. The abscissa represents the distance (on a linear scale), and the ordinate is the sound level (in dB). Solid curves *1–3* correspond to the spherical (curve *1*) and cylindrical decay laws, the latter being calculated for the transition distances $r_0 = 1$ km (curve *2*) and $r_0 = 10$ km (curve *3*). The decays of the total sound field (including both coherent and incoherent components) are shown in analog (Fig. 4a) and digital form (Fig. 4b) (the latter is presented after discrete piecewise averaging over 7-km fractions of the path). The vertical shaded area of Fig. 4b indicates the incoherent field components. In Fig. 4c, the level of the coherent component is shown as a function of the distance for discrete piecewise averaging over 700-m (dots) and 7-km (broken curve) fractions of the path. With an arbitrary processing procedure, the averaged decay law at distances of up to 300 km can be approximated by a cylindrical dependence with a transition distance r_0 of 5 to 10 km. At distances of 350–700 km, the value of r_0 becomes close to 12–13 km. At 700–1000 km, an exponential decay takes place, with the attenuation coefficient of the total field, which is 0.6 to 0.7 dB/km, with a value of 0.8 dB/km for the coherent component. If one assumes that, at the moment of measurements at the terminal point of the path, the sea state is the same on the entire path and the losses caused by reflection are uniformly distributed over the path, the loss will be equal to 0.018–0.020 and 0.024 dB/km for the total field and the coherent component, respectively, with transition distance of $r_0 = 10$ km.

The instability of the meteorological parameters during experimentation leads to a situation when the sound field levels and their decays can differ from each other either on different parts of the path or on the entire path at different times. In such situations, with insufficient information on the sea state over the path, one can hardly expect good agreement between the experimental data and calculations at an arbitrary frequency and on an arbitrary fraction of the path. However, it seems to be advantageous to compare the experimental results with calculations, at least for the simplest waveguide

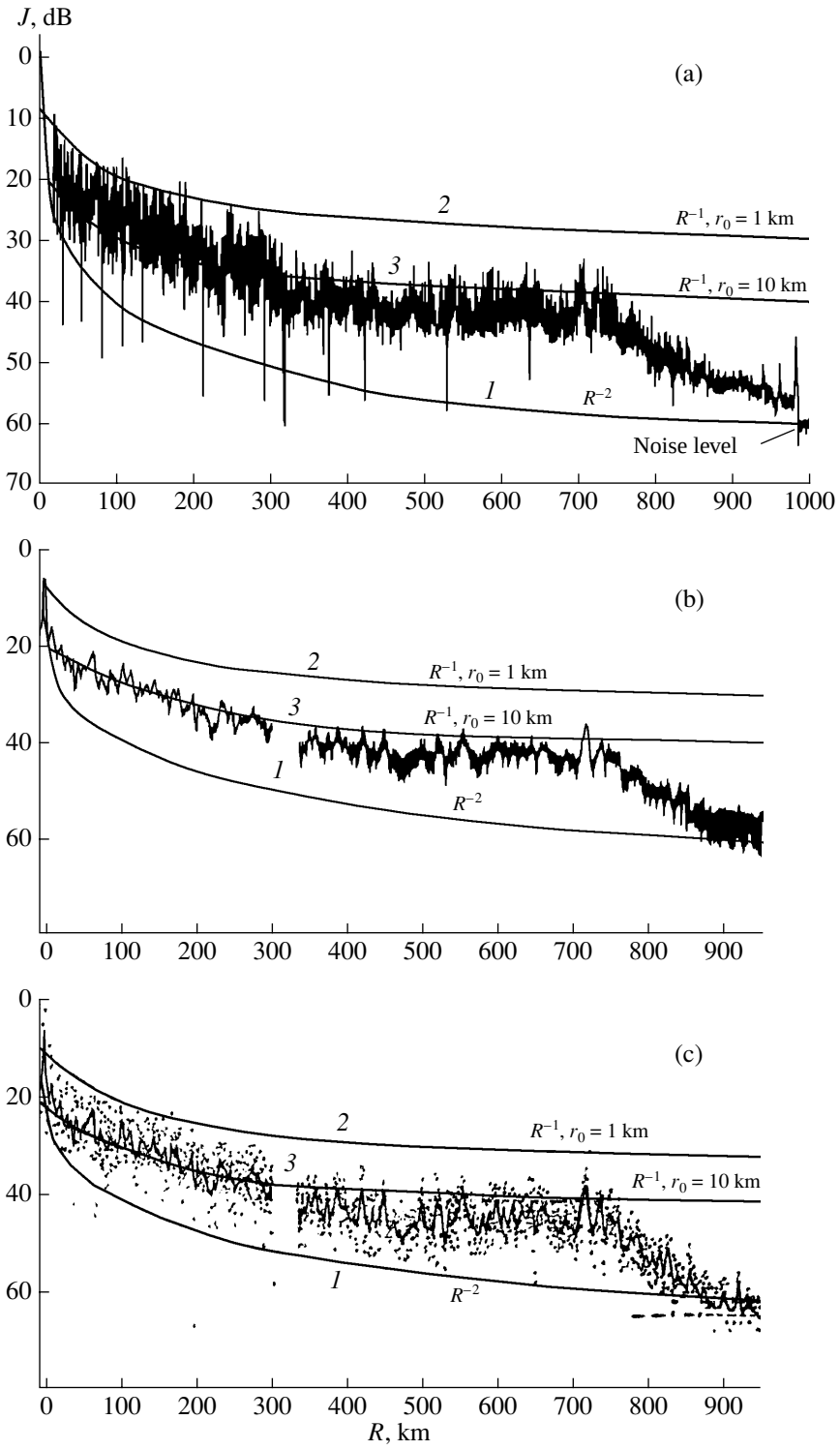

Fig. 4. Decay of the sound field level at a frequency of 230 Hz, as obtained by computer processing of the records: (a) the total field in analog form, (b) the total field (including the coherent and scattered components) in digital form, and (c) the coherent component. The shaded area in Fig. 4b corresponds to the incoherent field.

model, and to estimate the extent of the model adequacy. Because the waveguide at hand is the surface sound channel and the frequencies in use are rather high, ray considerations are appropriate as the first approximation. We used the ray code of Vagin and Maltsev [5], which takes into account the variable profile of the sound speed, the rough bottom relief, and the losses in the bottom and surface reflections. We used

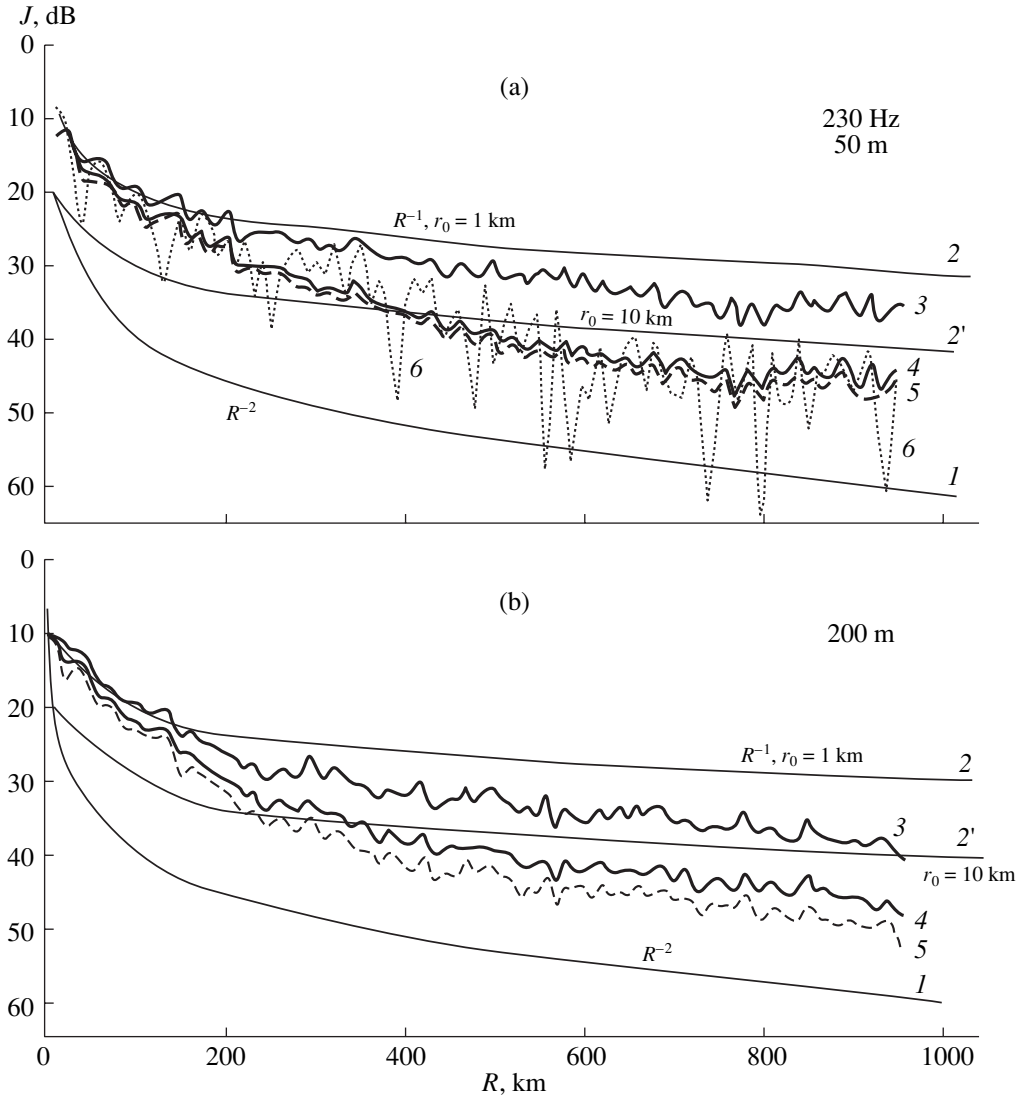

Fig. 5. Calculated decay laws for the sound field level at a frequency of 230 Hz for two reception depths: (a) 50 and (b) 200 m. Curves *1*, *2*, and *2*' correspond to the spherical and cylindrical decay laws; curves *3*, *4*, and *5* correspond to $h = 0$ and $\eta = 0.01$, $h = 3$ m and $\eta = 0.01$, and $h = 3$ m and $\eta = 0.1$, respectively; curve *6* (Fig. 5a) shows the result of phase-dependent summation for $h = 3$ m and $\eta = 0.01$.

the Rayleigh form for the coherent reflection from the surface. The spectrum of the surface waves was specified in the Pierson–Moskovitz form, which yields the following rms elevation of the surface: $h = 0.53 \times 10^{-2} v^2$, where h is expressed in meters and v is the wind speed in meters per second. The calculations were carried out for the frequencies of 230 and 400 Hz, with allowance for the measured bottom relief on the path, for a waterlike seafloor as an infinite half-space with a sound speed of 1550 m/s, a density of 1.6 g/cm^3, two different losses (η) of 0.1 and 0.01, and two wind speeds (v) that were taken to be 0 and 15 m/s over the entire path, these speeds corresponding to wave heights of 0 and 3 m. The sound speed profiles in the upper layers of the path were specified according to Fig. 1. In deeper layers, they corresponded to the data of other measurements [1]. The sound sources were supposed to be at a depth of 50 m, and the receivers were placed in the shelf zone, at depths of 50 and 200 m, 3 km away from the edge of the continental slope.

Figures 5a and 5b show the calculated levels of the coherent field at a frequency of 230 Hz with the summation of the field components in their intensities. Curves *1*, *2*, and *2*' represent the spherical and cylindrical decay laws. Curves *3*, *4*, and *5* are calculated with $h = 0$ and $\eta = 0.01$, $h = 3$ m and $\eta = 0.01$, and $h = 3$ m and $\eta = 0.1$, respectively. Curve *6* in Fig. 5a is obtained for the reception at a depth of 50 m with a phase-dependent summation of the components, at $h = 3$ m and $\eta = 0.01$. One can see that, even in the case of a smooth surface, the losses caused by bottom reflections in the wedge are 5–6 dB at 50 m and 8–10 dB at 200 m for a

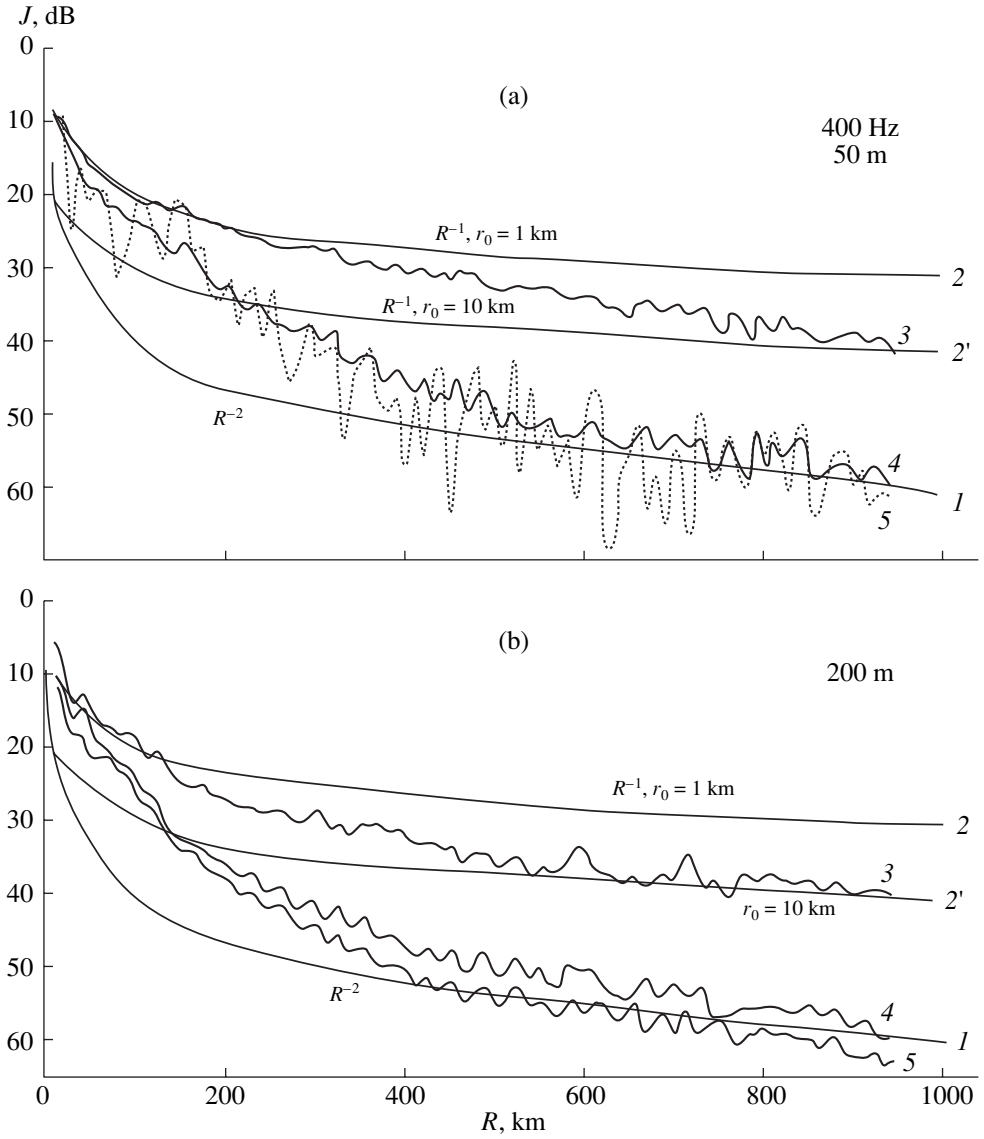

Fig. 6. Calculated decay laws for the sound field level at a frequency of 400 Hz for two reception depths: (a) 50 and (b) 200 m. Curves *1*, *2*, and *2*' correspond to the spherical and cylindrical decay laws; curves *3*, *4*, and *5* (the lower plot) correspond to $h = 0$ and $\eta = 0.01$, $h = 3$ m and $\eta = 0.01$, and $h = 3$ m and $\eta = 0.1$, respectively; curve *5* (the upper plot) shows the result of the phase-dependent summation for $h = 3$ m and $\eta = 0.01$.

distance of 1000 km, assuming that the decay law is cylindrical with the transition distance $r_0 = 1$ km. Additional losses caused by the surface waves with $h = 3$ m are as small as 10 dB, that is, less than 0.01 dB/km. The calculated total loss caused by the bottom and surface reflections is about 20 dB, which is close to the experimental data. Figure 6 shows the results of the calculation at 400 Hz with the same input data and the same curve designations as in Fig. 5. The losses caused by the bottom reflections in the wedge nearly coincide for both frequencies. However, the losses caused by the surface are substantially higher in this case: 20 dB at 760 km (with a 30-dB value of the total loss), which is close to the experimental data, precisely as at 230 Hz. If one specifies the losses caused by the bottom by a factor of 10 higher, the total losses will change insignificantly for the propagation conditions at hand. With a signal reception near the surface (50 m), the difference in the sound field levels is lower than 1–2 dB; it is within 3–4 dB at the 200-m horizon for all distances up to 1000 km at both frequencies. The close values of the calculated and experimental total loss can be obtained only for certain reception points. In general, the experimental and calculated levels of the sound field and its decay laws are different.

The results obtained can be summarized as follows:

(1) The intensity and space-time structures are studied for the sound fields generated by highly stable sound sources of 100, 230, and 400 Hz, on a 1000-km

path in winter, in the near-Kamchatka region of the Pacific Ocean, with a strong surface sound channel and wind surface waves.

(2) For the sound field levels, the decay laws are determined in the case of long-range propagation at low frequencies, in winter, with sound sources continuously towed for 115 hours, under varying sea states of Beoufort 1–2 to 5–6.

(3) The decay laws are estimated for the total (including both coherent and scattered components) and coherent components of the sound field at a frequency of 230 Hz.

(4) The experimental decay laws obtained at 230 and 400 Hz are compared with those calculated by the ray-theory algorithm taking into account the sound speed profiles and bottom relief varying along the path with various but path-constant bottom parameters and surface roughness.

(5) The results obtained are useful for both scientific studies of the sound field structure in natural waveguides and practical-purpose tasks of selecting the input data in estimating the efficiency of fixed underwater acoustic systems moored in the coastal-wedge regions, with allowance made for the wind-generated surface waves.

ACKNOWLEDGMENTS

I am grateful to A.S. Shilyakhin and V.Ya. Faizov for the assistance in performing the experiments, data processing, and computer calculations; I am grateful to G.A. Studenichnik for assistance in data processing and graphical representation of the results. This work was supported by the Russian Foundation for Basic Research, project no. 01-02-16636.

REFERENCES

1. N. V. Studenichnik, Akust. Zh. **46**, 850 (2000) [Acoust. Phys. **46**, 749 (2000)].
2. N. V. Studenichnik, Akust. Zh. **49**, 542 (2003) [Acoust. Phys. **49**, 455 (2003)].
3. G. V. Norton and J. C. Novarini, J. Acoust. Soc. Am. **103**, 1836 (1998).
4. N. V. Studenichnik, Akust. Zh. **48**, 123 (2002) [Acoust. Phys. **48**, 110 (2002)].
5. A. V. Vagin and N. E. Mal'tsev, Vopr. Sudostr., Ser. Akust., No. 9, 61 (1977).

Translated by E. Kopyl

Acoustical Physics, Vol. 49, No. 6, 2003, pp. 721–728. Translated from Akusticheskiĭ Zhurnal, Vol. 49, No. 6, 2003, pp. 843–851.

Waveguide Properties of a Plane Ring-Shaped Plate. I. Flexural Waves

V. V. Tyutekin

Andreev Acoustics Institute, Russian Academy of Sciences, ul. Shvernika 4, Moscow, 117036 Russia

e-mail: Tyutekin@akin.ru

Received February 26, 2003

Abstract—A new type of the so-called "angular" waves for flexural normal modes propagating in a ring-shaped plate is studied. A dispersion equation for wave numbers, an equation for critical frequencies, and expressions for the eigenfunctions of such a waveguide are derived. Solutions to these equations are obtained by numerical methods for various values of parameter *d*, which represents the relative width of the ring. The solutions are analyzed, and the main properties of dispersion curves are described. Individual normal modes are identified on the basis of the calculation and further analysis of eigenfunctions. *© 2003 MAIK "Nauka/Interperiodica".*

The propagation of elastic waves in rods, shells, plates, etc., is considered in numerous publications. The interest in this subject is connected, first of all, with the necessity to determine the dynamical properties of structures used in construction, transportation (in particular, shipbuilding and aircraft), and other areas of application. Papers concerned with the waveguide properties of plates or their parts represent a particular group of studies. Among the great number of such publications, here it is appropriate to note the papers by Konenkov [1, 2], which consider the properties of platelike strips performing flexural vibrations, and the papers by Bobrovnitskii [3, 4], which are devoted to the study of the properties of "angular" platelike structures whose waveguide properties are determined by the interaction of flexural and shear longitudinal waves.

This paper considers the waveguide properties of a ring-shaped flat plate, in which "angular" normal modes of the flexural type propagate. The normal modes of this type were studied earlier in several papers. For example, the sound waves inherent in an acoustic waveguide with curved walls were investigated in [5, 6]. Angular waves propagating along the surface of an elastic cylinder were considered (in the high-frequency approximation) in [7–9]. Such waves are taken into account, in particular, in solving the problems of diffraction by cylindrical obstacles [10, 11].

Since in this paper, as in the aforementioned papers, we assume that the polar angle θ varies within the range $-\infty < \theta < \infty$, the solution to the problem mathematically treated on a multisheeted Riemann surface. In this case, the physical object under study can be treated as a coil with a very small step (in vertical) under the assumption that only the waves of the flexural type remain, while the waves of the shear longitudinal type are absent. If polar angle θ varies within the limits $0 \le \theta \le \pi$, this part of the ring may be considered as an "insert" between two rectilinear strips performing flexural vibrations. From this point of view, the investigation of the waveguide properties of a ring-shaped plate is of great practical interest.

Let us set the geometrical dimensions of such a plate as follows: $r = a$ is the exterior boundary, $r = b$ is the interior boundary, and $2L = a - b$ is the width of the ring.

The equation of flexural vibrations of a plate in cylindrical coordinates has the form

$$(\Delta^2 - k_0^4)W = 0. \quad (1)$$

Here, W is the transverse displacement of a plate, k_0 is the wave number of flexural waves, $k_o^4 = \dfrac{\varepsilon h\omega^2}{D_m}$, ρ is the density, h is the plate thickness, $D_m = \dfrac{Eh^3}{12(1-\sigma^2)}$ is the flexural rigidity, E is Young's modulus, and σ is Poisson's ratio. The Laplacian Δ in cylindrical coordinates has the form $\Delta = \dfrac{\partial^2}{\partial r^2} + \dfrac{1}{r}\dfrac{\partial}{\partial r} + \dfrac{1}{r^2}\dfrac{\partial^2}{\partial\theta^2}$.

Equation (1) can be broken into two independent equations

$$\Delta W + k_0^2 W = 0, \quad (2)$$

$$\Delta W - k_0^2 W = 0. \quad (3)$$

We seek their solutions in the form of flexural waves propagating in the direction of increasing angle θ: $W = W_0(r)\exp(i\nu\theta)$, where $W_0(r)$ is the wave amplitude and

ν is an unknown constant playing the role of the angular wave number. Substituting this expression into Eqs. (2) and (3), we obtain

$$\frac{d^2W_0}{dr^2} + \frac{1}{r}\frac{dW_0}{dr} + \left(k_0^2 - \frac{\nu^2}{r^2}\right)W_0 = 0, \tag{4}$$

$$\frac{d^2W_0}{dr^2} + \frac{1}{r}\frac{dW_0}{dr} - \left(k_0^2 + \frac{\nu^2}{r^2}\right)W_0 = 0. \tag{5}$$

Linear-independent solutions to Eq. (4) are the Bessel $J_\nu(k_0r)$ and Neumann $Y_\nu(k_0r)$ functions, and the linear-independent solutions to Eq. (5) are the modified Bessel function $I_\nu(k_0r)$ and the Macdonald function $K_\nu(k_0r)$. The general solution for $W_0(r)$ has the form

$$\begin{aligned} W_0(r) &= AJ_\nu(k_0r) + BY_\nu(k_0r) \\ &+ CI_\nu(k_0r) + DK_\nu(k_0r), \end{aligned} \tag{6}$$

where A, B, C, and D are unknown constants.

We use the absence of stress at the internal $r = a$ and external $r = b$ boundaries of the ring as the boundary conditions, which can be expressed by the equations [12]

$$\begin{aligned} M_r = 0 \text{ and } V = Q_r - \frac{1}{r}\frac{\partial M_{r\theta}}{\partial\theta} = 0 \\ \text{at } r = a, b. \end{aligned} \tag{7}$$

Here,

$$M_r = -D_m\left[\frac{\partial^2W}{\partial r^2} + \sigma\left(\frac{1}{r}\frac{\partial W}{\partial r} + \frac{1}{r^2}\frac{\partial^2W}{\partial\theta^2}\right)\right]$$

is the bending moment,

$$Q_r = -D_m\frac{\partial}{\partial r}(\Delta W) \text{ is the shearing force, and}$$

$$M_{r\theta} = D_m(1-\sigma)\left(\frac{1}{r}\frac{\partial^2W}{\partial r\partial\theta} - \frac{1}{r^2}\frac{\partial W}{\partial\theta}\right)$$

is the torsional moment.

To represent the expressions obtained from the transformation of these formulas in a compact form, we introduce the operators

$$L_1^\pm(r, \nu) = \frac{(1-\sigma)}{k_0r}\frac{d}{d(k_0r)} + \left[\pm 1 + (1-\sigma)\left(\frac{\nu}{k_0r}\right)^2\right], \tag{8}$$

$$\begin{aligned} L_2^\pm(r, \nu) &= \left[\pm 1 + (1-\sigma)\left(\frac{\nu}{k_0r}\right)^2\right]\frac{d}{d(k_0r)} \\ &- \frac{(1-\sigma)}{k_0r}\left(\frac{\nu}{k_0r}\right)^2. \end{aligned} \tag{9}$$

Here, the upper sign (+) corresponds to the functions $J_\nu(k_0r)$ and $Y_\nu(k_0r)$, and the lower sign (–), to the functions $I_\nu(k_0r)$ and $K_\nu(k_0r)$. Using these notations, the generalized dimensionless stress can be represented in the form

$$\begin{aligned} \frac{M_r}{D_mk_0^2} &= L_1^+(r, \nu)[AJ_\nu(k_0r) + BY_\nu(k_0r)] \\ &+ L_1^-(r, \nu)[CI_\nu(k_0r) + DK_\nu(k_0r)], \end{aligned} \tag{10}$$

$$\begin{aligned} \frac{V}{D_mk_0^3} &= L_2^+(r, \nu)[AJ_\nu(k_0r) + BY_\nu(k_0r)] \\ &+ L_2^-(r, \nu)[CI_\nu(k_0r) + DK_\nu(k_0r)]. \end{aligned} \tag{11}$$

Substituting Eqs. (10) and (11) into boundary conditions (7), we obtain the following homogeneous set of equations with respect to the unknown coefficients A, B, C, and D:

$$\begin{aligned} &AL_1^+(a, \nu)J_\nu(k_0a) + BL_1^+(a, \nu)Y_\nu(k_0a) \\ &+ CL_1^-(a, \nu)I_\nu(k_0a) + DL_1^-(a, \nu)K_\nu(k_0a) = 0, \\ &AL_1^+(b, \nu)J_\nu(k_0b) + BL_1^+(b, \nu)Y_\nu(k_0b) \\ &+ CL_1^-(b, \nu)I_\nu(k_0b) + DL_1^-(b, \nu)K_\nu(k_0b) = 0, \\ &AL_2^+(a, \nu)J_\nu(k_0a) + BL_2^+(a, \nu)Y_\nu(k_0a) \\ &+ CL_2^-(a, \nu)I_\nu(k_0a) + DL_2^-(a, \nu)K_\nu(k_0a) = 0, \\ &AL_2^+(b, \nu)J_\nu(k_0b) + BL_2^+(b, \nu)Y_\nu(k_0b) \\ &+ CL_2^-(b, \nu)I_\nu(k_0b) + DL_2^-(b, \nu)K_\nu(k_0b) = 0. \end{aligned} \tag{12}$$

The condition for a nontrivial solution leads to a characteristic equation for the determination of the unknown value of the angular wave number ν:

$$\Delta(\nu) = \begin{vmatrix} L_1^+(a, \nu)J_\nu(k_0a) & L_1^+(a, \nu)Y_\nu(k_0a) & L_1^-(a, \nu)I_\nu(k_0a) & L_1^-(a, \nu)K_\nu(k_0a) \\ L_1^+(b, \nu)J_\nu(k_0b) & L_1^+(b, \nu)Y_\nu(k_0b) & L_1^-(b, \nu)I_\nu(k_0b) & L_1^-(b, \nu)K_\nu(k_0b) \\ L_2^+(a, \nu)J_\nu(k_0a) & L_2^+(a, \nu)Y_\nu(k_0a) & L_2^-(a, \nu)I_\nu(k_0a) & L_2^-(a, \nu)K_\nu(k_0a) \\ L_2^+(b, \nu)J_\nu(k_0b) & L_2^+(b, \nu)Y_\nu(k_0b) & L_2^-(b, \nu)I_\nu(k_0b) & L_2^-(b, \nu)K_\nu(k_0b) \end{vmatrix} = 0. \tag{13}$$

To calculate the derivatives of the cylindrical functions involved in the operators $L_{1,2}^{\pm}$, it is expedient in this case to use the formulas

$$\frac{dZ_\nu(x)}{dx} = \pm Z_{\nu+1}(x) + \frac{\nu}{x}Z_\nu(x), \qquad (13')$$

where the plus sign corresponds to the function $I_\nu(k_0 r)$ and the minus sign corresponds to the functions $J_\nu(k_0 r)$, $Y_\nu(k_0 r)$ and $K_\nu(k_0 r)$, $x = k_0 a, k_0 b$. The solution to the equation $\Delta(\nu) = 0$ has a set of roots $\nu = \nu_n(k_0 a, k_0 b)$, where index n determines different branches of the solution to the characteristic equation. To identify them and to check the fulfillment of boundary conditions (7), we assume that the roots $\nu_n(k_0 a, k_0 b)$ are calculated and determine the eigenfunctions (the modes) of the waveguide under consideration. To do this we use the first three equations of system (12) (it is evident that the fourth equation is their linear combination). Setting $A = 1$ (which does not violate the generality of the solution), we obtain an inhomogeneous set of equations for the determination of the remaining coefficients depending on both ν_n and n:

$$\begin{aligned}
&B_n L_1^+(a, \nu_n) Y_{\nu_n}(k_0 a) + C_n L_1^-(a, \nu_n) I_{\nu_n}(k_0 a) \\
&+ D_n L_1^-(a, \nu_n) K_{\nu_n}(k_0 a) = -L_1^+(a, \nu_n) J_{\nu_n}(k_0 a), \\
&B_n L_1^+(b, \nu_n) Y_{\nu_n}(k_0 b) + C_n L_1^-(b, \nu_n) I_{\nu_n}(k_0 b) \\
&+ D_n L_1^-(b, \nu_n) K_{\nu_n}(k_0 b) = -L_1^+(b, \nu_n) J_{\nu_n}(k_0 b), \\
&B_n L_2^+(a, \nu_n) Y_{\nu_n}(k_0 a) + C_n L_2^-(a, \nu_n) I_{\nu_n}(k_0 a) \\
&+ D_n L_2^-(a, \nu_n) K_{\nu_n}(k_0 a) = -L_2^+(a, \nu_n) J_{\nu_n}(k_0 a).
\end{aligned} \qquad (14)$$

The solution to system (14) can be represented in the form

$$B_n = \frac{\Delta_B(\nu_n)}{\Delta(\nu_n)}, \quad C_n = \frac{\Delta_C(\nu_n)}{\Delta(\nu_n)}, \quad D_n = \frac{\Delta_D(\nu_n)}{\Delta(\nu_n)}, \qquad (15)$$

where

$$\Delta(\nu_n) = \begin{vmatrix} L_1^+(a, \nu_n) Y_{\nu_n}(k_0 a) & L_1^-(a, \nu_n) I_{\nu_n}(k_0 a) & L_1^-(a, \nu_n) K_{\nu_n}(k_0 a) \\ L_1^+(b, \nu_n) Y_{\nu_n}(k_0 b) & L_1^-(b, \nu_n) I_{\nu_n}(k_0 b) & L_1^-(b, \nu_n) K_{\nu_n}(k_0 b) \\ L_2^+(a, \nu_n) Y_{\nu_n}(k_0 a) & L_2^-(a, \nu_n) I_{\nu_n}(k_0 a) & L_2^-(a, \nu_n) K_{\nu_n}(k_0 a) \end{vmatrix}$$

$$\Delta_B(\nu_n) = -\begin{vmatrix} L_1^+(a, \nu_n) J_{\nu_n}(k_0 a) & L_1^-(a, \nu_n) I_{\nu_n}(k_0 a) & L_1^-(a, \nu_n) K_{\nu_n}(k_0 a) \\ L_1^+(b, \nu_n) J_{\nu_n}(k_0 b) & L_1^-(b, \nu_n) I_{\nu_n}(k_0 b) & L_1^-(b, \nu_n) K_{\nu_n}(k_0 b) \\ L_2^+(a, \nu_n) J_{\nu_n}(k_0 a) & L_2^-(a, \nu_n) I_{\nu_n}(k_0 a) & L_2^-(a, \nu_n) K_{\nu_n}(k_0 a) \end{vmatrix}$$

$$\Delta_C(\nu_n) = -\begin{vmatrix} L_1^+(a, \nu_n) Y_{\nu_n}(k_0 a) & L_1^+(a, \nu_n) J_{\nu_n}(k_0 a) & L_1^-(a, \nu_n) K_{\nu_n}(k_0 a) \\ L_1^+(b, \nu_n) Y_{\nu_n}(k_0 b) & L_1^+(b, \nu_n) J_{\nu_n}(k_0 b) & L_1^-(b, \nu_n) K_{\nu_n}(k_0 b) \\ L_2^+(a, \nu_n) Y_{\nu_n}(k_0 a) & L_2^+(a, \nu_n) J_{\nu_n}(k_0 a) & L_2^-(a, \nu_n) K_{\nu_n}(k_0 a) \end{vmatrix}$$

$$\Delta_D(\nu_n) = -\begin{vmatrix} L_1^+(a, \nu_n) Y_{\nu_n}(k_0 a) & L_1^-(a, \nu_n) I_{\nu_n}(k_0 a) & L_1^+(a, \nu_n) J_{\nu_n}(k_0 a) \\ L_1^+(b, \nu_n) Y_{\nu_n}(k_0 b) & L_1^-(b, \nu_n) I_{\nu_n}(k_0 b) & L_1^+(b, \nu_n) J_{\nu_n}(k_0 b) \\ L_2^+(a, \nu_n) Y_{\nu_n}(k_0 a) & L_2^-(a, \nu_n) I_{\nu_n}(k_0 a) & L_2^+(a, \nu_n) J_{\nu_n}(k_0 a) \end{vmatrix}.$$

The waveguide eigenfunctions corresponding to the coefficients obtained above can be written in the form

$$\begin{aligned}
W_n &= J_{\nu_n}(k_0 r) + B_n Y_{\nu_n}(k_0 r) \\
&+ C_n I_{\nu_n}(k_0 r) + D_n K_{\nu_n}(k_0 r);
\end{aligned} \qquad (16)$$

$$\begin{aligned}
\frac{M_r}{D_m k_0^2} &= L_1^+(r, \nu_n) J_{\nu_n}(k_0 r) + B_n L_1^+(r, \nu_n) Y_{\nu_n}(k_0 r) \\
&+ C_n L_1^-(r, \nu_n) I_{\nu_n}(k_0 r) + D_n L_1^-(r, \nu_n) K_{\nu_n}(k_0 r);
\end{aligned} \qquad (17)$$

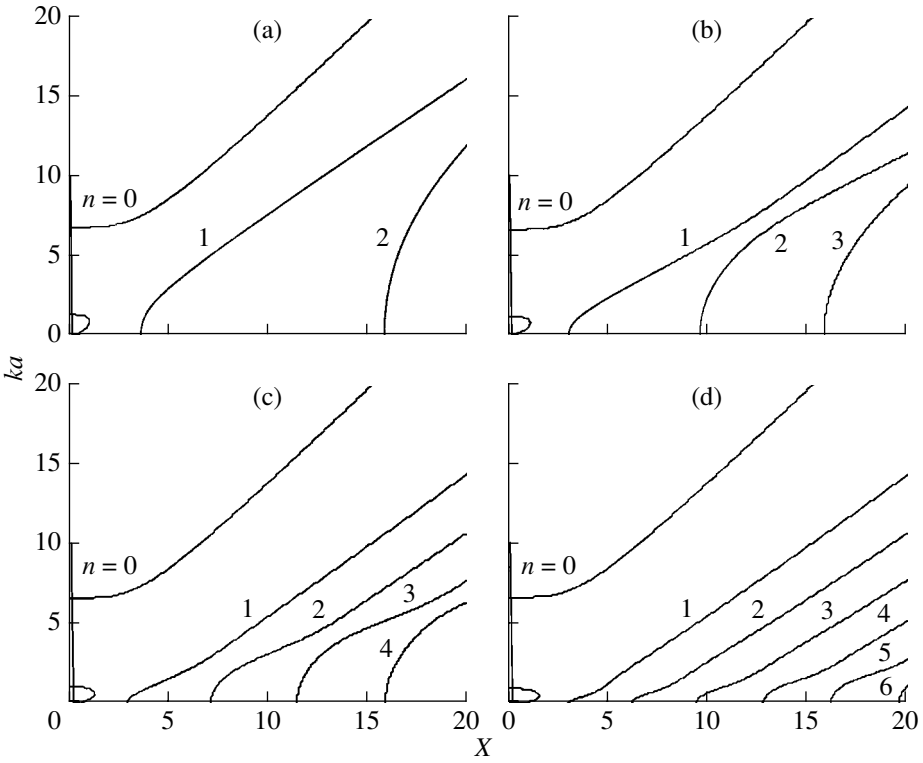

Fig. 1. Dispersion curves for the angular normal modes of a ring. The parameter is $X = k_0 a$; the values of parameter d are (a) 0.3; (b) 0.5; (c) 0.7; and (d) 0.9.

$$\frac{V}{D_m k_0^3} = L_2^+(r, \nu_n) J_{\nu_n}(k_0 r) + B_n L_2^+(r, \nu_n) Y_{\nu_n}(k_0 r) + C_n L_2^-(r, \nu_n) I_{\nu_n}(k_0 r) + D_n L_2^-(r, \nu_n) K_{\nu_n}(k_0 r). \quad (18)$$

Before discussing the results of calculations, it is necessary to make several remarks about their representation.

It was indicated above that the desired quantity ν plays the role of the angular wave number involved in the expression for the phase of a normal mode $\varphi = \nu\theta$. According to [6], we transform this expression as follows: $\varphi = \frac{\nu}{r} r\theta = k_r S$, where $k_r = \frac{\nu}{r}$ is the "linear" wave number and $S = r\theta$ is the arc length traveled by the wave. Choosing this form of representation for the results, we set $r = a$ for definiteness; i.e., we consider the wave number corresponding to the exterior boundary of the ring. In this case, in the given equations the unknown quantity ν can be replaced by $\nu = ka$ (here, we omit the subscript of k). The arguments involved in the equations given above can be selected in the form $k_0 a$ and $k_0 b = k_0 a(1 - d)$, where $d = 2L/a$ is the dimensionless width of the ring.

The "linear" velocity c also depends on the radius. Choosing the quantity $k_0 a$ as the main argument, the desired dimensionless velocity can be written in the form $C = \frac{c}{c_0} = \frac{k_0 a}{\nu} = \frac{k_0 a}{ka}$, where c_0 is the velocity of flexural waves in the plate.

Equation (13) was solved for the unknown quantity $\nu = ka$ as a function of the dimensionless frequency $k_0 a$ for different values of ring width d. The solution was performed using a special computer code. Figure 1 presents the results of calculation for different values of d. The quantity $X = k_0 a$ is plotted in the abscissa, and $\nu = ka$, in the ordinate.

This plot is typical of all values of the parameter $0 < d < 1$. Three groups of dispersion curves are observed: (1) single branches ($n = 0$) starting at zero frequency; (2) an infinite number of branches, which correspond (as in any waveguide) to the normal modes of higher orders whose number grows as d increases; and (3) single branches in the form of half-closed loops located in the immediate vicinity of the coordinate origin.

These branches are given in Fig. 2 for some values of parameter d. As far as we know, such branches for normal modes were never considered earlier in the theory of elastic waveguides. In this paper, the properties of such waves are not examined in detail.

Single branches ($n = 0$) have some specific properties. Since all their values of ν lie above the straight line $\nu = X$, the phase velocities of this type of waves are always smaller than the velocity of flexural waves in a

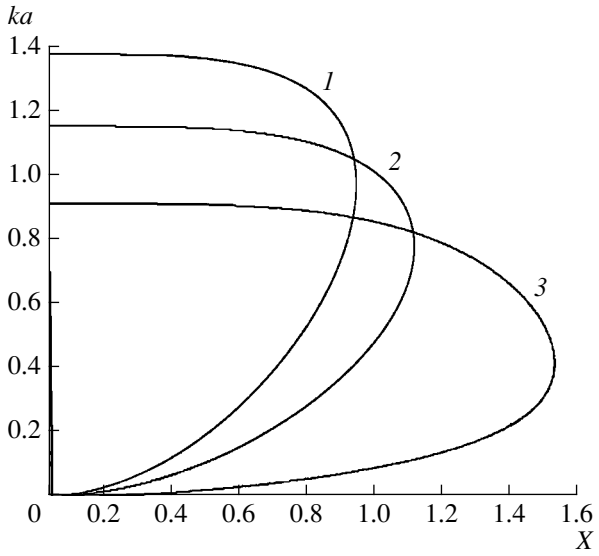

Fig. 2. Low-frequency half-closed branches for d = (*1*) 0.1; (*2*) 0.5; and (*3*) 0.9.

free plate. A characteristic property of these waves is their identity under the variation of parameter d, at least within the limits $0.3 < d < 1$. The divergence of branches manifests itself at smaller values of d, which can be seen in Fig. 3a, which shows the plots for different values of d. (This phenomenon will be explained below.) Another peculiarity of branches with $n = 0$ at low frequencies is the presence of horizontal sections, where the dimensionless velocity C linearly increases with frequency. This velocity can be represented by the expression $C \approx 0.15k_0a$ for values of $0.3 < d < 1$. In the case of the phase velocity of this wave, the above expression transforms to the formula $c = 0.15\omega a$, which gives a linear dependence on frequency and the outer size of the ring. This formula is valid up to values of $k_0a \approx 2$ (Fig. 3b). The same figure presents data for other values of d, which also give a linear dependence. At higher frequencies (parameter X), the values of C for all d tend to the asymptotic value $C_\infty \approx 0.825$ indicated in Fig. 3b by the dashed line. More detailed calculations conducted up to values of $\nu \approx 100$ show that, in this case, the quantity C can be represented in the form

$$C = \frac{c}{c_0} \approx C_\infty - \frac{1}{k_0 a}. \tag{19}$$

One can see from Fig. 1 that the normal modes of higher orders ($n \geq 1$) arise at $\nu_n = 0$. In this case, the quantities describing the field of flexural waves do not depend on polar angle θ. At the moment of initiation of each such wave, its wave front is a circle "coaxial" with the waveguide boundaries $r = a$ and $r = b$. In this case, the displacement is expressed via the cylindrical functions of zero order. In planar waveguides, the process of the formation of normal modes is analogous to that considered above: the wave front is parallel to the planar boundaries of a waveguide.

As in planar waveguides, critical frequencies exist in the system under study (the frequencies of wave initiation). An equation for critical frequencies can be derived readily from Eq. (13) by setting $\nu = \nu_n = 0$.

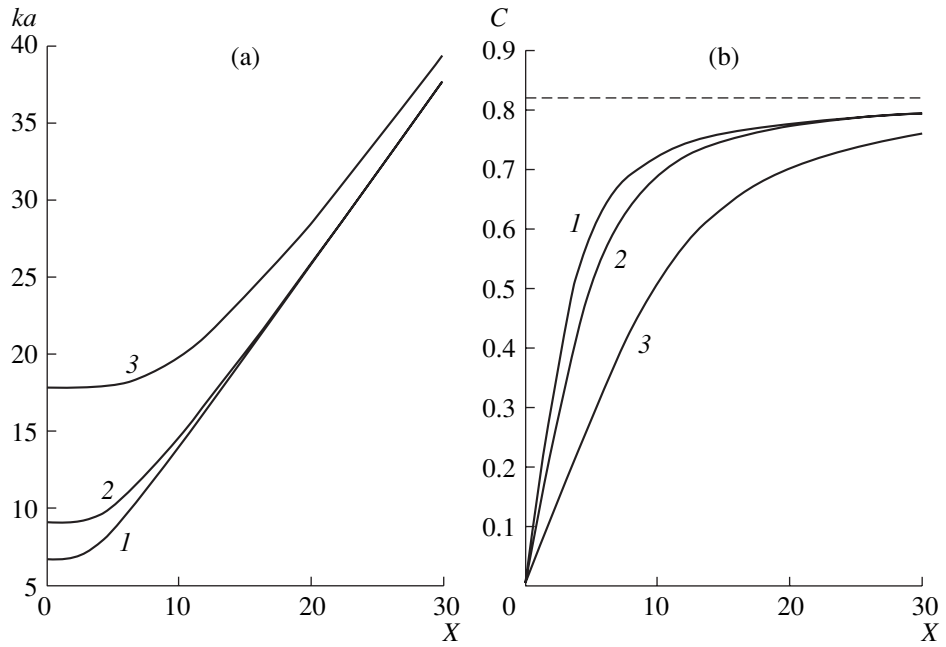

Fig. 3. Characteristics of normal modes with $n = 0$: (a) the dimensionless wave numbers and (b) the velocities; d = (*1*) 0.3–0.999; (*2*) 0.05; and (*3*) 0.01.

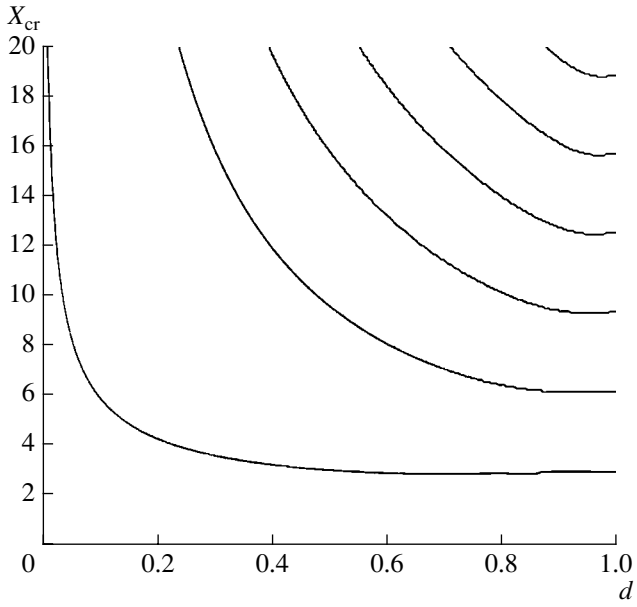

Fig. 4. Critical frequencies for normal modes with $n \geq 1$ as functions of parameter d.

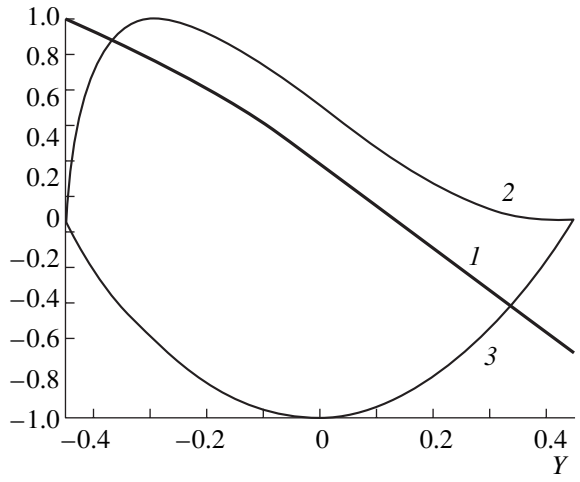

Fig. 5. Eigenfunctions for the normal mode with n =1 at d = 0.9: (*1*) displacement W; (*2*) moment M_r; and (*3*) force V.

Then, taking into account Eq. (13'), operators $L^{\pm}_{1,2}$ should be represented as

$$L^{\pm}_1(r, 0) = \frac{(1-\sigma)}{k_0^2 r}\frac{d}{dr} \pm 1; \quad L^{\pm}_2(r, 0) = \pm\frac{d}{k_0 dr},$$

and Eq. (13) takes the form

$$\begin{vmatrix} J(k_0a) & Y(k_0a) & I(k_0a) & K(k_0a) \\ J(k_0b) & Y(k_0b) & I(k_0b) & K(k_0b) \\ J_1(k_0a) & Y_1(k_0a) & I_1(k_0a) & K_1(k_0a) \\ J_1(k_0b) & Y_1(k_0b) & I_1(k_0b) & K_1(k_0b) \end{vmatrix} = 0, \qquad (20)$$

where additional notations are introduced:

$$J(x) = -\frac{1-\sigma}{x}J_1(x) + J_0(x);$$

$$Y(x) = -\frac{1-\sigma}{x}Y_1(x) + Y_0(x);$$

$$I(x) = \frac{1-\sigma}{x}I_1(x) + I_0(x);$$

$$K(x) = \frac{1-\sigma}{x}K_1(x) + K_0(x).$$

Figure 4 presents a solution to Eq. (20) in the form of the dependence of X_{cr} on parameter d, which gives the values of the dimensionless critical frequencies.

The calculation of eigenfunctions for displacement W, dimensionless moment M_r, and force V was conducted with the help of Eqs. (15)–(18) to identify different branches of the dispersion curves. The indicated values were normalized to their corresponding maximum values, and the dimensionless radial coordinate Y was set in the form $Y = \frac{r}{a} - \frac{a+b}{2a}$, so that the median line of the ring was taken for the coordinate origin and the value of Y varied within the limits $-\frac{d}{2} \leq Y \leq \frac{d}{2}$.

The results of calculation are given in the figures below.

Let us consider the results starting from the numbers $n \geq 1$. It is most convenient to represent the eigenfunctions at critical frequencies at $\nu = 0$ and d close to unity (the value of d = 0.9 was used). Figure 5 gives results for n = 1. One can see that the boundary conditions are satisfied to a good accuracy. Displacements W at the ring boundaries have opposite signs, and, therefore, this wave is "quasi-asymmetric": owing to the cylindrical divergence of the wave, the displacement at the outer boundary is smaller than that at the internal boundary, and it vanishes not at the ring center. In this case, the force functions are quasi-symmetric. Figure 6 presents the results for n = 2. They are analogous to those described above, but the wave is "quasi-symmetric": displacements W at the ring boundaries have the same signs and their maximum occurs near the median line of the ring. Figure 7 shows that the wave with n = 3 is quasi-asymmetric. Thus, the waves of higher orders are waves of alternating parity. In the case of rectilinear boundaries (a strip), they can be separated from each other already at the stage of solving the problem [4].

Similar plots for normal modes with n = 0 are presented in Figs. 8 and 9. The data are given for the parameter d = 0.05 at k_0a = 2, ν = 9.08 (Fig. 8a) and k_0a = 15, ν = 20.7 (Fig. 8b), and also for d = 0.3 at k_0a = 2, ν = 6.72 (Fig. 9a) and k_0a = 21, ν = 27 (Fig. 9b). One can see that, in the case of a small parameter d and low frequencies, the force functions have a strongly sym-

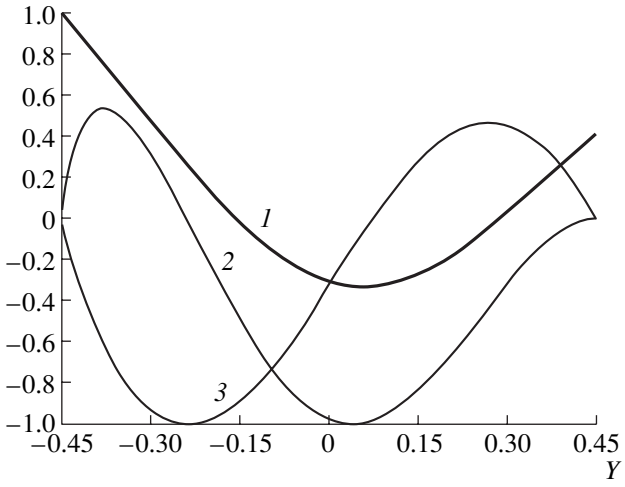

Fig. 6. The same as in Fig. 5 but for $n = 2$.

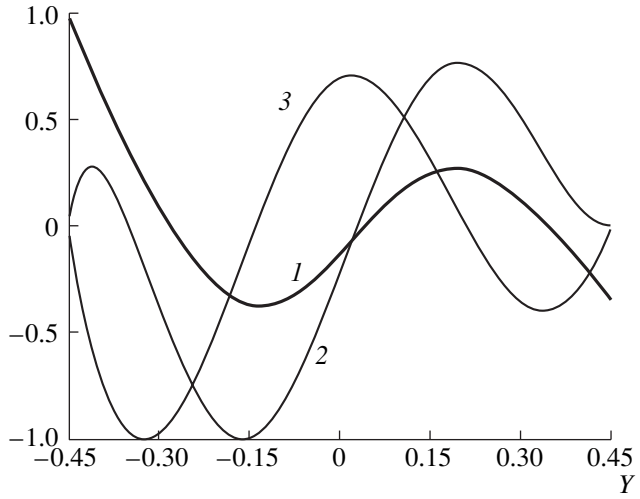

Fig. 7. The same as in Fig. 5 but for $n = 3$.

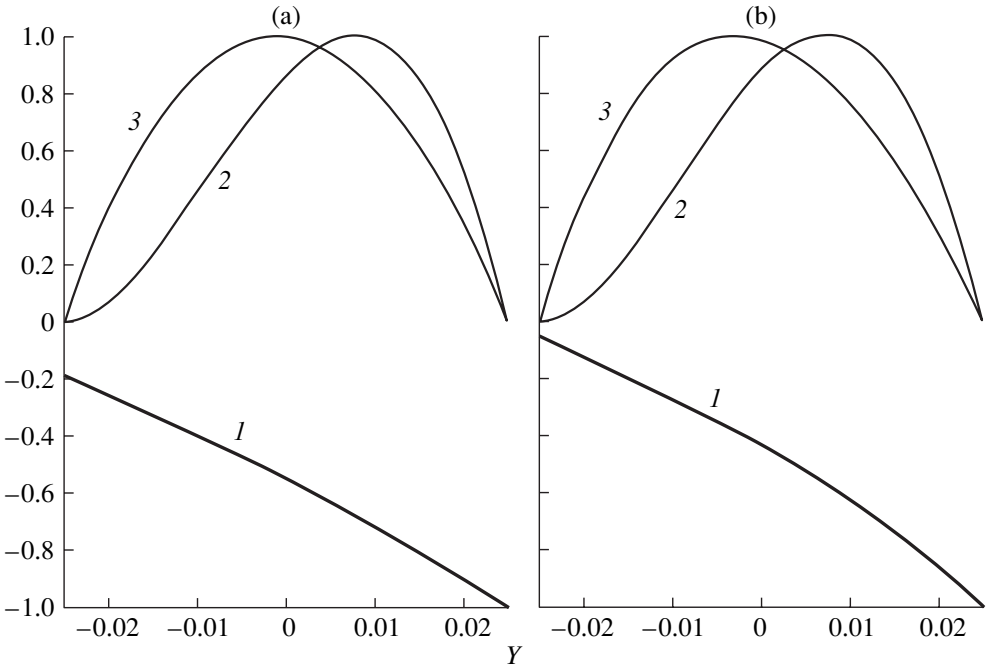

Fig. 8. Eigenfunctions for the normal mode with $n = 0$ at $d = 0.05$; X = (a) 2 and (b) 15.

metrical character and the displacement increases from the internal boundary of the ring towards the outer boundary with a maximum there. As frequency increases, this symmetry is partially violated and the displacement localization is enhanced. At $d = 0.3$ and above, this localization is observed even at a very low frequency. The maximum values of the force functions are also shifted towards the outer edge of the ring. When the frequency increases, the degree of localization of the total field grows. In this case, the internal boundary of the ring ceases to affect the characteristics of the normal modes, which can be seen in Fig. 3.

Thus, the normal modes with $n = 0$ at high frequencies represent the edge modes of the Rayleigh type, which are analogous to the so-called Konenkov waves [13].

In closing, it should be noted that, although it was possible to obtain and describe the basic properties of the new type of angular normal modes in this study, there still remain some questions about their other properties, such as the properties of the waves corre-

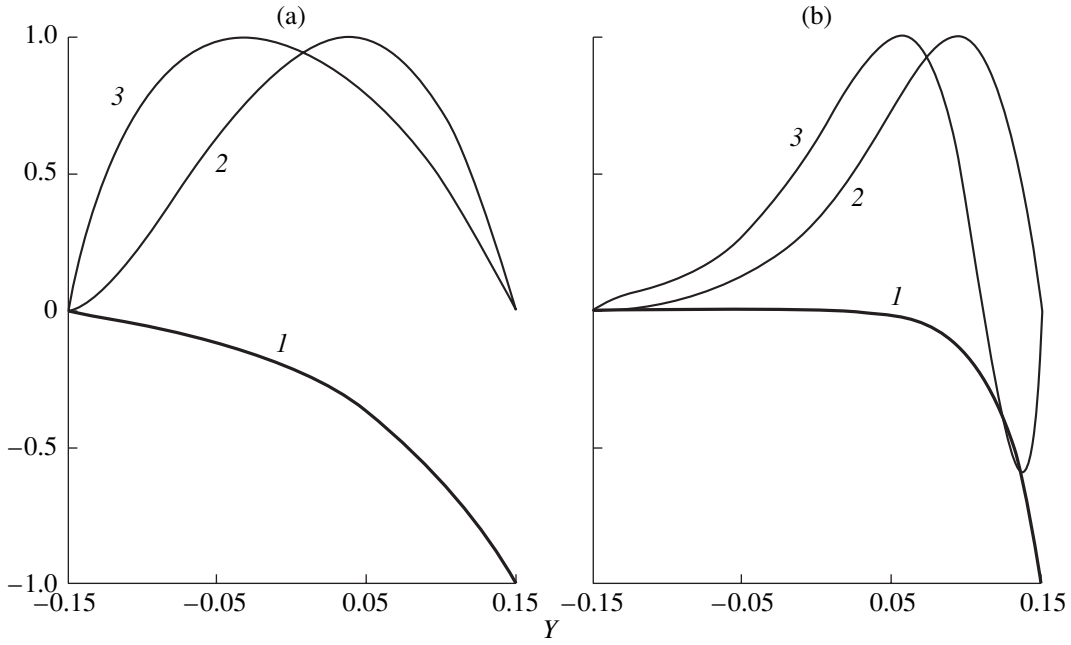

Fig. 9. The same as in Fig. 8 but for $d = 0.3$; X = (a) 2 and (b) 21.

sponding to closed branches, the asymptotic values of wave numbers for $n \geq 1$, etc. All these questions call for further investigation.

REFERENCES

1. Yu. K. Konenkov, Akust. Zh. **6**, 57 (1960) [Sov. Phys. Acoust. **6**, 52 (1960)].
2. Yu. K. Konenkov, Akust. Zh. **8**, 241 (1962) [Sov. Phys. Acoust. **8**, 187 (1962)].
3. Yu. I. Bobrovnitskiĭ, Akust. Zh. **23**, 209 (1977) [Sov. Phys. Acoust. **23**, 119 (1977)].
4. Yu. I. Bobrovnitskiĭ, Akust. Zh. **26**, 615 (1980) [Sov. Phys. Acoust. **26**, 343 (1980)].
5. A. Cummings, J. Sound Vibr. **35** (4), 451 (1974).
6. W. Rostafinski, J. Acoust. Soc. Am. **56**, 11 (1974).
7. L. M. Brekhovskikh, Akust. Zh. **13**, 541 (1968) [Sov. Phys. Acoust. **13**, 462 (1968)].
8. I. A. Viktorov, *Acoustic Surface Waves in Solids* (Nauka, Moscow, 1981).
9. E. V. Golubeva, Akust. Zh. **32**, 385 (1986) [Sov. Phys. Acoust. **32**, 238 (1986)].
10. G. Vboulis, S. A. Paipetis, and P. S. Theocaris, J. Sound Vibr. **35** (4), 521 (1974).
11. E. L. Shenderov, *Radiation and Scattering of Sound* (Sudostroenie, Leningrad, 1989), p. 301.
12. S. P. Timoshenko and S. Woinowsky-Krieger, *Theory of Plates and Shells*, 2nd ed. (McGraw-Hill, New York, 1959; Nauka, Moscow, 1966).
13. Yu. K. Konenkov, Akust. Zh. **6**, 57 (1960) [Sov. Phys. Acoust. **6**, 52 (1960)].

Translated by M. Lyamshev

Acoustical Physics, Vol. 49, No. 6, 2003, pp. 729–730. Translated from Akusticheskiĭ Zhurnal, Vol. 49, No. 6, 2003, pp. 852–854.

BRIEF COMMUNICATIONS

Choice of the Parameters of a Transmitting–Receiving System to Minimize the Output Pulse Duration

S. I. Konovalov and A. G. Kuz'menko

St. Petersburg State Electrotechnical University, ul. Prof. Popova 5, St. Petersburg, 197376 Russia

e-mail: root@post.etu.spb.ru

Received November 20, 2002

The problems of piezoelectric transducer operation in pulsed modes remain topical to this day. An example is [1], which compares the experimental and calculated pulses and signal spectra for combined direct transducers with qualitatively different protectors.

In our previous paper [2], we considered the possibility of reducing the pulse duration for a piezoelectric plate operating as a receiver in the fundamental mode of thickness vibrations with an inductive–resistive electric load connected in parallel to it. The receiver was assumed to be excited by a half-period of the particle velocity sinusoid.

In this paper, we consider a system consisting of a transmitting piezoelectric plate and a receiving one, both of them being immersed in water. We assume that the active material of the transducers is the TsTSNV-1 piezoelectric ceramics (a PZT ceramics). The bandwidth of the transmitter is broadened by using (*1*) a quarter-wave layer or (*2*) a mechanical damper. The piezoelectric receiver is connected in parallel to an electric load, which consists of an inductance L connected in series to an active resistance R (Fig. 1). The system under consideration is characterized by the following parameters: $Q = \omega_0 L/R$, $n = \omega_{el}/\omega_0$, $\omega_{el} = (LC)^{-0.5}$, and $\alpha = \omega_{rec}/\omega_0$, where ω_0 is the antiresonance frequency of the transmitting piezoelectric plate, C is the capacitance of the mechanically clamped piezoelectric receiver, and ω_{rec} is the antiresonance frequency of the receiving piezoelectric plate. The transmitter is excited by a voltage pulse representing a half-period of a sinusoid at the antiresonance frequency of the piezoelectric plate.

The purpose of our study is to determine parameters Q, n, and α so as to obtain the minimal duration of the output pulse of the receiving transducer. In Figs. 2–6, curves *1* refer to a transmitter with a matching layer, and curves *2*, to a transmitter with a mechanical damper. The specific acoustic impedance of the matching layer is assumed to be $z_I = 3.8 \times 10^6$ Pa s/m. This value provides the minimal duration of the acoustic pulse at the transmitter. In the case of a transmitter with a damper, the specific acoustic impedance of the damper is taken to be $z_d = 8 \times 10^6$ Pa s/m, which can be realized for dampers using epoxy-based compounds with a finely dispersed tungsten powder as a filler. This value provides the minimal duration of the acoustic pulse of a damped transducer. A further increase in z_d encounters technical difficulties.

Figure 2 shows the calculated dependences of the pulse duration on parameter α, which characterizes the difference between the antiresonance frequencies of the transmitter and the receiver, at $n = 1$ and $Q = 1$. From here on, the pulse duration is expressed in terms of the number of half-periods of frequency ω_0, within which the amplitude decreases to one-tenth of its maximal value. From Fig. 2, one can see that, at $\alpha \approx 1.3$, the pulse duration reaches its minimum $\tau_p \approx 9$. As α increases further, the value of τ_p does not change.

Figure 3 presents the dependences of the maximal amplitudes of the voltage pulses at the receiver output (in arbitrary units), U_{rec}, on parameter α for the same values of n and Q as in Fig. 2. One can see that, at $\alpha \approx 1.3$, the pulse amplitude obtained for a system with a matching layer is twice as great as the corresponding amplitude for a system with a damper.

Figures 4 and 5 show the dependences of pulse duration τ_p and pulse amplitude U_{rec} on parameter n at $\alpha = 1.3$ and $Q = 1$. One can see that the optimal values of n lie within $n = 0.9$–1.1. In this interval, τ_p is close to the minimum, while the signal amplitudes are close to the maximum. As in the previous case, the signal amplitude obtained in the system with a matching layer is twice as high as the amplitude obtained with a damper.

Figure 6 displays the pulse duration versus parameter Q at $\alpha = 1.3$ and $n = 1$. From the dependences shown in this figure it follows that, in the interval $0.8 < Q < 1.2$,

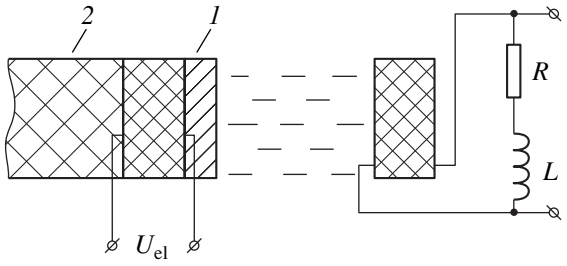

Fig. 1.

1063-7710/03/4906-0729$24.00

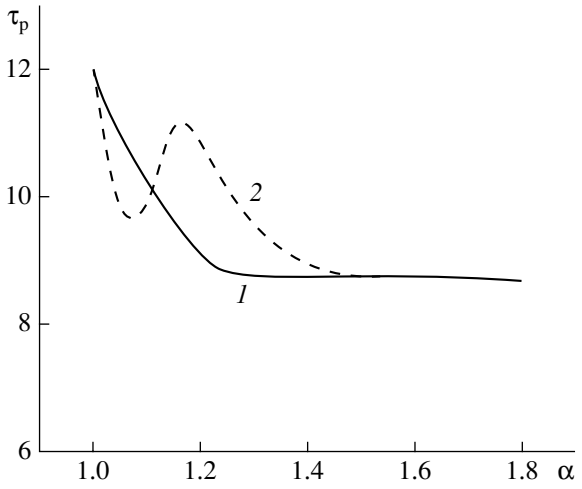

Fig. 2.

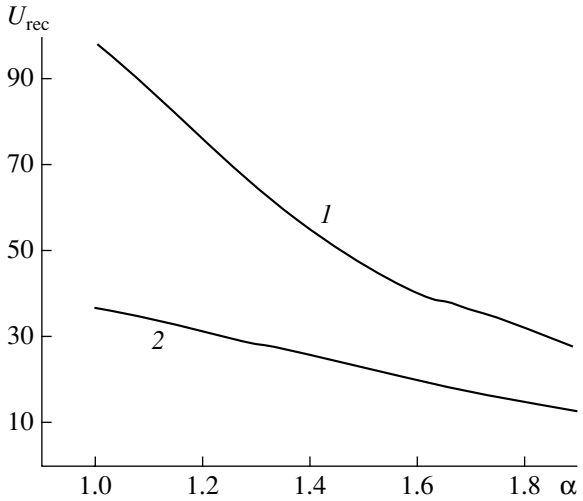

Fig. 3.

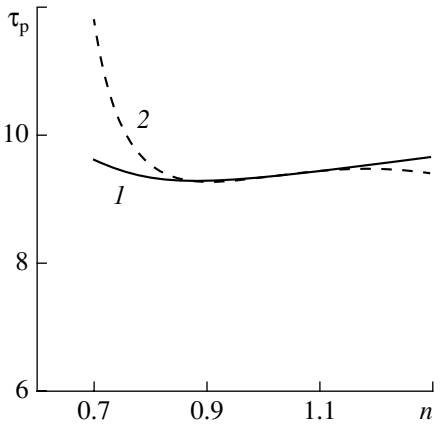

Fig. 4.

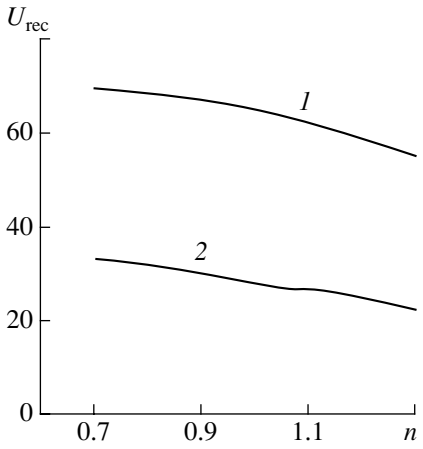

Fig. 5.

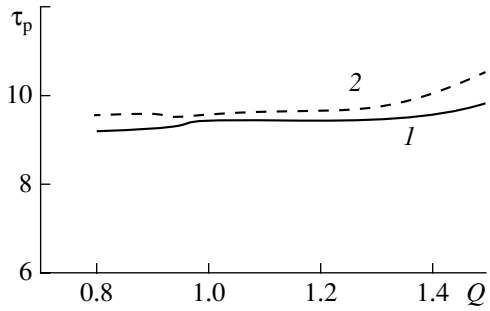

Fig. 6.

pulse duration τ_p is close to the minimum and is almost independent of Q.

Thus, the results of our calculations show that the minimal pulse duration is achieved when the parameters of the system under study take the following values: $\alpha = 1.3$–1.4, $n = 0.9$–1.1, and $Q = 0.9$–1.1. For the chosen material of the water-loaded transducers, the corresponding minimal pulse duration is $\tau_{min} \approx 9$. In the case of a transmitting transducer with a matching layer, the signal amplitude is approximately twice as high as in the case of a transmitter with a damper, while the pulse duration is practically the same.

As a result, we conclude that the use of a matching layer or a damper for the transmitter and an inductive-resistive load for the receiver, with the parameters specified above, can considerably reduce the pulse duration at the output of the transmitting–receiving system.

REFERENCES

1. V. N. Danilov and V. D. Korolev, Defektoskopiya, No. 1, 71 (2002).
2. S. I. Konovalov and A. G. Kuz'menko, Akust. Zh. **47**, 856 (2001) [Acoust. Phys. **47**, 758 (2001)].

Translated by E. Golyamina

Acoustical Physics, Vol. 49, No. 6, 2003, pp. 731–732. Translated from Akusticheskiĭ Zhurnal, Vol. 49, No. 6, 2003, pp. 855–857.

BRIEF COMMUNICATIONS

Monopole–Dipole Type Resonator in a Narrow Pipe

A. D. Lapin

Andreev Acoustics Institute, Russian Academy of Sciences, ul. Shvernika 4, Moscow, 117036 Russia
e-mail: mironov@akin.ru

Received January 22, 2003

A Helmholtz resonator without dissipation loss is an efficient reflector for sound propagating in an infinite narrow pipe [1–3]. At the resonance frequency, the incident sound wave is completely reflected from the resonator, so that no travelling wave is observed behind the resonator. The Helmholtz resonator is a resonator of the monopole type. A sound wave propagating in a narrow pipe can also be reflected by a dipole-type resonator [4]. The simplest version of the latter is a rigid sphere fastened to the pipe wall via a small bar. The radius of the sphere and the length of the bar are small compared to the sound wavelength. Under the effect of the incident wave, the rigid sphere fixed on the bar vibrates and generates a scattered field of dipole type. At the resonance frequency, the scattered field completely suppresses the incident wave behind the resonator. The friction in the resonator reduces the efficiency of its operation as a wave reflector. Resonators with friction absorb sound. Previous studies showed that a single Helmholtz resonator with optimal friction absorbs no more than half the energy of the incident wave. A complete absorption of sound at the resonance frequency can be achieved using a combination of a lossless resonator and a resonator with a certain loss (the friction resistance is equal to the radiation resistance) and with the distance between the two resonators being equal to an odd number of quarter-wavelengths [5].

This paper considers a single resonator of the monopole–dipole type in the form of a Helmholtz resonator fastened through a small bar to the pipe wall (see figure). In fact, this resonator is a combination of monopole and dipole resonators positioned at the same point. One can expect that, at a certain friction, such a monopole–dipole-type resonator will completely absorb the resonance-frequency sound in the narrow pipe.

In a pipe that is narrow compared to the wavelength, the pressure and the particle velocity depend only on the x coordinate measured along the pipe axis. Let us consider a Helmholtz resonator (a spherical cavity with a neck) connected via a small bar with the pipe wall at the point $x = 0$. Let a harmonic sound wave with the pressure $p_0(x) = \exp(ikx)$, where k is the wave number (the time factor $\exp(-i\omega t)$ is omitted), be incident on the resonator from the left. Under the effect of the incident wave, the Helmholtz resonator mounted on the bar is excited and generates fields of monopole and dipole types:

$$\begin{aligned} p_1(x) &= \frac{\rho c V}{2S}\exp(ik|x|), \\ p_2(x) &= -ik\,\mathrm{sgn}\,x\frac{\rho c M}{2S}\exp(ik|x|), \end{aligned} \tag{1}$$

where V is the volume velocity of the monopole (the Helmholtz resonator), M is the dipole moment (of the vibrating sphere), the dipole axis coincides with the x axis, ρ is the density of the medium filling the system, c is the velocity of sound in this medium, S is the cross-sectional area of the pipe, and $\mathrm{sgn}x = +1$ for $x > 0$ and -1 for $x < 0$. The total field in the pipe is $p = p_0 + p_1 + p_2$. We seek the parameters of the monopole–dipole-type resonator to obtain a complete absorption of the incident wave, i.e., $p(x < 0) = \exp(ikx)$ and $p(x > 0) = 0$.

The volume velocity of the monopole and the dipole moment are obtained from the equations of motion (volume oscillations and vibrations) of the resonator. The equation of the forced volume oscillations has the form

$$\begin{aligned} &m_1\ddot{\xi}_1 + r_1\dot{\xi}_1 + \kappa_1\xi_1 \\ &= -\sigma_1[p_0(0) + p_1(0) + p_2(0)]\exp(-i\omega t), \end{aligned} \tag{2}$$

where m_1 is the air mass in the resonator neck, $\xi_1(t)$ is the displacement of this mass, r_1 is the friction factor, κ_1 is the coefficient of elasticity, σ_1 is the cross-sectional area of the neck, $p_0(0) = 1$, $p_1(0) = \frac{\rho c V}{2S}$, and $p_2(0) = 0$. The volume velocity of the monopole is $V =$

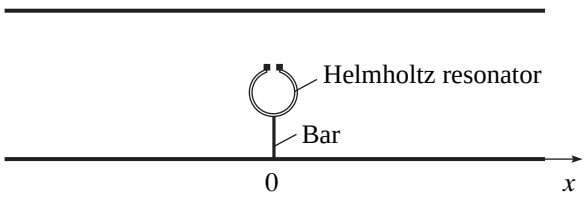

Monopole–dipole-type resonator in a pipe.

1063-7710/03/4906-0731$24.00

$\sigma_1 v_1$, where $v_1 = \dot{\xi}_1(t)\exp(i\omega t)$ is the complex amplitude of the particle velocity.

The equation of the forced vibrations performed by the resonator on the small bar under the effect of the sound field has the form

$$m_2\ddot{\xi}_2 + r_2\dot{\xi}_2 + \kappa_2\xi_2 = [F_0 + F_1 + F_2]\exp(-i\omega t), \quad (3)$$

where m_2 is the mass of the spherical cavity; $\xi_2(t)$ is the displacement of this mass; r_2 is the friction factor; κ_2 is the coefficient of elasticity; and F_0, F_1, and F_2 are the complex amplitudes of the resultant forces that arise due to the effect produced on the rigid sphere by the pressure fields p_0, p_1, and p_2, respectively. According to [2], for a small (compared to the sound wavelength) sphere, these force amplitudes are expressed as

$$F_0 = -i\frac{ka}{3}\sigma_2, \quad F_1 = 0, \quad F_2 = ika\frac{\rho c\sigma_2^2}{12S}(1 + ika)v_2,$$

where a is the radius of the sphere, $\sigma_2 = 4\pi a^2$ is its surface area, and $v_2 = \dot{\xi}_2(t)\exp(i\omega t)$ is the complex amplitude of the particle velocity. The dipole moment of the vibrating sphere is $M = 2\pi a^3 v_2$.

From Eqs. (2) and (3), we obtain the complex amplitudes of the particle velocities:

$$v_1 = -\frac{\sigma_1 p_0(0)}{Z_1} = -\frac{\sigma_1}{Z_1}, \quad v_2 = \frac{F_0}{Z_2} = -i\frac{ka}{3}\frac{\sigma_2}{Z_2},$$

where

$$Z_1 = \left\{(r_1 + R_1) + i\left(\frac{\kappa_1}{\omega} - \omega m_1\right)\right\},$$

$$Z_2 = \left\{(r_2 + R_2) + i\left[\frac{\kappa_2}{\omega} - \omega(m_2 + m)\right]\right\},$$

$R_1 = \dfrac{\sigma_1 p_1(0)}{v_1} = \dfrac{\rho c\sigma_1^2}{2S}$ is the monopole radiation resistance, $R_2 = -\mathrm{Re}\dfrac{F_2}{v_2} = (ka)^2\dfrac{\rho c\sigma_2^2}{12S}$ is the dipole radiation resistance, and $m = \dfrac{1}{\omega}\mathrm{Im}\dfrac{F_2}{v_2} = \dfrac{ka}{\omega}\dfrac{\rho c\sigma_2^2}{12S}$ is the associated mass of the dipole.

The total pressure in the pipe is expressed as

$$p = \exp(ikx) - \left\{\frac{R_1}{Z_1} + \frac{R_2}{Z_2}\mathrm{sgn}\,x\right\}\exp(ik|x|). \quad (4)$$

The monopole and dipole scattered fields produced by the resonator under study are orthogonal. The eigenfrequencies of the resonator are $\omega_1 = \sqrt{\kappa_1/m_1}$ and $\omega_2 = \sqrt{\kappa_2/(m_1 + m)}$ for the volume oscillations and vibrations, respectively. Note that the acoustic coupling of two closely spaced Helmholtz resonators in a free medium was studied in [6].

Let us consider the structure of the sound field given by Eq. (4) for some specific values of the resonator parameters.

(i) Let us set $Z_2 = \infty$ and $r_1 = 0$. This means that the Helmholtz resonator is rigidly fixed to the pipe wall and the friction in the resonator is absent. Then, at frequency ω_1, the incident wave is completely reflected from the resonator:

$$p(x < 0) = 2i\sin(kx), \quad p(x > 0) = 0.$$

(ii) Let $Z_1 = \infty$ and $r_2 = 0$. This means that the resonator neck is closed by a rigid cover and the resonator vibrates on the bar without loss. Then, at frequency ω_2, the incident wave is also completely reflected from the resonator:

$$p(x < 0) = 2\cos(kx), \quad p(x > 0) = 0.$$

(iii) Let $r_1 = r_2 = 0$ and $\omega_1 = \omega_2$. In this case, the volume oscillations and the vibrations occur without friction, and eigenfrequencies ω_1 and ω_2 coincide. Then, at the frequency $\omega = \omega_1 = \omega_2$, the incident wave is not reflected from the resonator but only changes its phase:

$$p(x < 0) = \exp(ikx), \quad p(x > 0) = -\exp(ikx).$$

(iv) Let $r_1 = R_1$, $r_2 = R_2$, and $\omega_1 = \omega_2$. This means that, for the volume oscillations and vibrations, the friction resistance is equal to the radiation resistance and the natural frequencies coincide. Then, at frequency $\omega = \omega_1 = \omega_2$, we have the field

$$p(x < 0) = \exp(ikx), \quad p(x > 0) = 0.$$

Hence, with these parameter values, a single resonator of the monopole–dipole-type completely absorbs the incident wave.

REFERENCES

1. M. A. Isakovich, *General Acoustics* (Nauka, Moscow, 1973).
2. S. N. Rzhevkin, *Course of Lectures on the Theory of Sound* (Mosk. Gos. Univ., Moscow, 1960).
3. P. Morse and U. Ingard, *Theoretical Acoustics* (McGraw-Hill, New York, 1986).
4. N. G. Kanev and M. A. Mironov, Akust. Zh. **49**, 372 (2003) [Acoust. Phys. **49**, 312 (2003)].
5. A. D. Lapin, Akust. Zh. **49**, 427 (2003) [Acoust. Phys. **49**, 363 (2003)].
6. T. Johansson and M. Kleiner, J. Acoust. Soc. Am. **110**, 1315 (2001).

Translated by E. Golyamina

Acoustical Physics, Vol. 49, No. 6, 2003, pp. 733–735. Translated from Akusticheskiĭ Zhurnal, Vol. 49, No. 6, 2003, pp. 858–860.

INFORMATION

Session of the Scientific Council on Acoustics of the Russian Academy of Sciences in Memory of Professor Leonid Mikhaĭlovich Lyamshev

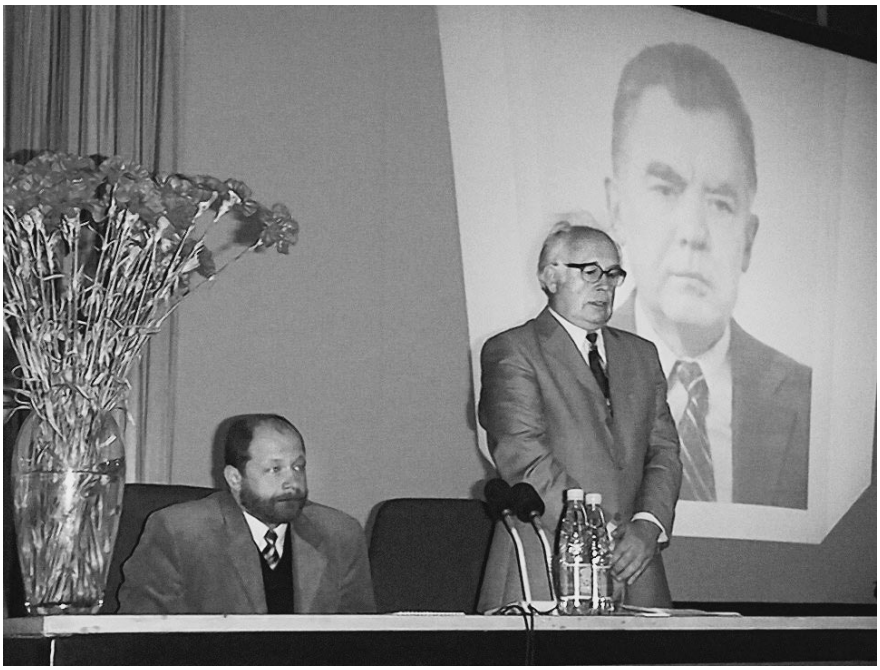

Professor N.A. Dubrovskiĭ, Director of the Andreev Acoustics Institute, addresses the audience. The person next to him is Professor S.V. Egerev, Chair of the Scientific Council on Acoustics.

On June 4, 2003, at the Andreev Acoustics Institute, a Session of the Scientific Council on Acoustics of the Russian Academy of Sciences (RAS) was held. The session was devoted to the memory of Professor Leonid Mikhaĭlovich Lyamshev, head of a laboratory at the Andreev Acoustics Institute, Chair of the Scientific Council on Acoustics, and Editor-in-Chief of *Acoustical Physics*. In addition to the members of the scientific council, the session was attended by guest participants—specialists in acoustics from Moscow, Nizhni Novgorod, and St. Petersburg.

The opening speech was given by Academician F.V. Bunkin, Director of the Wave Research Center of the General Physics Institute of the RAS. The guest participants were greeted by Professor N.A. Dubrovskiĭ, Director of the Andreev Acoustics Institute. Speakers noted that the pioneering works by Lyamshev in sound diffraction, acoustohydrodynamics, nonlinear acoustics, radiation acoustics, fractal acoustics, and photoacoustics laid the foundations of the fields of research without which the development of acoustics in the 21st century would be unthinkable. The wide scope of Lyamshev's scientific interests determined the polythematic character of the session. Seven scientific reports were presented.

Yu.I. Bobrovnitskiĭ (Institute of Mechanical Engineering, RAS) discussed "Reciprocity in the Problem of the Reflection and Transmission of Waves." He noted that the generally recognized contribution made by Lyamshev to the study of reciprocity, which is a cornerstone problem of acoustics, consists in that he gave the first general proof of the reciprocity theorem for an arbitrary medium; later, he extended this proof to the case of a moving medium. Bobrovnitskiĭ described the latest achievements in this field of research, namely, the application of the reciprocity theorem to the problems of reflection and transmission of waves. For solving such problems, it is necessary to apply the symmetrization procedure to the matrix of the reflection and transmission coefficients of sound. As an example, Bobrovnitskiĭ considered the solution for the practically important case of a flexurally vibrating bar.

1063-7710/03/4906-0733$24.00

The report entitled "Research into the Photoacoustic (PA) Tomography of Biological Objects at the Institute of Applied Physics, RAS" (by G.P. Volkov, A.V. Eroshin, A.G. Kirillov, and A.M. Reĭma from the Institute of Applied Physics, RAS) was concerned with the optimal configuration problem for a photoacoustic tomograph. Photoacoustic applications in tomography of biological tissues attract the attention of researchers from different countries. The essence of the effect is evident: a contactless heating of tissue by optical radiation with the appropriate recording of the response provides the localization of a tumor, which is characterized by a thermophysical contrast. However, the practical implementation of the effect requires rather sophisticated technical methods. The authors of the report discuss in detail the problems of the realization of PA tomographs, including the parameters of the receiving system and the algorithms of tumor localization by the acoustic response.

I.B. Esipov (Andreev Acoustics Institute) presented the report "Acoustic Effects in Granular Media." The subject of this report was the theoretical and experimental modeling of viscoelastic liquid flows through porous media. Such systems are described by hysteresis models and, from the viewpoint of a cyclic (e.g., acoustic) loading, possess pronounced nonlinear properties. A situation that requires the study of a granular medium soaked with a viscoelastic liquid is oil leakage through sand. The model described by Esipov shows that a cyclic loading of such a medium leads to the formation of a two-dimensional percolation cluster. Thus, the acoustic field changes the properties of the medium, and the nonlinear components of the acoustic response may serve for the diagnostics of this medium.

V.V. Zosimov (Algodign LLC), in his report "Elastic Vibrations in Complex Structures: Some Applications," considered the application of the modern methods of vibration theory to solving some key problems of computational chemistry and molecular biology, such as the evaluation of the degree of similarity of macromolecules and the determination of the free binding energy of molecules. As a result, the procedures of calculating the eigenfrequencies of molecules were developed, so that the difference between these frequencies can serve to evaluate the similarity. Today, the importance of solving such problems is beyond question: there are several million synthesized preparations that can be suggested for medical application on the condition that they are reliably identified.

The report by A.P. Brysev (Wave Research Center of the General Physics Institute, RAS) was entitled "Parametric Phase Conjugation for Ultrasonic Beams." It described the recent achievements in studying this interesting phenomenon. The effect of phase conjugation is known to compensate the phase distortions that occur in ultrasonic beams propagating in an inhomogeneous medium. Using this property, it is possible, e.g., to realize the self-guidance of a beam at a particular scattering object. Brysev presented new interesting areas of research: the methods of the parametric phase conjugation of ultrasonic beams beyond the threshold, the nonlinear acoustics of phase-conjugated beams, and the acoustic diagnostics and visualization of objects on the basis of phase conjugation.

The problem considered by E.A. Kopyl and Yu.P. Lysanov (Andreev Acoustics Institute) was formulated as the "Scattering and Attenuation of Low-Frequency Sound in the Ocean with Random Fractal Inhomogeneities." The study of this problem is important for the calculation of long-range propagation of low-frequency sound in a deep ocean. The scattering of sound by volume inhomogeneities is the main factor responsible for energy leakage from the underwater sound channel. A new approach to analyzing the sound scattering in the ocean was put forward by Lyamshev: he proposed performing the analysis on the basis of the concepts of fractal acoustics and ray chaos. These ideas were developed in the report by Kopyl and Lysanov. The new scattering models are incorporated into the computer programs for solving problems of underwater acoustics. In particular, they allow one to determine the mean decay laws governing the range dependence of the acoustic field. It is also evident that the new models offer considerable promise for solving inverse problems of acoustic oceanology.

The possible applications of the laser generation of sound in matter were considered by A.A. Karabutov (Moscow State University) in his report "Laser Photoacoustic Diagnostics." Two areas of application of this effect can be distinguished: photoacoustic tomography (where the PA transformation depends on the thermophysical inhomogeneities of the sample and serves for their localization) and photoacoustic structure metering (where the PA transformation serves as the source of a broadband precision probing acoustic signal). Correspondingly, two examples realizing these versions are considered: a photoacoustic tomograph for early diagnostics of oncological disorders of the mammary gland and a diagnostic device for the fine analysis of media with a complex structure (in particular, carbon–epoxy composites).

At the session, the full scientific council approved by the General Physics and Astronomy Division of the RAS in 1999 for a period of five years was presented with allowance for the corrections introduced by the Bureau of the Physical Science Division. Today, the council includes the following specialists in physics of wave processes and modern fields of acoustics:

Sergeĭ Viktorovich Egerev (Andreev Acoustics Institute), Chair of the Council

Georgiĭ Dmitrievich Mansfel'd (Institute of Radio Engineering and Electronics, RAS), Deputy Chair of the Council

Oleg Vladimirovich Abramov (Institute of Organic and Inorganic Chemistry, RAS)

Viktor Anatol'evich Akulichev, Member of the RAS (Pacific Oceanological Institute, Far-East Division, RAS)

Irina Arkad'evna Aldoshina (Bonch-Bruevich State University of Telecommunications, St. Petersburg)

Yuriĭ Ivanovich Bobrovnitskiĭ (Institute of Mechanical Engineering, RAS)

Leonid Maksimovich Brekhovskikh, Member of the RAS (Shirshov Oceanology Institute, RAS)

Fedor Vasil'evich Bunkin, Member of the RAS (Wave Research Center, General Physics Institute, RAS)

Valentin Andreevich Burov (Moscow State University)

Andreĭ Viktorovich Gaponov-Grekhov, Member of the RAS (Institute of Applied Physics, RAS)

Irina Petrovna Golyamina (Andreev Acoustics Institute)

Vladimir Semenovich Gorelik (Lebedev Physics Institute, RAS)

Éduard Petrovich Gulin (Andreev Acoustics Institute)

Yuriĭ Vasil'evich Gulyaev, Member of the RAS (Institute of Radio Engineering and Electronics, RAS)

Sergeĭ Nikolaevich Gurbatov (Nizhni Novgorod State University)

Nikolaĭ Andreevich Dubrovskiĭ (Andreev Acoustics Institute)

Aleksandr Mikhaĭlovich Dykhne, Member of the RAS (Troitsk Institute of Innovative and Thermonuclear Research)

Vladimir Ivanovich Erofeev (Nizhni Novgorod Branch of the Institute of Mechanical Engineering, RAS)

Igor' Borisovich Esipov (Andreev Acoustics Institute)

Boris Maksimovich Efimtsov (Zhukovskiĭ Central Aerohydrodynamics Institute)

Vitaliĭ Anatol'evich Zverev, Corresponding Member of the RAS (Institute of Applied Physics, RAS)

Viktor Vasil'evich Zosimov (LLC Algodign-Moscow)

Nikolaĭ Igorevich Ivanov (St. Petersburg Baltic State Technical University)

Sergeĭ Nikolaevich Ivanov (Institute of Radio Engineering and Electronics, RAS)

Vsevolod Feodos'evich Kazantsev (Moscow Automobile and Road Institute)

Margarita Aleksandrovna Kallistratova (Institute of Atmospheric Physics, RAS)

Valentin Kirillovich Kedrinskiĭ (Institute of Geography, Siberian Division, RAS)

Aleksandr Ivanovich Korobov (Moscow State University)

Sergeĭ Nikolaevich Kulichkov (Institute of Atmosphere Physics, RAS)

Boris Fedorovich Kur'yanov (Shirshov Oceanology Institute, RAS)

Mikhail Leonidovich Lyamshev (General Physics Institute, RAS)

Leonid Olegovich Makarov (Moscow Automobile and Road Institute)

Vladislav Georgievich Mikhalevich (General Physics Institute, RAS)

Vladislav Ivanovich Pustovoĭt, Corresponding Member, RAS (Institute of Instrument Engineering, RAS)

Oleg Vladimirovich Rudenko, Corresponding Member of the RAS (Moscow State University)

Samuil Akivovich Rybak (Andreev Acoustics Institute)

Oleg Anatol'evich Sapozhnikov (Moscow State University)

Vladimir Ivanovich Timoshenko (Taganrog Radio Engineering University)

Igor' Alekseevich Urusovskiĭ (Andreev Acoustics Institute)

Immanuil Lazarevich Fabelinskiĭ, Corresponding Member, RAS (Lebedev Physics Institute, RAS)

Andreĭ Viktorovich Fokin (Andreev Acoustics Institute), Scientist-Secretary of the Council

Vladimir Grigor'evich Shavrov (Institute of Radio Engineering and Electronics, RAS).

S. V. Egerev

Translated by E. Golyamina

Acoustical Physics, Vol. 49, No. 6, 2003, pp. 736–738. Translated from Akusticheskiĭ Zhurnal, Vol. 49, No. 6, 2003, pp. 861–863.

INFORMATION

New Books on Acoustics*

Acoustics of Inhomogeneous Media: Proceedings of Prof. S.A. Rybak's Seminar. 2002 Yearbook of the Russian Acoustical Society (Moscow, 2002), 165 pp.

Acoustics of Inhomogeneous Media: Proceedings of Prof. S.A. Rybak's Seminar. 2001 Yearbook of the Russian Acoustical Society (Moscow, 2001), Issue 2, 199 pp.

Ocean Acoustics: Proceedings of the IX Brekhovskikh Workshop Combined with the XII Session of the Russian Acoustical Society, Shirshov Oceanology Institute, Russian Academy of Sciences; Andreev Acoustics Institute (GEOS, Moscow, 2002), 577 pp.

Speech Acoustics: Medical and Biological Acoustics. Proceedings of the 11th Session of the Russian Acoustical Society, November 19–23, 2001 (GEOS, Moscow, 2001), Vol. 3, 210 pp.

Acoustical Measurements—Geoacoustics, Electroacoustics, and Ultrasound: Proceedings of the 11th Session of the Russian Acoustical Society, November 19–23, 2001 (GEOS, Moscow, 2001), Vol. 2, 311 pp.

Architectural Acoustics and Acoustics of Buildings: Noise and Vibration. Proceedings of the 11th Session of the Russian Acoustical Society, November 19–23, 2001 (GEOS, Moscow, 2001), Vol. 4, 192 pp.

Yu. V. Badikov, *Technique and Technology of Hydroacoustic Action in Chemical Technological Processes* (Reaktiv, Ufa, 2001), 203 pp.

K. T. Bogdanov and V. V. Moroz, *Structure, Dynamics, and Hydrological–Acoustic Characteristics of Waters of the Kurile Islands* (Dal'nauka, Vladivostok, 2000), 150 pp.

K. T. Bogdanov and V. V. Moroz, *Structure, Dynamics, and Acoustic Characteristics of Waters in the Straits of the Komandorski–Aleutian Islands* (Dal'nauka, Vladivostok, 2002), 137 pp.

V. A. Bulanov, *Introduction to Acoustic Spectroscopy of Microinhomogeneous Liquids*, Institute of Marine Technology Problems, Far-East Division, Russian Academy of Sciences (Dal'nauka, Vladivostok, 2001), 280 pp.

Underwater Acoustics: Collection of Scientific and Technical Publications, Ed. by Yu.A. Koryakin (Morfizpribor Central Research Institute, St. Petersburg, 2002), Issue 3, 128 pp.

Hydroacoustic Communication and Hydroacoustic Emergency Means: Proceedings of the First Scientific and Applied Conference, Volgograd, July 19–20, 2001, Ed. by S.G. Babkin *et al.* (Federal State Unitary Enterprise "Shtil' Research Institute of Underwater Communication," Volgograd, 2001), 130 pp.

F. F. Gorbatsevich, *Acoustic Polariscopy of Rock-forming Minerals and Crystalline Rocks (Devoted to the 50th Anniversary of the Geology Institute)*, (Kol'skiĭ Research Center "Geology Institute," Apatity, 2002), 140 pp.

Dynamics of a Continuous Medium: Proceedings of 6th Scientific Seminar of the Commonwealth of Independent States on Acoustics of Inhomogeneous Media, Issue 117 of *Acoustics of Inhomogeneous Media*, Ed. by V.K. Kelpinskiĭ (Novosibirsk, 2001), 173 pp.

N. P. Krasnenko, *Acoustic Sounding of the Atmosphere Boundary Layer*, Ed. by M.V. Kabanov (Institute of Optical Monitoring, Siberian Division, Russian Academy of Sciences, Tomsk, 2001), 279 pp.

V. P. Kuznetsov, B. G. Mordvinov, and V. I. Timoshenko, *Acoustic Oceanological Studies and Expeditions* (Rostizdat, Rostov-on-Don, 2002), 544 pp.

Methods of the Acoustic Diagnostics of Inhomogeneous Media: Collection of Papers (Institute of Applied Physics, Russian Academy of Sciences, Nizhni Novgorod, 2002), 275 pp.

Marine Technologies, Ed. by M.D. Ageev (Dal'nauka, Vladivostok, 2000–2003), Issues 3–5, Institute of Marine Technology Problems, Far East Division, Russian Academy of Sciences: Issue 3 (2000), 294 pp.; Issue 4 (2001), 227 pp.; Issue 5 (2003), 215 pp.

V. G. Nevolin, *Employment of Acoustic Vibrations in Oil Production* (Perm, 2001), 52 pp.

O. N. Pobol', *Foundations of Acoustic Ecology and the Noise Insulation of Machines: A Textbook on Specialty no. 656 100 "Technology and Design of Light Industry Products"* (Moscow, 2002), 269 pp.

Publications by the Staff Members of the Acoustics Institute Over a Period of 1992–2000: A Bibliography (AKIN, Moscow, 2001).

N. M. Ryskin and D. I. Trubetskov, *Nonlinear Waves: A University Textbook* (Fizmatlit, Nauka, Moscow, 2000), 272 pp.

Acoustical Engineering: Journal on Science and Engineering of the East-European Acoustical Association (St. Petersburg, 1999), Issues 3, 4; 64 pp.

* The bibliography is compiled on the basis of the information editions received by the Natural Science Libraries of the Russian Academy of Sciences and the library of the Andreev Acoustics Institute.

1063-7710/03/4906-0736$24.00

Proceedings of the Nizhni Novgorod Acoustical Science Session: Nizhni Novgorod State University, Russian Acoustical Society, Scientific Council on Acoustics of the Russian Academy of Sciences, Institute of Applied Physics of the Russian Academy of Sciences, et al., Ed. by S.N. Gurbatov (TALAM, Nizhni Novgorod, 2002), 409 pp.

Ultrasound and Thermodynamic Properties of Matter: Collection of Papers of the Russian Acoustical Society (Kursk State Pedagogical University, Kursk, 2002), Issue 28, 149 pp.

Elastic and Acoustic Properties of Ionic and Ceramic Dielectrics and High-Temperature Superconductors, Ed. by V.N. Belomestnykh, Yu.P. Pokholkov, V.L. Ul'yanov, and O.L. Khasanov (Tomsk Polytechnical University, Tomsk, 2001), 223 pp.

Physical Acoustics. Propagation and Diffraction of Waves: Proceedings of the 11th Session of the Russian Acoustical Society, November 19–23, 2001 (GEOS, Moscow, 2001), Vol. 1, 319 pp.

Physical and Nonlinear Acoustics: Proceedings of the Seminar of Krasil'nikov's Scientific School, Moscow State University (Moscow, 2002), 241 pp.

V. A. Shchurov, *Vector Ocean Acoustics* (Dal'nauka, Vladivostok, 2002), 306 pp.

Acoustical Imaging, Ed. by Huadel (Kluwer, New York, 2000), Vol. 24, 422 pp.

Acoustical Imaging, Ed. by P.N. Wells and M. Halliwell (Kluwer, New York, 2000), Vol. 25, 580 pp.

Ba-Ngu Vo, A. Cantoni, and Kok day Teo, *Filter Design with Time Domain Mask Constants: Theory and Applications* (Kluwer, Boston, 2001), 350 pp.

D. T. Blackstock, *Fundamentals of Physical Acoustics* (Wiley, S.L., 2000), 560 pp.

A. J. Bjorn, *Ultrasonic Imaging, Waves, Signals, and Signal Processing*, 2 Vols. (Trondheim, 2000), 1416 pp.

Boundary Element Acoustics: Fundamentals and Computer Codes, Ed. by T.W. Wu (WIT Press, Billerica, 2001), 256 pp.

V. Cerveny, *Seismic Ray Theory* (Cambridge University, New York, 2001), 713 pp.

D. Cheeke, *Fundamentals and Application of Ultrasonic Waves*, (CRC Press, Roca Raton, 2002), 360 pp.

Classic Papers in Shock Compression Science, Ed. by J.N. Johnson and R. Cheret (Springer, New York, 1998), 524 pp.

J. Dassios and R. Kleinman, *Low Frequency Scattering* (Claredon, New York, 2000).

Dictionary of Acoustics, Ed. by C.L. Morley (Academic, London, 2001), 430 pp.

D. S. Drumheller, *Introduction to Wave Propagation in Nonlinear Fluids and Solids* (Cambridge University Press, Cambridge, 1998).

Emerging Cognitive Abilities in Early Infancy, Ed. by F. Lacerda, C. von Hofsten, and M. Heimann (Lawrence Eribaum Assoc., New Jersey, 2001), 264 pp.

F. A. Everest, *Master Handbook of Acoustics* (McGraw Hill, New York, 2000), 592 pp.

Experimental Acoustic Inversion Methods for Exploration of the Shallow Water Environment, Ed. by A. Caifi; J.-P. Hermand, a.o. (Kluwer, S.I., 2000), 302 pp.

P. Filippi, D. Habault, J.P. Lefebvre, and A. Bergassoli, *Acoustics: Basic Physics, Theory and Methods* (Academic, London, 1999), 316 pp.

Forum Acoustics, Seville, 2002. Seville, Spain, September 16–20, 2002, on CD-ROM; *Revista di Acustica*, Vol. 33 (2002), Spec. Issue.

Handbook of Multimodal and Spoken Dialogue Systems: Resources, Terminology, and Product Evaluation (Kluwer, Netherlands, 2000).

Handbook of Neural Network Signal Processing, Ed. by Yu Hen Hu and Jeng-Neng Hwang (CRC Press, Boca Raton, 2001), 408 pp.

P. Haughton, *Acoustics for Audiologists* (Academic, New York, 2002), 456 pp.

T. R. Hueter and R. H. Bolt, *Sonics: Techniques for the Use of Sound and Ultrasound in Engineering and Science* (ASA, S.I., 2000), 456 pp.

Hydroacoustics: Annual Journal (Committee on Acoustics of Polish Acad. Sci., Sect. Hydroacoustics, Gdynia, 2001), Vol. 4, 266 pp.

Hydroacoustics: Proceedings of 2nd EAA International Symposium, Gdansk, May 24–27, 1999, Ed. by A. Stepnowski, S. Salamon, and E. Kozaczka (Technical University, Gdansk-Jurata, 1999), 346 pp.

17th International Congress on Acoustics, Rome, September 2–7, 2001: Book of Abstracts (Rome 2001), 416 pp.; Riv. Ital. Acustica, Vol. 25, Nos. 1–3 (2001).

16th International Symposium on Nonlinear Acoustics, Moscow State University, Moscow, August 19–23, 2002: Abstracts (State University, Moscow, 2002), 293 pp.

Proceedings of 8th International Workshop on Modern Acoustics: Nondestructive Evaluation (NDE), Nanjing, China, October 28–31, 2000 (Taylor, London, 2001), 387 pp.; Progress in Natural Science, Vol. 11 (2001), Suppl.

B. G. Katsnelson and V. G. Petnikov, *Shallow Water Acoustics* (Springer, Chichester, 2001), 267 pp.

Khanh Chau Le, *Vibration of Shells and Rods* (Springer, New York, 1999), 423 pp.

L. E. Kinsler, A. R. Frey, A. B. Coppens, and J. V. Sanders, *Fundamentals of Acoustics*, 4th ed. (Wiley, New York, 1999), 548 pp.

C. Langton, *Principles and Applications of Ultrasound* (Inst. Phys., S.I., 2002), 252 pp.

K. C. Le, *Vibration of Shells and Rods* (Springer, S.J., 1999), 423 pp.

Marine Mammals and Low-Frequency Sound: Progress since 1994, National Research Council (Natl. Acad. Press, Washington, 2000).

Microphone Arrays, Ed. by M. Brandstein and D. Ward (Springer, New York, 2001), 398 pp.

A. R. Moller, *Hearing: Its Physiology and Pathophysiology* (Academic, S.I., 2000), 515 pp.

S. Moller, *Assessment and Prediction of Speech Quality in Telecommunications* (Kluwer, Boston), 2000), 257 pp.

J.-C. Nedelec, *Acoustic and Electromagnetic Equations: Integral Representations for Harmonic Problem* (Springer, New York, 2001), 325 pp.

The Noise Manual, 5th ed., Ed. by E.H. Berger, L.H. Royster, a.o. (Amer. Industr. Hygiene Assoc., Fairfax, 2000), 796 pp.

Nonlinear Acoustics at the Turn of Millenium: ISNA-15, 15th International Symposium (AIP Conference Proceedings, 524), Ed. by W. Eauterborn and T. Kurz (Springer, S.I., 2000), 569 pp.

Nonlinear Acoustics at the Beginning of the 21st Century: Proceedings of the 16th International Symposium on Nonlinear Acoustics, Moscow, August 19–23, 2002, Ed. by O.V. Rudenko and O.A. Sapozhnikov, Vols. 1, 2 (St. Univ., Moscow, 2002); Vol. 1: pp. V–XIX, 3–622 pp.; Vol. 2: pp. V–XIII, 625–1264 (+CD).

Ocean 2000. MTS/IEEE: Conference and Exhibition (on CD-ROM).

Ocean Acoustics Interference Phenomena and Signal Processing: AIP Conference Proceedings, San Francisco, May 1–3, 2001, Ed. by W.A. Kuperman, G.L.D. Spain (AIP, New York, 2002), 277 pp.

Physical Acoustics: Principles and Methods, Vol. XXIII: *Ultrasonic Instruments and Devices. I. Reference for Modern Instrumentation, Techniques and Technology* (Academic, San Diego, 1999), 482pp.; Vol. XXIV: *Ultrasonic Instruments and Devices. II*, 372 pp.

Physical Acoustics, Vol. 25: *Cumulative Subject and Author Index Including Tables and Contents*, Ed. by R.H. Thurston and A.D. Pierce (Academic, S.I., 1999), 307 pp.

J. M. Pickett, *The Acoustics of Speech Communication: Fundamentals, Speech Perception Theory, and Contents* (Allyn and Bacon, Boston, 1999), 404 pp.

The Psychology of Music, 2nd ed., Ed. by D. Deutsch (Academic, London, 1999), 807 pp.

D. W. Schobben, *Real-Time Adaptive Concepts in Acoustics: Blind Signal Separation and Multichannel Echo Cancellation* (Kluwer, Dordrecht, 2001), 160 pp.

B. Snyder, *Music and Memory* (MIT, Cambridge, 2001), 370 pp.

A. Stepnowski, *Systemy akustycznego monitoringu srodowiska morskiego*, Gdanskie Towarzystwo naukowe. Wydzial IV Nauk Technicznych (Gdansk, 2001), 283 pp. (in Polish).

K. N. Stevens, *Acoustic Phonetics* (MIT Press, Cambridge, 1999), 607 pp.

Sung-Hwan Ko, Sangwoo Pyo, and Woojae Seong, *Structure-Borne and Flow Noise Reductions (Mathematical Modeling)* (Seoul Nat. University, Seoul, 2001).

D. C. Swanson, *Signal Processing for Intelligent Sensor Systems* (Marcel Dekker, New York, 2000), 616 pp.

Ultrasonics International'99 with 1999 World Congress on Ultrasonics, June 29–July 1, 1999: Book of Abstracts (Copenhagen, 1999), 366 pp.

Underwater Acoustics: Proceedings of 4th European Conference, Rome, September 21–25, 1998, Ed. by A. Alippi and G.B. Cannelli (CNR-IDAC, Rome, 1998), Vol. 2, 1003 pp.

J. Walker and I. Flindell, *Noise Pollution* (Wiley, S.I., 2003), 224 pp.

WESTPRAC: Proceedings of the 7th Western Pacific Regional Acoustics Conference, Kumamoto, 2000 (on CD-ROM).

W. A. Yost, *Fundamentals of Hearing* (Academic, S.I., 2000), 349 pp.

N. E. Shmakova

Acoustical Physics, Vol. 49, No. 6, 2003, p. 739. Translated from Akusticheskiĭ Zhurnal, Vol. 49, No. 6, 2003, p. 864.

INFORMATION

X Brekhovskikh's Workshop on Ocean Acoustics and the XIV Session of the Russian Acoustical Society

The Shirshov Oceanology Institute of the Russian Academy of Sciences and the Russian Acoustical Society invite researchers and engineers to the X Anniversary Brekhovskikh Workshop on Ocean Acoustics, which will be held May 25–28, 2004. The workshop will be combined with the XIV Session of the Russian Acoustical Society.

The program of the workshop includes lectures, as well as oral and poster presentations. The scope of the workshop is defined as follows:

—Sound propagation in the ocean

—Acoustic tomography

—Ambient noise of the ocean

—Scattering and reflection of sound

—Signal processing

—Acoustic methods and means for ocean studies

—Oceanological characteristics important for underwater acoustics

—Ecological factors in solving acoustic problems.

The information necessary for future participants of the workshop is available at

e-mail: rav@rav.sio.rssi.ru

Tel: (095) 129-1936; (095) 124-6351; (095) 126-9835

Web: http://rav.sio.rssi.ru/school10.html

Mailing address: Organizing Committee of the Workshop on Ocean Acoustics, Shirshov Oceanology Institute, Russian Academy of Sciences, Nakhimovskiĭ pr. 36, Moscow, 117851 Russia.

1063-7710/03/4906-0739$24.00 © 2003 MAIK "Nauka/Interperiodica"